# Leading the Charge in Bone Healing:
## Design of Compliant Layer Adaptive Composite Stacks for Electrical Stimulation in Orthopedic Implants

by

**Ember D. Krech**



B.S. Mechanical Engineering, New Mexico State University, 2015

Submitted to the graduate degree program in Bioengineering and the Graduate Faculty of the University of Kansas School of Engineering in partial fulfillment of the requirements for the degree of Doctor of Philosophy.

---

Co-Chair: Elizabeth Friis, Ph.D.

---

Co-Chair: Kenneth Fischer, Ph.D.

---

Ronald Barrett-Gonzalez, Ph.D.

---

Steven Soper, Ph.D.

---

Barbara Kerr, Ph.D.

Date Defended: 18 February 2020

The dissertation committee for Ember D. Krech certifies that this is the approved version of the following dissertation:

# Leading the Charge in Bone Healing:
## Design of Compliant Layer Adaptive Composite Stacks for Electrical Stimulation in Orthopedic Implants

_____

Co-Chair: Elizabeth Friis, Ph.D.

_____

Co-Chair: Kenneth Fischer, Ph.D.

Date Approved: 18 February 2020

**Abstract**

The overall aim of this research is to develop a robust, adaptable piezoelectric composite load-bearing biomaterial that when integrated with current implants, can harvest human motion and subsequently deliver electrical stimulation to trigger the natural bone healing and remodeling process. Building on the preclinical success of a stacked piezocomposite spinal fusion implant, compliant layer adaptive composite stacks (CLACS) were designed as a scalable biomaterial to increase efficiency of power generation while maintaining mechanical integrity under fatigue loading seen in orthopedic implants. Energy harvesting with piezoelectric material is challenging at low frequencies due to material properties that limit total power generation at these frequencies and brittle mechanical properties. Stacked generators increase power generation at lower voltage levels and resistances, but are not efficient at low frequencies seen in human motion. CLACS integrates compliant layers between the stiff piezoelectric elements within a stack, capitalizing on the benefits of stacked piezoelectric generators, while decreasing stiffness and increasing strain to amplify power generation. The first study evaluated CLACS under compressive loads, demonstrating the power amplification effect as the thickness of the compliant layer increases. The second study characterized the effect of poling direction of piezoelectric discs within a CLACS structure under multiaxial loads, demonstrating an additional increase in power generation when mixed poling directions are used to create mixed-mode CLACS. The final study compared the fatigue performance and power generation capability of three commercially fabricated piezoelectric stack generators with and without CLACS technology in modified implant assemblies. All configurations produced sufficient power to stimulate bone growth, and maintained mechanical strength throughout a high load, low cycle fatigue analysis, thus validating feasibility for use in orthopedic implants.

The presented work in this dissertation provides a robust experimental understanding of CLACS and a characterization of how piezoelectric properties and composite structures can be tailored within the CLACS structure to efficiently generate power in low frequency, low impedance applications. The main motivation of this work was to develop a thorough understanding of CLACS behavior for implementation into medical implants to deliver therapeutic electrical stimulation and accelerate rate of bone growth, helping patients completely heal faster. However, the ability to tune composite stiffness by changing compliant material properties, type of piezoelectric material and poling direction, or volume fractions could benefit the energy harvesting potential in fields ranging from civil infrastructure to wind energy, to wearables and athletic equipment.

**Acknowledgements**

The completion of this work would not have been possible without so many that have supported, encouraged, guided and challenged me throughout this process. I thank God, for granting me the opportunity to pursue this degree and surrounding me with the people that have been such an integral part of the process.

Thank you Dr. Friis, for not only being an incredible research advisor, but for being a mentor and leader that continually inspires me to question everything and find solutions that will genuinely make a difference. I am so grateful for your consistent help, support and guidance throughout my time here. Dr. Fischer, thank you for stepping in and ensuring that I could pursue exciting opportunities while finishing my degree. Dr. B, thank you for your patience and wealth of knowledge of the "piezo world," that have helped me place this research in the wider context of the field. Dr. Soper and Dr. Kerr, your outside perspective is such an integral part to communicating and translating this research, so thank you for your time and commitment. An additional big thank you to Dean Agah and his generous support and advocacy for graduate research through the School of Engineering.

I would also like to extend a huge thank you to the many past and present members of the Friis lab research group. You all have made my time here such a rewarding experience: Nikki Galvis, Hadley Sis, Saskia Biesinger, Kyle Coates, Kelly Tong, Colton Lowe, Zach Pessia, Craig Cunningham, Morghan Alters, Tori Drapal, Ryan Downing, Josh Koski, Luke Lindemann, Jordan Gamble, Chris Tacca, and Anna Norman. A very special thank you goes to Eileen Cadel, who walked through so much of this process with me and kept me sane when research made me crazy. Thank you for never turning down an emergency watermelon margarita or Sylas and

Maddy's ice cream run, introducing me to the magic of KU basketball, and for always reminding me to proceed as if success was inevitable.

I would also like to express my immeasurable gratitude to Madison and Lila Self for their immense generosity. None of this would have been possible without their support. The experience that SGF has provided me is something I will treasure forever. To my fellow Fellows, you all have truly inspired me and I look forward to cheering you on as each of you makes a real difference in this world. To Stefani Buchwitz, Amy Benoit-Warlick, Tammie Zordel, and Christine Caine: thank you all for your tireless work behind the scenes to provide us with such a meaningful program.

Lastly, but certainly not least, thank you is not enough to adequately express my gratitude to my family. Mom, Dad and Tor, you all are my rock and I could not have done any of this without you. Your love, unending support and belief in me got me through all the ups and downs of this journey, and you all deserve an honorary degree for putting up with me. To my Velocity family, thank you for making Lawrence home. Forever forward.

**Table of Contents**

**List of Figures**

**List of Tables**

## Chapter I: Introduction

Time and quality of bone healing from orthopedic surgeries is problematic for many patient populations, resulting in a tremendous increase in cost of patient care and persistent pain and disability. Spinal fusion surgeries and severe long bone fractures are some of the most common gap healing circumstances in which there is a high incidence of nonunions. Even with the use of implants for stabilization, gap healing is especially challenging in difficult-to-fuse patients with diabetes and tobacco users. Incomplete healing and nonunions cause additional financial burden on an already fragile patient population, and substantially decrease quality of life for patients.

To supplement bone healing, several adjunct therapies are used clinically including synthetic bone morphogenetic proteins, low intensity ultrasound and electrical stimulation. For decades, electrical stimulation has shown clinical success in promoting bone healing and decreasing healing times in multiple orthopedic procedures (nonunions, spinal fusions, pseudarthroses, and stress fractures), especially in difficult-to-fuse patients. Bone healing and remodeling is initiated and regulated by electrical potentials. Thus, electrical stimulation delivered to the healing site aims to trigger the body's natural response to grow bone, and promote an osteogenic response leading to complete healing and positive patient outcomes.

However, most devices must be worn externally for extended periods of time, providing dispersed, transcutaneous current and require patient compliance, which significantly limits their success. Internal electrical stimulation devices provide stimulation locally at the healing site but require a large battery pack that is surgically placed under the skin, involving a second surgical site and additional surgery to remove the battery pack. Higher risk of infection, secondary wound healing issues and repetitive intervention decrease value of current internal electrical stimulation

devices. Although current methods of providing electrical stimulation have shown clinical efficacy, the drawbacks of current clinical devices have limited use and potential success in helping patients heal.

Piezoelectric materials emit electric charge in response to cyclic mechanical loading and have been explored as an alternative to batteries in many different applications, including producing usable power from human motion and walking. Piezoelectric ceramics can be effective energy harvesters but are most efficient at high frequencies and high impedances. At low frequencies as seen in human motion, the mismatch in device frequency and loading frequency amplifies the limited charge density and strain amplitude, making them less effective.

Cofired piezoceramic stacks, multiple piezoelectric elements connected electrically in parallel and stacked mechanically in series, are widely used in industry as actuators and increase efficiency of power generation at lower resistances by lowering the source impedance of the device. However, these piezoceramic stacked generators are incredibly stiff and brittle, designed to generate power from purely compressive loads, and could not withstand the repetitive loads experienced by typical orthopedic implants. Because of their adaptability, if piezoceramic stacks could be mechanically toughened to withstand physiological loads and electrically adjusted to enhance effectiveness at low frequencies while producing sufficient power, incorporating them into orthopedic implants to provide internal electrical stimulation at the healing site without a battery pack could address a large clinical need.

Utilizing these principles, stacked piezoelectric composites embedded in a spinal fusion implant have been shown to produce enough power to generate bone healing electrical stimulation without the use of a battery. Histology and CT results from a pilot ovine study showed promising evidence of enhanced fusion due to mechanically synced, non-constant

electrical stimulation provided by those implants. However, difficulty with the fabrication processes, design limitations, and high source impedance prevented scalability of this material configuration for use in other orthopedic implants.

This dissertation presents the development and comprehensive assessment of a novel piezoelectric composite, Compliant Layer Adaptive Composite Stacks (CLACS). The long-term goal of this research is to develop a scalable piezocomposite load-bearing implant material that is mechanically and electrically compatible with bone, creating osteoinductive implants to improve gap healing rates for all patients. The objective of this dissertation is to design, validate and elucidate the power generation capability and fatigue resistance of CLACS under compressive, torsional, and fatigue loads to test feasibility for their use in orthopedic implants. It is hypothesized that the use of CLACS will increase power production and fatigue resistance under loading conditions seen in orthopedic implants, thus producing sufficient power to promote bone healing without need for a battery.

The first chapter addresses the background and significance of this research. The impact of bone healing issues will be discussed first, followed by a review of the biology of bone healing and remodeling and potential mechanisms of action for the osteogenic response triggered by electrical stimulation. A thorough explanation of piezoelectric materials and power generation will follow. Finally, the history of tissue stimulation using piezoelectric materials will lead into discussion on designing a robust, structural piezocomposite biomaterial.

Specific Aim 1 of this work was to characterize the power production performance of CLACS at compressive loads representative of low frequency human body motion. CLACS with four compliant layer thicknesses will be designed, manufactured and electromechanically tested to understand power production as a function of compliant layer thickness through a range of

compressive loads, frequencies and resistances. Chapters 3 and 4 will present and experimental and theoretical assessment of CLACS.

Chapter 5 will focus on Specific Aim 2 and will present mixed-mode CLACS (MMCLACS). The effect of poling direction on MMCLACS power production under multiaxial loads experienced in low frequency human motion will be evaluated. This study will present the experimental results of three MMCLACS configurations with various poling direction orientations to understand power production as a function of poling direction under compressive loads, torsional loads and frequencies common in orthopedic implants.

The final study will present the results from Specific Aim 3. This study was designed to assess the fatigue performance of three piezoelectric stack generators with and without CLACS technology in a modified implant configuration. Utilizing a modified ASTM F2077 test plan, the electrical and mechanical low cycle fatigue behavior of three commercially manufactured piezoelectric generator configurations was evaluated. Additionally, the effect on power generation of CLACS within the generator was assessed. Chapter 6 addresses this study.

Chapter 7 concludes with a summary of the work presented, and a discussion of suggested future work for furthering this research. This work was intended to develop a thorough understanding of the feasibility of piezocomposites, specifically CLACS, for use as a load-bearing orthopedic implant biomaterial. The results of this work validate the mechanical and electrical integrity of CLACS, suggesting that integration within existing implant designs could deliver local bone healing levels of electrical stimulation without a battery. This solution could provide tremendous advantages for patients, physicians and the over-taxed medical reimbursement system; increasing success of complete bone healing and decreasing healing times.

## Chapter 2: Background and Significance

### Bone Healing

Albert Einstein once stated, “the problems we face cannot be solved with the same thinking that created them.” In order to develop a comprehensive solution, it is important to fully understand the problem. This section presents a review of scientific research surrounding the incidence and current treatments for bone healing. The innovative solution supported by this research presents an integrative approach to bone growth stimulation. Instead of chemically treating the symptoms, if one takes a step back and assesses the system as a whole, treatments can be targeted to treat the pattern of dysfunction leading to the end result. In this case, understanding the natural bone healing and regeneration process can inform solution design that will work with the body’s natural processes, and stimulate a natural healing pathway: leading to quicker, healthier and lasting bone growth.

#### *The Problem*

Orthopedic procedures account for almost 20% of all surgeries in the United States, but unfortunately complete bone healing is very challenging for many populations [1]. The process of bone healing is a complex, dynamic process and when successful, results in robust regeneration and complete restoration of the injured area. Comprehensive bone healing is the end goal for a variety of orthopedic interventions including fracture fixation, spinal fusion procedures, osteotomies and other gap healing procedures. However, 5-30% of patients report compromised or delays with gap healing most seen in traumatic fracture fixations and fusions [2]–[6]. When the healing process fails, delayed unions, pseudarthroses, and malunions persist and often lead to a nonunion diagnosis, resulting in over 100,000 patients each year in the United States [7], [8].

Practically a nonunion is defined as a permanent failure of healing following a fracture and the development of a "false joint," often a soft tissue callus or scar tissue formation around the fracture site. Clinically, there is not a clear consensus in nonunion diagnosis, but the United States Food and Drug Administration (FDA) defines a nonunion as "a fracture that has not completely healed within 9 months". The variable incidence and prevalence of nonunions is attributed to the lack of a standard diagnosis criteria and variation in anatomical regions of treatment [7]. Delayed union and nonunions require secondary interventions, further delaying the patients return to health and normal living activities. The most common interventions include implants for stabilization (i.e. intramedullary nails, internal plate and screw fixation) or bone grafts, as shown in Figure 1B [9].

A pseudarthrosis is defined as a failed fusion following a spinal arthrodesis, or spinal fusion surgery (Figure 1A). When more conservative treatments are unsuccessful in treating low back pain, a spinal fusion is the most common surgical treatment to alleviate pain [10], [11]. Disc degeneration is a common cause of chronic low back pain; when the intervertebral disc is damaged and compressed, nerves are pinched between the posterior vertebral anatomy causing chronic pain and sensory issues [12]–[14]. As such, a spinal fusion procedure aims to restore proper spacing between vertebrae by mechanically stabilizing the pair of vertebrae surrounding the damaged disc. During the procedure, the disc is removed, replaced with an implant that restores disc height, and the end goal is for new bone growth to fill in the gap between the two vertebral bodies and fuse the joint. However, when the joint does not fully fuse, instead of solid bone a softer scar tissue develops, causing substantial pain, disability and instability, resulting in pseudarthrosis [15]. Lumbar spinal fusions have increased over 200% in the last decade, with almost half a million procedures performed in 2017 [10]. Despite the recent innovation in

implant technology, nonunion, or pseudarthrosis rates are as high as 47% in lumbar spinal fusion procedures [16], [17].

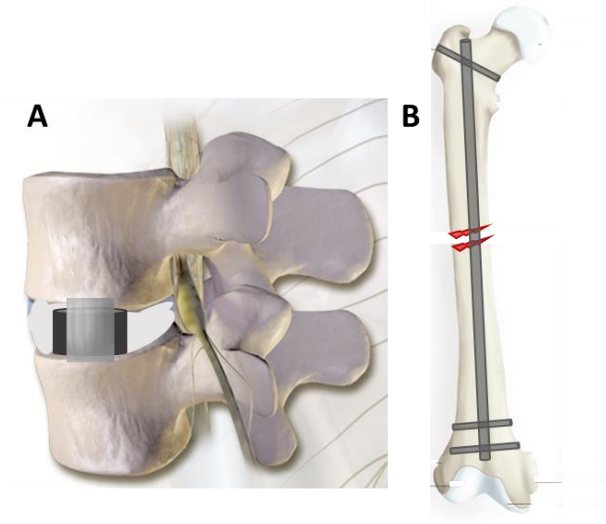


**Figure 1**. Implants used for mechanical stabilization of gap healing scenarios. **A.** Spinal fusion interbody implant with soft tissue formation. (Public domain, modified - Wikimedia.org) **B.** Intramedullary nail used to stabilize long bone fracture. (Public domain, modified – Wikimedia.org)

The specific cause, pathophysiological characteristics and universal definition of nonunion development remain unknown [18]. Comorbidities, age, sex, tobacco use, metabolic disease (i.e. diabetes), use of nonsteroidal anti-inflammatory drugs, and nutritional status are all patient dependent factors linked to an increase risk. Additionally, several patient independent factors can heighten risk of delayed healing including location of fracture, surgeon technique, soft tissue damage, gap width, and the presence of infection [2], [7], [19]. With the wide variety and severity of potential risk factors, it is estimated that over half of patients have at least one risk factor that can lead to the development of a nonunion or pseudarthrosis [19].

Because there is no expectation for nonunions or pseudarthroses to heal spontaneously, surgical (or other) intervention is necessary to stimulate the healing process [20]. Even with the use of implants to stabilize fractures, gap healing is especially challenging in difficult-to-fuse

populations, particularly patients with diabetes and those who use tobacco [21]–[25]. Specifically, diabetes and cigarette smoking have been associated with higher rates of pseudarthrosis, failed fusions, nonunions, and increased time to healing in a variety of orthopedic fracture and fusion procedures [26]–[31]. The presence of tobacco has been linked to higher rates of bone resorption and decreases in bone formation due decreased blood flow to the fusion site causing a lack of oxygen and calcium absorption at the desired site of healing [28], [30], [31]. Similarly, diabetes increases risk of infection and decreases production of growth factors causing a decrease in bone formation [27]. Failure rates of up to 50% have been reported for these patient populations, leaving surgeons with a challenging decision, some often choosing to forego surgery due to the high risk of failure, leaving patients without a solution [32], [33].

Tens of billions of dollars are spent each year in the United States to treat these conditions, and that does not include the socioeconomic burdens that bone healing complications cause such as loss of work, decreased productivity, limited functionality and most importantly a loss of quality of life for patients in which the bone never wholly heals [3], [34], [35]. Antonova *et al.* found that a tibial nonunion cost the patient $15,000 more than those without a nonunion, and were more likely to be prescribed strong opioids for longer periods of time [36]. The annual economic loss due to nonunions and delayed bone healing is estimated to be $3-6 billion [37].

Occurrence of nonunions are incredibly costly for patients, both financially and personally. The need for a second surgery drastically increases cost to the patient and causes extended pain, prolonged disability, and additional loss of work. In addition, physicians struggle to find effective treatment methods to successfully treat delayed healing in all patients, but especially the difficult-to-fuse patients with comorbidities. As the incidence of diabetes is expected to increase substantially in the next decade, as well as a continuing rising percentage of

patients with comorbidities, a cost-effective, efficient solution is necessary to help bone healing for these patients [33]. Despite recent improvements with orthopedic implants to stabilize fractures and gap healing, the rate of patients reporting unsatisfactory healing is too high, and the toll on society is rising with the aging population, presenting a substantial need for a clinical solution to prevent nonunions and pseudarthroses and their consequences.

*Current Adjunct Therapies*

To supplement bone healing and improve fracture and surgical fusion success rates, several adjunct therapies are used in addition to the primary implants. Revision procedures for nonunions are challenging for surgeons and typically require the use of implants to stabilize fracture and encourage natural bone regeneration [38], [39]. When surgeons feel that mechanical stabilization will not be sufficient for full fusion, bone stimulation therapies are prescribed. In the United States, bone stimulation is a $500 million market [40]. The most common stimulation treatments are bone graft, synthetic bone morphogenetic proteins (BMP), low intensity ultrasound and electrical stimulation.

An autologous bone graft (bone harvested from the patient's own body) is very common in lumbar spinal fusion procedures and is the current gold standard for fracture repair enhancement. This bone graft provides an osteoconductive and osteogenic environment and recruits osteoblasts (cells that form new bone) to the site, supporting new bone formation [41]. The side effects of autograft transplantation complicate the effectiveness; graft site pain, nerve and blood vessel injury, infection and wound problems all limit impact on bone healing at the fracture or fusion site [42].

Specifically in spinal fusion surgeries, over the last 15 years surgeons have combined synthetic BMPs with bone graft in hopes of accelerating the fusion process. BMPs are growth

factors that stimulate stem cells to differentiate into osteoblasts, inducing bone formation [43]. The combination of BMPs and bone marrow increased bone formation, suggesting a synergistic relationship and supporting use as an osteoinductive treatment option [44]. More recently, use has decreased due to incredibly expensive dosage and adverse events attributed to off-label use of BMP [45]. Several studies have linked use of BMP to major preoperative and postoperative morbidity, including ectopic bone growth causing nerve injury, bone graft failure, osteolysis, persistent motor deficits, infections and cancer [46]–[48]. Furthermore, BMP can cost $5,000-6,000 per fusion level, adding a significant cost to an already expensive fusion procedure [49]. When biochemical stimulation is not sufficient or preferred, surgeons also prescribe use of physical stimulation modalities through mechanical and electromagnetic measures to stimulate bone healing.

Low intensity pulsed ultrasound has gained some popularity recently as a bone growth stimulation therapy [50]. Utilizing therapeutic intensities of ~30mW/cm$^2$, daily treatments are applied to the healing site to induce bone growth. Studies have shown a decreased time to healing for some patient populations [51]. The exact mechanism of action for the bone growth stimulation is still unknown, but the micromechanical stress generated by the acoustic waves is thought to stimulate cellular responses and initiate osteoblastic activity and increase blood flow to the site [52]. Acceptance in the field is controversial, as there is not clear evidence for the effectiveness of therapeutic ultrasound for aiding the bone healing process [53].

*Electrical Stimulation*

Normal bone remodeling and fracture healing, discussed in the next section, is the result of signal cascades that trigger the cellular response for new bone formation. It has been shown that the signals that initiate this process are electrical in nature, thus the goal of all types of

electrical stimulation is to stimulate and/or enhance the signal cascade to supplement the bone regeneration process, leading to quicker, more robust bone regeneration and eventually a healthy, fully fused fracture or spinal arthrodesis.

The FDA has approved several different electrical stimulation treatments as adjunct therapies for nonunions and pseudarthroses. Direct current (DC) stimulation, capacitively coupled (CC) electrical stimulation, and pulsed electromagnetic fields (PEMF) are the main types of electrical stimulation used in the clinic. CC and PEMF are both non-invasive therapies that are delivered transcutaneously and rely on patient compliance. DC stimulators are implanted and provide stimulation directly to the fusion site. In a review of electrical stimulation effectiveness in spinal fusions, Cottrill *et al.* concluded that electrical stimulation increased odds of a successful fusion five-fold [54]. In 2016, Aleem *et al.* performed a meta-analysis of clinical studies focused on patient-important outcomes and concluded that patients treated with electrical stimulation as an adjunct therapy for bone healing were at a significantly reduced risk for nonunion and had less pain [55].

CC stimulation is applied through two electrodes placed on the skin overlaying the fracture/fusion site. An alternating current supplied by a low voltage external battery is applied which creates an oscillating electric field across the fracture site. The current levels are low enough that patient typically cannot feel the stimulation. Electric fields range from 1-100mV/cm and can be varied by adjusting the voltage amplitude and frequency within ranges of 1-10V and 20-200kHz, respectively [56]. Brighton *et al.* and Korenstein *et al.* found that osteoblast proliferation was increased with greater electric field strength and increase in time exposed to the electric field [57], [58]. Clinically, CC has been reported to increase lumbar spinal fusion success

[59]. In order to be effective, it is suggested that CC stimulation is applied for up to six months for 10-24 hours a day, and require frequent battery changes in the device [60].

PEMF, also known as inductive coupling, uses a device that houses a wire coil that induces a magnetic field when current is applied. When worn externally around the fracture/fusion site, the magnetic field creates an electromagnetic field across the injury, delivering a biphasic, quasi-rectangular waveform. Similar to CC, electric fields vary from 1-100mV/cm but vary over time based on the magnetic field [56]. Osteoblast proliferation is increased as well as upregulation in osteoinductive growth factors and calcium production, but a different cellular pathway is suggested as compared to CC cellular pathway [54], [61]. Several studies have shown positive results in increasing lumbar spinal fusion in high risk populations [16]. However, overall, PEMF has not shown consistent clinical success as a therapy for nonunions, and it is suggested that reliance on patient compliance and varied treatment times may cause the mixed results [40], [54]. This therapy also requires patients to wear a bulky, heavy device for ~2hours/day for up to nine months [54], [60].

Both CC and PEMF devices are utilized in the field as non-invasive adjunct therapies in gap healing orthopedic procedures. The electrical fields generated have shown some promising results in decreasing healing times for patients. However, both devices rely solely on patient compliance to wear devices for extensive hours at a time over a period of months in order to be effective, resulting in highly variable clinical data. Additionally, the stimulation is provided transcutaneously and is not delivered directly to the fusion site, potentially limiting the response due to a non-directed response through surrounding tissue. Implantable devices that provide electrical stimulation directly to the fusion site eliminate patient adherence issues and address issues with systemic responses.  In a recent review comparing types of electrical stimulation,

Cottrill *et al.* concluded that local DC stimulation provided by implantable devices lead to significant improvements in fusion rates in both preclinical studies (animal) and clinical studies, with exceptional results when used as a modality in difficult-to-fuse populations [54]. Among the discussed techniques, DC electrical stimulation is the most widely used in the clinic [62].

*Direct Current Electrical Stimulation*

For decades, constant DC electrical stimulation has shown clinical success in promoting bone healing in multiple orthopedic procedures, including nonunions, spinal fusions, pseudarthroses, and stress fractures [32], [63]–[69]. Implantable stimulators providing DC stimulation delivered directly to the gap healing site has shown great success in long bone fractures and spinal fusions [70]–[74]. Meril *et al.* and Rogonzinski *et al.* both found that overall fusion rates were increased with implanted bone growth stimulators, but the greatest increase was seen in smokers and high-risk patients [73], [74], and these results were supported with later studies [62].

DC electrical stimulation is applied through an implanted cathode (negative electrode) across the fracture/fusion site. An anode (positive electrode) is typically housed in an implantable battery pack that is placed in the soft tissue surrounding the gap healing site. Current clinical DC stimulation devices deliver constant current within a range of 5-100μA, but 20μA is most commonly used based on electrode surface area to deliver current densities in the range of 1-4μA/cm$^2$ [32], [56], [73]–[75]. Constant current is delivered to the cathode for six to eight months, increasing osteogenesis (bone formation) directly at the injury site. *In vitro* studies have shown that DC accelerates the proliferation and calcium ion metabolism, which plays a key role in regulation osteogenesis and bone metabolism, increasing regeneration rates [76]. The cellular pathway is not fully understood, but the most accepted theory is that a faradic reaction at the

cathode creates an electrochemical response. Specifically, hydrogen peroxide is produced and pH increases, thus decreasing oxygen concentrations which are linked to osteoblastic activity [77].

In all DC devices, the current is delivered through an electrode. Friedenberg *et al.* noted the importance of the spatial position of the cathode and anode, to obtain an effective current density across the fracture site [78]. In a review of electrical stimulation literature, Isaacson and Bloebaum suggest that current density and the subsequent electric field are the governing factors affecting the efficacy of DC electrical stimulation. Specifically, current density should remain under $2mA/cm^2$ to avoid injury from heat generation, and electric fields should remain below 10V/cm to prevent cell damage and death [79].

Improvements in fusion rates and decreased healing times are linked to the constant DC stimulation but current devices approved by the FDA use a battery to supply current to the cathode. The battery pack is implanted under the skin near the gap healing site, requiring an additional surgery site. Once the battery dies (typically after six to eight months), an additional surgery is required to remove the battery pack. The battery is typically removed six months following successful fusion, but often causes patient discomfort, immune reactions and increases risk of infection, often for high-risk patients [67], [80]. Surgeons also must be trained on electrode placement and battery placement, requiring additional training for correct implantation. Based on reoperation costs and device prices, the cost effectiveness of current DC stimulation devices may not be efficacious for most patients [54].

The majority of *in vivo* and *in vitro* studies have supplied a constant current to the electrode and have studied the effect of current levels, concluding that bone growth increases with increasing current [81]. Cho *et al.* studied the effect of pulsed DC electrical stimulation in a

rat model. They found that new bone volume and strength increased with the use of pulsed current (100μA, 100Hz, 200μs) as compared to constant 100μA current, suggesting that pulsed DC stimulation, which is more consistent with physiological signaling, may further increase effectiveness and decrease inflammation and necrosis [82]. Although DC stimulation has shown clinical efficacy, the drawbacks of current clinical devices have limited use and potential success in helping patients heal. An understanding of natural healing processes could lead to an integrative approach that builds on proven positive results of DC stimulation, while mitigating added risk present in current devices. The next section will focus on the natural bone healing process.

Biology of Bone Remodeling and Healing

All electrical stimulation adjunct therapies were developed based on a foundational understanding of bone remodeling and fracture healing. Bone is unique in its ability to regenerate and heal without formation of fibrous scar tissue and regain pre-injury mechanical properties. Bone healing and regeneration occurs in a stepwise process: initial hematoma development, inflammation, proliferation and differentiation, and finally ossification and remodeling [83]. After the inflammatory response, mechanical and molecular signals initiate the healing response. Typically, gap healing that is stabilized with implants (as seen in most long bone nonunion reoperations and spinal fusions) occurs through secondary healing. The transfer of load from implant to the gap healing site creates axial micromotion and mechanical stimulation which causes initial inflammation to form into fracture callus, followed by woven bone which is then remodeled into lamellar bone [3], [83]. It is important to note that the healing of bone in spinal fusions does differ slightly from bone healing through fractures. Fracture healing includes the

formation of callus and subsequent endochondral ossification, while the cartilage endplates of the vertebrae in a spinal fusion anchor the bone formation. However, the high-level understanding of the electrical signals that stimulate the bone healing process are similar.

*Endogenous Electrical Signals*

Electrical signals generated through mechanically mediated stimulation are thought to be a fundamental factor in the bone healing and remodeling process. Wolff's law states that "the basic form being given, bone adapts to the load applied," meaning bone architecture adapts in response to dynamic loads [75], [84]. This phenomenon is demonstrated through bone loss due to bed rest (or astronauts in orbit), and hypertrophy, or increased bone density seen in professional athletes.

In the 1950's research into electrical stimulation for bone regeneration progressed rapidly after Yasuda reported new bone growth surrounding a cathode delivering continuous negative current [85]. It was later discovered that when bone was subjected to bending loads, areas under compression developed electronegative potentials and electropositive potentials were generated under tensile stresses [85], [86]. Fukada and Yasuda were the first to describe the piezoelectric properties of dry bone, referring to the electropotentials generated in the collagen matrix under dynamic loads thought to trigger an osteogenic response [87]. Collagen fibers are oriented parallel to the long axis of the bone, thus in the direction of applied mechanical load which results in the piezoelectric response [88].

Bassett related the piezoresponse of dry bone to Wolff's Law and concluded that under applied loads, strain in less dense regions is transformed into negative electrical potentials (ions) that align in the extracellular matrix, signaling osteoblasts to remodel bone architecture to withstand the load applied. The more dense, stiffer regions, experience little to no strain, and

thus no electrical potentials develop. This was verified in a canine study that clearly indicated that negatively charged surfaces preferentially accelerated new bone growth [89], [90]. Recent studies have found that collagen is the major constituent of bone, cartilage and tendon responsible for the direct piezoelectric effect [91], [92]. The electric signals generated in response to internal forces in the collagen fibers in bone are transmitted through the extracellular matrix to the voltage receptive channels in the cell membrane. This process is known as mechanotransduction and is thought to be primarily regulated through osteocyte cells (osteoblasts that are embedded in new bone matrix). Osteocytes then communicate with the osteoblasts and osteoclasts to activate signaling cascades, that will be discussed in the next section. The intracellular signals are processed through the nucleus of the cells, leading to stimulation of cellular activity responsible for new bone matrix production, tissue repair and cell growth and proliferation [93].

Later, Friedenberg and Brighton suggested a different type of electrical potential that also plays a role in regeneration. They described an electronegative steady-state potential or bioelectric potential that occurred in non-stressed bone in areas of regeneration, active repair, and growth [94]. It was also shown that bone is formed under electronegative potentials and resorbed under electropositive potentials, and that adaptive remodeling following a fracture follows the same tendency [63], [95]. Further, experiments on wet bone demonstrated strain generated potentials that were developed from charged bone matrix proteins that generated streaming potentials during mechanical deformation. Ion flux generated within interstitial fluid through canaliculi applies shear stress to cells, increasing metabolic activity and stimulating bone growth [43], [76], [96]. In spite of considerable research in the field, there is not consensus on the role piezoelectricity and streaming potentials play in transient changes of electrical potentials

observed in bone remodeling and healing, or how cells respond to mechanical stimuli (mechanotransduction) to elicit specific responses – i.e. osteoblast activity and bone regeneration.

The role of strain and electrical potentials in bone repair are still not fully understood, however both have been reported to be an important component in the healing process. Following a fracture or bone injury, the area surrounding the break becomes electronegative, with the strongest peak of electronegativity appearing over the fracture site [97]. Zigman *et al.* measured electrical potentials within femur fractures intraoperatively, before and after fixation of the fracture. Near the fracture site strong negative potentials were measured (-200-270mV). Although not explicitly studied, it was concluded that osteosynthesis (bone fixation) affects the electric potentials of the operated bone. It was also found that the bone potential becomes more electronegative following reduction and fixation, which is suspected to initiate the bone healing process [98].

Although still not fully understood, the mechanical stress and subsequent electric field creation are generated within the complex structure of bone, resulting in both the presence of piezoelectric polarization and streaming potentials. Recently, Ahn and Grodzinsky proposed a hypothesis that piezoelectricity and streaming potentials work in conjunction; by changing the surface charge with mechanical stress, the piezoelectric response of collagen influences the magnitude of the streaming potential during compression [99]. Bone is a composite material, continuously changing over time in response to external stimulus. Therefore, developing a comprehensive, integrative understanding of the electric metrics associated with osteogenesis is likely not feasible because of the patient-specific characteristics, highly variable tissue conductivity and dielectric properties [79].

In summary, through the application of mechanical load, electrical stimulation occurs naturally in bone [75], [85], [86]. Under compressive loads electronegative potentials are generated and electronegative potentials have been shown to induce osteogenesis and form new bone [63], [90]. Clinical electrical stimulation of all types prescribed as an adjunct therapy to aid in gap healing (DC, CC, and PEMF) is meant to enhance the effect of natural electrical potentials and boost the natural osteogenic process.

Scientists and clinicians began to investigate the effects of electric fields on bone growth and repair, and clinical use of electrical stimulation was adopted by the early 1970's. Dwyer and Goldenberg both reported clinical success utilizing direct current stimulation for bone healing in spinal fusion procedures and treatment of nonunions, respectively [100], [101]. Measured endogenous electrical potentials led the design of implantable DC devices with the goal of modulating cellular activity that would enhance bone healing. It was found that following a fracture, there is a sharp peak in negativity measured at the fracture site, creating potential gradients between 10 and 50mV/cm [75]. Resistivity of bone has been measured to be ~30kΩ-cm [102], predicting endogenous current densities in the range of 3-20μA/cm$^2$. Consequently, this same range was found in strain-related potentials generated during bending [75]. This provides insight into current magnitudes used in initial DC bone growth stimulation studies that were consistently 10-20μA. Later studies have verified that increased current levels up to 100μA further increase rates of fusion [32], although current densities remained in the 3-5μA/cm$^2$ range. Current devices on the market (SPF Biomet) supply constant DC at densities <5μA/cm$^2$ [68], [74]. As discussed in the previous section, these current magnitudes, which match measured *in vivo* densities, have shown success in stimulating quicker and more robust fusion in long bone nonunions and spinal fusions.

*Mechanism of Action*

The dynamic nature of bone is regulated by a high rate of metabolic activity with constant formation and resorption through osteoblastic and osteoclastic activity, respectively. The rapid response to physical and biochemical signals is attributed to the highly vascular nature of healthy bone architecture [103]. In the case of nonunions and spinal fusion, full fusion is achieved when remodeling produces lamellar bone oriented along new lines of stress developed by the implant/bone interface, so the system can undergo physiologic loads without injury. *In vitro* studies have identified potential mechanisms that cause delayed healing and the development of pseudarthroses and nonunions. There is agreement that, on the cellular level, a decrease in osteoblast proliferation and function is a major cause. On a molecular level, two signal pathways, BMP and Wnt, both influence regulation of new bone growth and regeneration and have been the foundational science of most regenerative therapies used in the clinic.

Black suggests that there are two primary processes that occur at the electrode during a faradic reaction; electrical field generation and chemical changes to the microenvironment. In all DC devices, the electric field that is generated from the release of negative current at the implanted cathode is thought to attenuate through the tissue with the relationship $1/r^2$, where r is the distance from the electrode. The cellular response is expected to only be effective within this sphere of influence but was designed to mimic biopotentials measured in healthy bone. The exact form and reach of the stimulating signal(s) is not well understood. However, in CC and PEMF scenarios, changes to the biochemical environment surrounding the healing site are impossible with external electrodes, so the link to bone healing of those two stimulation mechanisms would lead to an assumption of electrical signals as the stimulatory trigger. Most *in vitro* studies on DC

stimulation conclude that there is a combined effect of chemical and electrical alterations at the healing site [75].

*BMP Pathway*

The cellular mechanism of action of DC stimulation is directly related to the upregulation of several osteoinductive (osteoinduction is the formation of osteoblasts from preosteoblast progenitor cells) regulators of bone formation. Most notably, DC stimulation upregulates several bone morphogenetic protein (BMP) growth factors, specifically BMP-2, BMP-6 and BMP-7. These are all linked to osteoblast and chondrocyte proliferation and differentiation, thus stimulating the ossification process of early healing callus and bone healing [104]. Electrode-based constant negative DC stimulation is thought to create a faradic reaction at the cathode (typically titanium).

The chemical reaction at the electrode results in a substantial reduction in oxygen, a slight increase in local pH and a modest production of hydrogen peroxide [77]. *In vitro* studies have shown that hypoxic environments increase osteoblastic proliferation and suggest a triggering role in bone remodeling [105]. Additionally, the production of hydrogen peroxide stimulates release of vascular endothelial growth factor (VEGF) which is suspected to promote differentiation of osteoblasts by increasing mineralization of bone matrix suggesting value in acceleration of large bone defect healing [106], [107]. Slight increase in pH has shown a decrease in osteoclastic resorption, allowing osteoblastic formation to progress, improving bone mineral accretion [108]. This chemical reaction is dependent on the biologically effective sphere or field of influence, and is estimated to be approximately 5-8mm away from the cathode [16], [75]. It is likely that the electrochemical reaction is responsible for the measured upregulation of BMP growth factors [16]. In summary, constant DC delivered through a metal cathode causes

both a local pH change and hypoxic environment, which stimulates a BMP regulated osteogenic response linked to accelerated bone growth.

*Wnt Pathway*

A different pathway suggests a second cellular mechanism of action related to the Wnt signaling pathway, which plays an important role in bone healing and inducing osteoblastic proliferation and differentiation [109]. *In vivo* studies have shown that Wnt signaling increases injury-induced proliferation and osteoblast differentiation in a fracture model, suggesting the Wnt pathway is among the most attractive therapeutic targets to treat bone defects and injuries [110]. Intracellular Wnt signaling has been separated into three main pathways, but the canonical Wnt signaling pathway has been investigated and characterized as the most strongly implicated in osteogenesis and bone turnover [111].

Specifically, sclerostin, a glycoprotein secreted by osteoblasts embedded in bone matrix (osteocytes), is an inhibitor of the Wnt canonical pathway [112]. Thus, antibodies directed against sclerostin have been studied as a therapeutic option in the treatment of diseases with increased bone resorption, such as osteoporosis [112]. A systemic sclerostin antibody has shown success in bone formation at fracture sites leading to improvements of bone strength, bone mass and fracture healing in animal studies [113]. Although not yet well understood, elucidating the complex mechanisms in sclerostin production and Wnt signaling remains important, as it could lead to development of novel therapies that specifically target the adaptive bone healing response to loading-induced stimuli rather than relying on synthetic, non-specific, ineffective treatments to prevent loss of bone mass and increase fracture healing rates.

As described in the previous section, mechanical loads directly stimulate osteoblasts. It has recently been discovered that mechanical loads on bone, in which electronegative potentials

are generated, also downregulate sclerostin production, which indirectly stimulates osteogenesis [112]. Sclerostin expression increases following unloading, in which positive electrical potentials are generated, with the consequent inhibition of Wnt signaling and associated bone loss [114]. Sclerostin secretion is in sync with mechanical loads experienced at the bone healing site, and bone formation is inhibited. To corroborate this with strain-induced bone formation, an inhibitory theory predicts that loading inhibits sclerostin production, thus allowing bone formation to proceed. It is likely that both the stimulatory and inhibitory pathways work synergistically to regulate load-adapted bone architecture [115].

To design effective therapies to aid in bone healing, sclerostin has recently been further studied. Veverka *et al.* studied the structure of sclerostin and identified binding sites for heparin. The primarily positive electrostatic potentials of the sclerostin molecule, provide several binding sites for heparin, a highly negatively charged molecule, suggesting a functional role in localizing sclerostin to the surface target cells related to Wnt inhibition [116]. Sclerostin expression inhibits the Wnt signaling cascade, but in response to electronegative signals, the positively charged sclerostin molecules are bound, allowing the Wnt pathway to proceed. DC electrical stimulation produces negative ions, which may attract and bond to sclerostin, thus facilitating the Wnt signaling cascade to progress, inducing osteogenesis and subsequent bone healing. Bone healing through sclerostin inhibition is thought to be faster than the faradic reaction and is linked to improved bone density, bone healing and could counteract osteoporosis [113], [114], [117].

*Bone Healing Summary*

The effect of DC stimulation is increased bone growth, but the exact mechanism of action is not fully understood. There is likely not a linear pathway regulating bone's adaptive responses to loading and electrical stimulation, but rather multiple pathways in which osteoblasts and

osteocytes play important roles [118]. Morse *et al.* investigated the effect of long-term sclerostin deficiency and mechanical load on bone formation in a mouse model. They found that sclerostin deficiencies protected from bone loss under decreased loads but resulted in increased bone formation under increased loads. Thus it was concluded that sclerostin is involved in mechanotransduction, but is not the sole modulator of load-induced bone adaptation [117]. The BMP pathway is understood to be a result of an electrochemical reaction at the negative electrode, and the Wnt pathway is suspected to be induced by cellular response due to electrical signals. Further research should investigate the possible combined result of both a faradic reaction BMP pathway and the Wnt pathway due to electronegative DC stimulation.

It is likely that electrical and chemical signaling play a role in both osteoblastic regulation and the mechanotransduction of osteocytes. Mechanically synced DC stimulation, specifically the release of negative current in sync with loading and unloading of the fusion site, would provide an effective, targeted therapy that addresses both potential pathways and stimulates faster, more robust bone healing, preventing development of nonunions and improving patient outcomes. Piezoelectric materials produce electrical signals in sync with repetitive mechanical loads, and could be investigated to stimulate a natural bone healing process.

## Design of Piezoelectrics for Power Generation

Energy harvesting is defined as the conversion of ambient energy to relatively low levels of power (typically in the nanowatt range) from mechanical load, vibrations, temperature gradients, or light. Extensive research has been initiated to further develop technology to convert sources of waste energy into viable electricity to power small electronic devices efficiently without need for a battery. Of the available energy sources, mechanical and vibration-based

sources have proven to provide more effective energy transfer due to the higher power density of such devices and the better lifespan [119]. Although several types of energy harvesters exist (piezoelectric, electromagnetic, electrostatic, etc.), piezoelectric devices provide the maximum conversion proficiency, have the most developed fabrication techniques and are the most easily integrated into existing complex systems [120]. Piezoelectric materials and devices have the ability to match both mechanical and electrical impedances of structures, increasing their energy conversion capability, and creating a vast research field over the last decade. For the rest of this dissertation, energy harvesting and power generation may be used interchangeably.

*Piezoelectric Materials*

As Fukada, Yasuda and Ahn observed, bone generates electrical potentials in response to dynamic mechanical loads and is described as piezoelectric [87], [99]. The Greek roots of the word 'piezoelectric", piezo meaning to press, and electric meaning a source of electric charge, describe the behavior of these materials: charge generation in response to applied load. This phenomenon was originally discovered in the crystal structure of quartz by Jaques and Pierre Curie in 1880 and was later found in other natural materials including tourmaline, topaz, and Rochelle salt. Crystalline minerals become electrically polarized when subjected to mechanical force, exhibiting the piezoelectric effect: tensile and compressive loads generate voltages of opposite polarity in proportion to the applied load. The electric fields generated in natural materials were quite small and not very useful for power generation.

However, ferroelectricity, or spontaneous electric polarization, was discovered in ceramic materials in the 1940s and 50s initiating research into piezoelectric performance, leading to the development of electric devices utilizing the piezoelectric effect. Specifically, the discovery of barium titanate and lead zirconate titanate (PZT) prompted decades of research into piezoelectric

ceramic formulations. Today, there are several classes of synthetic piezoelectric materials including single crystals, ceramics (piezoceramics), polymers, and various composites [121]–[123]. Piezoceramics are much more sensitive than natural materials, are chemically inert, more widely used in load-bearing applications due to their high strength, and are highly tailorable and inexpensive to manufacture, and thus are the industry standard [124]. Polyvinylidene fluoride (PVDF) is a widely used piezoelectric polymer because it has a large strain value and can be tailored as a composite to match various mechanical stiffnesses [125]. Although there is a vast variety of piezoelectric material compositions, including polymers and ceramics, the remainder of this section will focus on PZT, as it is the most efficient and widely used piezoelectric material in industry, and most applicable for this dissertation [124].

Piezoceramics, like PZT, make up a considerable group of piezoelectric materials and are defined as ferroelectric materials with polycrystalline structures. At high temperatures above the Curie temperature (>~300°C), within the crystal lattices there is a balanced equilibrium between positive and negative charges (cations and anions), creating a neutral polar axis and centrosymmetric state. At lower temperatures, the positive and negative charges move away from each other, creating spontaneous dipole moments within each crystal (i.e. ferroelectric materials). Among different ceramic grains (groups of crystals) the dipole moment orientation varies. The ability of piezoceramics to convert kinetic energy to electrical energy, and vice versa is dictated by the Curie temperature of the material. The piezoelectric property of the material is lost above the Curie temperature, limiting use of piezoceramics to fairly low temperature applications.

*Poling Piezoceramic Materials*

Due to the polycrystalline nature of most piezoceramics, a bulk piezoelectric response of the material requires uniform alignment of all dipoles. The dipoles are created by the position of the positive ion, and the poling direction is defined as the direction from the center of the crystal to that positive ion. The poling process is required in order to align the dipoles (polar axes of individual crystal segments) of the polycrystalline material. A domain is a region with like-oriented dipoles and the microscopic ferroelectric domains must be oriented in one uniform direction. A polycrystalline material, like piezoceramics and PZTs, consists of segments with different polar axes, resulting in a random alignment of dipoles. In this state, the material does not exhibit any piezoelectric effect; when strained the generated electrical potentials will be random and the material will not have a net polarization.

Poling makes a material piezoelectric by exposing the material to a strong direct current field, which causes molecules to move freely and thus the electric dipoles are aligned corresponding to the direction of the applied electric field (Figure 2). For PZT, poling is typically done in an elevated temperature (below the Curie temperature) oil bath at poling fields ranging from 2-4kV/mm [123]. When the electric field is removed, the majority of the dipoles remain permanently polarized and the bulk material is polarized in the direction of the applied field. This polarization direction is linearly related to the voltage polarity generated when load is applied in a direction parallel to the poling axis, and the amplitude of the voltage generated with respect to the direction of the load.

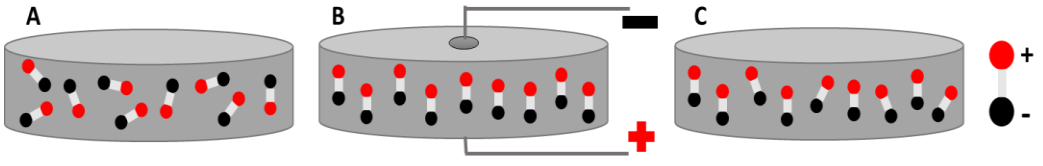


**Figure 2**. Poling process of a piezoelectric disc. **A.** Following sintering, the domains are randomly arranged. **B**. Application of an electric field using electrodes causes dipoles to align with applied field. **C.** After the field is removed, some domains shift, but overall polarization remains aligned with the applied field.

Most often, poling is done to make the PZT material more piezoelectrically sensitive in a prescribed direction parallel with the direction of the applied forces in the desired application. Poling of bulk piezoceramic materials can be done in multiple directions. The most common poling direction is axially, through the thickness of the material (Figure 3B). This relates to the most common use of PZT actuators and generators being used in compression, so the most efficient power generation is achieved when the compressive load is aligned with the axial poling direction [126]–[128]. Some applications, like ultrasonic motors and transducers, utilize radial poled piezoelectric cylinders or discs [129] (Figure 3A). In other applications, shear or longitudinal poled elements, are utilized as torsional actuators [130]. Following the poling process, electrodes are added to the material to collect generated charge in the final application. Electrodes can be applied in multiple configurations to increase efficiency for specific applications, though the standard application is a fired-on silver, nickel or gold electrode on the face of the bulk material shape (i.e. face of the disc or plate).

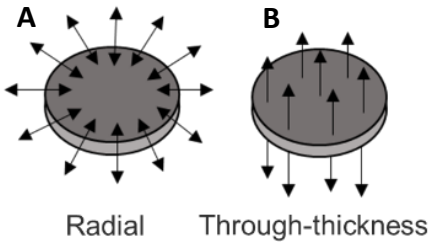


**Figure 3**. Radial and through-thickness poled PZT discs. Arrows represent positive poling direction.

*Piezoelectric Constants*

Several piezoelectric material constants are used to describe the measured and expected response of specific materials and configurations. When subjected to a mechanical stress, the internal structure of the crystals is deformed, causing an irregular arrangement of dipoles and disrupting the charge alignment. This separates the positive and negative charges on opposite

faces, subsequently creating an electric field across the material. The surface charge density can be collected via surface electrodes [121]. The electric charge that is generated is proportional to the deformation, and thus the load applied. The inverse piezoelectric effect, in which mechanical deformation of the crystalline structure is induced by an applied electric field, is utilized to create actuators. The variety of metal-oxide piezoceramics and subsequent engineered devices have developed a whole new field of research, and scientists have tailored material composition, shape, and electrode composition to meet design requirements for energy transduction [123].

The piezoelectric properties of PZT are determined by the perovskite structure of the crystal and the poling direction of the bulk material. A deformed PZT material will cause a dipole as the titanium ion or zirconium ion deviates from its position, creating a voltage. A compressive force parallel to the poling direction will generate a voltage of the same polarity as the poling voltage, and vice versa [131]. Under a dynamic load, piezoceramics produce an alternating voltage. When a compressive load is applied parallel to the poling direction, the voltage generated is linearly proportional, up to a material-dependent stress that damages the material.

The relation between the poling direction of PZT, the generated electric field, and the loading direction is described by several piezoelectric constants. The anisotropy of the piezoceramic creates physical constants that relate the energy conversion as a function of the poling direction and the direction of the load applied. Performance of PZT (and all piezoelectric materials) is described by several material property coefficients. In a short-circuit environment (no outside resistance), the deformation of domains generates charge according to the linear relationship given by

$$D_i = d_{ij}\sigma_j$$

where the charge per area that can be generated, $D_i$, by an applied mechanical stress, $\sigma_j$, is linearly related to $d$, the piezoelectric charge constant [132], [133]. This linear relationship is true at low voltages and low mechanical stress levels, as it does not account for the non-linear processes caused by reversible or irreversible domain wall displacements [131]. Thus, experimental measurements may only agree with these calculated values at very low voltages and low input frequencies, as such this relationship will be used illustrate the piezoelectric effect for this work.

$D_i$, the charge per area is a function of polarization and the subscript describes the surface direction of the electrode, specifically the direction perpendicular to the face of the surface electrodes on which the generated charge is collected. The subscript of the stress applied represents the direction of applied force [127]. A piezoelectric constant is defined by two subscripts, linking the electrical and mechanical quantities. Given a standard cartesian coordinate system, the first subscript is the poling direction and gives the direction of the dielectric charge produced. The second subscript is the direction of applied force, mechanical stress or strain. The piezoelectric charge constant, $d_{ij}$, describes the induced polarization per unit stress applied and is commonly expressed in Coulombs per Newton (C/N). This constant is also known as the piezoelectric modulus as it describes the change in volume upon application of an electric field [124].

The X, Y, Z of the coordinate system is represented by subscripts 1,2,3, respectfully, where '1' is parallel to the poling direction, and '2' and '3' are orthogonal to the polarization axis. "4", "5", and "6" represent the shear planes around '1', '2', and '3' respectively. Most PZT materials have three distinct piezoelectric constants $d_{31}$, $d_{33}$, and $d_{15}$, due to symmetry, crystal classes and other material constraints (assuming transverse isotropy). An electric field and

mechanical stress along the poling axis with electrodes perpendicular to the 3 axis, will be indicated with a '33' subscript. A '31' subscript indicates a stress applied orthogonal to the polarization axis, with the same electrode configuration as the '33' case. Conversely, a '15' subscript describes an applied shear stress with a resulting electric field that is perpendicular to the poling axis. Most often, the poling electrodes are removed and replaced by electrodes on a second pair of faces. Typically, $d_{31}$ is half of $d_{33}$, and $d_{15}$ is the largest and is often about five times larger than $d_{31}$ [134]. However, in practical applications, it is difficult to load a ceramic structure in shear, making generating voltage from the $d_{15}$ constant challenging. Figure 4 shows the three different relations given different loading and poling directions.

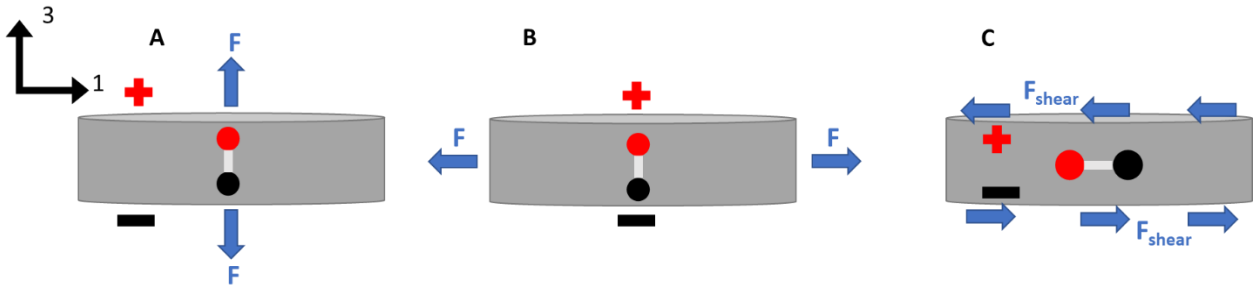


**Figure 4**. The red and black dipoles represent the alignment of dipoles (i.e. positive poling direction). Note for all discs, the top face is the positive electrode and the bottom face is the negative electrode. **A.** Represents loading and poling conditions that would invoke a 33-mode response. **B.** Represents loading and poling conditions that would invoke a 31-mode response. **C.** Represents loading and poling conditions that would invoke a 15-mode response.

The piezoelectric voltage constant $g_{ij}$ describes the induced electric field per unit of mechanical stress applied. Similar to $d$, $g$ can also be classified in terms of directions, with the same subscripts based on poling direction and load applied. It is related to the piezoelectric charge constant by the permittivity, $\epsilon$, of the material (the ability of the material to store electrical energy) given by

$$g = d/\epsilon$$

A high piezoelectric voltage constant, $g$ is desirable for high voltage generation due to an applied stress. The directional relationship of the $g$ constants for a given material follow the same relationship as the $d$ constants, due to the linear relationship between $g$ and $d$.

Although $d$ and $g$ are common in defining specific piezoelectric material properties, the electromechanical coupling factor is the best single measurement of the strength of the piezoelectric effect of a material [123]. The electromechanical coupling coefficient, $k$, is a parameter that is used to compare different piezoelectric materials, and the relation in terms of $k^2$ is given by

$$k^2 = \frac{mechanical\ energy\ converted\ to\ electrical\ energy}{input\ mechanical\ energy}$$

For a given electric field, it measures the fraction of mechanical energy converted to electrical energy, and is a great measure of efficiency [123]. In engineering and design applications, the electromechanical coupling should be sufficiently strong, and can aide in efficient design [135]. Due to the inability of complete conversion of mechanical to electrical energy, the value of $k$ is always less than one.

Piezoelectric material constants are useful to develop numerical and electromechanical models of PZT energy harvesting devices. The piezoelectric charge constant, $d_{33}$ is commonly utilized as a low cost means for characterizing a piezoelectric material. Batch quality, unit consistency, material defects, processing or handling issues, insufficient poling, and damage can all be reflected in a measured $d_{33}$ value [133]. Testing units used to measure material properties typically report values at the resonance frequency of the material. However, it should be noted that all piezoelectric properties are nonlinearly dependent on the amplitude and frequency of the load applied, as well as mechanical and electrical boundary conditions [126], [136]. The piezoelectric properties of bulk materials are typically measured using high frequencies

(typically at resonance), and may not be accurate at lower, off-resonance frequencies. When predicting the piezoelectric response, the model parameters should closely reflect the conditions for which the device will undergo.

*Hard and Soft PZT*

As mentioned above, PZT is the most common piezoceramic used in engineering applications. The development of PZT for various applications has led to two main compositions, hard and soft PZT. The perovskite crystal structure of PZT is tolerant of element substitution, commonly referred to as doping. Commercial PZT materials are often doped to tailor mechanical and piezoelectric properties. Hard PZT materials, commonly referred to as Navy Type I and Navy Type III (PZT-4, PZT-8), are often used in load-bearing applications because of their higher stability and high voltages. They do have a lower piezoelectric constant and a lower loss, because the oxygen vacancies within the crystal structure do not allow much domain wall motion. Conversely, soft PZT materials, commonly referred to as Navy Type II (PZT-5A, PZT-5H) have higher piezoelectric constants but larger losses. The metal vacancies in the crystal structure facilitate domain wall motion, and thus increased friction contributing to higher losses. In terms of design, soft PZT is utilized in low frequency applications because of the high electromechanical coupling, high permittivity and electrical resistance [120]. Shahab *et al.* found that soft PZT materials produced more power at off-resonance frequencies, as compared to hard PZT materials in a bimorph beam study [120]. In terms of energy harvesting research, PZT-5A and PZT-5H are most widely implemented [137].

*Material Configuration*

Piezoceramics, primarily barium titanate and PZT, have attracted the most attention in the energy harvesting field. The manufacturability of PZT is a benefit of design integration in energy

harvesting and power generation applications. PZT powder can be pressed and/or sintered into a wide variety of shapes and configurations. PZT formulations are often utilized to withstand large stresses and to match mechanical impedances of structures. They are brittle, strong materials, with an elastic modulus in the gigapascal range [133]. As mentioned earlier, PZT also has favorable piezoelectric properties, as compared to piezoelectric polymers, and is the most widely used in engineering applications. The mechanical design of the piezoceramic device also strongly affects the electrical performance and is a focus of research in the area.

In power generation applications the configuration of the material strongly impacts the efficiency of energy conversion. The ability for PZT to deform under load is directly related to the magnitude of charge generated. Tall PZT cylinders fixed at both ends will expand radially more than a thin plate of the same volume, subsequently converting more mechanical energy input to usable electrical energy. Monolithic structures and stacked layers of thin PZT elements are also used in specific applications to withstand higher loads or impact loading. Monolithic or bulk PZT cylinders have a fairly low capacitance, and thus tend to lose significant energy in post processing. To increase the capacitance, thin elements are often stacked together with alternating electrodes. These cofired stacks are used as sensors, generators and actuators in various applications. Most stacks consist of multiple PZT elements stacked mechanically in series and electrically connected in parallel (Figure 5). This technique increases energy conversion, while lowering impedance and increasing capacitance. With all elements adhered or sintered together, an axial force will act simultaneously on each element. The charge generated is a function of the $d_{33}$, the force applied and is proportional to the number of elements in the stack. However, the voltage generated is directly related to the $g_{33}$ constant and thickness of the element and inversely related to the cross-sectional area. In sensor applications with this stack configuration, the

voltage generated is linearly related to the force applied, but is the same for a monolithic element or a stacked configuration of the same volume. Stacks are commonly used for the higher charge generation, higher capacitance and thus lower impedance, as discussed in the next section.

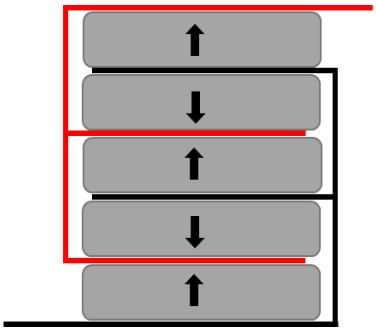

**Figure 5**. Schematic of a cofired PZT stack. Arrows represent the positive poling direction.

To harvest energy from cyclic motion, PZT thin films, thick films and plates are the most commonly used for their ease in integration into cantilever beams. Beams are the most widely researched configuration, and consist of one or two layers of active piezoelectric material bonded to a passive substrate. One end is fixed, creating a cantilever that can oscillate under a given electric field or produce usable energy from the vibrations. PZT particles and fibers are also used to create 0-3 or 1-3 composite structures, but not widely used in energy harvesting [119]. The mainstream focus of piezoelectric energy harvesting has been on linear and nonlinear beams and plates with piezoelectric layers [135]. The development of multiple numerical and electromechanical models has optimized the use of cantilevered energy harvesters and have developed optimal electrical and mechanical conditions [138], [139]. For the purposes of this dissertation, the focus of the rest of this chapter on power generation will emphasize design techniques for low frequency energy harvesting.

The electromechanical response of piezoceramics depends on a number of factors, including poling conditions, material composition, stress/strain direction and frequencies, and temperature, as shown in Figure 6 below. Although there are inconsistencies, the above material values are used to obtain expected responses for a given stimulus. Piezoelectric material properties are utilized to design and fabricate materials for a given energy conversion purpose. Piezoceramics, specifically PZT, are the most widely used in energy harvesting and exhibit much larger coupling and higher strength than natural crystals or polymeric materials. Designing a piezoelectric material for power generation is a balance between efficient use of materials and design constraints.

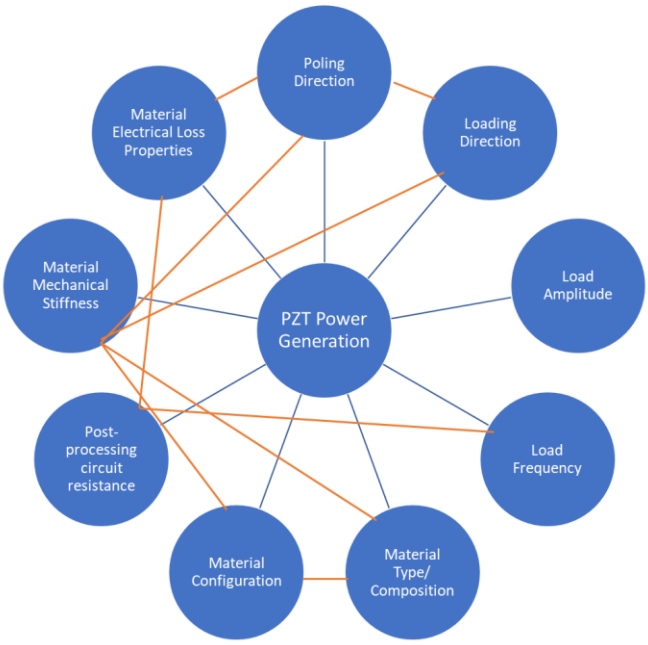


**Figure 6**. Piezoelectric power generation is an intricate balance between several electric and mechanical phenomena.

*Piezoelectric Power Generation*

The goal of all energy harvesting mechanisms is to generate low levels of power. The efficiency of energy harvesting devices is often measured by the amount of power generated for a given mechanical load, frequency and resistance. In typical benchtop testing of piezoelectric

energy harvesting devices, the power generated is calculated from voltage measured over a resistance given by:

$$P = \frac{V^2}{R}$$

where $P$ is the power generated, $V$ is the voltage measured across the resistance, $R$. At very small resistances, a short circuit is created and no voltage is measured. At very high resistances, an open circuit is created, where no current flows and no power is produced. Subsequently, there is an optimal resistance (source impedance) at which power production will be maximized.

Much of the design of a piezoelectric generator is based around matching the device source impedance to the resistance load across which the voltage is measured or collected. The source electrical impedance of the device is actually a multifactorial term, but in the simple power production case, it is simplified to represent the resistance at which maximum power is generated [126]. The source or device impedance is a function of the material and the frequency of load applied. The source impedance of bulk PZT material tends to be high, greater than 100kΩ, which can make the design of post-processing circuitry a challenge [124].

To increase functionality at lower resistances, piezoceramic stacks are used to lower the impedance of the structure. Stacks are most often cofired, meaning several thin elements are stacked together and subsequently sintered to create one uniform structure. The PZT elements are connected electrically in parallel and poled after the sintering process (Figure 5). In a study comparing a monolithic cylinder and a stack of equal volume, Platt *et al.* found that the two devices produced the same power, but the stack produced that power at a much lower kΩ resistance, as compared to GΩ of the cylinder [126]. To lower the source impedance and the necessary driving voltage for a desired displacement, multilayer actuators and generators have been studied, but are not often used in low frequency power generation applications [140].

*Low Frequency Power Generation*

Most low frequency energy harvesting or power generation device research has utilized inductive or electromagnetic devices, because the resonance frequency of piezoelectric devices is so high in comparison to ambient energy sources. However, inductive and electromagnetic devices are severely limited by the size of the required components and cannot be fabricated in an efficient manner for widespread use. At low frequencies, there is promise for piezoelectric materials to provide higher power densities, but as the size of the material decreases, the resonance frequency of the structure increases, presenting a fundamental challenge that must be overcome [127]. At low frequencies, the poor source characteristics of piezoelectric generators are amplified, making it challenging to overcome the high voltages, low currents, and high impedances to produce practical amounts of regulated power [126].

The overwhelming majority of research in piezoelectric energy harvesting is on unimorph and bimorph beams. These cantilever beams are created by bonding a thin layer of PZT (or other piezoelectric material) to one or two inactive metal or polymer substrates to create the unimorph or biomorph configurations, respectively. In power generation applications, the beam is fixed at one end and the structure oscillates, subsequently generating voltage from the axially poled PZT material. This strains the PZT material in the longitudinal direction inducing an electric field in the axial direction utilizing the $d_{31}$ operating mode. Recently, more research has focused on utilizing interdigitated electrodes to allow for the PZT to be poled in the longitudinal direction, thus activating a $d_{33}$ response and a higher voltage output [119]. Kim *et al.* compared identical beams acting in the two different modes, and experimentally found that the 31-mode produced more power than the 33-mode beam. Theoretical models predict a higher output power from the 33-mode beam, but found it was highly dependent on space between electrodes which introduces

significant manufacturing challenges [141]. However, there is still a mismatch in device resonance frequency and loading frequency, which makes power generation from off-resonance vibration ineffective.

To address this issue, several researchers have shown success in reducing the resonance frequency of the structure by adding a large tip mass to the end of a cantilever beam structure and decreasing beam stiffness [142]–[144]. Although it does reduce the frequency mismatch, the addition of large tip masses decreases the durability and life of the structure [127]. Ng *et al.* compared efficiency of both types of beams with a tip mass and concluded that unimorph beams are more efficient at low frequencies and typically have a lower source impedance, making them more efficient at lower resistances. At higher loads and frequencies, bimorph beams produced higher amounts of power [145]. To date, most of the research done on piezoelectric devices to overcome this suboptimal performance at low frequencies has been by modifying materials, mounting design configurations, and manufacturing processes in bimorph and unimorph beams [127], [146]–[150]. Spiral electrodes and an assortment of special shaped cantilevers have also all been utilized to improve function at low frequencies, but practical power generation (>100μW) occurs in the 60-70Hz range [119], [127].

When a rectangular beam shape is not applicable, other beam shapes have been investigated. Standard circular diaphragms consist of a thin PZT disc adhered to a round metal shim. Power is generated when the metal shim is fixed and the PZT element is compressed, activating the 31-mode to generate voltage. Wang *et al.* found that connecting several diaphragms electrically in parallel and adding a prestress to the stack increased power generation to 27mW at 150Hz loading frequency and a lower resistance [151]. Recent research has used similar interdigitated spiral electrode patterns on these PZT elements to activate the 33-mode,

creating actuators that have increased displacement at frequencies as low as 10Hz. However, energy harvesting using these devices has not been widely studied. Shaped cantilevers and circular zigzag cantilevers have also been developed, as their lower natural frequencies have led to reports of device resonant frequencies below 100Hz [127]. However, the specialized manufacturing methods for design incorporation have not yet been developed.

*Structural Piezoelectric Power Generation*

Other PZT configurations have been investigated and utilized in load bearing applications where a beam design would not be applicable. Utilizing disc, cylinder, and rod shaped PZT elements or stacks, allows the energy harvesting structure to be incorporated into a variety of load-bearing structures. Cymbal transducers and cofired stacks have been investigated in high load, low frequency energy harvesting. Cymbal transducers are designed to withstand high impact forces, thus requiring high forces to generate usable power. These devices typically consist of a PZT disc adhered between two metal end caps on both sides. The metal has a slightly lower compliance than the ceramic PZT, and thus radially expands under a high axial compressive load due to Poisson's ratio. The combination of both $d_{33}$ and $d_{31}$ amplify the charge generated for a given load, increasing power generation as compared to a beam. Additionally, cymbals can withstand higher load, which also generates more power. However, high load motion occurs at high frequencies, and cymbal transducers are most effective at frequencies above 100Hz [152], [153]. Bayrashev *et al.* studied an additional composite structural configuration similar to the cymbal concept. The novel magnetostrictive laminate consisted of a PZT disc sandwiched between two Terfenol-D layers, which constricted in response to a magnetic field. This strained the PZT disc and generated 80μW of power [154]. Although not a mechanical load, the concept of increasing strain on PZT within a composite

material could be utilized to increase low frequency power generation from structural piezoceramic materials.

Piezoelectric stacks are used to lower source impedance and increase functionality at lower resistances and have been used in several studies to harvest energy from frequencies in the 1-10Hz range [126], [155]–[158]. Xu *et al.* found that a PZT stack was more efficient at off-resonance frequencies than beams of similar dimensions due to the higher mechanical to electrical energy conversion, but also reported a performance spike at the resonant frequency of the device (~1200Hz) [158]. Cofired PZT stacks typically consist of hundreds of thickness poled PZT wafers that are mechanically bonded in series and electrically wired in parallel. This utilizes the 33-mode to generate power from compressive loads. Goldfarb and Jones studied the efficiency of a PZT stack under steady-state sinusoidal compressive forces. The analytical model and experimental results led to the conclusion that stacks most efficiently generate power from large amplitude compressive forces at low frequencies (<5Hz) with a high resistance [159].

The ultra-high stiffness of PZT stacks makes direct use as an energy harvester without use of an auxiliary structure not practical in many applications, which has fueled the vast research into beam and inertial mass configurations due to their flexibility. The high mechanical stiffness of PZT stacks limit the amount of strain applied to the PZT crystals, thus limiting power generation [134]. Feenstra *et al.* designed a mechanically amplified piezoelectric stack that was integrated into a backpack strap to harvest energy. At 2.5Hz and 5Hz, the stack generated ~.5-1mW of power [155]. To date, little work has been done to increase efficiency of power generation utilizing piezoelectric stacks because of the limitations discussed (Figure 7). However, in a model for efficiency based on piezoelectric material properties, Richards *et al.*

suggest that the largest increase in efficiency of a piezoelectric device will stem from a decrease in structural stiffness [160].

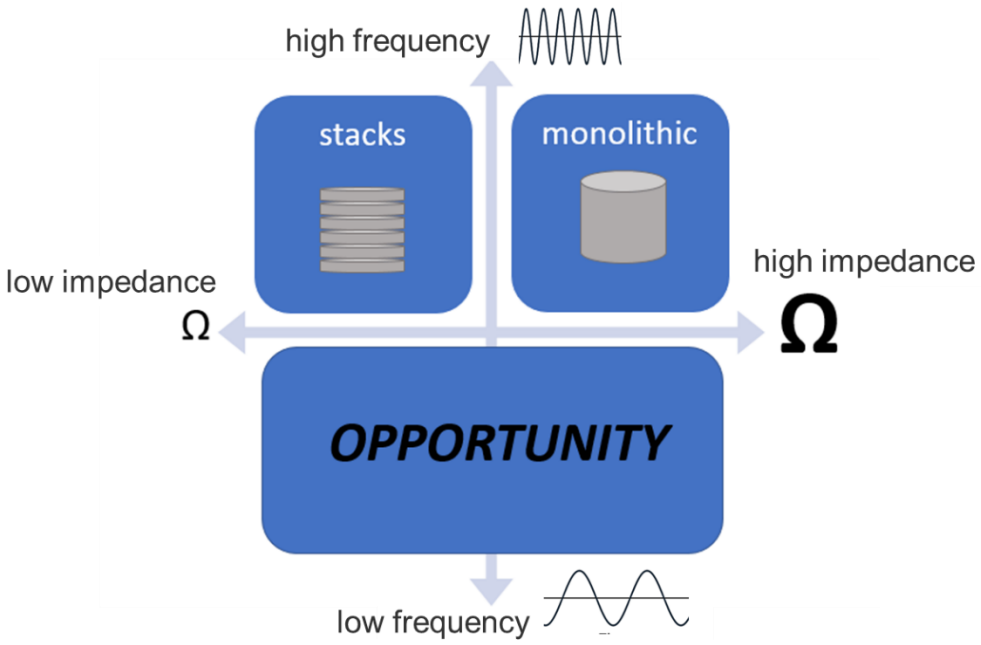


**Figure 7**. Increasing low frequency piezo stack power generation efficiency presents an opportunity for innovation.

*Piezoelectric Power Generation Summary*

Because power generation is a direct result of material, design and functional (load, frequency) characteristics, comparing power generation across devices is challenging. In general terms, efficiency is the ratio of device power output to mechanical input power [161]. Although this definition is similar to the electromechanical coupling factor $k^2$, the efficiency aims to include both the PZT material efficiency and account for the structural design of the energy harvesting device. As such, there is a large discrepancy in reported energy conversion efficiencies. Some studies report efficiencies as high as 80%, while other studies claim operation at an optimized state would only yield efficiencies less than 50% [162]. There is also varying claims regarding the relationship between efficiency and frequency; some claiming efficiency is

maximum at resonance and some claiming efficiency decreases as frequency increases [162]. When assessing the piezoelectric properties and energy harvesting capability of a structure, it is important to consider the effects of bonding, structural, and experimental conditions to account for the sensitive nature of the specific PZT material being used (i.e. hard vs. soft) and variations in material performance.

Designing an efficient piezoelectric generator or energy harvesting device is a balance of multiple factors: compactness, output power density, lifetime, cost, operating frequency, and input force amplitude [127]. Often, the integration of the energy harvester is an important part of design, so the mechanical stiffness, fatigue resistance and strength of the material are all important factors. Additionally, the piezoelectric performance is dependent on the poling direction in relation to the loading direction and the material choice. Although unimorph and bimorph beams are used most often to capitalize on the $g_{31}$ piezoelectric constant, the challenge in structural integration and the space required for oscillation must be considered. Electrode design and beam shape have been optimized to create efficient power generation for certain applications but have not solved the challenge of structural integration efficiency at frequencies below resonance. When a cofired stack is desired for structural rigidity, the source impedance can be adjusted by increasing the number of layers in the stack to increase power production at lower resistances, but the high stiffness may require additional structures to account for the high stiffness in device integration.

Some disadvantages of piezoceramics include their rigidity, brittleness, lack of design flexibility, toxicity and inefficient functionality at low frequencies. Not much research has been conducted to increase low frequency power generation utilizing piezoelectric stacks. However, some researchers suggest that more power may be available by amplifying the force on less

piezoelectric elements, rather than increasing the total volume of piezoelectric material [126]. Designing piezoelectric devices to integrate with medical devices requires efficient energy harvesting from human motion. The range of human motion frequency is 0.5 to 50Hz, from walking to heartbeats and breathing [163], [164]. Additionally, the brittle nature of piezoceramics make device integration challenging due to the high stiffness and low fatigue life of the ceramic material. Interfacing with the human body, either as an implantable device or a wearable external device, will require a compact, efficient, adaptable piezoelectric energy harvesting material. Any medical device or external wearable device will undergo long-term cyclic loading, and thus must withstand high loads for long periods of time. Designing piezoelectric materials for use in the body to stimulate tissue healing will be discussed in the next section.

## Design of Piezoelectrics for Tissue Stimulation

The development of a wide variety of piezoelectric energy harvesting materials and devices and the increasing understanding of electrical stimulation in tissue/bone maintenance and regeneration has improved piezoelectric biomaterial design. Piezoelectric properties in a wide range of biological materials have been studied, ranging from muscle to hair, bone as previously discussed, and soft tissue including lung tissue and skin [165]. Researchers have worked to discover the source of the piezoelectric response, and have found that proteins, primarily collagen, keratin, elastin, actin and myosin are responsible for the charge generation in response to mechanical loading [165]. Mirroring the natural healing processes present in the body, designing piezoelectric biomaterials require specific considerations, the most important being biocompatibility.

Medical implants and energy harvesting devices intended to utilize organ motion or gait motion ideally should not include hazardous chemicals (like lead in PZT) or must be hermetically sealed. Piezoelectric biomaterials allow for the local delivery of an electrical stimulus, while eliminating the need for an external power source. Theoretical analyses have shown that humans can generate sufficient electrical power with ordinary movements: walking can generate 5-8.3W of power, while breathing can generate 200mW of power [166]. Because of the source characteristics of piezoelectric energy harvesting materials discussed in the previous section, innovative design of piezoelectric biomaterials is critical, but could make an impact on tissue and bone healing.

*Energy Harvesting from Walking*

Human gait provides a consistent high load, low frequency ambient motion from which energy can be harvested. Several researchers have studied the application of different piezoelectric configurations, including modified unimorph or bimorph beams and PVDF laminates in the heels of shoes to harvest power from walking [144], [150], [166]–[168]. Kymissis *et al.* compared a unimorph PZT composite beam in the heel of the shoe and a PVDF laminate installed in the front part of the sole. At 1Hz, the integrated system produced ~1mW of usable power. The limited power production and low electromechanical efficiency (1.5%) were attributed to the lack of required deformation of the PZT beam, and the inefficient 33-mode power generation of the PVDF laminate [144]. Later, Shenck and Paradiso iterated on the PZT bimorph and included it in the heel of a US Navy work boot to increase the load applied to the beam. The power increased to ~8mW of power, and a reported 20% efficiency, but the device also generated remarkably high voltages, amplifying the resonance and load frequency mismatch and limiting effective power generation [167]. Because walking occurs at off-resonant

frequencies and the devices have high source impedance [169], Niu *et al.* suggests that piezoelectrics might not be the most effective method for harvesting energy from heel strike. In an analytical model, it was predicted that a PZT plate inserted into the heel of a shoe loaded in compression would generate 14μW of power, suggesting a PZT stack could increase efficiency of power generation from walking loads [170].

Utilizing a different approach, Renaud *et al.* and Fan *et al.* investigated the effectiveness of harvesting arm and wrist and lower limb motion, respectively, during walking to power electronics [171], [172]. In both studies, a non-resonant system was designed, consisting of two cantilever beams housed in a frame with a sliding mass that oscillates the frame and beams, thus generating a piezoelectric response and subsequent power. It was predicted that 40μW could be generated and that low frequency power could be generated, but the clunky device and inefficient energy transduction would limit effectiveness. As mentioned earlier, Feenstra *et al.* was also able to mechanically amplify a PZT stack to generate ~1mW from walking, but there is concern about the energy loss at the contact points between the amplification structure and the PZT elements, limiting conversion efficiency [155].

These devices have furthered the field of human motion powered piezoelectric design, but were designed to power external devices and wearable electronics. Tissue stimulation piezoelectric devices require an implantable device that would eliminate need for a battery. Additionally, an efficient piezoelectric energy harvesting biomaterial could potentially power artificial organs.

*Implantable Piezoelectric Devices for Tissue Stimulation*

Mechanotransduction and cell signaling in response to a tissue piezoelectric response is not fully understood, as discussed in the second section. The electrical signals that signal

intracellular activity is thought to be transmitted through the extracellular matrix. Standard tissue engineering scaffolds designed to mimic the natural extracellular matrix are often composed of nonconductive materials, thus interfering with signal conduction and interrupting signaling pathways. To address this issue, piezoelectric materials are being developed as a conductive tissue engineering scaffold material [173]. Not only can these piezoelectric scaffolds act as a conduit for mechanotransduction, they can also enhance tissue regeneration at the impaired site as a result of the electrical stimulation.

There is a wide variety of piezoelectric films and composite materials being developed for soft tissue regeneration, internal sensors and actuators [173]–[175]. Tissue engineering scaffolds containing piezoelectric materials generate electric pulses in response to transient mechanical deformations, subsequently initiating or boosting the cellular response at the site. PVDF is the most widely used in biomedical applications and has been used in scaffolds, sensors and self-powered devices [173], [174]. PVDF and other PVDF composite films are flexible and thus can be conformed to pulsing arteries, expanding diaphragms and lungs, and attached to the beating heart [163]. PZT and barium titanate nanowires included into a polymer film have increased energy transduction efficiency and have shown promise as an energy harvesting material to power small implantable devices [165]. PVDF has also been used to stimulate wound healing [173]. The wide variety of applications for these flexible sensor, energy harvesting and stimulating biomaterials is promising, but much of this work is in early research and development stages, and scalable fabrication techniques have not yet been developed [176]. For the purposes of this work, the remainder of this section will focus on the use of piezoceramic materials in implantable, load-bearing medical devices.

*Piezoceramics in Implants*

There is scarce use of PZT as a non-load bearing implantable material. PZT has been used in animal studies to stimulate neuron activity [177], but concerns of the lead content in PZT has limited widespread research. To increase biocompatibility and prevent dissolution of ions, PZT is often embedded in a polymer matrix. PZT micro actuators have been integrated into cochlear implants to combine electrical and acoustic stimulation and improve hearing for patients [178]. Research is still in the early stages, and device circuit integration may be a challenge. In addition, the long-term safety and efficacy of this use of PZT should be evaluated.

Several groups have investigated the implementation of PZT stacks in a total knee replacement for sensing purposes [126], [156], [179], [180]. The motivation of the work was to harvest energy generated from walking to power sensors capable of collecting diagnostic information following a total knee replacement with the motivation of assessing ligamentous balance after surgery. Several cofired PZT stacks were installed in the tibial plateau of the implant, and the assembled joint replacement prosthesis was modeled and tested under physiological loads. The maximum experimental power generated was ~5mW of power [126], [156]. The combination of the load-bearing PZT stacks and the efficiency of the power generation at lower resistances (~1MΩ) makes PZT stacks a promising material for energy harvesting within implants. Orthopedic implants require structural rigidity to withstand high mechanical loads, but the ceramic PZT stacks are brittle, designed primarily for compression, and susceptible to crack propagation under long-term loading. Although the power produced is higher than other piezoelectric energy harvesters at walking frequencies (1-2Hz), more power may be necessary to provide tissue stimulation.

All piezoelectric energy harvesters generate alternating current (AC) signals. As explained in the previous section, the most efficient power generation occurs at the resonance frequency of the device. Some tissues respond favorably to AC current, other tissues, namely bone do not. Bone growth is stimulated by negative currents, while bone resorption is stimulated by positive current. Thus, in order to stimulate bone growth and regeneration, a negative DC stimulation must be delivered to the bone healing site. Therefore, design of a piezoelectric biomaterial to supply this stimulation requires a rectifying circuit to change the AC to DC, condition and subsequently deliver the negative current. There is quite a bit of research into signal conditioning and rectification circuits [127], but impedance matching between the circuit and the piezoelectric device is critical to increase usable power generation efficiency. Decreasing the source impedance by increasing the number of piezoelectric layers connected electrically in parallel, is a promising technique for effective integration with a circuit while minimizing electric losses.

Because of their adaptability, if PZT stacks could be mechanically toughened to withstand physiological loads and electrically adjusted to enhance effectiveness at low frequencies while producing sufficient power, incorporating them into orthopedic implants to provide internal DC stimulation at the healing site without a battery pack could address a large clinical need.

*In Vivo Piezoelectric Stimulation*

To eliminate the need for an invasive battery pack with an implantable device, several different piezoelectric material configurations have been used to power devices and provide electrical stimulation at the site of desired bone healing [181]–[184]. In the 1980's, several groups utilized monolithic piezoelectric material implanted *in vivo* and found voltage was

generated under physiological loading [182], [184], [185]. Park *et al.* proved the biocompatibility of barium titanate [186], and then used a monolithic piece of barium titanate to fill a femoral void in a canine study. It was found that there was increased voltage produced after 86 days *in vivo*, although there was not claim of enhanced bone regeneration [183]. Later, the comparison of a 33-mode poled porous plug was compared to the unpoled plug, resulting in similar bone ingrowth and biocompatibility results [184]. The results did not show enhanced bone healing through the electrical signals supplied.

In a similar study with PZT, Schumacher *et al.* compared polarized and depolarized blocks of PZT implanted in the metatarsus of cocks. The developed tissue surrounding the blocks was identical, leading to the authors' conclusion that there was no positive influence on bone formation [185]. Both Park *et al.* and Schumacher *et al.* stated that experimental design limited the loading on the implanted piezoceramics, and thus the lack in bone response was attributed to the negligent piezoelectric behavior [184], [185]. Additionally, it was not clear in either study exactly how the electrical signals were conditioned and subsequently delivered in the animal models, which could have greatly impacted the material's ability to produce sufficient negative current to stimulate bone growth.

Cochran *et al.* completed a similar series of studies in which a 'piezoplate' was utilized to stimulate bone growth in a canine study. The monolithic PZT plates were attached to internal fracture fixation plates. Ultrasonic loading was utilized to stimulate the piezoelectric response of the PZT [182]. Cochran's group also developed a rectifying circuit to ensure the current delivered *in vivo* was a conditioned, negative DC signal [187]. In a canine study, walking loads generated peak to peak voltages of 25V and rectified current of 0.3μA. External ultrasound generated conditioned currents exceeding 20μA [187]. Benchtop and canine tests demonstrated

efficacy of the device to generate DC stimulation in the range linked to bone healing, but the effect of the DC stimulation on bone healing was not directly reported. There was not conclusive evidence of bone healing directly related to the stimulation provided by the 'piezoplate,' but several design suggestions were made: compact, tough piezoelectric generator, carefully designed rectifying circuit, and importance for ultrasound stimulation when weight-bearing is not applicable.

In a similar configuration, McDowell *et al.* proposed the use of a piezoelectric element embedded into a prosthetic hip stem. The exposed piezoelectric generator was configured to deliver electric current to specific locations around the implant. There is not a clear understanding of the success of the system, as the energy is unregulated and generated voltages were high [188].

None of these studies showed promising results from the use of synthetic piezoceramics for bone growth via electrical stimulation delivered by the piezoceramic. As a result, for many years there was no further research investigating the use of piezoelectric implants because of the challenges of integrating the piezoelectric material into an implant, conditioning the AC signal to deliver DC, and the high resonant frequency and high source impedance of the piezoceramic material. It is important to note that no adverse biological reactions were reported. Recent work has reported that PZT is chemically inert and shows promising biocompatibility in an *in vitro* cell study [189].

Reis *et al.* developed PVDF actuators, utilizing the converse piezoelectric effect, to mechanically stimulate bone growth. In a preliminary sheep study, PVDF films were seeded with cells and adhered to an actuator device that was encapsulated in polymethylmethacrylate (PMMA). The PVDF films were placed inside an osteotomy cavity and stimulated with a 5V AC

signal. New bone growth, an increase in bone area and bone deposition rate were all significantly higher in the mechanically stimulated osteotomy healing sites. However, the authors did raise a concern about the biocompatibility of PVDF. Histology results showed a fibrous capsule surrounding each device separating them from neighboring bone [190].

More recently, Goetzinger *et al.* utilized stacked piezoelectric element concepts to design a multilayer macro fiber composite spinal fusion implant [191]. The piezocomposite implant was designed to deliver DC signals in sync with mechanical loading to a titanium electrode at the fusion site. A theoretical model of the implant design suggested utilizing a 1-3 composite, with macro piezoelectric fibers evenly distributed in a polymer matrix aligned axially with the load. The epoxy-fiber biomaterial was predicted to not only produce enough power to stimulate bone growth (>140μW) but would also be mechanically tough with a fatigue limit over 7kN [192]. Following this proposed design, Goetzinger *et al.* fabricated the implants using PZT fibers and a medical grade epoxy and studied the effect of the number of layers on power output. To overcome the high source impedance of the PZT at frequencies of human motion, layers were stacked such that they were electrically connected in parallel and mechanically loaded in series, similar to cofired PZT stacks. The multi-step fabrication process (cleaning fibers, fiber-epoxy composite creation, slicing layers, electrode deposition, stacking, electrical connection, and poling) limited implant consistency and scalability [191].

Keeping volume constant, power output of one, three, six and nine layered implants (Figure 8A) were compared under physiologic compressive loads and frequencies (100-1000N amplitude loads at 1-5Hz). All implants produced similar maximum power ~1132μW at 1000N and 2Hz (a conservative estimate for loads experienced in the spine during walking [193]), but the resistance at which maximum power occurred decreased from 1GΩ to 17MΩ as the layers increased from

one to nine, respectively. The power produced was substantially higher than that required for appropriate levels of electronegative stimulation but would be an appropriate amount to ensure successful rectification through a conditioning circuit that may use a considerable amount of power to function.

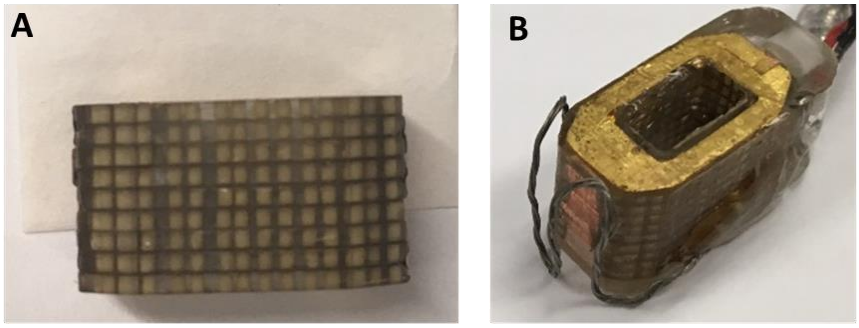


**Figure 8**. Macro fiber implant used in the pilot sheep study. **A.** Side view showing stacked layers with fibers encapsulated with epoxy. **B.** Isometric view showing exposed titanium electrode.

To increase mechanical integrity of the implant and account for the biocompatibility concerns of PZT in an implant, Tobaben *et al.* studied the effect of encapsulation on power output of the same implants from the Goetzinger *et al.* study [191], [194]. The implants were encapsulated in the same matrix epoxy used in the fiber composite layers and increased the loaded surface area by 84%. Subsequent power decreased by 39%, as expected due to the 46% decrease in effective stress on the PZT fibers. Encapsulation did not change the resistance at which maximum power occurred. To verify usability in an animal study, power output at 500N amplitude loads and 2Hz were measured, and encapsulated implants produced ~200µW of power at 160MΩ [194].

A preliminary proof of concept sheep study utilized the encapsulated implants to study the effect of mechanically synced DC stimulation in a lumbar spinal fusion procedure [181]. Two nine-layer macro fiber implants were fabricated, poled, encapsulated, connected to a rectifying circuit, and implanted in the lumbar spine of two sheep. An external titanium electrode

was attached to the negative terminal of the circuit and the positive electrode was exposed on the circuit board (Figure 8B). Based on the benchtop testing from the two studies described above and the proprietary circuit design, expected output was as follows: 10μA/cm$^2$ current density and 100μW at 40kΩ [191], [194]. Two unpoled nine-layer, encapsulated implants that were not connected to a circuit and did not have an external electrode were used as controls.

The histology and CT results showed evidence of enhanced fusion due to the mechanically synced, non-constant DC stimulation provided by these piezoelectric spinal fusion implants as compared to the control implants that did not fuse [181]. There was strong evidence of quicker more robust healing in the active implants from the 6-week CT scans. The histology results showed healthy, non-ectopic bone growth in and around the active implants, and soft tissue callus formation in the control, non-active implants (Figure 9). Post-mortem biomechanical studies showed increased stiffness and decreased range of motion in the active implants, validating the promising CT and histology results. These foundational, positive results strongly support the efficacy of piezocomposite implants providing mechanically synced DC stimulation at the fusion site and have initiated further development of the PZT composite material addressed in this dissertation.

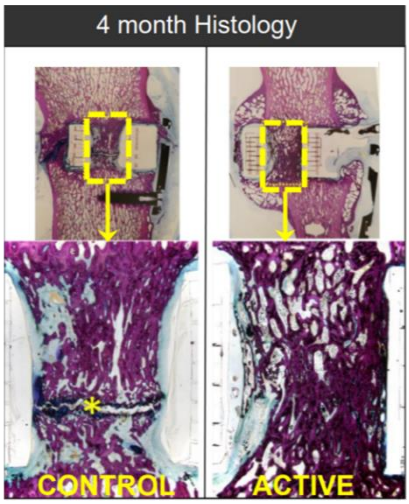


**Figure 9**. 4-month histology results. *marks formation of soft tissue callus.

## Designing a Robust Piezocomposite Biomaterial

Although the piezoelectric spinal fusion implant did generate sufficient power to improve bone growth, mechanical studies showed maximum power output occurred at a range that was much higher than the resistance of a rectifying circuit necessary to convert the voltage to a DC signal [191], [192], [194]. The thickness of the layers was limited to >1mm due to insufficient fiber-matrix interface strength, limiting power generation at lower resistances. Because implants must fit within the disc space in between vertebrae, overall implant height is limited, and thus decreasing layer height is critical to increase the number of layers and further decrease the source impedance. Additionally, the use of piezoelectric fibers and the associated difficulty with fabrication of the implant prevented scalability for use in multiple orthopedic implants.

The use of traditional cofired piezoelectric stacks would improve manufacturability, while lowering source impedance and producing more power at lower resistances [126], thus overcoming obstacles in practical implementation of the piezoelectric component of the implant. Traditional stacks are made of PZT, a brittle ceramic that would not withstand physiological loads experienced by orthopedic implants. If piezoceramic stacks could be toughened to withstand multiaxial loads experienced *in vivo*, they could act as an effective generator for a DC electrical stimulation device within an implant.

### *Fatigue Resistance*

Fatigue of piezoelectric materials is an important consideration when designing a biomaterial. When subjected to repeated mechanical loads, piezoceramic materials lose functionality as the material depoles, cracks form and propagate, and electrodes delaminate from the ceramic surface [195]. The fatigue performance is strongly dependent on the amplitude and frequency of the applied load and the composition of the material [196]. Crack formation and

propagation during cyclic loading leads to a decrease in stiffness, which accelerates crack propagation [195]. For use as a structural biomaterial, a piezocomposite biomaterial will undergo high load, low frequency conditions for several years, and thus must be able to withstand such loading. There is limited understanding of the low frequency, high load performance of PZT.

Platt *et al.* found that a cofired PZT stack subjected to a periodic 440-N, 1Hz load for an approximated 1.5 million cycles exhibited logarithmic progressive degradation of power generation [126]. There was little degradation in power output for the first 10,000 cycles, and output degraded logarithmically over time. It was concluded that the stack could produce usable power for millions of cycles. The authors also stated that there was significant recovery of the piezoelectric generator during pauses in loading greater than 30 minutes. These findings are promising for the design of piezocomposite implants utilizing PZT stacks, as loads on implants will likely be intermittent, allowing for time for the PZT to recover.

Additionally, there is promising evidence that creating a composite material utilizing PZT stacks and a polymer matrix would extend the functional lifetime of the material. In a study assessing the integrated effects of PZT actuator design and material properties on the fatigue life of a PZT stacked actuator, van den Ende *et al.* found crack initiation starts early in the loading process, and propagation is strongly affected by external factors (i.e. humidity) and the microstructure (ceramic-electrode interface) [195]. Two multilayer cofired PZT stacks were adhered together with either an epoxy-based glue or a silicone-based glue. In an accelerated lifetime test, the stacked actuators were subjected to 150V at 20Hz. The thickness and compliance of the adhesive layer affected the stress experienced by the PZT elements, and slightly reduced the effectiveness of the piezoelectric actuation. Most notably, the silicone adhesive prevented severe crack formation and limited propagation. The authors state that the

slight loss in actuation (<10%) is negligent compared to the significant increase in functional lifetime, especially at low frequencies [195]. Although these results were found for PZT stack actuators, it is expected that including a polymer within a PZT generator would result in similar fatigue resistance.

*Multiaxial Loads*

Forces on orthopedic implants are controlled by the patient's weight and activity. Specifically, forces on the skeleton are a result of the weight, external forces, inertial forces due to motion and internal muscular forces. During walking and other activities of daily living, loads in spinal fusion implants can range from ~1-3 times body weight (>1500N) [193], [197], [198]. Multiaxial loads and subsequent resultant forces are common as the position of the spine changes with different activities and how each patient performs such activities [197]. With posterior instrumentation, which is common in lumbar spinal fusion procedures, the load on the implant is halved [199], [200]. A conservative estimate for compressive loads acting on spinal fusion interbody implants is a 500N amplitude load at a frequency of 2Hz [198]. Therefore, it is crucial that a piezocomposite biomaterial produce ample power at a frequency much lower than its resonant frequency and maintain mechanical and electrical integrity for millions of cycles at high loads.

The success of an intramedullary (IM) nail to facilitate healing across a gap in a long bone (i.e. femur or tibia), is largely dependent on the torsional and bending stiffness of the implant construct. The diameter of the nail, the material, the cross-section (open or closed), and material properties of the design all strongly influence strength and stiffness of the nail [201]. Thus, when designing a piezoelectric composite IM nail, it is critically important to consider load transfer through the metal, piezocomposite interface. Piezoceramics are designed for purely

compressive loads and are incredibly stiff and brittle. Integrating a tough matrix material with the strong piezoceramic would not only decrease stiffness to better match the bone stiffness and prevent stress shielding, it would also increase mechanical integrity to withstand multiaxial loads experienced by fracture fixation implants.

Multiaxial loads, especially torsion, along the shaft of the femur and tibia during activities of daily living are challenging to measure with the lack of conventional approaches to do so *in vivo,* and has not been successfully modeled due to variation in muscle forces, posture and gait patterns of individual patients [202]. There is evidence to suggest that torsion and bending could be the primary loading of long bones in the legs (femur and tibia) during walking and running [203], [204]. Although not common, torques as high as 11N-m can be experienced by the long axis of the femur [201], [205]. Schneider *et al.* measured the change in load in an IM nail before and after fracture healing and found that there was a steep decrease between six and eight weeks. But even after healing, 50% of loads were transmitted through the nail. Muscle forces, acting in multiple directions, axial, torsion, and transverse forces were still significant and expected to increase with the re-establishment of normal activities for the patient [201]. Thus, these implants must be able to withstand multiaxial loads, even after healing occurs.

Because such a significant percentage of the forces acting on IM nails is suspected to be torsion, it would be advantageous to design a piezocomposite that could generate power from off axis loading. Standard PZT stacked generators utilize the 33-mode to generate power from compressive loads. Exploring the novel use of radial or shear poled PZT elements to activate the 31-mode and 15-mode respectively, would be an inventive way to increase power generation efficiency. In addition, most patients are non or limited weight-bearing for several weeks following a fracture fixation or spinal fusion. Designing a piezocomposite that could be

stimulated with ultrasound as Cochran et. al demonstrated, would provide a novel treatment option to activate early healing [187]. Exploring the effect of poling direction of PZT elements on power generation from multiaxial loads and ultrasound may provide meaningful design criteria for a comprehensive piezocomposite biomaterial.

*Regulatory and Clinical Design Considerations*

It could be argued that one of the most critical aspects in designing a medical device is the regulatory pathway and subsequent approval process. It is also important to consider the entire cycle of care associated with the product, including everything from scalable manufacturing in approved facilities, biocompatibility, surgeon use and adoption, reimbursement, cost and patient outcomes. A clear understanding of how functional design decisions will impact each of these areas is critical for successful translation of a piezocomposite biomaterial. The FDA does not universally approve or clear a material; therefore, safety and efficacy of each device must be ensured. Appropriate testing of orthopedic implants should incorporate both standard mechanical and strength of materials considerations and the biomechanics of the implant, body and the interface between the implant and the body [206]. Utilizing FDA guidance and their approved standards (ASTM, ISO) for mechanical testing of the piezocomposite material and related devices is an important aspect of design verification and validation.

Much of the pushback of current DC electrical stimulation devices on the market is the additional surgery time and sites. The electrodes are flimsy and must be carefully placed around the fusion and/or fracture, and then the battery must be implanted in the soft tissue and later removed. These factors have contributed to the lack of widespread use of implantable DC stimulators, despite their positive clinical outcomes. The use of the piezoelectric generator to

harvest energy from patient motion will eliminate the need for a battery, while providing DC electric stimulation directly to the gap healing site. In addition, with careful design and an increase in power generation efficiency at low frequencies, it is possible that the piezocomposite could be designed to fit within existing implants (i.e. spinal fusion interbody implants and IM nails). This would allow an existing surgical technique to be used for implantation and would not require development of new instrumentation, increasing likelihood of clinician adoption.

Through the application of mechanical load, electrical potentials occur naturally in bone [75], [85], [90]. Under compressive loads electronegative potentials are generated and electronegative potentials have been shown to induce osteogenesis and form new bone [63]. Similarly, including a piezocomposite biomaterial within an implant would provide electrical stimulation in sync with mechanical loading of the bone. The alternating signal that is generated from the piezoelectric material will be conditioned, rectified and subsequently delivered to the injury site through an electrode as a negative current. As such, when the implant is loaded, it triggers the body's natural response to grow bone. Additionally, as bone grows through and around the implant, loading on the implant is reduced, decreasing the natural osteogenic process triggered by the piezoelectric powered stimulation. As fusion occurs across the healing site, the implant will naturally turn itself off and act as a standard orthopedic implant for stabilization (Figure 10).

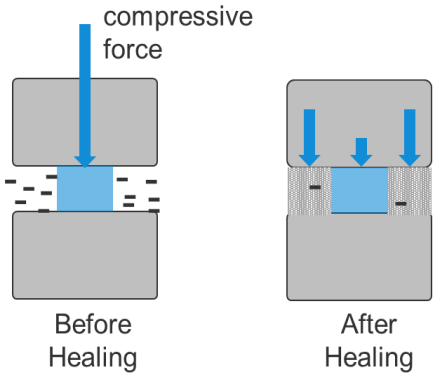


**Figure 10**. As fusion occurs, the mechanically synced electrical stimulation will decrease as the new bone growth shields the implant, decreasing the load and subsequent stimulation from the implant.

Based on this information, this dissertation will outline the development and testing of a novel configuration of a piezoelectric composite stack, compliant layer adaptive composite stacks (CLACS), for incorporation into orthopedic implants that will provide mechanically synced DC stimulation and enhance bone growth. The overall goal is to increase bone healing rates from multiple gap healing surgical procedures for the difficult-to-fuse population, although this technology would help all patients. The following three studies will describe the development and electromechanical characterization of the CLACS structure as it pertains to implant design.

Background Summary

Time and quality of bone healing from orthopedic surgeries is problematic for many patient populations. The rise in delayed and incomplete healing leading to nonunion/pseudarthrosis and associated costs is a growing societal issue. Electrical stimulation has a strong clinical history of stimulating bone growth, leading to improved surgery success rates and decreasing healing times in difficult-to-fuse patients. However, external application requires patient compliance and invasive devices require implanted transcutaneous battery packs that must be removed post healing, often due to patient discomfort. Electric potentials that trigger bone regeneration and healing occur in response to mechanical loading, suggesting that an electrically active implant may improve healing of the surrounding gap healing site, addressing the high incidence of delayed and nonunions.

Piezoelectric materials produce an electrical signal under cyclic mechanical loads, and have been used to harvest human motion and subsequently generate power for tangential devices, eliminating the need for a battery. However, standard piezoceramic configurations are challenging to integrate into implants and are inefficient at low frequencies. Piezoelectric fiber composites embedded in a spinal fusion implant were investigated as a method of providing electrical stimulation at the bone healing site in sync with mechanical loading. In fact, a piezoelectric composite spinal fusion implant, produced enough power to generate bone healing DC stimulation without the use of a battery. These piezocomposite implants stimulated healthy bone growth and fusion in a pilot ovine study However, a single supplier of the piezoelectric fibers, extremely high failure rates and difficulty with the fabrication processes prevented scalability of this material configuration for use in other orthopedic implants, or as a scalable option to mass produce implants.

Building on that foundation, the ongoing aim of this work is to develop a piezocomposite load-bearing implant material that is mechanically and electrically compatible with bone. This material should mechanically withstand physiological loading conditions, while producing sufficient power under the same loading conditions to deliver bone healing DC stimulation. The following chapters will detail the design, validation, power generation capability and fatigue resistance of CLACS to test feasibility for their use in orthopedic implants.

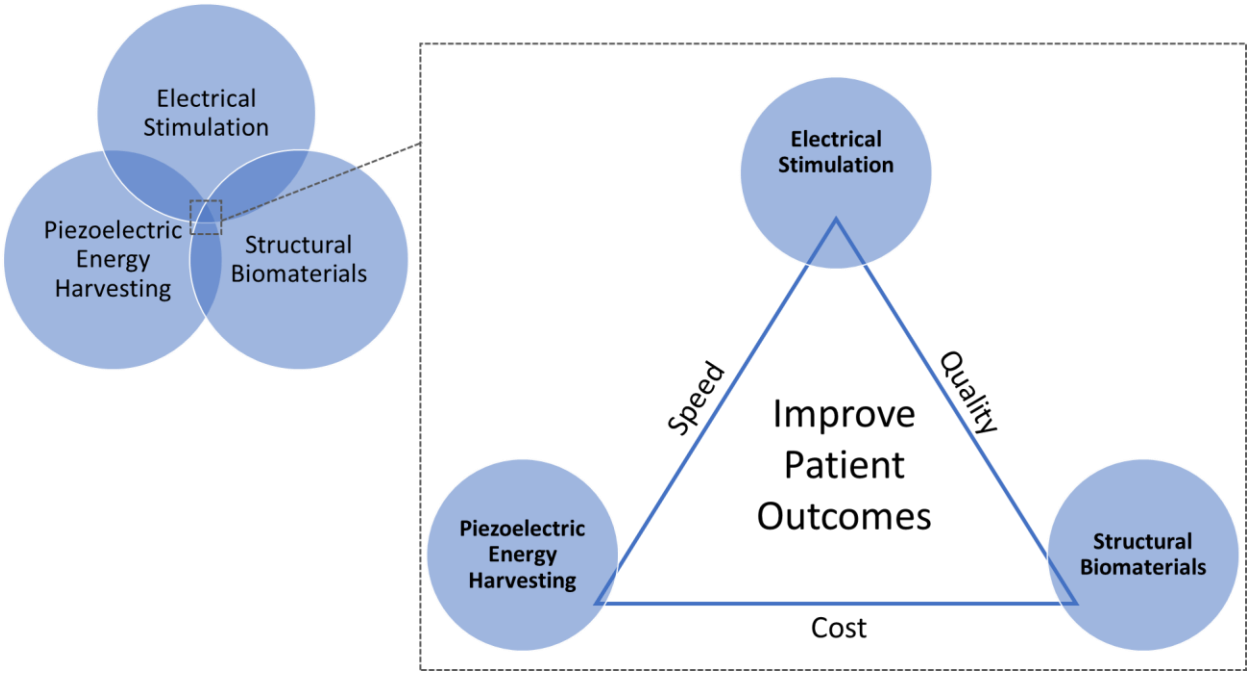


**Figure 11**. Schematic of research framework.

The design of such an adaptable biomaterial requires an integrative approach that overlaps three main areas of interest: electrical stimulation for bone healing, piezoelectric energy harvesting, and structural (or load-bearing) implant material science. This chapter has discussed details of all three, and the following chapters will focus on the investigation of piezoelectric energy harvesting and structural biomaterials as it pertains to implant design capable of supplying electrical stimulation without a battery. The mechanically synced electrical stimulation

provided by the piezocomposite material could increase the speed of healing, thus efficient, cost-effective design for manufacturability is an important factor in the piezocomposite integration with the implant. To prevent stress shielding and bone resorption, the structural properties of the implant material must be compatible with bone, and will directly affect the quality of bone healing stimulation delivered. Through the lens of improving patient outcomes, this research aims to balance electrical stimulation, piezoelectric energy harvesting and structural biomaterials to create a cost-effective, efficient, innovative biomaterial (Figure 11). The remaining chapters focus on the development and verification of a novel piezoelectric composite, Compliant Layer Adaptive Composite Stacks (CLACS), through this framework. If proven mechanically and electrically feasible, using CLACS for internal electrical stimulation could have tremendous advantages for patients, physicians and the over-taxed medical reimbursement system; increasing the success of complete bone healing and decreasing healing times.

References


[1] K. (Truven H. A. Fingar, C. (AHRQ) Stocs, A. (Truven H. A. Weiss, and C. (AHRQ) Steiner, "Most Frequent Operation Room Procedures Performed in U.S. Hospitals, 2003-2012," Agency for Helathcare Research and Quality, Rockville, MD, HCUP Statistical Brief #186, Dec. 2014.

[2] T. A. Einhorn, "Enhancement of fracture-healing," *Journal of Bone*, vol. 77, no. 6, pp. 940–956, Jun. 1995.

[3] S. Morshed, "Current Options for Determining Fracture Union," *Adv Med*, vol. 2014, 2014, doi: 10.1155/2014/708574.

[4] C. Tzioupis and P. V. Giannoudis, "Prevalence of long-bone non-unions," *Injury*, vol. 38, pp. S3–S9, May 2007, doi: 10.1016/S0020-1383(07)80003-9.

[5] C. L. Ekegren, E. R. Edwards, R. de Steiger, and B. J. Gabbe, "Incidence, Costs and Predictors of Non-Union, Delayed Union and Mal-Union Following Long Bone Fracture," *Int J Environ Res Public Health*, vol. 15, no. 12, 13 2018, doi: 10.3390/ijerph15122845.

[6] J. J. Reid, J. S. Johnson, and J. C. Wang, "Challenges to bone formation in spinal fusion," *J Biomech*, vol. 44, no. 2, pp. 213–220, Jan. 2011, doi: 10.1016/j.jbiomech.2010.10.021.

[7] J. Bishop, A. Palanca, M. Bellino, and D. Lowenberg, "Assessment of Compromised Fracture Healing," *Journal of the American Academy of Orthopaedic Surgeons*, vol. 20, no. 5, pp. 273–282, May 2012, doi: 10.5435/JAAOS-20-05-273.

[8] J. A. Buza and T. Einhorn, "Bone healing in 2016," *Clin Cases Miner Bone Metab*, vol. 13, no. 2, pp. 101–105, 2016, doi: 10.11138/ccmbm/2016.13.2.101.

[9] J. D. Heckman and J. Sarasohn-Kahn, "The economics of treating tibia fractures. The cost of delayed unions," *Bull Hosp Jt Dis*, vol. 56, no. 1, pp. 63–72, 1997.

[10] R. A. Deyo, "Fusion surgery for lumbar degenerative disc disease: still more questions than answers," *The Spine Journal*, vol. 15, no. 2, pp. 272–274, Feb. 2015, doi: 10.1016/j.spinee.2014.11.004.

[11] D. C. Cherkin, R. A. Deyo, K. Wheeler, and M. A. Ciol, "Physician views about treating low back pain. The results of a national survey," *Spine*, vol. 20, no. 1, pp. 1–9; discussion 9-10, Jan. 1995, doi: 10.1097/00007632-199501000-00001.

[12] J. N. Katz, "Lumbar disc disorders and low-back pain: socioeconomic factors and consequences," *J Bone Joint Surg Am*, vol. 88 Suppl 2, pp. 21–24, Apr. 2006, doi: 10.2106/JBJS.E.01273.

[13] H. An, S. D. Boden, J. Kang, H. S. Sandhu, W. Abdu, and J. Weinstein, "Summary statement: emerging techniques for treatment of degenerative lumbar disc disease," *Spine*, vol. 28, no. 15 Suppl, pp. S24-25, Aug. 2003, doi: 10.1097/01.BRS.0000076894.33269.19.

[14] S. S. Rajaee, H. W. Bae, L. E. A. Kanim, and R. B. Delamarter, "Spinal fusion in the United States: analysis of trends from 1998 to 2008," *Spine*, vol. 37, no. 1, pp. 67–76, Jan. 2012, doi: 10.1097/BRS.0b013e31820cccfb.

[15] J. C. Steinmann and H. N. Herkowitz, "Pseudarthrosis of the spine," *Clin. Orthop. Relat. Res.*, no. 284, pp. 80–90, Nov. 1992.

[16] J. C. Gan and P. A. Glazer, "Electrical stimulation therapies for spinal fusions: current concepts," *Eur Spine J*, vol. 15, no. 9, pp. 1301–1311, Sep. 2006, doi: 10.1007/s00586-006-0087-y.

[17] B. Knox and T. Chapman, "Anterior Lumbar Interbody Fusion for Discogram Concordant Pain," *Journal of Spinal Disorders*, vol. 6, no. 3, pp. 242–244, Jun. 1993.

[18] M. Panteli, I. Pountos, E. Jones, and P. V. Giannoudis, “Biological and molecular profile of fracture non-union tissue: current insights,” *J Cell Mol Med*, vol. 19, no. 4, pp. 685–713, Apr. 2015, doi: 10.1111/jcmm.12532.
[19] R. K. Hernandez, T. P. Do, C. W. Critchlow, R. E. Dent, and S. S. Jick, “Patient-related risk factors for fracture-healing complications in the United Kingdom General Practice Research Database,” *Acta Orthop*, vol. 83, no. 6, pp. 653–660, Dec. 2012, doi: 10.3109/17453674.2012.747054.
[20] M. Bhandari, K. Fong, S. Sprague, D. Williams, and B. Petrisor, “Variability in the definition and perceived causes of delayed unions and nonunions: a cross-sectional, multinational survey of orthopaedic surgeons,” *J Bone Joint Surg Am*, vol. 94, no. 15, pp. e1091-1096, Aug. 2012, doi: 10.2106/JBJS.K.01344.
[21] C. Marin, F. P. Luyten, B. Van der Schueren, G. Kerckhofs, and K. Vandamme, “The Impact of Type 2 Diabetes on Bone Fracture Healing,” *Front Endocrinol (Lausanne)*, vol. 9, p. 6, 2018, doi: 10.3389/fendo.2018.00006.
[22] R. C. Castillo, M. J. Bosse, E. J. MacKenzie, B. M. Patterson, and the L. S. Group, “Impact of Smoking on Fracture Healing and Risk of Complications in Limb-Threatening Open Tibia Fractures,” *Journal of Orthopaedic Trauma*, vol. 19, no. 3, p. 151, Mar. 2005.
[23] S. Ho, “Quit Smoking before Orthopaedic Surgery,” *Journal of Orthopaedics, Trauma and Rehabilitation*, vol. 23, pp. A1–A3, Dec. 2017, doi: 10.1016/j.jotr.2017.10.001.
[24] W. M. Ricci, P. N. Streubel, S. Morshed, C. A. Collinge, S. E. Nork, and M. J. Gardner, “Risk factors for failure of locked plate fixation of distal femur fractures: an analysis of 335 cases,” *J Orthop Trauma*, vol. 28, no. 2, pp. 83–89, Feb. 2014, doi: 10.1097/BOT.0b013e31829e6dd0.
[25] T. C. Kwiatkowski, E. N. Hanley, and W. K. Ramp, “Cigarette smoking and its orthopedic consequences,” *Am J. Orthop.*, vol. 25, no. 9, pp. 590–597, Sep. 1996.
[26] D. Berman, J. H. Oren, J. Bendo, and J. Spivak, “The Effect of Smoking on Spinal Fusion,” *Int J Spine Surg*, vol. 11, Nov. 2017, doi: 10.14444/4029.
[27] J. A. Browne, C. Cook, R. Pietrobon, M. A. Bethel, and W. J. Richardson, “Diabetes and Early Postoperative Outcomes Following Lumbar Fusion,” *Spine*, vol. 32, no. 20, p. 2214, Sep. 2007, doi: 10.1097/BRS.0b013e31814b1bc0.
[28] H. Y. Chung, P. Machado, D. van der Heijde, M.-A. D’Agostino, and M. Dougados, “Smokers in early axial spondyloarthritis have earlier disease onset, more disease activity, inflammation and damage, and poorer function and health-related quality of life: results from the DESIR cohort,” *Ann. Rheum. Dis.*, vol. 71, no. 6, pp. 809–816, Jun. 2012, doi: 10.1136/annrheumdis-2011-200180.
[29] S. P. Ganesh, R. Pietrobon, W. A. C. Cecílio, D. Pan, N. Lightdale, and J. A. Nunley, “The impact of diabetes on patient outcomes after ankle fracture,” *J Bone Joint Surg Am*, vol. 87, no. 8, pp. 1712–1718, Aug. 2005, doi: 10.2106/JBJS.D.02625.
[30] N. Vo *et al.*, “Differential effects of nicotine and tobacco smoke condensate on human annulus fibrosus cell metabolism,” *Journal of Orthopaedic Research*, vol. 29, no. 10, pp. 1585–1591, doi: 10.1002/jor.21417.
[31] G. D. Schroeder, C. K. Kepler, and A. S. Hilibrand, “The effect of smoking on patients having spinal surgery,” *Current Orthopaedic Practice*, vol. 27, no. 2, p. 140, Apr. 2016, doi: 10.1097/BCO.0000000000000331.

[32] J. M. Toth, H. B. Seim, J. D. Schwardt, W. B. Humphrey, J. A. Wallskog, and A. S. Turner, “Direct current electrical stimulation increases the fusion rate of spinal fusion cages,” *Spine*, vol. 25, no. 20, pp. 2580–2587, Oct. 2000.
[33] B. I. Martin, S. K. Mirza, B. A. Comstock, D. T. Gray, W. Kreuter, and R. A. Deyo, “Are Lumbar Spine Reoperation Rates Falling With Greater Use of Fusion Surgery and New Surgical Technology?,” *Spine*, vol. 32, no. 19, pp. 2119–2126, Sep. 2007, doi: 10.1097/BRS.0b013e318145a56a.
[34] N. K. Kanakaris and P. V. Giannoudis, “The health economics of the treatment of long-bone non-unions,” *Injury*, vol. 38 Suppl 2, pp. S77-84, May 2007.
[35] Z. Dahabreh, G. M. Calori, N. K. Kanakaris, V. S. Nikolaou, and P. V. Giannoudis, “A cost analysis of treatment of tibial fracture nonunion by bone grafting or bone morphogenetic protein-7,” *Int Orthop*, vol. 33, no. 5, pp. 1407–1414, Oct. 2009, doi: 10.1007/s00264-008-0709-6.
[36] E. Antonova, T. K. Le, R. Burge, and J. Mershon, “Tibia shaft fractures: costly burden of nonunions,” *BMC Musculoskelet Disord*, vol. 14, p. 42, Jan. 2013, doi: 10.1186/1471-2474-14-42.
[37] F. R. T. Nelson *et al.*, “Use of physical forces in bone healing,” *J Am Acad Orthop Surg*, vol. 11, no. 5, pp. 344–354, Oct. 2003, doi: 10.5435/00124635-200309000-00007.
[38] D. Gebauer, E. Mayr, E. Orthner, and J. P. Ryaby, “Low-intensity pulsed ultrasound: effects on nonunions,” *Ultrasound Med Biol*, vol. 31, no. 10, pp. 1391–1402, Oct. 2005, doi: 10.1016/j.ultrasmedbio.2005.06.002.
[39] R. Leighton, J. T. Watson, P. Giannoudis, C. Papakostidis, A. Harrison, and R. G. Steen, “Healing of fracture nonunions treated with low-intensity pulsed ultrasound (LIPUS): A systematic review and meta-analysis,” *Injury*, vol. 48, no. 7, pp. 1339–1347, Jul. 2017, doi: 10.1016/j.injury.2017.05.016.
[40] B. Mollon, V. da Silva, J. W. Busse, T. A. Einhorn, and M. Bhandari, “Electrical stimulation for long-bone fracture-healing: a meta-analysis of randomized controlled trials,” *J Bone Joint Surg Am*, vol. 90, no. 11, pp. 2322–2330, Nov. 2008, doi: 10.2106/JBJS.H.00111.
[41] C. Myeroff and M. Archdeacon, “Autogenous bone graft: donor sites and techniques,” *J Bone Joint Surg Am*, vol. 93, no. 23, pp. 2227–2236, Dec. 2011, doi: 10.2106/JBJS.J.01513.
[42] E. M. Younger and M. W. Chapman, “Morbidity at bone graft donor sites,” *J Orthop Trauma*, vol. 3, no. 3, pp. 192–195, 1989, doi: 10.1097/00005131-198909000-00002.
[43] M. Lind and C. Bünger, “Factors stimulating bone formation,” *Eur Spine J*, vol. 10 Suppl 2, pp. S102-109, Oct. 2001, doi: 10.1007/s005860100269.
[44] J. M. Lane *et al.*, “Bone Marrow and Recombinant Human Bone Morphogenetic Protein-2 in Osseous Repair,” *Clinical Orthopaedics and Related Research®*, vol. 361, p. 216, Apr. 1999.
[45] N. E. Epstein, “Complications due to the use of BMP/INFUSE in spine surgery: The evidence continues to mount,” *Surg Neurol Int*, vol. 4, no. Suppl 5, pp. S343–S352, Jul. 2013, doi: 10.4103/2152-7806.114813.
[46] N. E. Epstein, “Basic science and spine literature document bone morphogenetic protein increases cancer risk,” *Surg Neurol Int*, vol. 5, no. Suppl 15, pp. S552–S560, Dec. 2014, doi: 10.4103/2152-7806.148039.

[47] E. J. Woo, “Adverse events reported after the use of recombinant human bone morphogenetic protein 2,” *J. Oral Maxillofac. Surg.*, vol. 70, no. 4, pp. 765–767, Apr. 2012, doi: 10.1016/j.joms.2011.09.008.
[48] M. G. Lykissas *et al.*, “Nerve injury after lateral lumbar interbody fusion: a review of 919 treated levels with identification of risk factors,” *Spine J*, vol. 14, no. 5, pp. 749–758, May 2014, doi: 10.1016/j.spinee.2013.06.066.
[49] N. E. Epstein, “Pros, cons, and costs of INFUSE in spinal surgery,” *Surg Neurol Int*, vol. 2, p. 10, Jan. 2011, doi: 10.4103/2152-7806.76147.
[50] L. Claes and B. Willie, “The enhancement of bone regeneration by ultrasound,” *Prog. Biophys. Mol. Biol.*, vol. 93, no. 1–3, pp. 384–398, Apr. 2007, doi: 10.1016/j.pbiomolbio.2006.07.021.
[51] S. Lou, H. Lv, Z. Li, L. Zhang, and P. Tang, “The effects of low-intensity pulsed ultrasound on fresh fracture: A meta-analysis,” *Medicine*, vol. 96, no. 39, p. e8181, Sep. 2017, doi: 10.1097/MD.0000000000008181.
[52] R. Mundi, S. Petis, R. Kaloty, V. Shetty, and M. Bhandari, “Low-intensity pulsed ultrasound: Fracture healing,” *Indian J Orthop*, vol. 43, no. 2, pp. 132–140, 2009, doi: 10.4103/0019-5413.50847.
[53] J. W. Busse, M. Bhandari, A. V. Kulkarni, and E. Tunks, “The effect of low-intensity pulsed ultrasound therapy on time to fracture healing: a meta-analysis,” *CMAJ*, vol. 166, no. 4, pp. 437–441, Feb. 2002.
[54] E. Cottrill *et al.*, “The effect of electrical stimulation therapies on spinal fusion: a cross-disciplinary systematic review and meta-analysis of the preclinical and clinical data,” *J Neurosurg Spine*, pp. 1–21, Oct. 2019, doi: 10.3171/2019.5.SPINE19465.
[55] I. S. Aleem *et al.*, “Efficacy of Electrical Stimulators for Bone Healing: A Meta-Analysis of Randomized Sham-Controlled Trials,” *Sci Rep*, vol. 6, Aug. 2016, doi: 10.1038/srep31724.
[56] P. R. Kuzyk and E. H. Schemitsch, “The science of electrical stimulation therapy for fracture healing,” *Indian J Orthop*, vol. 43, no. 2, pp. 127–131, 2009, doi: 10.4103/0019-5413.50846.
[57] C. T. Brighton, E. Okereke, S. R. Pollack, and C. C. Clark, “In vitro bone-cell response to a capacitively coupled electrical field. The role of field strength, pulse pattern, and duty cycle,” *Clin. Orthop. Relat. Res.*, no. 285, pp. 255–262, Dec. 1992.
[58] R. Korenstein, D. Somjen, H. Fischler, and I. Binderman, “Capacitative pulsed electric stimulation of bone cells. Induction of cyclic-AMP changes and DNA synthesis,” *Biochim. Biophys. Acta*, vol. 803, no. 4, pp. 302–307, Apr. 1984, doi: 10.1016/0167-4889(84)90121-6.
[59] C. B. Goodwin, C. T. Brighton, R. D. Guyer, J. R. Johnson, K. I. Light, and H. A. Yuan, “A double-blind study of capacitively coupled electrical stimulation as an adjunct to lumbar spinal fusions,” *Spine*, vol. 24, no. 13, pp. 1349–1356; discussion 1357, Jul. 1999, doi: 10.1097/00007632-199907010-00013.
[60] M. Griffin and A. Bayat, “Electrical Stimulation in Bone Healing: Critical Analysis by Evaluating Levels of Evidence,” *Eplasty*, vol. 11, Jul. 2011.
[61] M. Nagai and M. Ota, “Pulsating electromagnetic field stimulates mRNA expression of bone morphogenetic protein-2 and -4,” *J. Dent. Res.*, vol. 73, no. 10, pp. 1601–1605, Oct. 1994, doi: 10.1177/00220345940730100401.

[62] D. W. Kucharzyk, “A controlled prospective outcome study of implantable electrical stimulation with spinal instrumentation in a high-risk spinal fusion population,” *Spine*, vol. 24, no. 5, pp. 465–468; discussion 469, Mar. 1999.
[63] A. Rubinacci, J. Black, C. T. Brighton, and Z. B. Friedenberg, “Changes in bioelectric potentials on bone associated with direct current stimulation of osteogenesis,” *J. Orthop. Res.*, vol. 6, no. 3, pp. 335–345, 1988, doi: 10.1002/jor.1100060305.
[64] C. T. Brighton, J. Black, Z. B. Friedenberg, J. L. Esterhai, L. J. Day, and J. F. Connolly, “A multicenter study of the treatment of non-union with constant direct current,” *J Bone Joint Surg Am*, vol. 63, no. 1, pp. 2–13, Jan. 1981.
[65] C. T. Brighton, Z. B. Friedenberg, L. M. Zemsky, and P. R. Pollis, “Direct-current stimulation of non-union and congenital pseudarthrosis. Exploration of its clinical application,” *J Bone Joint Surg Am*, vol. 57, no. 3, pp. 368–377, Apr. 1975.
[66] C. T. Brighton, P. Shaman, R. B. Heppenstall, J. L. Esterhai, S. R. Pollack, and Z. B. Friedenberg, “Tibial nonunion treated with direct current, capacitive coupling, or bone graft,” *Clin. Orthop. Relat. Res.*, no. 321, pp. 223–234, Dec. 1995.
[67] J. B. Haddad, A. G. Obolensky, and P. Shinnick, “The Biologic Effects and the Therapeutic Mechanism of Action of Electric and Electromagnetic Field Stimulation on Bone and Cartilage: New Findings and a Review of Earlier Work,” *Journal of Alternative & Complementary Medicine*, vol. 13, no. 5, pp. 485–490, Jun. 2007, doi: 10.1089/acm.2007.5270.
[68] W. J. Kane, “Direct current electrical bone growth stimulation for spinal fusion,” *Spine*, vol. 13, no. 3, pp. 363–365, Mar. 1988.
[69] N. Kahanovitz, “The Use of Adjunctive Electrical Stimulation to Enhance the Healing of Spine Fusions:,” *Spine*, vol. 21, no. 21, pp. 2523–2525, Nov. 1996, doi: 10.1097/00007632-199611010-00026.
[70] N. A. Tejano, R. Puno, and J. M. Ignacio, “The use of implantable direct current stimulation in multilevel spinal fusion without instrumentation. A prospective clinical and radiographic evaluation with long-term follow-up,” *Spine*, vol. 21, no. 16, pp. 1904–1908, Aug. 1996.
[71] A. Saxena, L. A. DiDomenico, A. Widtfeldt, T. Adams, and W. Kim, “Implantable Electrical Bone Stimulation for Arthrodeses of the Foot and Ankle in High-Risk Patients: A Multicenter Study,” *The Journal of Foot and Ankle Surgery*, vol. 44, no. 6, pp. 450–454, Nov. 2005, doi: 10.1053/j.jfas.2005.07.018.
[72] D. C. Paterson, G. N. Lewis, and C. A. Cass, “Treatment of delayed union and nonunion with an implanted direct current stimulator,” *Clin. Orthop. Relat. Res.*, no. 148, pp. 117–128, May 1980.
[73] A. J. Meril, “Direct current stimulation of allograft in anterior and posterior lumbar interbody fusions,” *Spine*, vol. 19, no. 21, pp. 2393–2398, Nov. 1994, doi: 10.1097/00007632-199411000-00004.
[74] A. Rogozinski and C. Rogozinski, “Efficacy of implanted bone growth stimulation in instrumented lumbosacral spinal fusion,” *Spine*, vol. 21, no. 21, pp. 2479–2483, Nov. 1996.
[75] J. Black, *Electrical Stimulation: Its Role in Growth, Repair, and Remodeling of the Musculoskeletal System*. Praeger, 1987.
[76] Q. Wang *et al.*, “Osteogenesis of electrically stimulated bone cells mediated in part by calcium ions,” *Clin. Orthop. Relat. Res.*, no. 348, pp. 259–268, Mar. 1998.

[77] T. Bodamyali, J. M. Kanczler, B. Simon, D. R. Blake, and C. R. Stevens, “Effect of faradic products on direct current-stimulated calvarial organ culture calcium levels,” *Biochem. Biophys. Res. Commun.*, vol. 264, no. 3, pp. 657–661, Nov. 1999, doi: 10.1006/bbrc.1999.1355.
[78] Z. B. Friedenberg, L. M. Zemsky, and R. P. Pollis, “The Response of Non-Traumatized Bone to Direct Current,” *JBJS*, vol. 56, no. 5, p. 1023, Jul. 1974.
[79] B. M. Isaacson and R. D. Bloebaum, “Bone bioelectricity: what have we learned in the past 160 years?,” *J Biomed Mater Res A*, vol. 95, no. 4, pp. 1270–1279, Dec. 2010, doi: 10.1002/jbm.a.32905.
[80] R. D. Evans, D. Foltz, and K. Foltz, “Electrical stimulation with bone and wound healing,” *Clin Podiatr Med Surg*, vol. 18, no. 1, pp. 79–95, vi, Jan. 2001.
[81] L. M. Dejardin, N. Kahanovitz, S. P. Arnoczky, and B. J. Simon, “The effect of varied electrical current densities on lumbar spinal fusions in dogs,” *Spine J*, vol. 1, no. 5, pp. 341–347, Oct. 2001, doi: 10.1016/s1529-9430(01)00100-0.
[82] P. G. Cho, G. Y. Ji, Y. Ha, H. Y. Lee, and D. A. Shin, “Effect of the type of electrical stimulation on spinal fusion in a rat posterolateral spinal fusion model,” *The Spine Journal*, vol. 19, no. 6, pp. 1106–1120, Jun. 2019, doi: 10.1016/j.spinee.2018.12.011.
[83] P. J. Harwood, J. B. Newman, and A. L. R. Michael, “(ii) An update on fracture healing and non-union,” *Orthopaedics and Trauma*, vol. 24, no. 1, pp. 9–23, Feb. 2010, doi: 10.1016/j.mporth.2009.12.004.
[84] H. M. Frost, “Wolff’s Law and bone’s structural adaptations to mechanical usage: an overview for clinicians,” *Angle Orthod*, vol. 64, no. 3, pp. 175–188, 1994, doi: 10.1043/0003-3219(1994)064<0175:WLABSA>2.0.CO;2.
[85] I. Yasuda, “Fundamental aspects of fracture treatment,” *J Kyoto Med SOC*, vol. 4, p. 392, 1953.
[86] C. A. Bassett and R. O. Becker, “Generation of electric potentials by bone in response to mechanical stress,” *Science*, vol. 137, no. 3535, pp. 1063–1064, Sep. 1962, doi: 10.1126/science.137.3535.1063.
[87] E. Fukada and I. Yasuda, “On the Piezoelectric Effect of Bone,” *J. Phys. Soc. Jpn.*, vol. 12, no. 10, pp. 1158–1162, Oct. 1957, doi: 10.1143/JPSJ.12.1158.
[88] E. Fukada and I. Yasuda, “Piezoelectric Effects in Collagen,” *Jpn. J. Appl. Phys.*, vol. 3, no. 2, p. 117, Feb. 1964, doi: 10.1143/JJAP.3.117.
[89] C. A. L. Bassett, “Biologic significance of piezoelectricity,” *Calc. Tis Res.*, vol. 1, no. 1, pp. 252–272, Dec. 1967, doi: 10.1007/BF02008098.
[90] C. A. L. Bassett, R. J. Pawluk, and R. O. Becker, “Effects of Electric Currents on Bone In Vivo,” *Nature*, vol. 204, no. 4959, pp. 652–654, Nov. 1964, doi: 10.1038/204652a0.
[91] J. Jacob, N. More, K. Kalia, and G. Kapusetti, “Piezoelectric smart biomaterials for bone and cartilage tissue engineering,” *Inflamm Regen*, vol. 38, p. 2, 2018, doi: 10.1186/s41232-018-0059-8.
[92] C. Halperin *et al.*, “Piezoelectric Effect in Human Bones Studied in Nanometer Scale,” *Nano Lett.*, vol. 4, no. 7, pp. 1253–1256, Jul. 2004, doi: 10.1021/nl049453i.
[93] B. Miara, E. Rohan, M. Zidi, and B. Labat, “Piezomaterials for bone regeneration design—homogenization approach,” *Journal of the Mechanics and Physics of Solids*, vol. 53, no. 11, pp. 2529–2556, Nov. 2005, doi: 10.1016/j.jmps.2005.05.006.
[94] Z. B. Friedenberg and C. T. Brighton, “Bioelectric potentials in bone,” *J Bone Joint Surg Am*, vol. 48, no. 5, pp. 915–923, Jul. 1966.

[95] R. B. Borgens, “Endogenous ionic currents traverse intact and damaged bone,” *Science*, vol. 225, no. 4661, pp. 478–482, Aug. 1984, doi: 10.1126/science.6740320.
[96] S. R. Pollack, R. Salzstein, and D. Pienkowski, “Streaming potentials in fluid-filled bone,” *Ferroelectrics*, vol. 60, no. 1, pp. 297–309, Oct. 1984, doi: 10.1080/00150198408017530.
[97] Z. B. Friedenberg, P. G. Roberts, N. H. Didizian, and C. T. Brighton, “Stimulation of fracture healing by direct current in the rabbit fibula,” *J Bone Joint Surg Am*, vol. 53, no. 7, pp. 1400–1408, Oct. 1971.
[98] T. Zigman *et al.*, “Intraoperative measurement of bone electrical potential: a piece in the puzzle of understanding fracture healing,” *Injury*, vol. 44 Suppl 3, pp. S16-19, Sep. 2013, doi: 10.1016/S0020-1383(13)70191-8.
[99] A. C. Ahn and A. J. Grodzinsky, “Relevance of collagen piezoelectricity to ‘Wolff’s Law’: a critical review,” *Med Eng Phys*, vol. 31, no. 7, pp. 733–741, Sep. 2009, doi: 10.1016/j.medengphy.2009.02.006.
[100] A. F. Dwyer and G. G. Wickham, “Direct current stimulation in spinal fusion,” *Med. J. Aust.*, vol. 1, no. 3, pp. 73–75, Jan. 1974.
[101] D. M. Goldenberg and H. J. Hansen, “Electric enhancement of bone healing,” *Science*, vol. 175, no. 4026, pp. 1118–1120, Mar. 1972.
[102] P. A. Williams and S. Saha, “The electrical and dielectric properties of human bone tissue and their relationship with density and bone mineral content,” *Ann Biomed Eng*, vol. 24, no. 2, pp. 222–233, Apr. 1996, doi: 10.1007/bf02667351.
[103] S. Stewart, S. J. Bryant, J. Ahn, and K. D. Hankenson, “Chapter 24 - Bone Regeneration,” in *Translational Regenerative Medicine*, A. Atala and J. G. Allickson, Eds. Boston: Academic Press, 2015, pp. 313–333.
[104] D. C. Fredericks *et al.*, “Effects of Direct Current Electrical Stimulation on Gene Expression of Osteopromotive Factors in a Posterolateral Spinal Fusion Model:,” *Spine*, vol. 32, no. 2, pp. 174–181, Jan. 2007, doi: 10.1097/01.brs.0000251363.77027.49.
[105] O. C. Tuncay, D. Ho, and M. K. Barker, “Oxygen tension regulates osteoblast function,” *Am J Orthod Dentofacial Orthop*, vol. 105, no. 5, pp. 457–463, May 1994, doi: 10.1016/S0889-5406(94)70006-0.
[106] M. Cho, T. K. Hunt, and M. Z. Hussain, “Hydrogen peroxide stimulates macrophage vascular endothelial growth factor release,” *Am. J. Physiol. Heart Circ. Physiol.*, vol. 280, no. 5, pp. H2357-2363, May 2001, doi: 10.1152/ajpheart.2001.280.5.H2357.
[107] N. C. Keramaris, G. M. Calori, V. S. Nikolaou, E. H. Schemitsch, and P. V. Giannoudis, “Fracture vascularity and bone healing: a systematic review of the role of VEGF,” *Injury*, vol. 39 Suppl 2, pp. S45-57, Sep. 2008, doi: 10.1016/S0020-1383(08)70015-9.
[108] D. A. Bushinsky, “Metabolic alkalosis decreases bone calcium efflux by suppressing osteoclasts and stimulating osteoblasts,” *American Journal of Physiology-Renal Physiology*, vol. 271, no. 1, pp. F216–F222, Jul. 1996, doi: 10.1152/ajprenal.1996.271.1.F216.
[109] Y. Chen and B. A. Alman, “Wnt pathway, an essential role in bone regeneration,” *J. Cell. Biochem.*, vol. 106, no. 3, pp. 353–362, Feb. 2009, doi: 10.1002/jcb.22020.
[110] J.-B. Kim *et al.*, “Bone regeneration is regulated by wnt signaling,” *J. Bone Miner. Res.*, vol. 22, no. 12, pp. 1913–1923, Dec. 2007, doi: 10.1359/jbmr.070802.
[111] K. S. Houschyar *et al.*, “Wnt Pathway in Bone Repair and Regeneration – What Do We Know So Far,” *Front Cell Dev Biol*, vol. 6, Jan. 2019, doi: 10.3389/fcell.2018.00170.

[112] B. Pietrzyk, M. Smertka, and J. Chudek, “Sclerostin: Intracellular mechanisms of action and its role in the pathogenesis of skeletal and vascular disorders,” *Adv Clin Exp Med*, vol. 26, no. 8, pp. 1283–1291, Nov. 2017, doi: 10.17219/acem/68739.
[113] M. S. Ominsky *et al.*, “Inhibition of sclerostin by monoclonal antibody enhances bone healing and improves bone density and strength of nonfractured bones,” *J. Bone Miner. Res.*, vol. 26, no. 5, pp. 1012–1021, May 2011, doi: 10.1002/jbmr.307.
[114] G. L. Galea, L. E. Lanyon, and J. S. Price, “Sclerostin’s role in bone’s adaptive response to mechanical loading,” *Bone*, vol. 96, pp. 38–44, Mar. 2017, doi: 10.1016/j.bone.2016.10.008.
[115] R. F. M. van Oers, B. van Rietbergen, K. Ito, P. A. J. Hilbers, and R. Huiskes, “A sclerostin-based theory for strain-induced bone formation,” *Biomech Model Mechanobiol*, vol. 10, no. 5, pp. 663–670, Oct. 2011, doi: 10.1007/s10237-010-0264-0.
[116] V. Veverka *et al.*, “Characterization of the structural features and interactions of sclerostin: molecular insight into a key regulator of Wnt-mediated bone formation,” *J. Biol. Chem.*, vol. 284, no. 16, pp. 10890–10900, Apr. 2009, doi: 10.1074/jbc.M807994200.
[117] A. Morse *et al.*, “Mechanical load increases in bone formation via a sclerostin-independent pathway,” *J. Bone Miner. Res.*, vol. 29, no. 11, pp. 2456–2467, Nov. 2014, doi: 10.1002/jbmr.2278.
[118] W. R. Thompson, C. T. Rubin, and J. Rubin, “Mechanical regulation of signaling pathways in bone,” *Gene*, vol. 503, no. 2, pp. 179–193, Jul. 2012, doi: 10.1016/j.gene.2012.04.076.
[119] H. Li, C. Tian, and Z. D. Deng, “Energy harvesting from low frequency applications using piezoelectric materials,” *Applied Physics Reviews*, vol. 1, no. 4, p. 041301, Nov. 2014, doi: 10.1063/1.4900845.
[120] S. Shahab, S. Zhao, and A. Erturk, “Soft and Hard Piezoelectric Ceramics and Single Crystals for Random Vibration Energy Harvesting,” *Energy Technology*, vol. 6, no. 5, pp. 935–942, 2018, doi: 10.1002/ente.201700873.
[121] S. Mishra, L. Unnikrishnan, S. K. Nayak, and S. Mohanty, “Advances in Piezoelectric Polymer Composites for Energy Harvesting Applications: A Systematic Review,” *Macromolecular Materials and Engineering*, vol. 304, no. 1, p. 1800463, 2019, doi: 10.1002/mame.201800463.
[122] M. S. Vijaya, *Piezoelectric materials and devices: applications in engineering and medical sciences*. Hoboken, NJ: CRC Press, 2012.
[123] B. Jaffe, W. R. Cook, and H. L. Jaffe, *Piezoelectric ceramics*. 1971.
[124] S. Waqar, L. Wang, and S. John, “9 - Piezoelectric energy harvesting from intelligent textiles,” in *Electronic Textiles*, T. Dias, Ed. Oxford: Woodhead Publishing, 2015, pp. 173–197.
[125] K. S. Ramadan, D. Sameoto, and S. Evoy, “A review of piezoelectric polymers as functional materials for electromechanical transducers,” *Smart Mater. Struct.*, vol. 23, no. 3, p. 033001, Jan. 2014, doi: 10.1088/0964-1726/23/3/033001.
[126] S. R. Platt, S. Farritor, and H. Haider, “On low-frequency electric power generation with PZT ceramics,” *IEEE/ASME Transactions on Mechatronics*, vol. 10, no. 2, pp. 240–252, Apr. 2005, doi: 10.1109/TMECH.2005.844704.

[127] S. Priya *et al.*, “A Review on Piezoelectric Energy Harvesting: Materials, Methods, and Circuits,” *Energy Harvesting and Systems*, vol. 4, no. 1, pp. 3–39, 2017, doi: 10.1515/ehs-2016-0028.
[128] Sodano H. A., Park G., and Inman D. J., “Estimation of Electric Charge Output for Piezoelectric Energy Harvesting,” *Strain*, vol. 40, no. 2, pp. 49–58, May 2004, doi: 10.1111/j.1475-1305.2004.00120.x.
[129] J. Xu, S. Lin, Y. Ma, and Y. Tang, “Analysis on Coupled Vibration of a Radially Polarized Piezoelectric Cylindrical Transducer,” *Sensors (Basel)*, vol. 17, no. 12, Dec. 2017, doi: 10.3390/s17122850.
[130] A. E. Glazounov, Q. M. Zhang, and C. Kim, “Piezoelectric actuator generating torsional displacement from piezoelectric d15 shear response,” *Appl. Phys. Lett.*, vol. 72, no. 20, pp. 2526–2528, May 1998, doi: 10.1063/1.121408.
[131] R. S. Dahiya and M. Valle, *Robotic Tactile Sensing: Technologies and System*. Springer Netherlands, 2013.
[132] “IEEE Standard on Piezoelectricity,” *ANSI/IEEE Std 176-1987*, pp. 0_1-, 1988, doi: 10.1109/IEEESTD.1988.79638.
[133] A. I. Ltd, *Piezoelectric Ceramics: Principles and Applications*. APC International, 2011.
[134] J. Baker, S. Roundy, and P. Wright, “Alternative Geometries for Increasing Power Density in Vibration Energy Scavenging for Wireless Sensor Networks,” in *3rd International Energy Conversion Engineering Conference*, American Institute of Aeronautics and Astronautics.
[135] A. Erturk and D. J. Inman, *Piezoelectric Energy Harvesting*. John Wiley & Sons, 2011.
[136] D. Damjanovic, “Stress and frequency dependence of the direct piezoelectric effect in ferroelectric ceramics,” *Journal of Applied Physics*, vol. 82, no. 4, pp. 1788–1797, Aug. 1997, doi: 10.1063/1.365981.
[137] K. A. Cook-Chennault, N. Thambi, and A. M. Sastry, “Powering MEMS portable devices—a review of non-regenerative and regenerative power supply systems with special emphasis on piezoelectric energy harvesting systems,” *Smart Mater. Struct.*, vol. 17, no. 4, p. 043001, Jun. 2008, doi: 10.1088/0964-1726/17/4/043001.
[138] G. K. Ottman, H. F. Hofmann, and G. A. Lesieutre, “Optimized piezoelectric energy harvesting circuit using step-down converter in discontinuous conduction mode,” *IEEE Transactions on Power Electronics*, vol. 18, no. 2, pp. 696–703, Mar. 2003, doi: 10.1109/TPEL.2003.809379.
[139] Y. C. Shu and I. C. Lien, “Analysis of power output for piezoelectric energy harvesting systems,” *Smart Mater. Struct.*, vol. 15, no. 6, p. 1499, 2006, doi: 10.1088/0964-1726/15/6/001.
[140] J. Pritchard, C. Bowen, and F. Lowrie, “Multilayer Actuators: Review,” *British Ceramic Transactions*, vol. 100, pp. 265–273, Jun. 2001, doi: 10.1179/096797801681549.
[141] S.-B. Kim, H. Park, S.-H. Kim, H. C. Wikle, J.-H. Park, and D.-J. Kim, “Comparison of MEMS PZT Cantilevers Based on $_{31}$ and $_{33}$ Modes for Vibration Energy Harvesting,” *Journal of Microelectromechanical Systems*, vol. 22, no. 1, pp. 26–33, Feb. 2013, doi: 10.1109/JMEMS.2012.2213069.
[142] W. J. Choi, Y. Jeon, J.-H. Jeong, R. Sood, and S. G. Kim, “Energy harvesting MEMS device based on thin film piezoelectric cantilevers,” *J Electroceram*, vol. 17, no. 2, pp. 543–548, Dec. 2006, doi: 10.1007/s10832-006-6287-3.

[143] H. Liu, C. Lee, T. Kobayashi, C. J. Tay, and C. Quan, “Piezoelectric MEMS-based wideband energy harvesting systems using a frequency-up-conversion cantilever stopper,” *Sensors and Actuators A: Physical*, vol. 186, pp. 242–248, Oct. 2012, doi: 10.1016/j.sna.2012.01.033.
[144] J. Kymissis, C. Kendall, J. Paradiso, and N. Gershenfeld, “Parasitic power harvesting in shoes,” in *Digest of Papers. Second International Symposium on Wearable Computers (Cat. No.98EX215)*, 1998, pp. 132–139, doi: 10.1109/ISWC.1998.729539.
[145] T. H. Ng and W. H. Liao, “Sensitivity Analysis and Energy Harvesting for a Self-Powered Piezoelectric Sensor,” *Journal of Intelligent Material Systems and Structures*, vol. 16, no. 10, pp. 785–797, Oct. 2005, doi: 10.1177/1045389X05053151.
[146] L. Gu, “Low-frequency piezoelectric energy harvesting prototype suitable for the MEMS implementation,” *Microelectronics Journal*, vol. 42, no. 2, pp. 277–282, Feb. 2011, doi: 10.1016/j.mejo.2010.10.007.
[147] C. A. Howells, “Piezoelectric energy harvesting,” *Energy Conversion and Management*, vol. 50, no. 7, pp. 1847–1850, Jul. 2009, doi: 10.1016/j.enconman.2009.02.020.
[148] M. Colin, S. Basrour, L. Rufer, C. Bantignies, and A. Nguyen-Dinh, “Highly Efficient Low-frequency Energy Harvester Using Bulk Piezoelectric Ceramics,” *J. Phys.: Conf. Ser.*, vol. 476, no. 1, p. 012133, 2013, doi: 10.1088/1742-6596/476/1/012133.
[149] G. Zhang, S. Gao, and H. Liu, “A utility piezoelectric energy harvester with low frequency and high-output voltage: Theoretical model, experimental verification and energy storage,” *AIP Advances*, vol. 6, no. 9, p. 095208, Sep. 2016, doi: 10.1063/1.4962979.
[150] J. F. Antaki *et al.*, “A Gait-Powered Autologous Battery Charging System for Artificial Organs,” *ASAIO Journal*, vol. 41, no. 3, p. M588, Sep. 1995.
[151] W. Wang, T. Yang, X. Chen, and X. Yao, “Vibration energy harvesting using a piezoelectric circular diaphragm array,” *IEEE Transactions on Ultrasonics, Ferroelectrics, and Frequency Control*, vol. 59, no. 9, pp. 2022–2026, Sep. 2012, doi: 10.1109/TUFFC.2012.2422.
[152] H. W. Kim *et al.*, “Energy Harvesting Using a Piezoelectric ‘Cymbal’ Transducer in Dynamic Environment,” *Jpn. J. Appl. Phys.*, vol. 43, no. 9R, p. 6178, Sep. 2004, doi: 10.1143/JJAP.43.6178.
[153] R. E. Newnham, J. Zhang, and R. Meyer, “Cymbal transducers: a review,” in *ISAF 2000. Proceedings of the 2000 12th IEEE International Symposium on Applications of Ferroelectrics (IEEE Cat. No.00CH37076)*, 2000, vol. 1, pp. 29–32 vol. 1, doi: 10.1109/ISAF.2000.941506.
[154] A. Bayrashev, W. P. Robbins, and B. Ziaie, “Low frequency wireless powering of microsystems using piezoelectric–magnetostrictive laminate composites,” *Sensors and Actuators A: Physical*, vol. 114, no. 2, pp. 244–249, Sep. 2004, doi: 10.1016/j.sna.2004.01.007.
[155] J. Feenstra, J. Granstrom, and H. Sodano, “Energy harvesting through a backpack employing a mechanically amplified piezoelectric stack,” *Mechanical Systems and Signal Processing*, vol. 22, no. 3, pp. 721–734, Apr. 2008, doi: 10.1016/j.ymssp.2007.09.015.
[156] S. R. Platt, S. Farritor, K. Garvin, and H. Haider, “The use of piezoelectric ceramics for electric power generation within orthopedic implants,” *IEEE/ASME Transactions on Mechatronics*, vol. 10, no. 4, pp. 455–461, Aug. 2005, doi: 10.1109/TMECH.2005.852482.

[157] S. Zhao and A. Erturk, “Deterministic and band-limited stochastic energy harvesting from uniaxial excitation of a multilayer piezoelectric stack,” *Sensors and Actuators A: Physical*, vol. 214, pp. 58–65, Aug. 2014, doi: 10.1016/j.sna.2014.04.019.
[158] T.-B. Xu *et al.*, “Energy harvesting using a PZT ceramic multilayer stack,” *Smart Mater. Struct.*, vol. 22, no. 6, p. 065015, 2013, doi: 10.1088/0964-1726/22/6/065015.
[159] M. Goldfarb and L. D. Jones, “On the Efficiency of Electric Power Generation With Piezoelectric Ceramic,” *J. Dyn. Sys., Meas., Control*, vol. 121, no. 3, pp. 566–571, Sep. 1999, doi: 10.1115/1.2802517.
[160] C. D. Richards, M. J. Anderson, D. F. Bahr, and R. F. Richards, “Efficiency of energy conversion for devices containing a piezoelectric component,” *J. Micromech. Microeng.*, vol. 14, no. 5, p. 717, 2004, doi: 10.1088/0960-1317/14/5/009.
[161] M. Kim, J. Dugundji, and B. L. Wardle, “Efficiency of piezoelectric mechanical vibration energy harvesting,” *Smart Mater. Struct.*, vol. 24, no. 5, p. 055006, Apr. 2015, doi: 10.1088/0964-1726/24/5/055006.
[162] Z. Yang, A. Erturk, and J. Zu, “On the efficiency of piezoelectric energy harvesters,” *Extreme Mechanics Letters*, vol. 15, pp. 26–37, Sep. 2017, doi: 10.1016/j.eml.2017.05.002.
[163] M. Amin Karami and D. J. Inman, “Powering pacemakers from heartbeat vibrations using linear and nonlinear energy harvesters,” *Appl. Phys. Lett.*, vol. 100, no. 4, p. 042901, Jan. 2012, doi: 10.1063/1.3679102.
[164] P. V. Malaji and S. F. Ali, “Analysis of energy harvesting from multiple pendulums with and without mechanical coupling,” *Eur. Phys. J. Spec. Top.*, vol. 224, no. 14, pp. 2823–2838, Nov. 2015, doi: 10.1140/epjst/e2015-02591-7.
[165] M. Chen-Glasser, P. Li, J. Ryu, and S. Hong, “Piezoelectric Materials for Medical Applications,” *Piezoelectricity - Organic and Inorganic Materials and Applications*, Aug. 2018, doi: 10.5772/intechopen.76963.
[166] T. Starner, “Human-powered wearable computing,” *IBM Systems Journal*, vol. 35, no. 3.4, pp. 618–629, 1996, doi: 10.1147/sj.353.0618.
[167] N. S. Shenck and J. A. Paradiso, “Energy scavenging with shoe-mounted piezoelectrics,” *IEEE Micro*, vol. 21, no. 3, pp. 30–42, May 2001, doi: 10.1109/40.928763.
[168] L. Mateu and F. Moll, “Optimum Piezoelectric Bending Beam Structures for Energy Harvesting using Shoe Inserts,” *Journal of Intelligent Material Systems and Structures*, vol. 16, no. 10, pp. 835–845, Oct. 2005, doi: 10.1177/1045389X05055280.
[169] G. Poulin, E. Sarraute, and F. Costa, “Generation of electrical energy for portable devices: Comparative study of an electromagnetic and a piezoelectric system,” *Sensors and Actuators A: Physical*, vol. 116, no. 3, pp. 461–471, Oct. 2004, doi: 10.1016/j.sna.2004.05.013.
[170] P. Niu, P. Chapman, R. Riemer, and X. Zhang, “Evaluation of motions and actuation methods for biomechanical energy harvesting,” in *2004 IEEE 35th Annual Power Electronics Specialists Conference (IEEE Cat. No.04CH37551)*, 2004, vol. 3, pp. 2100-2106 Vol.3, doi: 10.1109/PESC.2004.1355442.
[171] M. Renaud, T. Sterken, P. Fiorini, R. Puers, K. Baert, and C. van Hoof, “Scavenging energy from human body: design of a piezoelectric transducer,” in *The 13th International Conference on Solid-State Sensors, Actuators and Microsystems, 2005. Digest of Technical Papers. TRANSDUCERS ’05.*, 2005, vol. 1, pp. 784-787 Vol. 1, doi: 10.1109/SENSOR.2005.1496534.

[172] K. Fan, B. Yu, Y. Zhu, Z. Liu, and L. Wang, “Scavenging energy from the motion of human lower limbs via a piezoelectric energy harvester,” *International Journal of Modern Physics B*, vol. 31, p. 1741011, Mar. 2017, doi: 10.1142/S0217979217410119.
[173] A. H. Rajabi, M. Jaffe, and T. L. Arinzeh, “Piezoelectric materials for tissue regeneration: A review,” *Acta Biomaterialia*, vol. 24, pp. 12–23, Sep. 2015, doi: 10.1016/j.actbio.2015.07.010.
[174] C. Dagdeviren *et al.*, “Conformal piezoelectric energy harvesting and storage from motions of the heart, lung, and diaphragm,” *PNAS*, vol. 111, no. 5, pp. 1927–1932, Feb. 2014, doi: 10.1073/pnas.1317233111.
[175] C. Dagdeviren *et al.*, “Recent progress in flexible and stretchable piezoelectric devices for mechanical energy harvesting, sensing and actuation,” *Extreme Mechanics Letters*, vol. 9, pp. 269–281, Dec. 2016, doi: 10.1016/j.eml.2016.05.015.
[176] P. Martins, A. C. Lopes, and S. Lanceros-Mendez, “Electroactive phases of poly(vinylidene fluoride): Determination, processing and applications,” *Progress in Polymer Science*, vol. 39, no. 4, pp. 683–706, Apr. 2014, doi: 10.1016/j.progpolymsci.2013.07.006.
[177] P. J. Larson and B. C. Towe, “Miniature ultrasonically powered wireless nerve cuff stimulator,” in *2011 5th International IEEE/EMBS Conference on Neural Engineering*, 2011, pp. 265–268, doi: 10.1109/NER.2011.5910538.
[178] C. Luo *et al.*, “Direct Intracochlear Acoustic Stimulation Using a PZT Microactuator,” *Trends Hear*, vol. 19, Nov. 2015, doi: 10.1177/2331216515616942.
[179] M. Safaei, R. M. Meneghini, and S. R. Anton, “Energy Harvesting and Sensing With Embedded Piezoelectric Ceramics in Knee Implants,” *IEEE/ASME Transactions on Mechatronics*, vol. 23, no. 2, pp. 864–874, Apr. 2018, doi: 10.1109/TMECH.2018.2794182.
[180] S. Almouahed, M. Gouriou, C. Hamitouche, E. Stindel, and C. Roux, “The Use of Piezoceramics As Electrical Energy Harvesters Within Instrumented Knee Implant During Walking,” *IEEE/ASME Transactions on Mechatronics*, vol. 16, no. 5, pp. 799–807, Oct. 2011, doi: 10.1109/TMECH.2011.2159512.
[181] E. Friis, S. Galvis, and P. Arnold, “DC Stimulation for Spinal Fusion with a Piezoelectric Composite Material Interbody Implant: An Ovine Pilot Study,” presented at the Society for Biomaterials 2015 Annual Meeting, Charlotte, NC, 15-Apr-2015.
[182] G. V. B. Cochran, M. W. Johnson, M. P. Kadaba, F. Vosburgh, M. W. Ferguson-Pell, and V. R. Palmeiri, “Piezoelectric internal fixation devices: A new approach to electrical augmentation of osteogenesis,” *Journal of Orthopaedic Research*, vol. 3, no. 4, pp. 508–513, doi: 10.1002/jor.1100030414.
[183] J. B. Park, A. F. von Recum, G. H. Kenner, B. J. Kelly, W. W. Coffeen, and M. F. Grether, “Piezoelectric ceramic implants: A feasibility study,” *Journal of Biomedical Materials Research*, vol. 14, no. 3, pp. 269–277, 1980, doi: 10.1002/jbm.820140308.
[184] J. B. Park, B. J. Kelly, G. H. Kenner, A. F. von Recum, M. F. Grether, and W. W. Coffeen, “Piezoelectric ceramic implants: in vivo results,” *Journal of Biomedical Materials Research*, vol. 15, no. 1, pp. 103–110, 1981, doi: 10.1002/jbm.820150114.
[185] D. Schumacher, V. Strunz, and U. Gross, “Does piezoceramic influence avian bone formation in the early postoperative phase?,” *Biomaterials*, vol. 4, no. 3, pp. 215–217, Jul. 1983, doi: 10.1016/0142-9612(83)90014-5.

[186] J. B. Park, G. H. Kenner, S. D. Brown, and J. K. Scott, “Mechanical property changes of barium titanate (ceramic) after in vivo and in vitro aging,” *Biomater Med Devices Artif Organs*, vol. 5, no. 3, pp. 267–276, 1977, doi: 10.3109/10731197709118677.
[187] G. V. Cochran, M. W. Johnson, M. P. Kadaba, V. R. Palmieri, and G. Mahaffey, “Design considerations in development of a prototype, piezoelectric internal fixation plate: a preliminary report,” *J Rehabil Res Dev*, vol. 24, no. 2, pp. 39–50, 1987.
[188] C. S. McDowell, “Implanted bone stimulator and prosthesis system and method of enhancing bone growth,” US6143035A, 07-Nov-2000.
[189] T. D. Nguyen *et al.*, “Piezoelectric nanoribbons for monitoring cellular deformations,” *Nature Nanotech*, vol. 7, no. 9, pp. 587–593, Sep. 2012, doi: 10.1038/nnano.2012.112.
[190] J. Reis *et al.*, “A New Piezoelectric Actuator Induces Bone Formation In Vivo: A Preliminary Study,” *BioMed Research International*, 2012. [Online]. Available: https://www.hindawi.com/journals/bmri/2012/613403/. [Accessed: 10-Jan-2020].
[191] N. C. Goetzinger, E. J. Tobaben, J. P. Domann, P. M. Arnold, and E. A. Friis, “Composite piezoelectric spinal fusion implant: Effects of stacked generators,” *J. Biomed. Mater. Res.*, vol. 104, no. 1, pp. 158–164, Jan. 2016, doi: 10.1002/jbm.b.33365.
[192] N. E. Tobaben, J. P. Domann, P. M. Arnold, and E. A. Friis, “Theoretical model of a piezoelectric composite spinal fusion interbody implant,” *J. Biomed. Mater. Res.*, vol. 102, no. 4, pp. 975–981, Apr. 2014, doi: 10.1002/jbm.a.34750.
[193] D. Ignasiak, A. Rüeger, R. Sperr, and S. J. Ferguson, “Thoracolumbar spine loading associated with kinematics of the young and the elderly during activities of daily living,” *Journal of Biomechanics*, vol. 70, pp. 175–184, Mar. 2018, doi: 10.1016/j.jbiomech.2017.11.033.
[194] E. J. Tobaben, N. C. Goetzinger, J. P. Domann, R. Barrett-Gonzalez, P. M. Arnold, and E. A. Friis, “Stacked macro fiber piezoelectric composite generator for a spinal fusion implant,” *Smart Mater. Struct.*, vol. 24, no. 1, p. 017002, 2015, doi: 10.1088/0964-1726/24/1/017002.
[195] D. A. van den Ende, B. Bos, W. A. Groen, and L. M. J. G. Dortmans, “Lifetime of piezoceramic multilayer actuators: Interplay of material properties and actuator design,” *J Electroceram*, vol. 22, no. 1, pp. 163–170, Feb. 2009, doi: 10.1007/s10832-007-9411-0.
[196] G. Yang, S.-F. Liu, W. Ren, and B. K. Mukherjee, “Uniaxial stress dependence of the piezoelectric properties of lead zirconate titanate ceramics,” in *ISAF 2000. Proceedings of the 2000 12th IEEE International Symposium on Applications of Ferroelectrics (IEEE Cat. No.00CH37076)*, 2000, vol. 1, pp. 431–434 vol. 1, doi: 10.1109/ISAF.2000.941588.
[197] A. Rohlmann *et al.*, “Activities of Everyday Life with High Spinal Loads,” *PLoS One; San Francisco*, vol. 9, no. 5, p. e98510, May 2014, doi: http://dx.doi.org/10.1371/journal.pone.0098510.
[198] R. Arshad, L. Angelini, T. Zander, F. Di Puccio, M. El-Rich, and H. Schmidt, “Spinal loads and trunk muscles forces during level walking – A combined in vivo and in silico study on six subjects,” *Journal of Biomechanics*, Aug. 2017, doi: 10.1016/j.jbiomech.2017.08.020.
[199] Y.-H. Tsuang, Y.-F. Chiang, C.-Y. Hung, H.-W. Wei, C.-H. Huang, and C.-K. Cheng, “Comparison of cage application modality in posterior lumbar interbody fusion with posterior instrumentation—A finite element study,” *Medical Engineering & Physics*, vol. 31, no. 5, pp. 565–570, Jun. 2009, doi: 10.1016/j.medengphy.2008.11.012.

[200] A. Rohlmann, G. Bergmann, and F. Graichen, “Loads on an internal spinal fixation device during walking,” *Journal of Biomechanics*, vol. 30, no. 1, pp. 41–47, Jan. 1997, doi: 10.1016/S0021-9290(96)00103-0.
[201] E. Schneider, M. C. Michel, M. Genge, K. Zuber, R. Ganz, and S. M. Perren, “Loads acting in an intramedullary nail during fracture healing in the human femur,” *J Biomech*, vol. 34, no. 7, pp. 849–857, Jul. 2001, doi: 10.1016/s0021-9290(01)00037-9.
[202] P.-F. Yang *et al.*, “Torsion and Antero-Posterior Bending in the In Vivo Human Tibia Loading Regimes during Walking and Running,” *PLOS ONE*, vol. 9, no. 4, p. e94525, Apr. 2014, doi: 10.1371/journal.pone.0094525.
[203] P.-F. Yang *et al.*, “On the relationship between tibia torsional deformation and regional muscle contractions in habitual human exercises in vivo,” *Journal of Biomechanics*, vol. 48, no. 3, pp. 456–464, Feb. 2015, doi: 10.1016/j.jbiomech.2014.12.031.
[204] G. N. Duda, E. Schneider, and E. Y. S. Chao, “Internal forces and moments in the femur during walking,” *Journal of Biomechanics*, vol. 30, no. 9, pp. 933–941, Sep. 1997, doi: 10.1016/S0021-9290(97)00057-2.
[205] V. D’Angeli, C. Belvedere, M. Ortolani, S. Giannini, and A. Leardini, “Load along the femur shaft during activities of daily living,” *J Biomech*, vol. 46, no. 12, pp. 2002–2010, Aug. 2013, doi: 10.1016/j.jbiomech.2013.06.012.
[206] E. Friis, *Mechanical Testing of Orthopaedic Implants*, 1 edition. Duxford, United Kingdom ; Cambridge, MA: Woodhead Publishing, 2017.

**Chapter 3: Effect of compliant layers within piezoelectric composites on power generation providing electrical stimulation in low frequency applications**

Manuscript submitted to Journal of Mechanical Behavior of Biomedical Materials

Published August 2018

E. D. Krech[1], E. S. Cadel[1], R. M. Barrett[2], E. A. Friis[1,3]

[1]University of Kansas, Bioengineering Graduate Program, Lawrence, KS, USA;

[2]University of Kansas, Department of Aerospace Engineering, Lawrence, KS USA;

[3]University of Kansas, Department of Mechanical Engineering, Lawrence, KS, USA

**Corresponding Author**:

Elizabeth A. Friis
Professor, Mechanical Engineering
University of Kansas
1530 W. 15th St., 3138 Learned Hall
Lawrence, KS 66045
lfriis@ku.edu
785-550-3725
785-864-5254 (fax)

**Keywords:** human powered implants, piezoelectric composite, electrical stimulation, low frequency, power generation

**Highlights:**

- Compliant layers between stacked PZT discs significantly increases power generation
- Use of novel composite stacks allows efficient energy harvesting at low frequencies
- At low frequencies, power generation increases linearly with increasing frequency
- Consistent effect of compliant layers as load, frequency, and resistance increase

Abstract

For patients that use tobacco or have diabetes, bone healing after orthopedic procedures is challenging. Direct current electrical stimulation has shown success clinically to significantly improve bone healing in these difficult-to-fuse populations. Energy harvesting with piezoelectric material has gained popularity in the last decade, but is challenging at low frequencies due to material properties that limit total power generation at these frequencies. Stacked generators have been used to increase power generation at lower voltage levels but have not been widely explored as a load-bearing biomaterial to provide DC stimulation. To match structural compliance levels and increase efficiency of power generation at low frequencies, the effect of compliant layers between piezoelectric discs was investigated. Compliant Layer Adaptive Composite Stacks (CLACS) were manufactured using five PZT discs connected electrically in parallel and stacked mechanically in series with a layer of low modulus epoxy between each disc. The stacks were encapsulated, keeping PZT and overall volume constant. Each stack was electromechanically tested by varying load, frequency, and resistance. As compliant layer thickness increased, power generation increased significantly across all loads, frequencies, and resistances measured. As expected, increase in frequency significantly increased power output for all groups. Similarly, an increase applied peak-to-peak mechanical load also significantly increased power output. The novel use of CLACS for power generation under load and frequencies experienced by typical orthopedic implants could provide an effective method to harvest energy and provide power without the use of a battery in multiple low frequency applications.

Introduction

Orthopedic surgeries account for almost 20% of all operating room procedures in the United States and have the highest aggregate hospital costs compared to other specialties, including cardiac and childbirth [1,2]. Complete bone healing can be challenging in many orthopedic cases, particularly for diabetic patients and tobacco users [3-6]. Specifically, diabetes and cigarette smoking have been associated with significantly higher rates of pseudarthrosis, failed fusions, non-unions, and increased time to healing in a variety of orthopedic fracture and fusion procedures [7-11]. To overcome these challenges, adjunct therapies are used to enhance bone healing and improve fracture and surgical fusion success rates. Direct current (DC) electrical stimulation has over a 35-year history of successful clinical use in promoting bone healing in multiple orthopedic procedures, including non-unions, spinal fusions, and stress fractures [12-16]. DC stimulation has been linked to osteogenesis [16,17] and Tejano *et al.* showed significantly improved patient outcomes after spinal fusion with the use of DC stimulation, even without the use of posterior instrumentation [18]. Electrical stimulation improves healing rates while keeping cost down and decreasing likelihood of additional surgeries or hospital stays [19].

Because of their inherent ability to emit electric charge from mechanical loading, many different types of piezoelectric energy harvesters have been explored as an alternative to batteries [20]. Several different piezoelectric material configurations have been used to power devices and provide electrical stimulation at the site of desired bone healing [21-24]. Park *et al.* and Cochran *et al.* utilized monolithic piezoelectric material implanted *in vivo* and found voltage was generated under physiological loading. However, their results showed no enhanced bone healing through the electrical signals supplied. It was not clear in either study exactly how the electrical signals were conditioned and subsequently delivered in the animal models which could have

greatly impacted the material's ability to produce sufficient current to stimulate bone growth [21,24].

More recently, Goetzinger *et al.* utilized stacked piezoelectric element concepts to design a multilayer macro fiber composite spinal fusion implant to generate power and deliver DC stimulation to a titanium electrode at the fusion site [22, 25]. Friis *et al.* studied use of these piezoelectric composites in an interbody fusion implant design in a pilot ovine study. The piezoelectric implants delivered sufficient DC stimulation in sync with mechanical loading to enhance healthy bone growth and lead to successful fusion, as compared to control implants that did not fuse [22]. In this specific electrical stimulation application, the goal was not to maximize power, but instead to produce sufficient power to induce targeted bone growth at the low frequencies generated by normal human body motion.

While the Friis *et al.* composite piezoelectric device did deliver sufficient power to improve bone growth, mechanical studies showed peak power output occurred at a range that was much higher than the resistance of a rectifying circuit necessary to convert the voltage to a DC signal [25-27]. Additionally, the difficulty of the fabrication processes associated with the use of fibers prevented scalability for use in medical devices. The use of piezoelectric stacks would improve manufacturability, while lowering source impedance and producing more power at lower resistances, thus overcoming obstacles in practical implementation of the piezocomposites in spinal fusion implants. Additionally, piezocomposite stacks would more closely match the structural compliance of adjacent bone and other biological tissue, as compared to a co-fired stack or monolithic polycrystalline piezoelectric ceramic generator. The present study investigated the use of Compliant Layer Adaptive Composite Stacks (CLACS) and characterized power at loads representative of low frequency human body motion. It was

hypothesized that the inclusion of a compliant polymer layer between piezoelectric discs changes strain patterns within the piezoelectric discs and enhances power production, given constant piezoelectric volume, size, and shape. It was expected that power production would be consistent with results of previous studies on frequency and load under mechanical loading conditions applicable for medical devices.

## Methods

### *CLACS Generation*

#### Materials Considerations

The piezoelectric discs used were commercially available modified Navy Type I Lead Zirconate Titanate, PZT-4 material (SM111, STEMiNC, Doral, FL). This material was chosen for the high coupling coefficient ($k_t$=0.45) and desirable mechanical properties appropriate for the physiological loading conditions [28]. Both the fired-on silver electrodes and electrical poling were completed by the manufacturer under controlled conditions. The discs were axially poled though the thickness (3-direction), with the positive and negative electrodes on the top and bottom faces. Because the discs were loaded axially in compression, the thickness poling direction would best utilize the power generation characteristics of the discs. The matrix material used was a room temperature cure, two-part, medical grade epoxy (EPO-TEK® 301, Epoxy Technology, Billerica, MA). In its cured state, EPO-TEK 301 has similar mechanical strength properties as common polymers used in implantable medical devices, and has desirable dielectric properties for use in a piezocomposite.

#### Specimen Fabrication

CLACS with three different compliant layer thicknesses (n=5 in each group) were fabricated using five 10x0.4 mm PZT discs and were encapsulated in epoxy, keeping volume of PZT, overall height, and surface area constant (Figure 12). The five PZT discs were electrically

connected in parallel using conductive epoxy (EPO-TEK® H20E, Epoxy Technology, Billerica, MA) and thin strips of copper foil. The positive poling direction of each disc was verified, and discs were connected in a chain. This connection method was used for its feasibility for modification with the compliant layers and ease of repeatability in a laboratory setting. The chains of PZT discs were folded in an accordion manner to create stacks mechanically in series. This resulted in alternating poling directions of the discs but maintained parallel electrical connection and separation of the positive and negative electrodes. Slices of 11x11 mm cured epoxy of varying thicknesses (0.4 and 0.8 mm ± 0.02 mm) were made to create the compliant layers. For the 0.0 mm CLACS group, a minimal amount of epoxy was used to adhere the discs together to create a stack. For the remaining groups, the compliant layers were adhered and interdigitated between the discs to create the CLACS. All stacks were encapsulated with EPO-TEK 301 to create 11x11x9 mm specimens. The volume of PZT (157 $mm^3$), volume of epoxy (932 $mm^3$), overall height and surface area were kept constant throughout all specimens. Electrical connectivity and system-level impedance was verified before each stack was electromechanically tested.

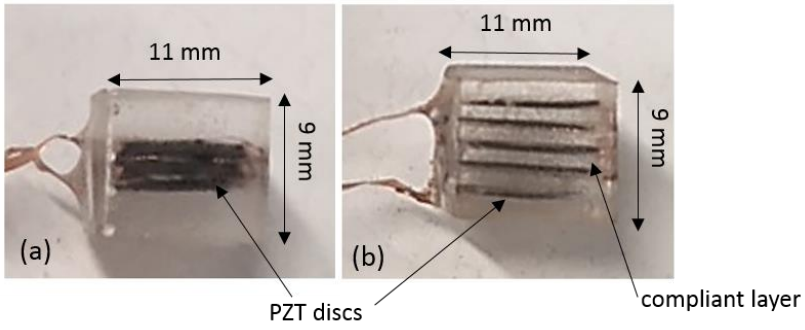


**Figure 12**. Side view of Compliant Layer Adaptive Composite Stacks. (a) 0.0mm CLACS, and (b) 0.8mm CLACS

*Electromechanical Testing*

Specimens were electromechanically tested to compare voltage produced at varying mechanical loads, frequencies, and resistance loads. A 1200 N preload was applied, followed by cyclic compression at three peak-to-peak loads of 100 N, 500 N, and 1000 N at varying frequencies of 1 Hz, 2 Hz, 3 Hz and 5 Hz using an MTS MiniBionix 858 (MTS, Eden Prairie, MN) with a self-aligning platen and 2.5 kN load cell. Conservative estimates for loads seen in generic orthopedic implants were considered to develop the loading conditions and characterize CLACS behavior during typical human body motion [29,30].

For each loading condition, voltage output of the stack was measured across a shunting resistance sweep ranging from 15 kΩ to 63.4 MΩ. Resistance values were chosen to characterize the behavior of the stacks at lower resistances necessary for circuit design, as well as to capture the resonance behavior at the matched impedance. A sampling rate of 512 Hz was used for all test conditions and data was collected for 15 cycles to capture the steady-state behavior. A custom MATLAB (Mathworks, Natick, MA) code was generated for data analysis. The measured voltage was converted to RMS, $V_{RMS} = V_{out}/\sqrt{2}$, and the average amplitude of the middle 5 cycles was used for power calculations. Power for each loading condition and resistance was calculated, $P = V_{RMS}^2/R$, and a two-way ANOVA was used to compare power production as a function of compliant layer thickness and resistance for each load. Tukey Kramer post-hoc analysis was performed to determine differences between groups ($\alpha$=0.05). The log transformation of the data was used to satisfy normality and equal variance assumptions.

## Results

*Power Generation*

The power generation capability of each CLACS was characterized over a shunting resistance sweep of 15 kΩ to 63.4 MΩ. Figure 13 shows the average power generated as a

function of compliant layer thickness for a 2 Hz, 1000 N sine wave input force, chosen to represent typical loading on an implant while walking. The shape of the power generation curve in Figure 13 was consistent for all loads and frequencies tested. The addition of a compliant layer did not affect the source impedance, as each stack type exhibited maximum power at the same resistance (6 MΩ) for the 2 Hz frequency. Table 1 shows the effect of the compliant layer on overall maximum power output for each of the CLACS.

**Table 1**. Average maximum power output measured with respect to compliant layer thickness (1000N, 5Hz, 2.5MΩ)

| Compliant Layer Thickness (mm) | Average Maximum Power (μW) |
|---|---|
| 0.0 | 3036 ± 267 |
| 0.4 | 3912 ± 708 |
| 0.8 | 4883 ± 813 |

As expected, maximum power generation occurred at the highest tested load and frequency (1000 N, 5 Hz) for all CLACS. Maximum power increased by 29% and 61% for the 0.4 mm and 0.8 mm groups respectively as compared to maximum power from the 0.0 mm baseline ($p<.05$). Additionally, the 0.8mm group produced significantly more power than the 0.4 mm group with a 25% increase ($p<.05$). This relationship held true across all 12 loading conditions tested ($p<.05$).

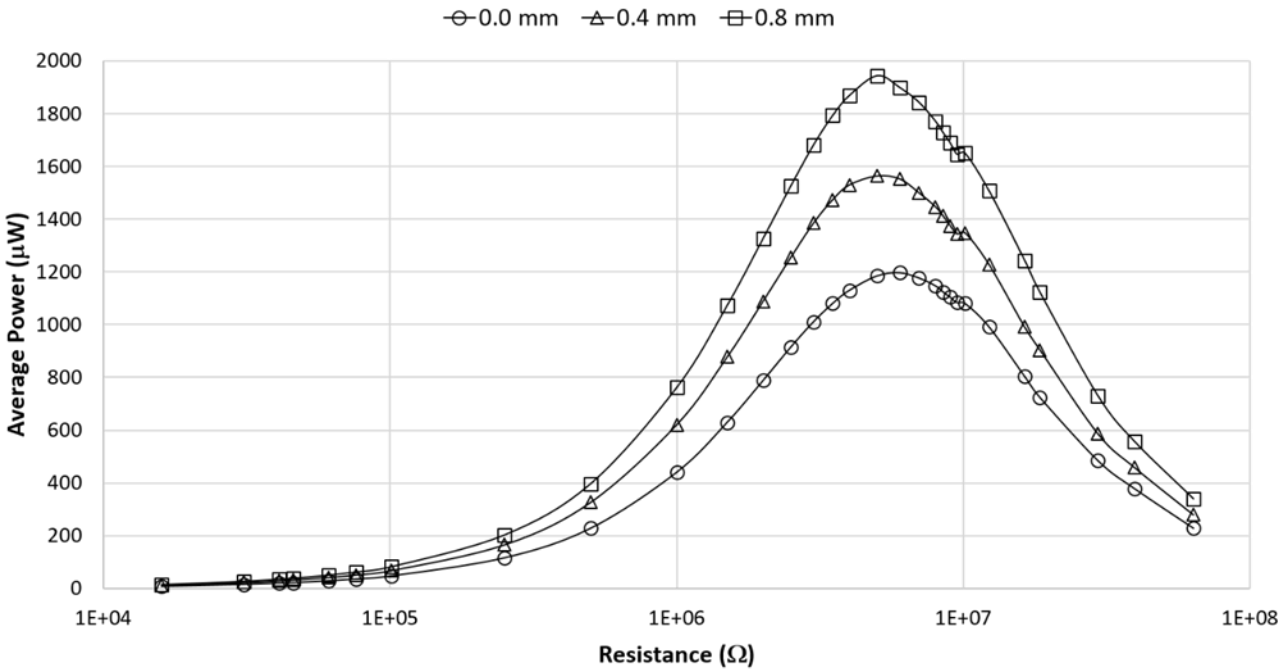


**Figure 13**. Average power output as a function of compliant layer thickness and resistance load. Average power generation curve for all groups at 1000 N and 2 Hz loading condition.

*Frequency*

The average power generated for each stack type as a function of frequency and compliant layer thickness is shown in Figure 14. Average power was reported at the resistance corresponding to maximum power for each frequency (12 MΩ at 1 Hz, 6 MΩ for 2 Hz, 4 MΩ for 3 Hz, 2.5 MΩ for 5 Hz). As frequency increased, average power occurred at a lower resistance. The statistical differences between compliant layer groups seen in the power generation curves and overall maximum power were consistent for all frequencies tested. The 0.4 mm and 0.8 mm CLACS produced significantly more power than the 0.0 mm CLACS for all frequencies ($p<.05$). The 0.8 mm CLACS also produced significantly more power than the 0.4 mm CLACS ($p<.05$). These results were consistent for all applied loads and all resistances. Additionally, an increase in frequency significantly increased power output for all groups ($p<.05$). At each given load level

tested, the increase in power generation due to the increasing frequency was as expected and primarily linear, with a two-fold increase from 1 to 2 Hz, a three-fold increase from 1 to 3 Hz, and a five-fold increase from 1 to 5 Hz. These relationships were consistent for all CLACS types for all compliant layer thicknesses for the load levels, resistances, and frequencies tested.

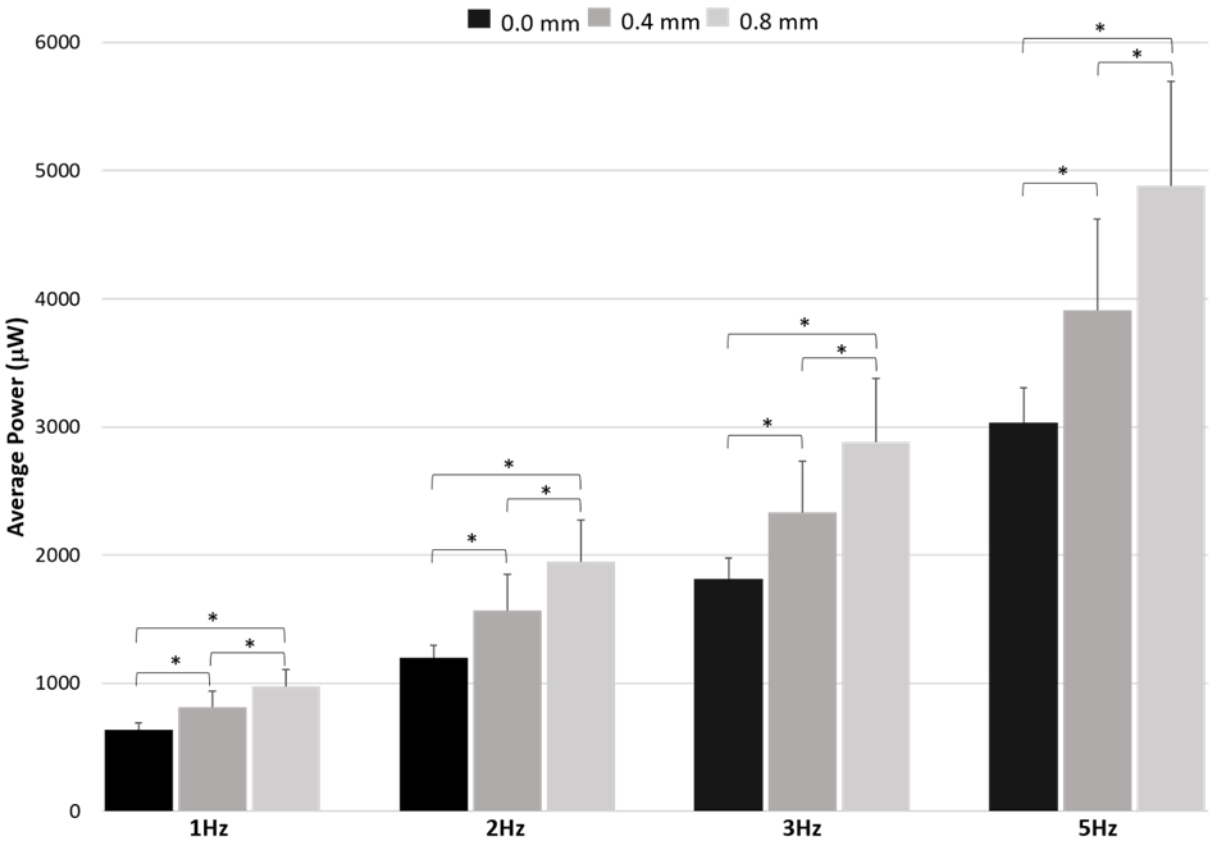


**Figure 14.** Average power generation as a function of compliant layer thickness and frequency at 1000 N. Average power presented at the resistance corresponding to peak power for each frequency (12 MΩ for 1 Hz, 6 MΩ for 2 Hz, 4 MΩ for 3 Hz, 2.5 MΩ for 5 Hz). * represents significant difference ($p<.05$).

*Load*

Increased mechanical load levels significantly increased power output for all groups ($p<.05$). With the increase in load, there was a consistent percent increase in power for all frequencies, resistances, and CLACS type. At a given frequency, the maximum power generated

was approximately 100 times greater with an increase from 100 N to 1000 N, approximately 27 times greater with an increase from 100 N to 500 N, and approximately 4 times greater with the increase from 500 N to 1000 N. This nonlinear increase was consistent throughout all specimens and loading conditions. Figure 15 demonstrates the relationship of average power generation as a function of compliant layer thickness and mechanical load applied at 5 Hz and 2.5 MΩ. At 5 Hz, maximum power generation occurred at 2.5 MΩ for all CLACS types. The statistical relationships between compliant layer groups were the same in varying loads as with frequency variation. Both the 0.4 mm and 0.8 mm compliant layer thickness CLACS produced significantly more power as compared to the 0.0 mm ($p<.05$), and the power generated from the 0.8 mm CLACS was significantly greater than 0.4 mm CLACS ($p<.05$).

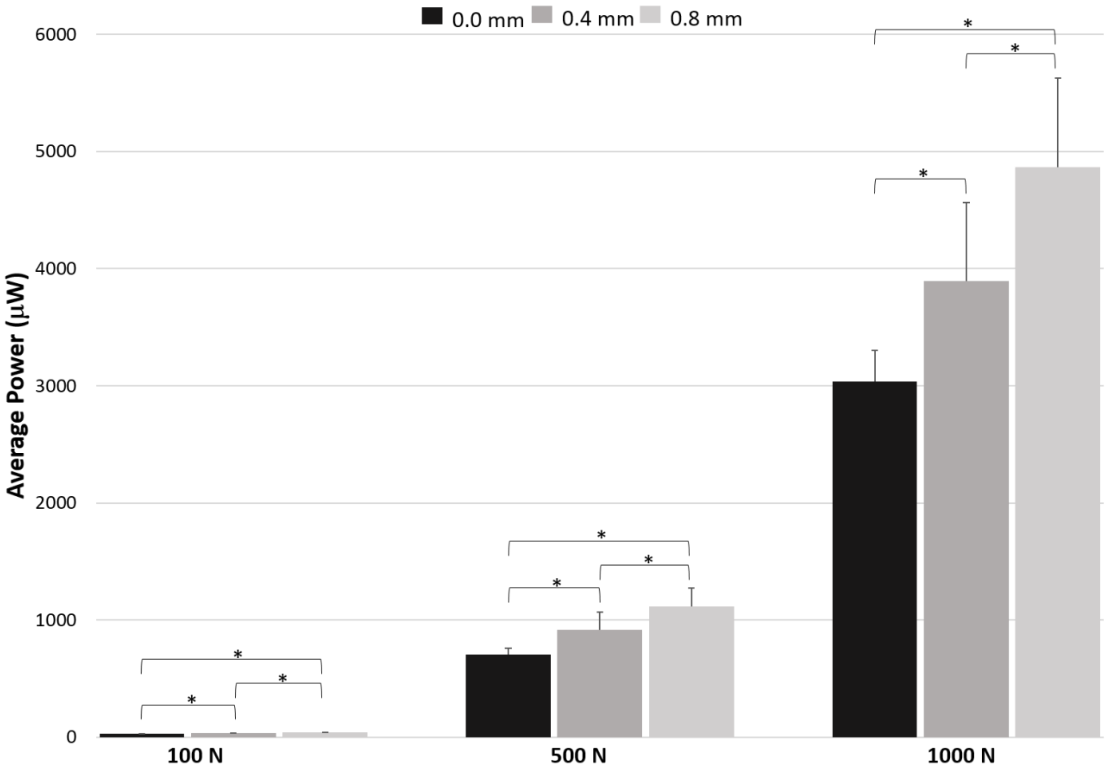


**Figure 15.** Average power as a function of compliant layer thickness and load at 5 Hz and 2.5MΩ. * represents significant difference ($p<.05$).

Discussion

This study was designed to investigate the feasibility of CLACS for use in enhancing power generation under human motion loading, specifically for use in implantable orthopedic devices to increase bone healing with DC stimulation. The goal was to measure the effect of compliant layers between PZT discs and quantify increased efficiency in harvesting energy at low frequencies due to increasing compliant layer thickness. The loads and frequencies tested in the present study define the power generation capability of CLACS under conservative estimates of loading in generic orthopedic implants, but there are other off-resonance frequencies and applications (i.e. civil infrastructure) for which CLACS could be used as an efficient energy harvesting mechanism [31].

The results of this study showed that there was a significant increase in power due to compliant layers between PZT discs in a stack at all loads and frequencies, and across all resistances measured. The addition of the compliant layer between each disc increased the positive strain in the in-plane directions of the disc while compressive loads are applied to the stack in the through-thickness direction, thus effectively amplifying the piezoelectric effect of the material and increasing the voltage (and power) produced [32]. Although a different type of PZT composite was used, Cao *et al.* and Challagulla *et al.* both showed that the deformation relationship between the piezoelectric ceramic and an elastic material in a 2-2 layer composite predicted an increase in the piezoelectric effect of the active material due to an inhomogeneous shear stress and enhancement of the piezoelectric coupling coefficient [33,34]. Additionally, Bayrashev *et al.* demonstrated that an increase in strain of the PZT increased the generated electric field by 35%, further supporting the notion that increase in strain leads to an increase in power [35].

It is known that stacks of piezoelectric elements connected electrically in parallel and stacked mechanically in series lowers the source impedance, but to date little has been done to investigate the influence of interdigitated compliant layers in piezoelectric stacks. Platt *et al.* showed that a stack of PZT elements lowers the source impedance, allowing maximum power generation at a lower load resistance, as compared to a monolithic material of the same volume [36]. To the best of our knowledge, no other studies have shown that the use of a compliant layer between PZT discs (i.e., CLACS) results in a significant increase in power generated while keeping PZT volume constant. Because the fundamental resonant frequency of most piezoelectric stacks used to convert mechanical energy to usable electrical power is in the kHz or MHz range, harvesting energy at lower frequencies can be very difficult [37]. Including a compliant layer within the stacks could increase efficiency of energy harvesting at frequencies seen in human body motion, civil infrastructure systems, and other low frequency applications.

The novel CLACS structure increased efficiency and lowered the source impedance at maximum power while maintaining the tough mechanical properties. Both attributes are required for use in medical implants and devices subjected to relatively low frequency loading conditions [22,25]. While other studies have used human motion to harvest power from piezoelectric materials, it is challenging to directly compare results because of differences in piezoelectric material properties and volume, geometric configurations, and loading conditions, all significantly affect power production. Although geometric configurations and piezoelectric volume and type were not identical to the present study, Goetzinger *et al.* tested spinal implants under the same loading conditions. At 1000 N and 2 Hz, a loading condition that mimics loads in the spine during walking [38], implants used in Goetzinger *et al.* generated 566 μW at 16 MΩ when converted to RMS. The volume of PZT used in that study was 217 $mm^3$ [25]. Despite

having 27% less volume of PZT (157 $mm^3$), the 0.0 mm, 0.4 mm, and 0.8 mm CLACS, generated 804 μW, 991 μW, 1243 μW respectively under the same loading conditions and applied resistance. Additionally, the maximum power from all CLACS groups occurred at 5 MΩ and produced more power at every applied resistance.

The addition of the compliant layer did not change the resistance at which maximum power was generated for all CLACS groups. It is important that a DC signal is delivered to the desired bone healing site, so the alternating signal produced by the piezoelectric material must be conditioned and rectified. A rectification circuit small enough to fit within an orthopedic implant would also have a small resistance. The ability of the CLACS to produce significantly more power than traditional stacks at lower resistances is beneficial for medical device design.

A lower bound theoretical model for ideal power generation from a stack with no compliant layers (0.0 mm CLACS) was developed. Assuming the PZT discs were loaded in pure compression with uniaxial deformation, the work ($W$) done on each disc was calculated given the elastic modulus of the PZT material reported by the manufacturer ($Y_{33}$ = 73 GPa) and 1000 N load applied [28]. A lower bounding expression for power ($P$) can be estimated assuming through thickness compression of the piezoelectric elements using the electromechanical coupling coefficient ($k_{33}$) and the frequency ($f$) of the applied load as seen in Eq. (1). This relationship stems from the definition of the $k_{33}$ material property, which is a measure of piezoelectric capacity of the material, and describes the relationship between electrical energy generated per mechanical load applied [39]. The value used in this calculation was the $k_t$ coefficient (0.45) provided by the manufacturer [28].

$$P = W * f * k_{33}^2 \quad (1)$$

The results from the present study found that the relationship between power generated and frequency increase is approximately linear. These results are further confirmed by the relationship between power and frequency in the theoretical model (Figure 16). This same relationship held true as the compliant layer increased in thickness. However, it is not clear if the increase in power due to the addition of compliant layers would also hold true for higher frequencies due to the viscoelastic nature of the compliant material. The theoretical model for pure PZT stacks predicts the maximum power generation (1000 N, 5 Hz) capability of the 0.0 mm specimen without any compliant layers within 30%. As shown in Figure 15, the 0.0 mm specimens produced more power than expected for all frequencies. This difference could be explained in part by the manner in which the 0.0 mm specimens were manufactured.

The discs in the 0.0 mm stacks were adhered together mechanically in series with a thin layer of epoxy to ensure correct alignment once encapsulated. The additional deformation this thin layer of epoxy allowed in the discs in the 0.0 mm CLACS could explain the difference from the theoretical model. The theoretical model under predicted power for the 0.0 mm thickness CLACS, suggesting the small amount of epoxy could have accounted for part of the 30% difference. This suggests that even a small compliant layer could increase power generation as compared to a pure PZT stack. Understanding the fatigue and multiaxial loading behavior of materials used in orthopedic devices is critical to design and mechanical assessment [40]. A pure PZT stack has poor fatigue resistance because it is ceramic [36]. The compliant layer, even a very thin layer, would not only increase power as seen in CLACS, but could also increase the mechanical toughness of the material and improve fatigue behavior.

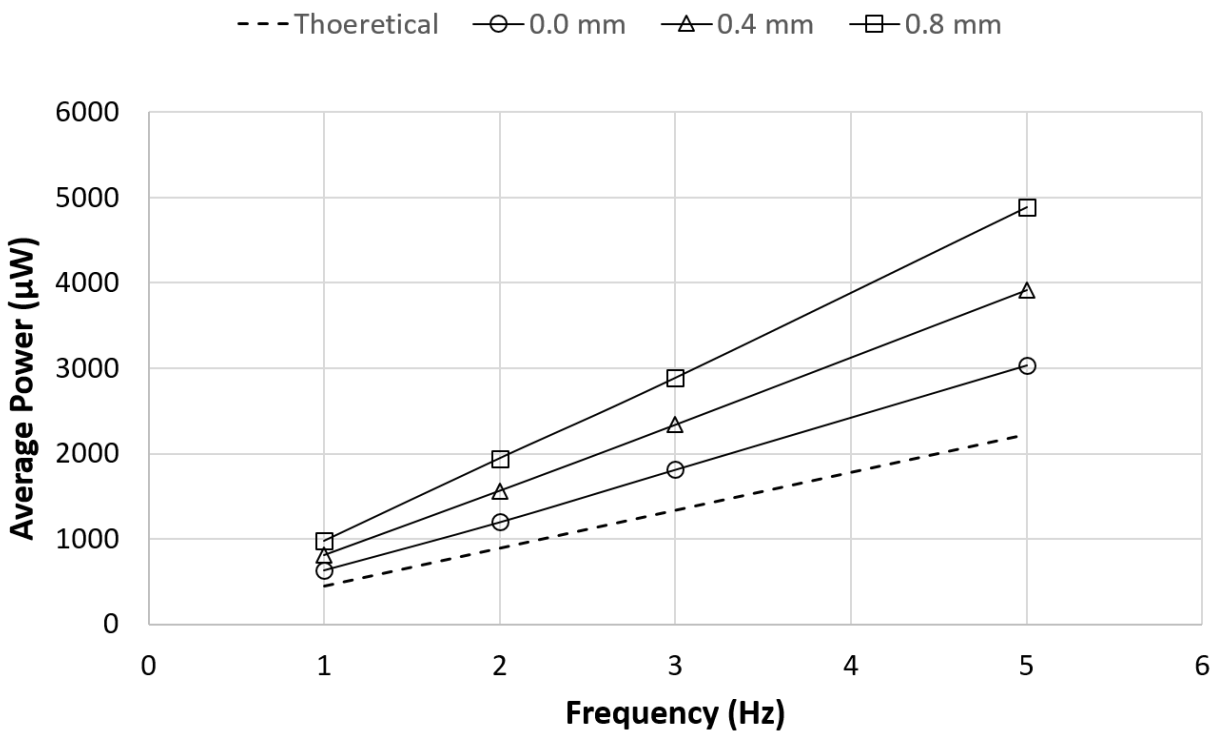


**Figure 16.** Comparison of experimental results and theoretical predictions of power generation and the effect of compliant layer thickness with respect to frequency at 1000 N and the resistance corresponding to maximum power.

Future work should include further mechanical testing of the CLACS to characterize the failure of the material in different loading conditions, as necessary for testing of orthopedic implants. Power generation of CLACS was only characterized under pure compressive loads, but applying torsion or multiaxial loads would further explain the power generation capabilities and efficacy for use in implants that experience off axis loading. Additionally, this study only investigated compliant layers that were up to twice the thickness of the PZT discs. Further work could include finding the limit of the increase in power generation due to addition of the compliant layer. Finally, the lower bounding theoretical model used in this study did not take into account the influence of the compliant layer on power generation. Theoretical models are currently being developed to explain the amplification mechanisms due to the compliant layer.

## Conclusions

The addition of a compliant layer between PZT discs to form CLACS significantly increased the power production capabilities of PZT stacks across all compressive mechanical loading conditions and resistances, while PZT volume remained constant. Previous studies have shown that piezoelectric stacks can produce identical power compared to a monolithic element at a lower impedance, but have not shown an increase in power generation with a constant volume of piezoelectric material as seen in this study. The novel use of compliant layers in piezoelectric stacks for power generation could provide an effective method for energy harvesting, without the use of a battery, in low frequency applications.

## Acknowledgements

This work was supported by an NIH STTR Phase 1 grant (R41 AR070088). The authors would like to thank Kelly Tong and Kyle Coates of The University of Kansas for their assistance in specimen manufacturing and Leighton LaPierre of Evoke Medical for his guidance and support for clinical relevance. The authors would also like to thank the Madison and Lila Self Graduate Fellowship for generous funding of graduate research at The University of Kansas.

References


[1] Fingar KR (Truven Health Analytics), Stocks C (AHRQ), Weiss AJ (Truven Health Analytics), Steiner CA (AHRQ). Most Frequent Operating Room Procedures Performed in U.S. Hospitals, 2003-2012. HCUP Statistical Brief #186. December 2014. Agency for Healthcare Research and Quality, Rockville, MD. http://www.hcup-us.ahrq.gov/reports/statbriefs/sb186-Operating-Room-Procedures-United-States-2012.pdf.

[2] Weiss AJ, Elixhauser A, Andrews RM. Characteristics of Operating Room Procedures in U.S. Hospitals, 2011. HCUP Statistical Brief #170. February 2014. Agency for Healthcare Research and Quality. Rockville, MD. http://www.hcup-us.ahrq.gov/reports/statbriefs/sb170-Operating-Room-Procedures-United-States-2011.pdf.

[3] S. Ho, Adverse Effects of Smoking on Outcomes of Orthopaedic Surgery: Journal of Orthopaedics, Trauma and Rehabilitation. 23 (2017) 54–58. doi:10.1016/j.jotr.2017.04.001.

[4] T.C. Kwiatkowski, E.N. Hanley, W.K. Ramp, Cigarette smoking and its orthopedic consequences, Am J. Orthop. 25 (1996) 590–597.

[5] C. Marin, F.P. Luyten, B. Van der Schueren, G. Kerckhofs, K. Vandamme, The Impact of Type 2 Diabetes on Bone Fracture Healing, Front Endocrinol (Lausanne). 9 (2018) 6. doi:10.3389/fendo.2018.00006.

[6] W.M. Ricci, P.N. Streubel, S. Morshed, C.A. Collinge, S.E. Nork, M.J. Gardner, Risk factors for failure of locked plate fixation of distal femur fractures: an analysis of 335 cases, J Orthop Trauma. 28 (2014) 83–89. doi:10.1097/BOT.0b013e31829e6dd0.

[7] D. Berman, J.H. Oren, J. Bendo, J. Spivak, The Effect of Smoking on Spinal Fusion, Int J Spine Surg. 11 (2017). doi:10.14444/4029.

[8] J.A. Browne, C. Cook, R. Pietrobon, M.A. Bethel, W.J. Richardson, Diabetes and Early Postoperative Outcomes Following Lumbar Fusion, Spine. 32 (2007) 2214. doi:10.1097/BRS.0b013e31814b1bc0.

[9] H.Y. Chung, P. Machado, D. van der Heijde, M.-A. D'Agostino, M. Dougados, Smokers in early axial spondyloarthritis have earlier disease onset, more disease activity, inflammation and damage, and poorer function and health-related quality of life: results from the DESIR cohort, Ann. Rheum. Dis. 71 (2012) 809–816. doi:10.1136/annrheumdis-2011-200180.

[10] S.P. Ganesh, R. Pietrobon, W.A.C. Cecílio, D. Pan, N. Lightdale, J.A. Nunley, The impact of diabetes on patient outcomes after ankle fracture, J Bone Joint Surg Am. 87 (2005) 1712–1718. doi:10.2106/JBJS.D.02625.

[11] N. Vo, D. Wang, G. Sowa, W. Witt, K. Ngo, P. Coelho, R. Bedison, B. Byer, R. Studer, J. Lee, Y.P. Di, J. Kang, Differential effects of nicotine and tobacco smoke condensate on human annulus fibrosus cell metabolism, Journal of Orthopaedic Research. 29 (n.d.) 1585–1591. doi:10.1002/jor.21417.

[12] C.T. Brighton, J. Black, Z.B. Friedenberg, J.L. Esterhai, L.J. Day, J.F. Connolly, A multicenter study of the treatment of non-union with constant direct current, J Bone Joint Surg Am. 63 (1981) 2–13.

[13] C.T. Brighton, Z.B. Friedenberg, L.M. Zemsky, P.R. Pollis, Direct-current stimulation of non-union and congenital pseudarthrosis. Exploration of its clinical application, J Bone Joint Surg Am. 57 (1975) 368–377.

[14] J.B. Haddad, A.G. Obolensky, P. Shinnick, The Biologic Effects and the Therapeutic Mechanism of Action of Electric and Electromagnetic Field Stimulation on Bone and

Cartilage: New Findings and a Review of Earlier Work, Journal of Alternative & Complementary Medicine. 13 (2007) 485–490. doi:10.1089/acm.2007.5270.
[15] W.J. Kane, Direct current electrical bone growth stimulation for spinal fusion, Spine. 13 (1988) 363–365.
[16] A. Rubinacci, J. Black, C.T. Brighton, Z.B. Friedenberg, Changes in bioelectric potentials on bone associated with direct current stimulation of osteogenesis, J. Orthop. Res. 6 (1988) 335–345. doi:10.1002/jor.1100060305.
[17] K. Yonemori, S. Matsunaga, Y. Ishidou, S. Maeda, H. Yoshida, Early effects of electrical stimulation on osteogenesis, Bone. 19 (1996) 173–180.
[18] N.A. Tejano, R. Puno, J.M. Ignacio, The use of implantable direct current stimulation in multilevel spinal fusion without instrumentation. A prospective clinical and radiographic evaluation with long-term follow-up, Spine. 21 (1996) 1904–1908.
[19] J.M. Khalifeh, Z. Zohny, P. Gamble, M. MacEwan, W.Z. Ray, Electrical Stimulation and Bone Healing: A Review of Current Technology and Clinical Applications, IEEE Reviews in Biomedical Engineering. (2018) 1–1. doi:10.1109/RBME.2018.2799189.
[20] S.R. Anton, H.A. Sodano, A review of power harvesting using piezoelectric materials (2003–2006), Smart Mater. Struct. 16 (2007) R1. doi:10.1088/0964-1726/16/3/R01.
[21] G.V.B. Cochran, M.W. Johnson, M.P. Kadaba, F. Vosburgh, M.W. Ferguson-Pell, V.R. Palmeiri, Piezoelectric internal fixation devices: A new approach to electrical augmentation of osteogenesis, Journal of Orthopaedic Research. 3 (1985) 508–513. doi:10.1002/jor.1100030414.
[22] E. Friis, S. Galvis, P. Arnold, DC Stimulation for Spinal Fusion with a Piezoelectric Composite Material Interbody Implant: An Ovine Pilot Study, (2015). http://abstracts.biomaterials.org/data/papers/2015/abstracts/809.pdf.
[23] J.B. Park, A.F. von Recum, G.H. Kenner, B.J. Kelly, W.W. Coffeen, M.F. Grether, Piezoelectric ceramic implants: A feasibility study, Journal of Biomedical Materials Research. 14 (1980.) 269–277. doi:10.1002/jbm.820140308.
[24] J.B. Park, B.J. Kelly, G.H. Kenner, A.F. von Recum, M.F. Grether, W.W. Coffeen, Piezoelectric ceramic implants: *in vivo* results, Journal of Biomedical Materials Research. 15 (1981) 103–110. doi:10.1002/jbm.820150114.
[25] N.C. Goetzinger, E.J. Tobaben, J.P. Domann, P.M. Arnold, E.A. Friis, Composite piezoelectric spinal fusion implant: Effects of stacked generators, J. Biomed. Mater. Res. 104 (2016) 158–164. doi:10.1002/jbm.b.33365.
[26] E.J. Tobaben, N.C. Goetzinger, J.P. Domann, R. Barrett-Gonzalez, P.M. Arnold, E.A. Friis, Stacked macro fiber piezoelectric composite generator for a spinal fusion implant, Smart Mater. Struct. 24 (2015) 17002. doi:10.1088/0964-1726/24/1/017002.
[27] N.E. Tobaben, J.P. Domann, P.M. Arnold, E.A. Friis, Theoretical model of a piezoelectric composite spinal fusion interbody implant, J. Biomed. Mater. Res. 102 (2014) 975–981. doi:10.1002/jbm.a.34750.
[28] STEMiNC, "Piezo Material Properties," Steiner Martins Inc [Online]. Available: http://www.steminc.com/piezo/PZ_property.asp.
[29] R. Arshad, L. Angelini, T. Zander, F. Di Puccio, M. El-Rich, H. Schmidt, Spinal loads and trunk muscles forces during level walking – A combined in vivo and in silico study on six subjects, Journal of Biomechanics. (2017). doi:10.1016/j.jbiomech.2017.08.020.
[30] R. Cromwell, A.B. Schultz, R. Beck, D. Warwick, Loads on the lumbar trunk during level walking, J. Orthop. Res. 7 (1989) 371–377. doi:10.1002/jor.1100070309.

[31] S. Roundy, P.K. Wright, J. Rabaey, A study of low level vibrations as a power source for wireless sensor nodes, Computer Communications. 26 (2003) 1131–1144. doi:10.1016/S0140-3664(02)00248-7.
[32] H. Li, C. Tian, Z.D. Deng, Energy harvesting from low frequency applications using piezoelectric materials, Applied Physics Reviews. 1 (2014) 41301. doi:10.1063/1.4900845.
[33] W. Cao, Q.M. Zhang, L.E. Cross, Theoretical study on the static performance of piezoelectric ceramic-polymer composites with 2-2 connectivity, IEEE Transactions on Ultrasonics, Ferroelectrics, and Frequency Control. 40 (1993) 103–109. doi:10.1109/58.212557.
[34] K.S. Challagulla, T.A. Venkatesh, Electromechanical response of 2-2 layered piezoelectric composites: A micromechanical model based on the asymptotic homogenization method, Philosophical Magazine. 89 (2009) 1197–1222. doi:10.1080/14786430902915412.
[35] A. Bayrashev, W.P. Robbins, B. Ziaie, Low frequency wireless powering of microsystems using piezoelectric–magnetostrictive laminate composites, Sensors and Actuators A: Physical. 114 (2004) 244–249. doi:10.1016/j.sna.2004.01.007.
[36] S.R. Platt, S. Farritor, H. Haider, On low-frequency electric power generation with PZT ceramics, IEEE/ASME Transactions on Mechatronics. 10 (2005) 240–252. doi:10.1109/TMECH.2005.844704.
[37] S. Zhao, A. Erturk, Deterministic and band-limited stochastic energy harvesting from uniaxial excitation of a multilayer piezoelectric stack, Sensors and Actuators A: Physical. 214 (2014) 58–65. doi:10.1016/j.sna.2014.04.019.
[38] D. Ignasiak, A. Rüeger, R. Sperr, S.J. Ferguson, Thoracolumbar spine loading associated with kinematics of the young and the elderly during activities of daily living, Journal of Biomechanics. 70 (2018) 175–184. doi:10.1016/j.jbiomech.2017.11.033.
[39] B. Jaffe, W.R. Cook jr., H. Jaffe, CHAPTER 3 - MEASUREMENT TECHNIQUES, in: Piezoelectric Ceramics, Academic Press, 1971: pp. 23–47. https://www.sciencedirect.com/science/article/pii/B9780123795502500077.
[40] E. Friis, Mechanical Testing of Orthopaedic Implants, 1 edition, Woodhead Publishing, Duxford, United Kingdom ; Cambridge, MA, 2017.

## Chapter 4: Power Generation Amplification and Stack Toughening Via Compliant Layer Interdigitation

Conference paper submitted to the ASME 2018 Conference on Smart Materials, Adaptive Structures and Intelligent Systems

Published September 2018

**Ember D. Krech**
The University of Kansas
Lawrence, Kansas 66045 USA

**Dr. Ronald M. Barrett**
The University of Kansas
Lawrence, Kansas 66045 USA

**Eileen S. Cadel**
The University of Kansas
Lawrence, Kansas 66045 USA

**Dr. Elizabeth A. Friis**
The University of Kansas
Lawrence, Kansas 66045 USA

Abstract

Energy harvesting from low frequency cyclic motion is possible in a variety of applications, but generating power with piezoelectric stacks at low, off-resonance frequencies is challenging. In this study, Compliant Layer Adaptive Composite Stacks (CLACS) were investigated as a toughened piezoelectric generator to increase efficiency at low frequencies and match the compliance of many commercial devices.

CLACS were manufactured with PZT discs, interdigitated epoxy layers of varying thicknesses, and encapsulated in epoxy. Energy production of each CLACS type as a function of compliant layer thickness was characterized. Power amplification of CLACS was modeled assuming discs remain planar, volume of epoxy was conserved, and total epoxy deformations were small. Shear lag theory demonstrated increases in positive in-plane strains induced by external through-thickness compression. This amplified sensitivity of the entire stack to through-thickness compressions, substantially increases power generation capability.

Experimental data showed that increases in compliant layer thickness resulted in increased power generation in all loading conditions. The shear lag structural mechanics model showed good correlation with theoretical predictions, assuming small deformation of the compliant layer. In addition to reducing composite stiffness, the CLACS generated 61% more power than conventional stack actuators with the same PZT volume via lateral strain amplification effects.

## Introduction

Piezoelectric elements can be effective energy harvesters, but are most efficient when the device matches both the electrical and mechanical impedances of the loading conditions [1]. At low frequencies, the mismatch in device resonance frequency and loading frequency amplifies the limited charge density and strain amplitude, making them less effective [2]. To date, most of the research done on piezoelectric devices to overcome this suboptimal performance at low frequencies has been by modifying materials, mounting design configurations, and manufacturing processes in bimorph beams [3–7]. Additionally, several researchers have studied the application of different piezoelectric configurations, including modified unimorph or bimorph beams and PVDF laminates in the heels of shoes to harvest power from walking [8–12]. However, because walking occurs at off-resonant frequencies and the devices have high source impedance [13], Niu *et al.* suggests that piezoelectrics might not be the most effective method for harvesting energy from heel strike [14].

Piezoelectric stacks are used to lower source impedance and increase functionality at lower resistances [15] and have been used in several studies to harvest energy from low frequency motion [1,15–18]. Xu *et al.* found that a PZT stack was more efficient at off-resonance frequencies than beams of similar dimensions due to the higher mechanical to electrical energy conversion [18]. In addition, Platt *et al.* found that, under the same mechanical loading conditions, a stack and monolithic cylinder produced the same amount of power, but the source impedance of the stack was much lower than that of the cylinder [15]. To date, little work has been done to increase efficiency of power generation utilizing piezoelectric stacks because of the limitations discussed. However, in a model for efficiency based on piezoelectric material

properties, Richards *et al.* suggest that the largest increase in efficiency of a piezoelectric device will stem from a decrease in structural stiffness [19].

The present study presents a novel manufacturing method of creating Compliant Layer Adaptive Composite Stacks (CLACS). This method of toughening a piezoelectric stack was modeled theoretically and experimentally verified through electromechanical testing at low frequencies. The effect of the compliant layer thickness on voltage, power, and mass power density for each stack type was compared.

Nomenclature

| | | |
|---|---|---|
| AF | | Amplification Factor ~ |
| E | extensional stiffness | Pa (psi) |
| G | shear modulus | Pa (psi) |
| L | length | mm (in) |
| t | thickness | mm (in) |
| T | temperature | °C (°F) |
| g | piezoelectric voltage constant | Vm/N |
| d | piezoelectric charge constant | m/V |
| k | electromechanical coupling factor | ~ |
| f | frequency | Hz |
| u, v, w | deflections in the x, y and z directions | mm (in) |
| x, y, z | principal ply and laminate directions | ~ |

*Greek Symbols*

| | | |
|---|---|---|
| ε | strain | ~ |
| σ | stress | Pa (psi) |

*Subscripts*

| | |
|---|---|
| CL | relating to the compliant layer |
| PZT | relating to the piezoelectric material |
| 1,2,3 | along the piezoelectric 1,2,3 directions |
| x,y,z | along the composite x,y,z directions |

*Acronyms*

| | |
|---|---|
| PZT | lead zirconate titanate |
| CLACS | compliant layer adaptive composite stack |

Experimental Methods

To investigate the effect of toughening piezoelectric stacks by adding compliant layers in between the discs, CLACS were manufactured. Compliant layers were sliced from cured

EPO-TEK 301 epoxy (Epoxy Technology, Billerica, MA) in two different thicknesses 0.4mm±0.02mm and 0.8mm±0.02mm. These thicknesses were chosen based on the thickness of the PZT discs used. 10x0.4mm modified PZT-4 (SM111) discs were chosen for the favorable coupling coefficient (0.45) and sizes that would allow efficient manufacturing in the laboratory. Chains of five PZT discs (STEMiNC, Doral, FL) were connected using copper foil and EPO-TEK H20E conductive epoxy (Epoxy Technology, Billerica, MA), ensuring parallel electrical connectivity. CLACS were created by adhering the compliant layers in between each of the PZT discs, alternating the poling direction of each adjacent disc (Figure 17). Stacks without a compliant layer (0.0mm group) were also manufactured as a control for comparison. The 0.0mm stacks were connected as described above and stacked with a single droplet of epoxy to ensure proper alignment once encapsulated. Each CLACS type (n=5 in each group) were encapsulated in EPO-TEK 301, ensuring that the overall volume (11x11x9.5mm) remained constant (Figure 17).

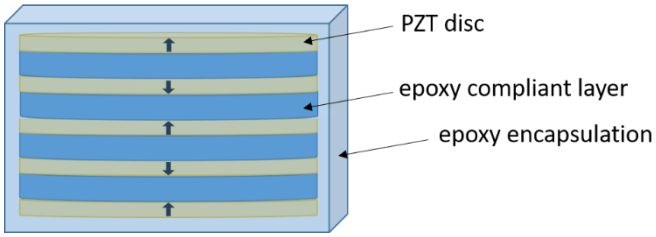


**Figure 17**. CLACS schematic. Arrows represent poling direction.

Following the manufacturing of the CLACS, electromechanical testing was completed to characterize the power production capabilities of each stack type. Pure compressive loads were applied using an MTS MiniBionix 858 (MTS, Eden Prairie, MN) with a self-aligning platen (Figure 18). The loading conditions were chosen to characterize the effect of the compliant layer as a function of three loads and four frequencies. Following a 1200N compressive preload, a

cyclic load of 100N was applied for 15 cycles at each frequency tested (1Hz, 2Hz, 3Hz and 5Hz). The same procedure was followed for a 500N and 1000N load at each frequency. All four frequencies tested were chosen to be well below the resonant frequency (5MHz) of the PZT discs. For each load and frequency combination, steady-state voltage output from each CLACS was measured across a shunt resistance sweep from 15kΩ to 63MΩ. The measured voltage was converted to RMS, scaled to reflect voltage output of the CLACS, and the average amplitudes of the middle five cycles was used for the voltage and power comparisons. For each load, frequency and resistance, power output was calculated. Results were compared using a two-way ANOVA with a Tukey-Kramer post-hoc analysis ($\alpha$=.05).


**Figure 18**. Experimental setup. Compressive load applied to CLACS and voltage measured across shunt resistance in series with CLACS.

Model

Through-thickness compression modeling is accomplished, assuming that the piezoelectric elements remain planar throughout all deflections and that the epoxy modulus is much lower than the modulus of the piezoelectric elements. The resins used in the CLACS elements are typically two orders of magnitude lower than the piezoelectric elements. As a result, the gross modulus of the CLACS is a much closer match to biological tissues than a conventional

piezoelectric stack. The overall deformation geometry of the stack is also different when loaded as seen in Figure 19.

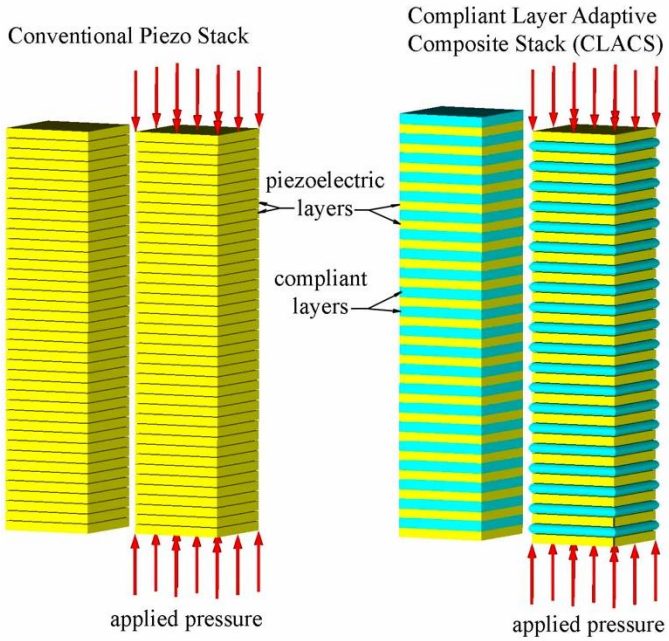


**Figure 19**. Conventional piezo stack and Compliant Layer Adaptive Composite Stacks (CLACS) under design loads.

Given a compressive load on a conventional stack and a CLACS, individual piezoelectric element loading is far more complex in the CLACS as compared to a conventional stack. Figure 20 shows a closer view of an individual element highlighting the deformed compliant layer shape, which plays a very significant role in electrical power generation.

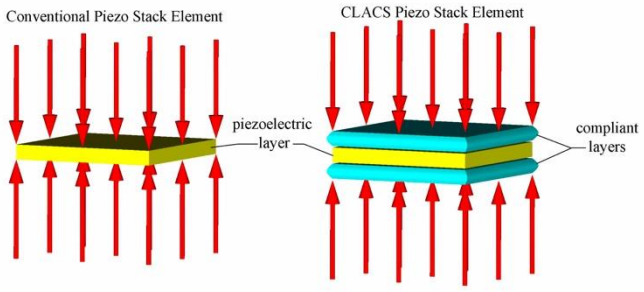


**Figure 20**. Individual conventional piezo stack and CLACS elements under design loads.

As demonstrated in Figure 20, the loading case between the two are not quite the same. The loading of the elements in a conventional piezoelectric stack are textbook straightforward; however, the CLACS element loading is more complicated. A still closer examination of an individual analysis element will illuminate the differences in stresses induced in the CLACS element. A convenient analysis element is composed of two half-compliant layers placed on top and bottom of a piezoelectric layer. The balanced, symmetric laminate of these elements clearly generates stresses that are different than those of a conventional element as shown in Figure 21.

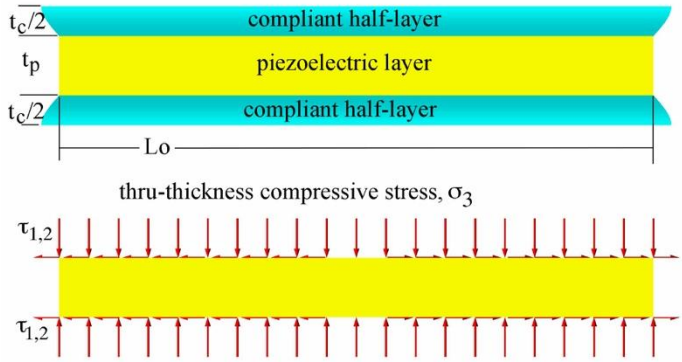


**Figure 21**. Single analysis element of a CLACS element showing surface traction and resulting thru-thickness ($\sigma_3$) and in-plane stresses ($\tau_{1,2}$).

To model the behavior of the element, an idea of the shape function governing the deformations needed to be determined. To get a good approximation of the shape function (which could be circular arc, parabolic, elliptical etc.), a simple experimental model was made and tested. A compliant layer (purple) of matrix was cast between two aluminum plates of two orders of magnitude higher stiffness. The aluminum-compliant layer sandwich was exposed to higher and higher stresses, causing the purple matrix to compress through the thickness and deform laterally as seen below in Figure 22 (A - D).

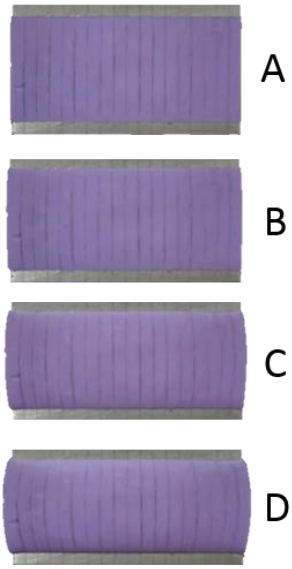


**Figure 22**. Compliant Layer (purple, vertically striped), between two Stiff (aluminum) plates undergoing increasing compressive stress and deformation (A-D).

The compliant purple layer shown in Figure 22 was scored vertically so that resulting deformations could be shown and a shape function could be determined. From photogrammetric analysis, it was determined that the shape functions are parabolic with a coefficient of determination, $R^2$ in excess of 0.999. If one examines the distribution of the shear stresses applied in the form of surface traction to the element, it can be seen that the shear strain, $\gamma(x,0)$ on the surface varies from zero to a maximum level at the end of the element as shown in Figure 23.

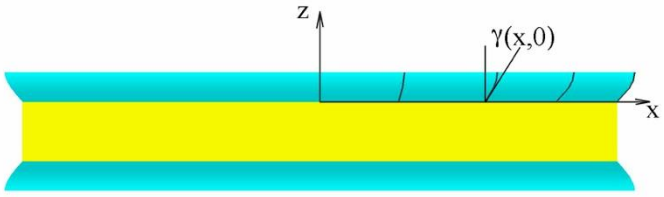


**Figure 23.** Parabolic deformation of compliant layer along the length of the element.

Clearly, the applied surface shear stresses, $\tau(x,0) = G\,\gamma(x,0)$. Assuming the compliant layer is incompressible and constrained primarily by the piezoelectric layer, the work performed by the

through-thickness force in the bond will be roughly equal to the in-plane constraining work. This assumes an ideal work transfer, which breaks down at very high bond thicknesses. However, for comparatively small, low modulus bond lines, a comparatively simple expression may be seen.

If one then looks for a factor, relating the amount of charge (or power) generated from such an element, considering a baseline amount of power, $P_0$, stemming from only considering through-thickness compression and the piezoelectric constant $d_{33}$, an "amplification factor" ($AF$) can be determined:

$$AF = \frac{P}{P_0} \sim 1 + \left|\frac{d_{31}}{d_{33}}\right| \sqrt{\frac{t_{CL}}{2t_{PZT}} \frac{E_{PZT}}{E_{CL}}} \qquad (1)$$

The expression for $AF$ represents an ideal level of work transfer from through-thickness compression to lateral work. These assumptions provide a bounding case of work estimation. Higher fidelity modeling using computational techniques is necessary to capture the behavior more accurately.

Experimental Results

All CLACS groups were experimentally tested as explained above and average voltage and power output as a function of compliant layer thickness and optimal load resistance can be seen in Table 2. The optimal load resistance for all groups was 2.5MΩ (1000N, 5Hz). For all loading conditions tested, an increase in compliant layer thickness significantly increased power generation ($p<.0001$). The 0.8mm group produced on average 61% and 25% more power than the 0.0mm and 0.4mm groups, respectively. Similarly, the 0.4mm group produced 29% more average power than the 0.0mm group. Voltage significance follows the same statistical trends ($p<.05$), with an 11% increase due to the 0.4mm thickness as compared to the 0.0mm group, and an 26% increase due to the 0.8mm thickness compared to the 0.0mm group. There was no statistical difference

between voltage produced by the 0.4mm and 0.8mm groups at this specific load, frequency and resistance (p=.08).

**Table 2**. Average peak power and voltage output of each CLACS group at 1000N, 5Hz, 2.5MΩ. *represents significant difference from 0.0mm group. # represents significant difference from 0.4mm group.

| Compliant Layer Thickness (mm) | Average Voltage at Maximum Power (V) | Average Maximum Power (μW) |
|---|---|---|
| 0.0 | 87.1 ± 3.8 | 3036 ± 267 |
| 0.4 | 98.3 ± 8.1 * | 3912 ± 708 * |
| 0.8 | 110.0 ± 8.4 * | 4883 ± 813 *# |

The average voltage produced as a function of frequency and compliant layer thickness is shown in Figure 23. Results are presented at optimal resistance for all groups. As anticipated, average voltage produced by the CLACS increased with increasing frequency. With increasing frequency, an increase in compliant layer thickness has a larger effect on voltage output. The 0.4mm group produced on average 11% more voltage compared to the 0.0mm group and the 0.8mm group produced on average 23% and 11% more voltage than the 0.0mm and 0.4mm groups, respectively (p<.05). These statistical trends and percent changes were consistent for all four frequencies tested. The nonlinearity of the voltage-frequency relationship (Figure 24) suggests that the increase in voltage due to the compliant layer is most effective at low frequencies.

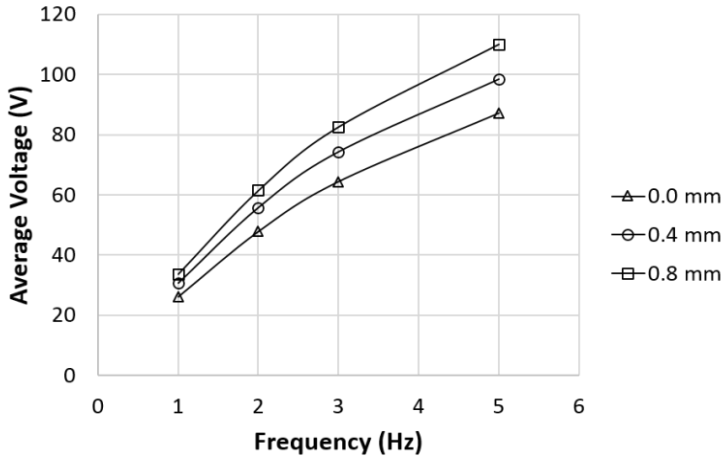


**Figure 24.** Average voltage as a function of compliant layer thickness and frequency. Representative voltage data presented at maximum power (1000N, 2.5MΩ).

Additionally, as anticipated an increase in load significantly increased voltage produced for all groups ($p<.05$), as seen in Figure 25. Specifically, an increase in load from 100N to 500N led to a 4.7-fold increase for all groups, 500N to 1000N led to a 2.2-fold increase, and 100N to 1000N led to a 10.5-fold increase in voltage produced. At 100N, an increase in compliant layer thickness significantly increased voltage produced ($p<.05$). At 500N and 1000N, the 0.4mm and 0.8mm groups both produced significantly more voltage as compared to the 0.0mm group ($p<.05$) and were trending toward a significant difference from each other ($p<.1$).

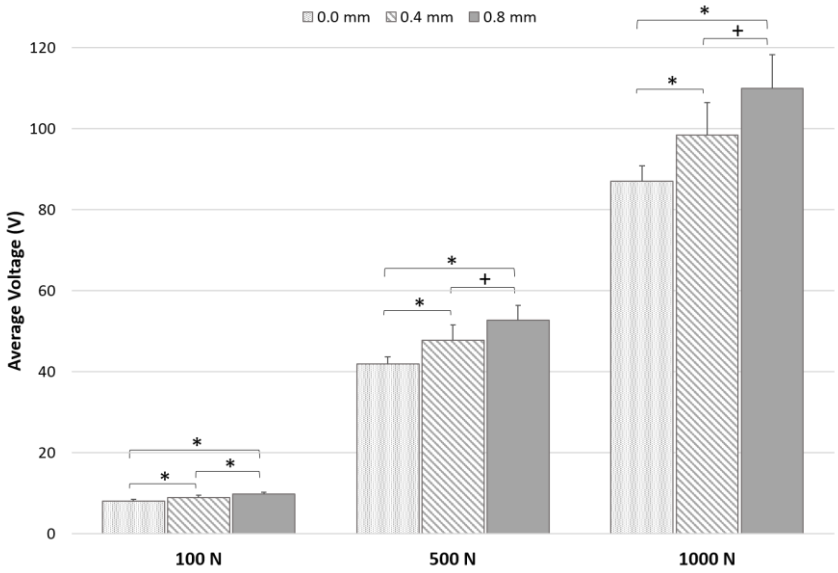


**Figure 25**. Average voltage as a function of compliant layer thickness and pure compressive load applied. Representative voltage data presented at 5Hz and 2.5MΩ. * represents significant difference ($p<.05$). + represents trend toward significant difference ($p<.1$).

The mass power density as a function of compliant layer thickness and load applied can be seen in Figure 26. This increase in mass power density as a function of applied load was found for all frequencies and resistances tested. Again, an increase in compliant layer thickness increased the mass power density. Additionally, with an increase in load applied, the effect of compliant layer on mass power density was consistent.

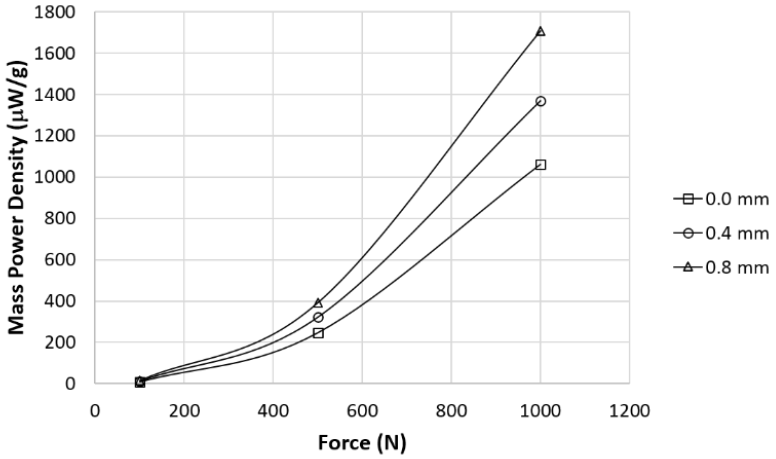


**Figure 26.** Average mass power density of each of the CLACS groups with respect to load applied (5Hz, 2.5MΩ).

Future experimental work should investigate the relationship between frequency and the compliant layer thickness and material properties. The data suggests that there may be a frequency below resonance that the effect of the compliant layer becomes negligible. Because the addition of the compliant layer increases strain generation in the piezoelectric material, there could be a risk of de-poling the PZT under high loads or frequencies. Consequently, the relationship between the stiffness of the two materials could be investigated in depth, concluding what the optimal range is to most effectively increase power generation without de-poling the piezoelectric material.

## Model Verification/Discussion

The high voltages and power output capability of the CLACS seen in the experimental results was verified in the analytical model by including the effects of the in-plane extension on voltage generation of each disc. Under a compressive load, $g_{33}$ governs the voltage output in a through-thickness poled PZT disc. However, with the expansion of the compliant layer between two discs, the traction force applied in the perpendicular direction also induces an additional voltage

generation due to $g_{31}$. Previous works have assessed the predicted power output of piezoelectric stacks under different loading conditions using several different analytical models [20–22]. The predicted power output analyzed is a function of a load or electric field applied in the direction of poling, thus only accounting for piezoelectric effect in the longitudinal direction ($g_{33}$). These models accurately predict efficiency for a typical piezoelectric stack, however would not be appropriate for predicting efficiency of CLACS because of the amplification factor due to the expansion of the compliant layer. The present model accurately predicts the significant increase in efficiency seen experimentally, and demonstrates the mechanics causing the increase in power production.

In order to validate the upper bounding predictions of the amplification factor, experimental power as a function of compliant layer thickness was compared to the predicted values. The baseline theoretical power from a piezoelectric stack without compliant layers ($P_0$) was calculated. Assuming ideal compression with no shear traction, the work done on each disc was calculated ($W$). Power as a function of the electromechanical coupling factor ($k_{33}$) and the frequency ($f$) of the load applied was found, as seen below.

$$P_0 = W * f * k_{33}^2 \qquad (2)$$

$P_0$ was calculated for 5 discs, assuming perfect bond of the discs to each other, to understand baseline power production of CLACS without a compliant layer (Eq. 2). $P$ was calculated for 0.0mm, 0.4mm, and 0.8mm CLACS, adjusting $P_0$ by the amplification factor from Eq. 1 for each compliant layer thickness. Because the 0.0mm CLACS used a single droplet of epoxy (~0.1mm) to ensure layers were mechanically in series and the poling direction was aligned with the axial load, $P$ was adjusted by an $AF$ using a nominal $t_{CL}$ of 0.1mm.

$P$ as a function of compliant layer thickness was compared to experimental results (Figure 11) at maximum power (1000N, 5Hz, 2.5MΩ). The fidelity of the amplification factor was refined by finding a contiguity factor ($c$=.57) that accounts for the variability in the manufacturing process.

$$AF = \frac{P}{P_0} \sim 1 + \left|\frac{d_{31}}{d_{33}}\right| c \sqrt{\frac{t_{CL}}{2t_{PZT}} \frac{E_{PZT}}{E_{CL}}} \quad (3)$$

The relationship between power and compliant layer thickness is the same experimentally and in the model as shown in Figure 26. However, the model over predicts power at each layer thickness. The piezoelectric material properties used in the model are defined as a function of the material resonant frequency, which is magnitudes higher than the frequencies tested experimentally, and could explain the deficit. Additionally, it is likely that the work transfer is not ideal, and energy is lost during the transfer from disc to disc and through electrodes. Although $c$ could account for some of the variability in the manufacturing process, there is still misalignment of the CLACS within the encapsulation, causing the poling direction of the PZT discs to not be parallel to the axis of the applied compressive load, decreasing effectiveness of the piezoelectric effect.

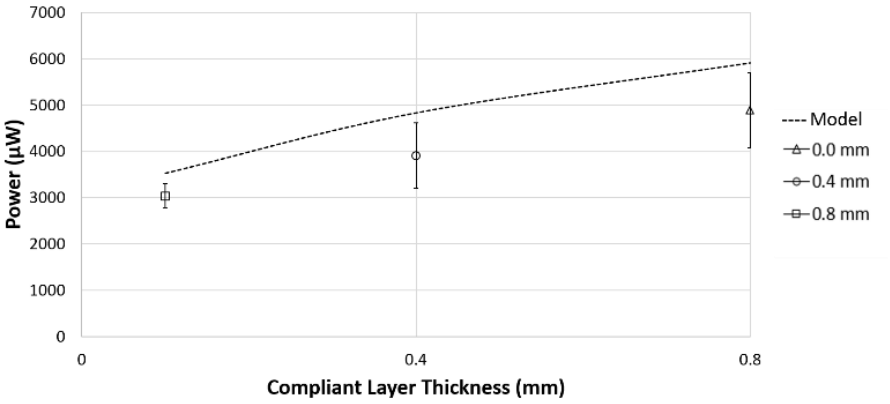


**Figure 27.** Comparison of experimental power and model predictions as an effect of compliant layer thickness. Experimental average power presented for each group at 1000N, 5Hz, 2.5MΩ. Note that the 0.0mm data was adjusted for nominal thickness of epoxy between discs.

## Conclusions

The use of a low-stiffness compliant layer in between discs of PZT ceramic has shown to significantly increase power produced by the stacks across a range of loading, off-resonant frequencies, and shunting resistances. The changes in strain patterns, proven by the theoretical model and primarily driven by the stiffness ratio, have not been previously explored analytically or experimentally, up to this point. This study suggests that, at low frequencies, the use of CLACS could increase functionality and efficiency of energy harvesting at low frequencies in many applications. The ability to tune the composite stiffness by changing the compliant material properties, type of piezoelectric material utilized, or volume fractions could benefit the energy harvesting potential in fields ranging from medical implantable devices and athletic equipment to civil infrastructure and wearables.

References


[1] Feenstra, J., Granstrom, J., and Sodano, H., 2008, "Energy Harvesting through a Backpack Employing a Mechanically Amplified Piezoelectric Stack," Mechanical Systems and Signal Processing, **22**(3), pp. 721–734.

[2] Jaffe, B., Cook jr., W. R., and Jaffe, H., 1971, "CHAPTER 12 - APPLICATIONS OF PIEZOELECTRIC CERAMICS," *Piezoelectric Ceramics*, Academic Press, pp. 271–280.

[3] Gu, L., 2011, "Low-Frequency Piezoelectric Energy Harvesting Prototype Suitable for the MEMS Implementation," Microelectronics Journal, **42**(2), pp. 277–282.

[4] Howells, C. A., 2009, "Piezoelectric Energy Harvesting," Energy Conversion and Management, **50**(7), pp. 1847–1850.

[5] Priya, S., 2007, "Advances in Energy Harvesting Using Low Profile Piezoelectric Transducers," J Electroceram, **19**(1), pp. 167–184.

[6] Colin, M., Basrour, S., Rufer, L., Bantignies, C., and Nguyen-Dinh, A., 2013, "Highly Efficient Low-Frequency Energy Harvester Using Bulk Piezoelectric Ceramics," J. Phys.: Conf. Ser., **476**(1), p. 12133.

[7] Zhang, G., Gao, S., and Liu, H., 2016, "A Utility Piezoelectric Energy Harvester with Low Frequency and High-Output Voltage: Theoretical Model, Experimental Verification and Energy Storage," AIP Advances, **6**(9), p. 95208.

[8] Starner, T., 1996, "Human-Powered Wearable Computing," IBM Systems Journal; Armonk, **35**(3,4), pp. 618–629.

[9] Shenck, N. S., and Paradiso, J. A., 2001, "Energy Scavenging with Shoe-Mounted Piezoelectrics," IEEE Micro, **21**(3), pp. 30–42.

[10] Antaki, J. F., Bertocci, G. E., Green, E. C., Nadeem, A., Rintoul, T., Kormos, R. L., and Griffith, B. P., 1995, "A Gait-Powered Autologous Battery Charging System for Artificial Organs," ASAIO Journal, **41**(3), p. M588.

[11] Mateu, L., and Moll, F., 2005, "Optimum Piezoelectric Bending Beam Structures for Energy Harvesting Using Shoe Inserts," Journal of Intelligent Material Systems and Structures, **16**(10), pp. 835–845.

[12] Kymissis, J., Kendall, C., Paradiso, J., and Gershenfeld, N., 1998, "Parasitic Power Harvesting in Shoes," *Digest of Papers. Second International Symposium on Wearable Computers (Cat. No.98EX215)*, pp. 132–139.

[13] Poulin, G., Sarraute, E., and Costa, F., 2004, "Generation of Electrical Energy for Portable Devices: Comparative Study of an Electromagnetic and a Piezoelectric System," Sensors and Actuators A: Physical, **116**(3), pp. 461–471.

[14] Niu, P., Chapman, P., Riemer, R., and Zhang, X., 2004, "Evaluation of Motions and Actuation Methods for Biomechanical Energy Harvesting," *2004 IEEE 35th Annual Power Electronics Specialists Conference (IEEE Cat. No.04CH37551)*, p. 2100–2106 Vol.3.

[15] Platt, S. R., Farritor, S., and Haider, H., 2005, "On Low-Frequency Electric Power Generation with PZT Ceramics," IEEE/ASME Transactions on Mechatronics, **10**(2), pp. 240–252.

[16] Platt, S. R., Farritor, S., Garvin, K., and Haider, H., 2005, "The Use of Piezoelectric Ceramics for Electric Power Generation within Orthopedic Implants," IEEE/ASME Transactions on Mechatronics, **10**(4), pp. 455–461.

[17] Zhao, S., and Erturk, A., 2014, “Deterministic and Band-Limited Stochastic Energy Harvesting from Uniaxial Excitation of a Multilayer Piezoelectric Stack,” Sensors and Actuators A: Physical, **214**, pp. 58–65.
[18] Xu, T.-B., Siochi, E. J., Kang, J. H., Zuo, L., Zhou, W., Tang, X., and Jiang, X., 2013, “Energy Harvesting Using a PZT Ceramic Multilayer Stack,” Smart Mater. Struct., **22**(6), p. 65015.
[19] Richards, C. D., Anderson, M. J., Bahr, D. F., and Richards, R. F., 2004, “Efficiency of Energy Conversion for Devices Containing a Piezoelectric Component,” J. Micromech. Microeng., **14**(5), p. 717.
[20] Lee, A. J., Wang, Y., and Inman, D. J., 2013, “Energy Harvesting of Piezoelectric Stack Actuator From a Shock Event,” J. Vib. Acoust, **136**(1), pp. 11016-11016–7.
[21] Goldfarb, M., and Celanovic, N., 1997, “Modeling Piezoelectric Stack Actuators for Control of Micromanipulation,” IEEE Control Systems, **17**(3), pp. 69–79.
[22] Shevtsov, S., and Chang, S.-H., 2016, “Modeling of Vibration Energy Harvesting System with Power PZT Stack Loaded on Li-Ion Battery,” International Journal of Hydrogen Energy, **41**(29), pp. 12618–12625.

## Chapter 5: Power production enhanced by varying poling direction in piezoelectric composite stacks

Manuscript prepared for submission to Advanced Functional Materials.

Submitted February 2020

*Ember Krech, Evan Haas, Grace Tideman, Bonnie Reinsch, and Elizabeth Friis**

E. Krech, Dr. E. Friis
Bioengineering Graduate Program, University of Kansas, Lawrence, KS, 66049, USA
Email: lfriis@ku.edu

E. Haas, G. Tideman, Dr. E. Friis
Department of Mechanical Engineering, University of Kansas, Lawrence, KS, 66049, USA

B. Reinsch
Department of Chemical Engineering, University of Kansas, Lawrence, KS, 66049, USA

Keywords: piezoelectric composite, energy harvesting, low frequency, power generation, poling direction

Abstract

Energy harvesting utilizing piezoelectric materials has been widely studied for powering devices without a battery. Most piezoelectric energy harvesters are unimorph or bimorph beams that operate most effectively at high frequencies near resonance (~k-MHz), limiting power generation from most environmental energy sources. This work characterizes the efficient power generation capability of a novel composite piezoceramic material under low frequency mechanical loads (~1-5Hz). Building on compliant layer adaptive composite stacks (CLACS), the power generation of mixed-mode CLACS (MMCLACS) is characterized. Utilizing poling direction to capitalize on in-plane strain generation due to compliant layer expansion, MMCLACS significantly increased power output compared to a standard piezo stack, resulting in a power density of 8700μW/cm$^3$. The combination of radial and through-thickness poled piezoelectric elements within a stack to create MMCLACS significantly increases power generation under low frequency dynamic loads. This technology can be adapted to a variety of architectures and assembled as a load-bearing energy harvester within several different fields of devices including medical implants, wearables, and civil infrastructure.

Introduction

Piezoelectric materials emit electric charge from cyclic mechanical loading and have been explored as an alternative to batteries in many different applications.[1,2] Specifically, piezoelectric ceramics have been widely explored as effective actuators and energy harvesters but are most efficient when the device matches the electrical and mechanical impedances of the loading conditions.[3-5] As a result, nearly all reported devices operate at frequencies far above many ambient mechanical energy sources as seen in human motion, civil infrastructure, vehicle motion and sway, thus limiting their efficient use in these applications. The overwhelming majority of research on piezoelectric energy harvesters centers on optimization of unimorph or bimorph cantilever beam configurations by enhancing material properties, crystalline structure, electrode patterns and base excitation analysis.[6-12] However, as the size of these elements is reduced the mechanical resonances tend to increase[13] and at low frequencies (<10Hz) the mismatch in device resonance frequency and loading frequency worsens the limited charge density and strain amplitude, making sufficient power generation challenging.[14] Beam generators also require space for oscillation and relatively long aspect ratios, making incorporation as a structural element within a device challenging, limiting their practical use within load-bearing applications.

In contrast, cofired piezoelectric stacks are most often utilized as actuators in load-bearing applications, [15,16] but little work has been done to increase efficiency of low frequency power generation from a stack. Cofired stacked generators lower source impedance compared to monolithic elements, improving energy harvesting at lower resistances and improving compatibility with post-processing circuitry.[3,17] However, these piezoceramic stacked generators are stiff, brittle, difficult to fabricate, and prone to failure under repetitive loads

experienced by power generation devices. If power production of piezoelectric stacks could be increased, their adaptability makes them an attractive option to harvest mechanical energy and subsequently utilize the generated electrical power to recharge batteries, power tangential assessment sensors, or provide *in vivo* electrical stimulation. In a model for efficiency based on piezoelectric material properties, Richards *et al.* suggests that the largest increase in efficiency of a piezoelectric device will stem from a decrease in structural stiffness. [18]

Recently, a composite piezoelectric material, compliant layer adaptive composite stacks (CLACS) was proposed as a load-bearing structural material to provide *in vivo* electrical stimulation.[19] CLACS was originally designed to be a structural load-bearing element within an implant but was found to exhibit a significant increase in power production compared to stacks without compliant layers. Here we propose use of a new structural material which we call mixed-mode CLACS (MMCLACS). In this work, we demonstrate that poling direction of piezoelectric elements can be exploited to achieve enhanced power production from a composite piezoelectric stack. This solution enables effective energy harvesting from multiple loading directions, while maintaining necessary strength to be utilized as a structural material to generate practical electrical power from low frequency mechanical loads.

Piezoelectric Composite Stack Power Generation

Compared to beams, stacks of similar piezoelectric volume have increased conversion efficiency, increasing power generation at off-resonance frequencies, and have been characterized at frequencies ~10Hz.[5,20,21] However, the stiff mechanical properties of these '33' stacks make incorporation into energy harvesting structures difficult.[21] For a given volume of lead zirconate titanate (PZT), CLACS produced over 60% more power as compared to a cofired '33' stack analog, under a range of frequencies and compressive loads.[19,22] The piezoelectric

voltage constant, $g_{33}$, governs the voltage output in a through-thickness ('33') poled piezoelectric disc in compression. Including an interdigitated compliant layer (i.e., CLACS) increases lateral strain, invoking an additional voltage from the off-axis piezoelectric constant, $g_{31}$, subsequently increasing overall power production.[23] Finite element modeling of CLACS showed that the compliant layer expansion increased the PZT radial strain more than the through-thickness strain.[24]

The purpose of this study was to elucidate the effect of PZT poling direction on power production of MMCLACS under multiaxial low frequency loads. Power generation of piezoelectric composite stacks with mixed poling directions under compressive and torsional loads has not previously been investigated. The compliant layer expansion within CLACS changes the micromechanical loading across the face of the PZT discs but the effect of poling direction is not understood. The piezoelectric elements in traditional stacked generators are poled axially through-thickness, parallel to the direction of compressive loads applied (Fig. 28a). To the best of our knowledge, little work has been done to investigate use of radially poled stacks to harvest energy from multiaxial loading. Combining radial and through-thickness piezoelectric elements within a stack is a novel configuration that we expected to provide interesting power producing capability in torsion and compression.

Because traditional cofired stacks cannot vary poling direction of individual piezoelectric elements, CLACS fabrication methods were used in this study.[19] Commercially available, pre-poled PZT discs were used to manufacture three MMCLACS groups as in **Figure 28** (see Experimental Section). According to the manufacturer, radially poled discs were poled on the radial direction with electrodes on the top and bottom faces (R discs). Through-thickness poled discs were poled axially with electrodes on the top and bottom faces (T discs). R-CLACS (Figure

28b), RT-CLACS (Figure 28c), and T-CLACS (Figure 28d) were fabricated and encapsulated in epoxy cylinders. The volume of PZT remained constant in all specimens. Power produced from each MMCLACS configuration was characterized over a range of dynamic compressive and torsional load amplitudes, low frequencies and electrical load resistances (see Experimental Section, Figures 33-36).

Results

*Compressive Load Characterization*

Average power generated as a function of poling direction and load and frequency is presented in **Figure 29**. As expected, increased compressive load amplitudes and frequencies increased power output for all groups ($p<.05$). Within each group the relationship between power produced and load was consistent and independent of frequency: a 112-fold increase from 100-1000N, a 4-fold increase from 500-1000N, and a 27-fold increase from 500-1000N. Within each group the increased power due to increased frequency was consistent across all loads: 2-fold increase from 1-2Hz, 3-fold increase from 1-3Hz, and 5-fold increase from 1-5Hz. Conventional piezoelectric stacks are composed of through-thickness poled elements like T-CLACS. Although unconventional, R-CLACS and RT-CLACS power generation behavior as a function of load and frequency followed the same percent increases as T-CLACS; percent increases were consistent across all MMCLACS.

At all loads and frequencies tested, RT-CLACS produced significantly more power than T-CLACS ($p<.05$). Across most loads and frequencies, RT-CLACS produced significantly more power than R-CLACS, and R-CLACS produced significantly more power than T-CLACS ($p<.05$). At the maximum load and frequency (1000N, 5Hz, 0.97MΩ) RT-CLACS produced 818μW, 27% more power than T-CLACS (646μW). RT-CLACS produced 12% more than R-

CLACS (730μW). R-CLACS produced 13% more than T-CLACS. These statistical trends and percent increases in power produced were consistent for all loads, frequencies and resistances tested, demonstrating consistent increase in power due to RT-CLACS and R-CLACS, as compared to T-CLACS.

**Figure 30**a-c shows power and voltage produced as a function of resistance and poling direction for each load tested at 2Hz. This is a typical walking frequency and demonstrates functionality of MMCLACS at low frequencies, far below resonance of the PZT. RMS voltage is plotted with the calculated power across the sweep of resistances on a semi-log scale for clarity. Poling direction did not affect source impedance, nor resistance at which maximum power occurred. At 2Hz, the source impedance for all groups was 2.5MΩ. RT-CLACS produced more power than both other groups across all resistances tested, and R-CLACS produced more than T-CLACS. The influence of frequency on source impedance is shown in Figure 30d-f. Although alternating poling direction significantly increased power generation, it was not due to a change in impedance; all three groups exhibited the same experimental source impedances across all frequencies. As frequency increased, power increased and impedance decreased, as shown by maximum power occurring at lower resistances. The optimal resistances for all groups were as follows: 5MΩ at 1Hz, 2.5MΩ at 2Hz, 1.5MΩ at 3Hz, 0.97MΩ at 5Hz. The significant increase in power output of RT-CLACS validates use as an efficient energy harvester at all resistances and frequencies far below PZT resonance.

**Figure 31** presents average voltage as a function of frequency and load for each group at several different resistances. At 10MΩ, RT-CLACS produced on average 3V more than R-CLACS and T-CLACS, which produced approximately the same voltage. At 1MΩ, voltage increased by approximately 1-1.5V from T-CLACS to R-CLACS to RT-CLACS across all four

frequencies. At low resistances the differences were less between the three groups, suggesting that RT-CLACS most effectively increase voltage at higher resistances.

Power density as a function of poling direction and load applied demonstrate the efficiency of RT-CLACS (**Figure 32**a). The increase in power density was consistent for all loads, frequencies, and resistances tested. Figure 32b shows power density as a function of frequency. Results are presented at the resistance of maximum power for each frequency. At 1000N, 2Hz a reasonable load and frequency for human motion, RT-CLACS produced 3.5μW/mm$^3$, R-CLACS produced 3.1 μW/mm$^3$, and T-CLACS produced 2.7 μW/mm$^3$. Even at frequencies below resonance, all MMCLACS groups produced practical power densities under reasonable compressive loads, generating usable power across multiple frequencies and resistances.

Stacks without compliant layers (R0, RT0, T0 in Figure 32) were made to validate the CLACS effect paired with the effect of poling direction (see Experimental Section). CLACS substantially increased power density, as found previously: T-CLACS power density is approximately double T0 power density. Power increase due to compliant layer interdigitation in T-CLACS is consistent with previous work on CLACS.[19,22,23] RT-CLACS increased power density by 100%, and R-CLACS increased power density by approximately 60%, as compared to RT0 and R0 stacks respectively. Comparing the effect of poling direction within a stack without compliant layers, it should be noted that R0 stacks generated slightly higher power densities than RT0 stacks, and both R0 and RT0 stacks generated more power than T0 stacks. These results suggest that radially poled piezoelectric elements within a cofired stack could be an effective way to increase efficiency.

We note that the MMCLACS configurations presented are conceptual constructions that are not yet optimized to achieve maximum overall combined power generation from addition of compliant layers and mixed poling directions. While these opportunities for further optimization of device geometry and properties are worth highlighting and are currently the subject of additional investigation, we focus here on further experimental demonstration of power generation capabilities of these three MMCLACS groups.

*Torsional Load Characterization*

MMCLACS were designed to be a versatile energy harvesting structural material for use in applications experiencing multiaxial loading. To further characterize MMCLACS, power generated from low frequency torsional loads was also evaluated (Table 3 and Figures 36-38). These results provide a basis for analyzing viability of MMCLACS power generation from off-axis loading.

At all torques and frequencies, R-CLACS and T-CLACS produced more power than RT-CLACS ($p<.05$), producing $1.14 \pm 0.55\mu W$ and $1.35 \pm 0.54\mu W$ respectively at maximum power (8N-m, 3Hz, 1.6MΩ). RT-CLACS produced approximately 70% less ($0.36 \pm 0.29\mu W$) at the same torque and frequency. Maximum power occurred at the same resistance for all MMCLACS groups and increasing frequency decreased source impedance as expected: 12MΩ at 0.5Hz, 5.6MΩ at 1Hz, 2.6MΩ at 2Hz, and 2.1MΩ at 3Hz.

Power output increased with increasing torque and frequency consistently for all groups; 4.3-fold increase from 2-4N-m and 4-8N-m, and 19-fold increase from 2-8N-m. Similar to behavior under compression, as frequency increased power production increased uniformly independent of load and resistance: from 0.5-1Hz and 1-2Hz the power doubled, from 2-3Hz there was a 1.5-fold increase, and from 1-3Hz there was a 3-fold increase.

R0, RT0, and T0 stacks were also tested in torsion. R0 and RT0 stacks produced approximately 4 times more power than R-CLACS and RT-CLACS. In contrast, T0 and T-CLACS produced approximately the same amount of power. R0, RT0, and T0 stacks followed the same impedance trends as the R-CLACS, RT-CLACS and T-CLACS. These findings suggest that a radially poled PZT cofired stack would be most efficient for power generation under pure torsional loads.

To the best of our knowledge power generation capability of piezocomposite stacks from torsion has not been previously investigated. Power generated from MMCLACS at tested torques was a fraction of that generated from compression and may not be enough power for some applications. However, when smaller amounts of power are necessary (i.e. micro/nano generators) utilizing MMCLACS may be a viable option to harvest energy from torsional loads and generate power in the nanowatt range.

## Discussion and Conclusion

### *Technological Perspective and Outlook*

Translation of MMCLACS would address two technical issues in practical applications of piezoceramic stack energy harvesting – poor low frequency power generation efficiency and low fatigue performance. The PZT discs used here in T-CLACS were soft PZT, while the PZT discs used in the initial CLACS study were hard PZT.[19] The increase in power output due to compliant layers that were twice PZT disc thickness was consistent across both studies: approximately 60% increase in CLACS and approximately 100% increase in the T-CLACS in this study. This suggests that the effect of interdigitated compliant layers within a soft PZT stack further enhances power generation. Soft PZT has also been shown to be more efficient at off-resonance, lower frequencies in other energy harvesting applications.[11] The unique MMCLACS

fabrication technique allows pre-poled PZT discs to be combined into one uniform mechanical structure, coupling the effect of poling direction and CLACS. R-CLACS increased power production by 125% as compared to T0 stacks, an additional 25% due to radially poled discs. Alternating R and T discs to create RT-CLACS, increased power output by a total of 250%, as compared to T0 stacks (cofired stack analog). This compelling result presents opportunities for all MMCLACS to be utilized as a structural energy harvesting material to generate usable power from common low frequency cyclic motion.

This characterization of MMCLACS exemplifies the versatility of CLACS technology to generate power more efficiently at low frequencies seen in implantable medical devices, wearables, civil infrastructure and a variety of self-powered devices. Reported peak power densities for piezoelectric materials range from 50μW/cm$^3$ to 2700μW/cm$^3$ from a variety of loading conditions.[8,13,25,26] Several of these devices are beams, requiring high frequency excitation vibrations (>100Hz) and space for maximum beam deflection. It is difficult to make direct comparisons with other devices due to vast differences in material, loads applied and device structure. However, it is notable that at 1000N and the exceptionally low, off-resonance frequency of 5Hz, RT-CLACS, R-CLACS, and T-CLACS in this study produced 8700μW/cm$^3$, 7800μW/cm$^3$, and 6900μW/cm$^3$ respectively.

Most piezoelectric energy harvesting applications require circuits for signal conditioning and/or rectification. Several rectification components require higher voltage outputs than most piezoelectric generators produce under low frequency loads.[27] The threshold voltage requirements and expected loss during rectification limit circuit design. MMCLACS produce significantly higher voltages at lower frequencies and resistances than standard piezoelectric energy harvesters, thus overcoming these rectification issues, increasing circuit design options

and potential for miniaturization for use in microelectromechanical systems. In addition, the composite material provides toughness where brittle, cofired stacks would not be appropriate. This allows MMCLACS to be incorporated as a load-bearing material within existing structures, broadening potential use in devices that require fatigue-resistant energy harvesting (i.e. sidewalks, roadways, medical implants, shoes, etc.).

MMCLACS capitalize on expansion of the compliant layer and induce charge generation from several piezoelectric properties not possible in a traditional stack,[23] subsequently harvesting energy from multi-axial loads, not just pure compression. Although not yet completely understood, some piezoelectric models predict a coupling between radial and longitudinal partial systems at certain aspect ratios, and infer that an angled poling direction could activate an electric field from three different modes simultaneously ($d_{31}$, $d_{33}$, $d_{15}$) .[28,29] Looking at RT-CLACS as a uniform structure, the 'composite poling direction' would be at an angle, invoking voltage generation from all three modes, and could explain the increase in power generation.

In this work, we strategically explored the impact of poling direction on power generation. Although this work was focused on initial characterization, further work should explore ability of MMCLACS to produce power from cyclic tensile loads, something that is not possible for traditional piezoceramic energy harvesting devices. Further work characterizing and defining relationships of PZT disc/compliant layer aspect ratio and stiffness could generate an ideal composition for desired applications. It is likely that a specific compliant layer material and thickness would optimize power generation of MMCLACS and should be further explored. The RT-CLACS structure in this work represents one possible configuration of alternating poling directions, but several other approaches can be imagined, capitalizing on disc position within the

stack and incorporating overall device structure into design decisions. An elaborate finite element analysis of both conventional CLACS and MMCLACS is of great interest, is under way, and left for further investigation.

*Conclusion*

A new class of energy harvesters, MMCLACS, has been proposed and initially investigated. This structural material shows the impact of poling direction on power generation in a piezoelectric composite stack. The functional performance of these devices under compressive and torsional low frequency loads was validated. RT-CLACS generate more power than both R-CLACS and T-CLACS under compressive loads with power densities of 3500μW/cm$^3$, 3100μW/cm$^3$, 2700μW/cm$^3$ respectively, at a common walking load of 1000N, 2Hz.[30] Torsional loads produced limited power, but design would need to be optimized for use in most applications. Because of the higher power densities generated from RT-CLACS under moderate compressive loads, the wide and varied use of this technology could greatly increase efficiency of power generation from human motion, roadways, wearables, wind energy, etc. The ability to overcome efficiency losses due to frequency mismatches provides a promising route for further exploration and a practical material for energy harvesting implementation utilizing existing devices and technology.

Experimental Section

*Material Considerations*

Three configurations of MMCLACS, R-CLACS, RT-CLACS, and T-CLACS, were used to investigate the effect of poling direction on power generation. All MMCLACS groups utilized commercially available PZT discs made with the same type of PZT, a PZT-5A Navy Type II (SM412, STEMiNC, Doral, FL). Discs were chosen to keep PZT type, size, and electrode

type/size constant to isolate the effect of poling direction. This material was chosen based on the high electromechanical coupling coefficient ($k_t$ = 0.42) and the reasonable stiffness ($Y_{33}$ = 56GPa) for high load, low frequency applications. All discs were electroded and poled at the manufacturer. The electrodes were fired on silver and were applied to the top and bottom faces of the discs. The poling was completed under controlled conditions. According to STEMiNC, the radially poled discs (SMD10T02F412S) were poled on the radial direction, and the through-thickness discs (SMD10T02F412T) were poled axially. To create the composite CLACS material, the epoxy used as the matrix material was a room-temperature cure, two-part epoxy (EPO-TEK 301, Epoxy Technology, Billerica, MA). This material was chosen for its mechanical strength properties and desirable dielectric properties to decrease loss within the piezocomposite.

*MMCLACS Fabrication*

All MMCLACS were fabricated using the methods from the Krech *et al.* CLACS study.[19] Each type of MMCLACS (n=5 in each group) were composed of six PZT discs that were 10x0.2mm. The R-CLACS were made with six radially poled discs, and T-CLACS were made with six through-thickness poled discs. The RT-CLACS were made with three radially poled discs and three through-thickness poled discs, alternating R and T. For all groups, all six discs were connected electrically in parallel in chains using conductive epoxy (EPO-TEK H20E, Epoxy Technology, Billerica, MA) and thin strips of copper foil connecting all the positive electrodes together and connecting all negative electrodes together. The positive poling direction of each disc was verified before connection using the pyrolytic effect. The chains of discs were then folded in an accordion manner and stacked mechanically in series (see Fig. 28b-d). This folding technique creates a stack with alternating positive poling directions and separation of negative and positive electrodes to prevent shorting.

The compliant layers were manufactured using 0.4mm thick slices of a cured 11x11mm column of EPO-TEK 301. The slices were made using an IsoMet Low Speed Cutter. The thickness was chosen to be twice the thickness of the PZT discs based on the results from Krech *et al.*[19]. The compliant layers were adhered between the PZT discs with a small amount of goopy EPO-TEK 301 to create CLACS, ensuring the compliant layers were the same thickness and stacks were uniform. The stacks were then encapsulated in EPO-TEK 11x45mm cylinders (see Figure 33), ensuring the MMCLACS stacks were centered and aligned along the center axis of the cylinder. Molds were made of silicone using a custom negative. The cylindrical shape with tabs was designed to interface with the hydraulic grips used in testing, while maintaining an even stress distribution across the MMCLACS in compression and torsion.

For the cofired stack analog comparison, stacks without compliant layers (R0, RT0, and T0) were manufactured (n=2 in each group). Six discs were connected as explained above. A minimal amount of EPO-TEK 301 epoxy was used to adhere the discs together to create a uniform stack and ensure proper alignment once encapsulated.

The volume of PZT ($94mm^3$), volume of epoxy, overall height and surface area was kept constant throughout all specimens. The electrical connection, impedance and capacitance was verified before each specimen was tested.

*Experimental Electromechanical Testing*

For all electromechanical testing, a biaxial MTS MiniBionix 858 with 647 Hydraulic Wedge Grips was used to ensure consistency in testing across different loading conditions (MTS, Eden Prairie, MN). Tests were conducted in load-control utilizing a 25KN, 250N-m load cell. The gripping pressure used for all tests was 5MPa, and was calculated based on specimen size and material from manufacturer recommendations. The MMCLACS voltage output was

measured across a load resistance (utilizing an RC-box and resistors) and collected during each dynamic loading condition. The voltage, load and displacement data were all recorded utilizing the MTS DAQ system at a continuous sampling rate of 512Hz. Conservative estimates for loads seen in multiple low frequency energy harvesting applications were considered to develop loading conditions and characterize MMCLACS behavior across a range of inputs.

*Compression Testing*

A 1200N preload was applied to ensure the specimen remained in compression throughout all loads tested. Cyclic compression at 100N, 500N, and 1000N load amplitudes were applied at four low frequencies of 1Hz, 2Hz, 3Hz and 5Hz (see Figure 34). For each load and frequency, the voltage output was measured across a shunting resistance sweep of 20kΩ-20MΩ. Resistance values were chosen to characterize the behavior of MMCLACS at a range of resistances necessary for circuit design and to capture the resonance behavior at the matched impedance of the specimen. Voltage data for each load, frequency and resistance was collected for 15 cycles to capture steady-state behavior. A custom MATLAB (Mathworks, Natick, MA) code was used to filter the voltage data, remove the beginning and end cycles, and calculate the average maxima. The average voltage amplitude of the middle five cycles was converted to RMS ($V_{RMS} = V_{amp}/\sqrt{2}$) and used for power calculations ($P = V_{RMS}^2/R$). Power for each loading condition was calculated (see Figure 34). Power output of each MMCLACS type as a function of poling direction was compared using a one-sided Wilcoxon Rank Sum test ($\alpha$=.05).

*Torsion Testing*

To test the power production capability of each MMCLACS type in torsion, R-CLACS, RT-CLACS and T-CLACS were also electromechanically tested under pure torsional loads. A constant 200N compressive preload was applied first to ensure the axial load on the MMCLACS

remained constant throughout the remainder of the torsion loading cycles. Three torques, 2N-m, 4N-m, and 8N-m, were applied at four frequencies 0.5Hz, 1Hz, 2Hz, and 3Hz (see Figure 36). Voltage output was measured across a shunt resistance sweep of 20kΩ-20MΩ, and power output was calculated as a function of applied torque, frequency and applied resistance. The same MATLAB code and calculations from the compression testing were used. Maximum power output of each MMCLACS type as a function of poling direction was compared using a one-sided Wilcoxon Rank Sum test ($\alpha$=.05). The standard deviations in this test were high, so further statistical analysis and claims were not made.

References


[1] Priya, S. *et al.* A Review on Piezoelectric Energy Harvesting: Materials, Methods, and Circuits. *Energy Harvest. Syst.* 4, 3–39 (2017).

[2] Anton, S. R. & Sodano, H. A. A review of power harvesting using piezoelectric materials (2003–2006). *Smart Mater. Struct.* 16, R1 (2007).

[3] Platt, S. R., Farritor, S. & Haider, H. On low-frequency electric power generation with PZT ceramics. *IEEEASME Trans. Mechatron.* 10, 240–252 (2005).

[4] Li, H., Tian, C. & Deng, Z. D. Energy harvesting from low frequency applications using piezoelectric materials. *Appl. Phys. Rev.* 1, 041301 (2014).

[5] Zhao, S. & Erturk, A. Deterministic and band-limited stochastic energy harvesting from uniaxial excitation of a multilayer piezoelectric stack. *Sens. Actuators Phys.* 214, 58–65 (2014).

[6] Elka, E., Elata, D. & Abramovich, H. The electromechanical response of multilayered piezoelectric structures. *J. Microelectromechanical Syst.* 13, 332–341 (2004).

[7] Lee, S.-W. R. & Li, H. L. Development and characterization of a rotary motor driven by anisotropic piezoelectric composite laminate. *Smart Mater. Struct.* 7, 327–336 (1998).

[8] Roundy, S. *et al.* Improving power output for vibration-based energy scavengers. *IEEE Pervasive Comput.* 4, 28–36 (2005).

[9] Sodano, H. A., Lloyd, J. & Inman, D. J. An experimental comparison between several active composite actuators for power generation. *Smart Mater. Struct.* 15, 1211–1216 (2006).

[10] Priya, S. Advances in energy harvesting using low profile piezoelectric transducers. *J. Electroceramics* 19, 167–184 (2007).

[11] Shahab, S., Zhao, S. & Erturk, A. Soft and Hard Piezoelectric Ceramics and Single Crystals for Random Vibration Energy Harvesting. *Energy Technol.* 6, 935–942 (2018).

[12] Caliò, R. *et al.* Piezoelectric Energy Harvesting Solutions. *Sensors* 14, 4755–4790 (2014).

[13] El-hami, M. *et al.* Design and fabrication of a new vibration-based electromechanical power generator. *Sens. Actuators Phys.* 92, 335–342 (2001).

[14] Jaffe, B., Cook jr., W. R. & Jaffe, H. CHAPTER 12 - APPLICATIONS OF PIEZOELECTRIC CERAMICS. in *Piezoelectric Ceramics* 271–280 (Academic Press, 1971). doi:10.1016/B978-0-12-379550-2.50016-8.

[15] Mitrovic, M., P. Carman, G. & K. Straub, F. Response of piezoelectric stack actuators under combined electro-mechanical loading. *Int. J. Solids Struct.* 38, 4357–4374 (2001).

[16] Pritchard, J., Bowen, C. & Lowrie, F. Multilayer Actuators: Review. *Br. Ceram. Trans.* 100, 265–273 (2001).

]17] Platt, S. R., Farritor, S., Garvin, K. & Haider, H. The use of piezoelectric ceramics for electric power generation within orthopedic implants. *IEEEASME Trans. Mechatron.* 10, 455–461 (2005).

[18] Richards, C. D., Anderson, M. J., Bahr, D. F. & Richards, R. F. Efficiency of energy conversion for devices containing a piezoelectric component. *J. Micromechanics Microengineering* 14, 717 (2004).

[19] Krech, E. D., Cadel, E. S., Barrett, R. M. & Friis, E. A. Effect of compliant layers within piezoelectric composites on power generation providing electrical stimulation in low frequency applications. *J. Mech. Behav. Biomed. Mater.* (2018) doi:10.1016/j.jmbbm.2018.08.027.

[20] Xu, T.-B. *et al.* Energy harvesting using a PZT ceramic multilayer stack. *Smart Mater. Struct.* 22, 065015 (2013).
[21] Feenstra, J., Granstrom, J. & Sodano, H. Energy harvesting through a backpack employing a mechanically amplified piezoelectric stack. *Mech. Syst. Signal Process.* 22, 721–734 (2008).
[22] Cadel, E. S., Krech, E. D., Arnold, P. M. & Friis, E. A. Stacked PZT Discs Generate Necessary Power for Bone Healing through Electrical Stimulation in a Composite Spinal Fusion Implant. *Bioengineering* 5, 90 (2018).
[23] Krech, E. D., Barrett, R. M., Cadel, E. S. & Friis, E. A. Power Generation Amplification and Stack Toughening via Compliant Layer Interdigitation. V002T07A010 (2018) doi:10.1115/SMASIS2018-8043.
[24] Cadel, E. S., Frazer, L. L., Krech, E. D., Fischer, K. J. & Friis, E. A. Analysis of how compliant layers and encapsulation affect power generated from piezoelectric stacked composites for bone healing medical devices. *J. Biomed. Mater. Res. A* 107, 2610–2618 (2019).
[25] Ali, S. F., Friswell, M. I. & Adhikari, S. Analysis of energy harvesters for highway bridges. *J. Intell. Mater. Syst. Struct.* 22, 1929–1938 (2011).
[26] Shen, D. *et al.* Micromachined PZT cantilever based on SOI structure for low frequency vibration energy harvesting. *Sens. Actuators Phys.* 154, 103–108 (2009).
[27] Kim, S.-B. *et al.* Comparison of MEMS PZT Cantilevers Based on $_{31}$ and $_{33}$ Modes for Vibration Energy Harvesting. *J. Microelectromechanical Syst.* 22, 26–33 (2013).
[28] Kiran, R., Kumar, A., Kumar, R. & Vaish, R. Poling direction driven large enhancement in piezoelectric performance. *Scr. Mater.* 151, 76–81 (2018).
[29] Xu, J., Lin, S., Ma, Y. & Tang, Y. Analysis on Coupled Vibration of a Radially Polarized Piezoelectric Cylindrical Transducer. *Sensors* 17, 2850 (2017).
[30] Ignasiak, D., Rüeger, A., Sperr, R. & Ferguson, S. J. Thoracolumbar spine loading associated with kinematics of the young and the elderly during activities of daily living. *J. Biomech.* 70, 175–184 (2018).

Figures

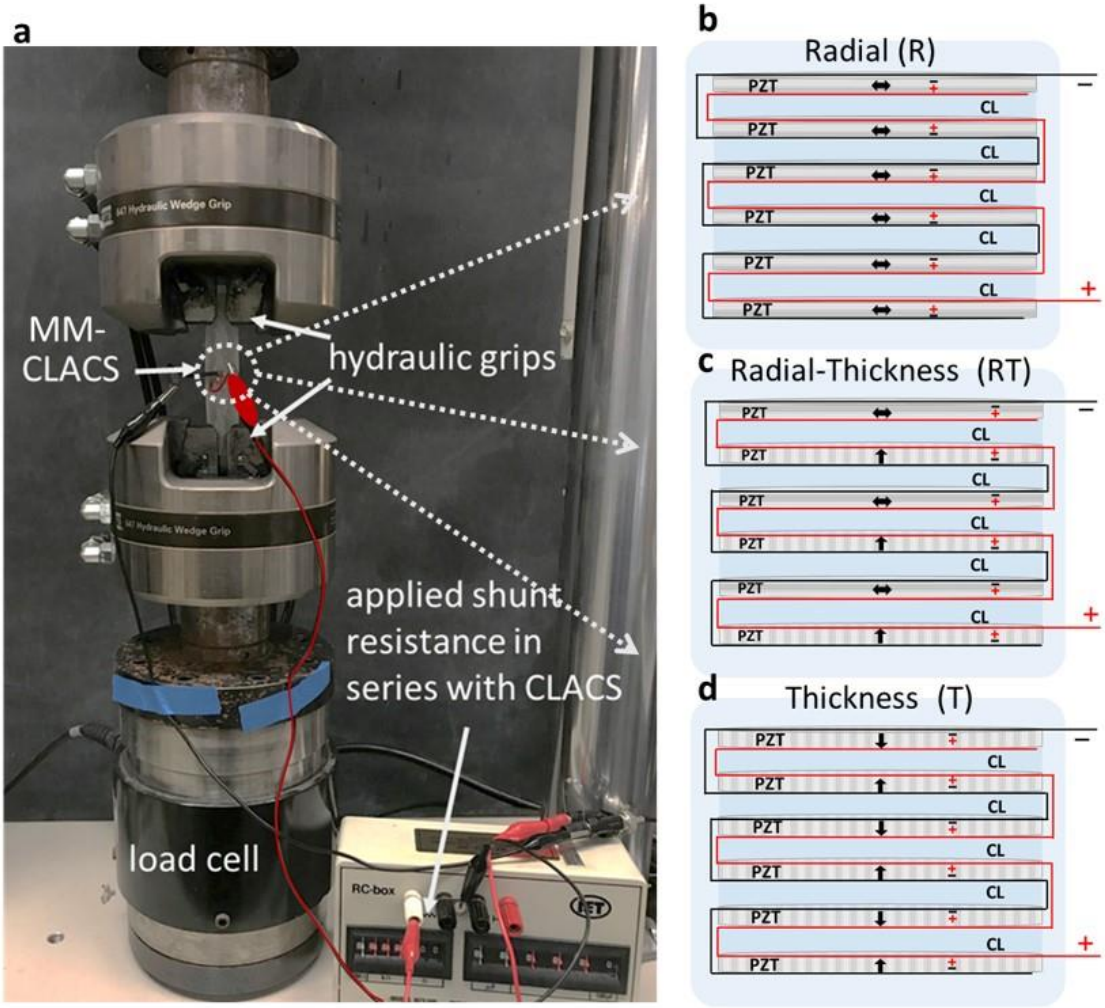


**Figure 28.** Experimental electromechanical setup and MMCLACS configurations**. a.** MMCLACS were electromechanically tested to compare voltage and power produced at varying low frequency, sinusoidal compressive and torsion load using a biaxial MTS MiniBionix 858 with hydraulic grips. Load was applied and voltage output was measured across a shunt resistance sweep in series with MMCLACS. **b.** Schematic showing R-CLACS layup. **c.** Schematic showing RT-CLACS layup. **d.** Schematic showing T-CLACS layup. In **b-d.** arrows represent poling direction and positive/negative electrodes are labeled on each PZT disc. CL represents the compliant layers interdigitated between each PZT disc.

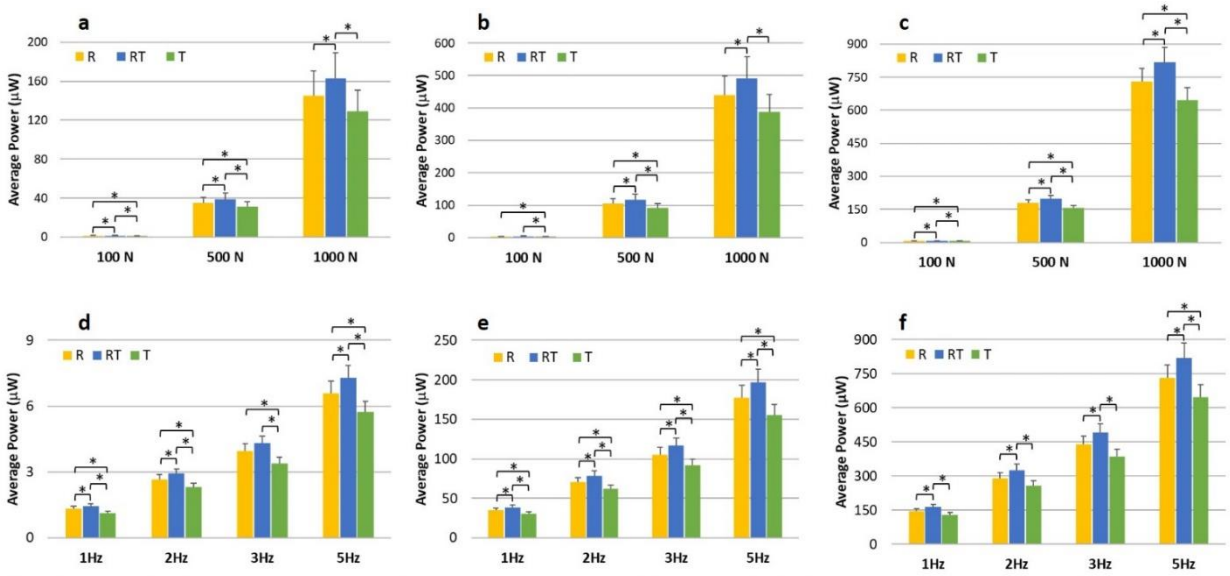


**Figure 29.** Average power as a function of poling direction. Power data presented at the optimal resistance for each load, frequency. **a.** 1Hz and 5MΩ. **b.** 3Hz and 1.5MΩ. **c.** 5Hz and 0.97MΩ. For **d-f**, power data is presented at the resistance corresponding to maximum power for each frequency 5MΩ at 1Hz, 2.5MΩ at 2Hz, 1.5MΩ at 3Hz, 0.97MΩ at 5Hz **d.** 100N. **e.** 500N. **f.** 1000N. Error bars represent one standard deviation. Power generated was compared as a function of poling direction using a one-sided Wilcoxon Rank Sum test (α=.05). *represents a significant difference (p<.05).

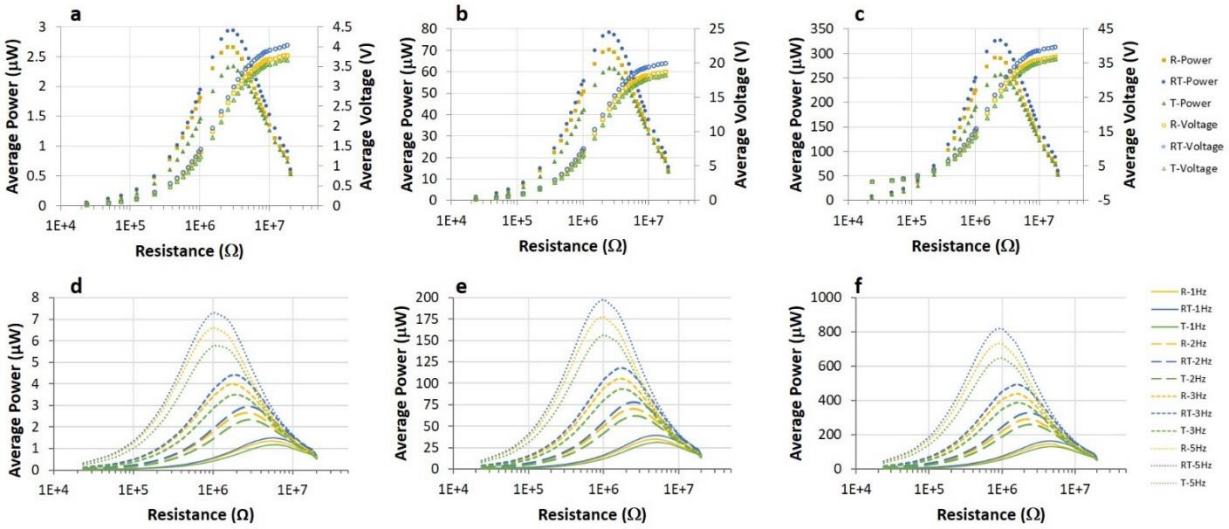


**Figure 30.** Average power generation curves. Average power and voltage output for each MMCLACS group as a function of poling direction and resistance applied. Note the resistance is plotted on a log scale for clarity. **a-c.** The voltage presented is the VRMS equivalent calculated from the average amplitude of the AC voltage signal collected at each load, frequency and resistance. **a.** Power and voltage at 100N, 2Hz. **b.** Power and voltage at 500N, 2Hz. **c.** Power and voltage at 1000N, 2Hz. **d-f.** Average power generation curves as a function of resistance for each MMCLACS group presented at each frequency tested. This demonstrates the effect of frequency on power generated and resistance of maximum power generation, or optimal resistance. **d.** 100N **e.** 500N **f.** 1000N. Error bars left off for clarity.

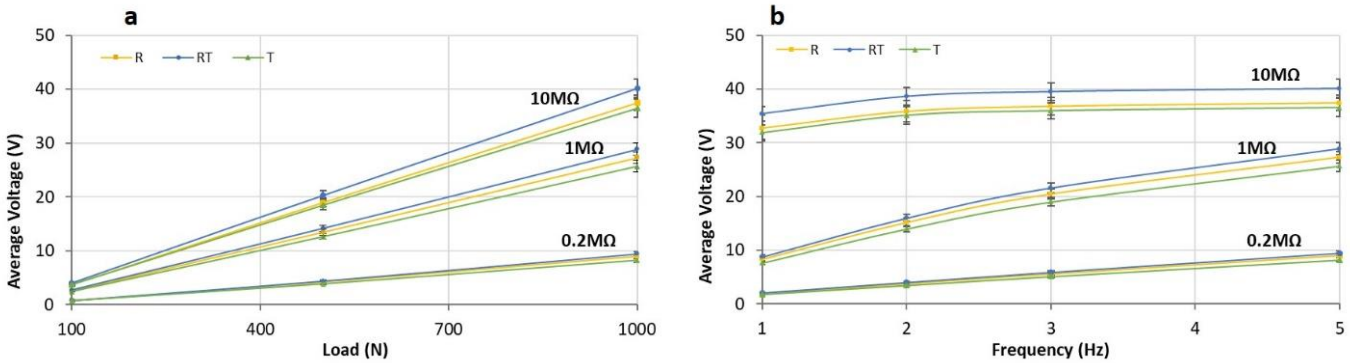


**Figure 31**. Average voltage as a function of frequency and poling direction. **a.** Average voltage generated from each MMCLACS group as a function of load applied. Voltage is the $V_{RMS}$ equivalent calculated from the average amplitude of the AC voltage signal collected at each load, frequency and resistance. Error bars represent one standard deviation. **b.** Average voltage generated from each MMCLACS group as a function of frequency applied. Voltage is the $V_{RMS}$ equivalent calculated from the average amplitude of the AC voltage signal collected at each load, frequency and resistance. Error bars represent one standard deviation.

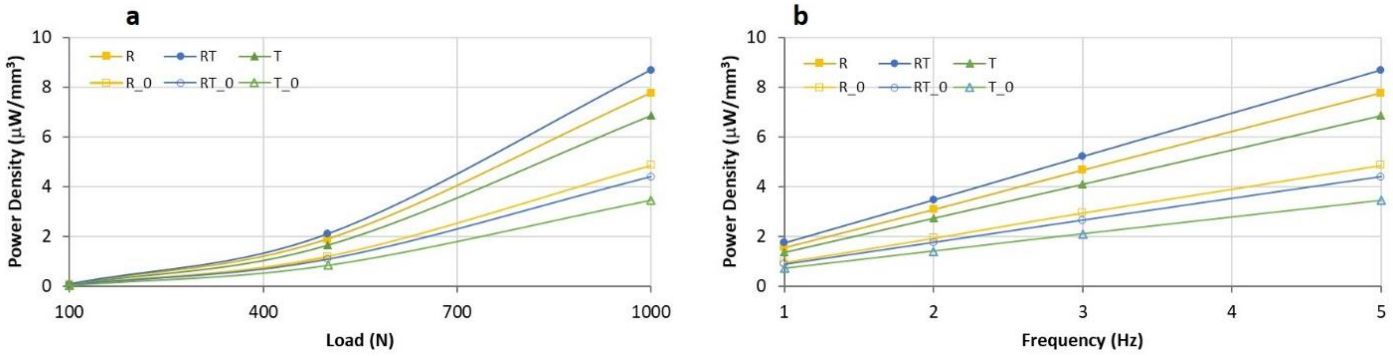


**Figure 32**. Power density as a function of poling direction, load and frequency**. a.** Average power density for each MMCLACS group as a function of load applied. Data presented for 5Hz frequency and resistance of maximum power, 0.97MΩ. The volume of PZT was constant across all groups ($94mm^3$) and was used to calculate power density. The R_0, RT_0, and T_0 data were collected from R, RT, and T stacks without compliant layers (see Experimental Section). **b.** Average power density for each MMCLACS group as a function of frequency applied. Power data is presented at 1000N and the the resistance of maximum power for each frequency: 5MΩ at 1Hz, 2.5MΩ at 2Hz, 1.5MΩ at 3Hz, 0.97MΩ at 5Hz. The volume of PZT was used to calculate power density. The R_0, RT_0, and T_0 data were collected from R, RT, and T stacks without compliant layers (see Experimental Section). Error bars left off for clarity.

Supplementary Information

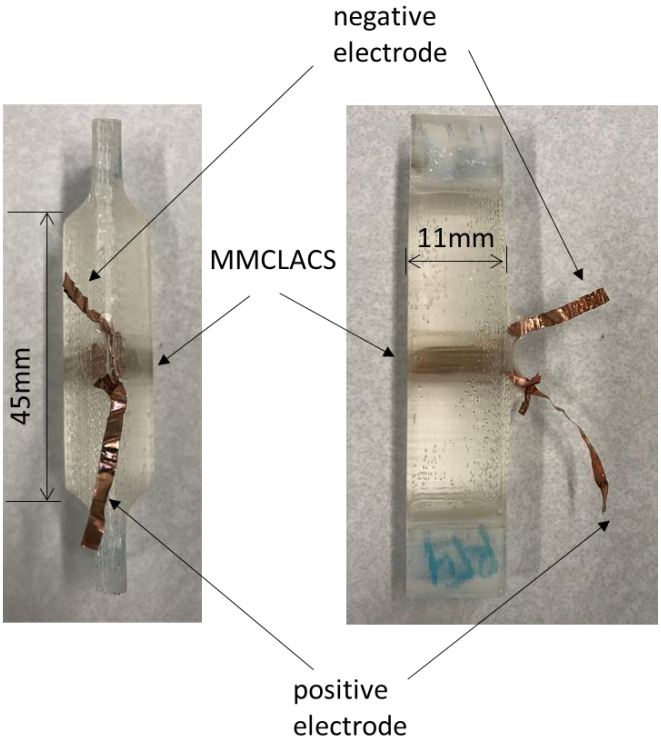


**Figure 33**. Encapsulation cylinders for MMCLACS. Each MMCLACS specimen was stacked as described in the Methods section, and then encapsulated in the cylinders as seen below. The height was chosen to ensure an equal stress distribution on MMCLACS, and the tabs were designed for integration with the hydraulic grips used on the MTS machine.

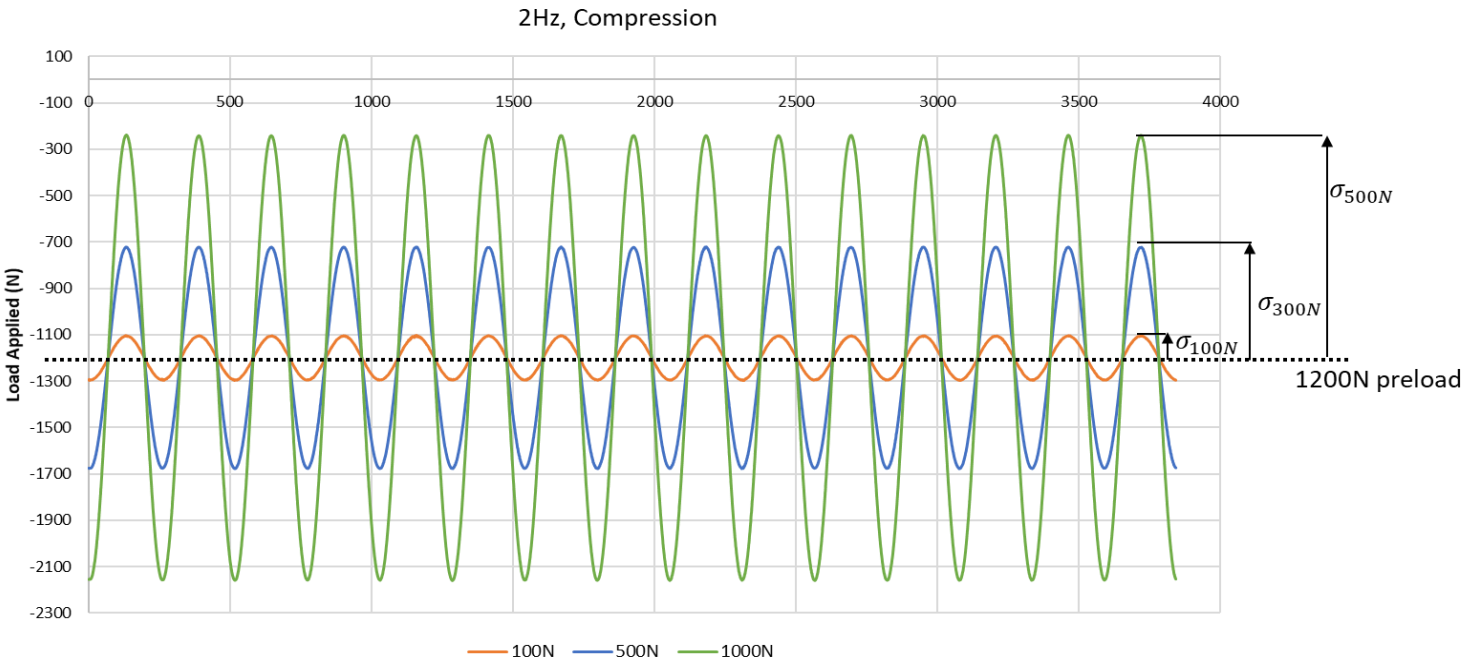


**Figure 34**. Compressive load amplitudes at 2Hz as a function of time. Load data collected during a 2Hz frequency, showing the 1200N preload and three different amplitudes applied, 100N, 500N, and 1000N. The same load amplitudes were applied at the other three frequencies tested (1Hz, 3Hz, and 5Hz). The load data was collected and verified for all tests to ensure loads were consistent across all tests.

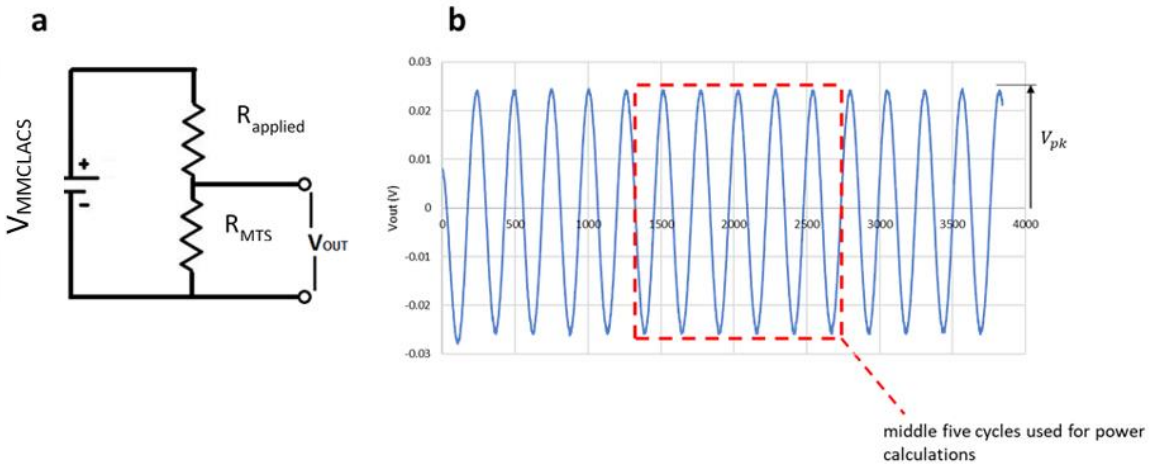


**Figure 35**. Electromechanical testing circuit diagram and sample voltage data. $R_{applied}$ is the shunt resistance sweep (20kΩ-20MΩ). $R_{MTS}$ is constant, 23kΩ. $V_{out}$ is a sinusoidal voltage collected directly into the MTS DAQ. 15 cycles of AC voltage are collected, and the middle 5 cycles are used for power calculations. Power is calculated for each $R_{applied}$ and plotted across the resistance sweep on a log scale.

$$V_{MMCLACS} = V_{out} * (1 + \frac{R_{applied}}{R_{MTS}})$$

$$V_{pk} = \frac{\max(V_{MMCLACS}) - \min(V_{MMCLACS})}{2}$$

$$V_{RMS} = \frac{V_{pk}}{\sqrt{2}}$$

$$P = \frac{V_{RMS}^2}{R_{applied} + R_{MTS}}$$

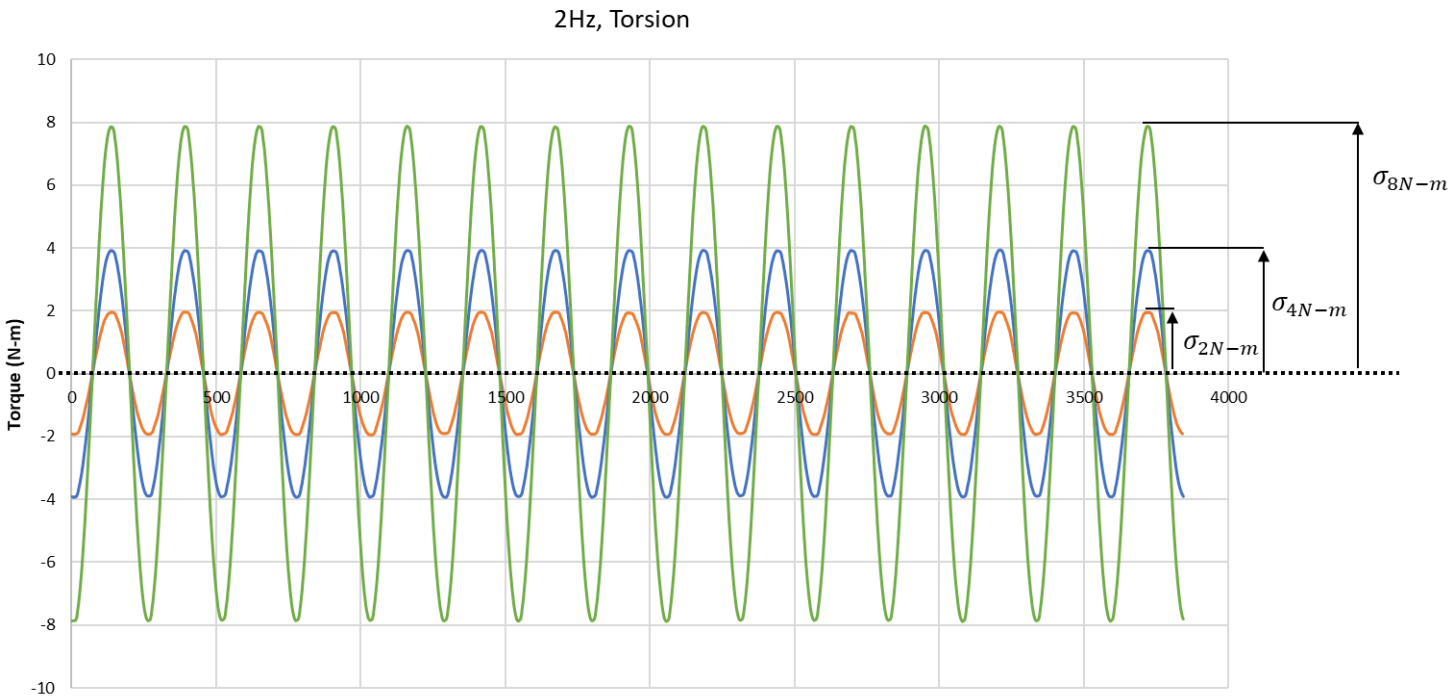


**Figure 36**. Torsion load amplitudes at 2Hz as a function of time. Load data collected during a 2Hz frequency, showing the three different amplitudes applied, 2N-m, 4N-m, and 8N-m. The same load amplitudes were applied at the other three frequencies tested (0.5Hz, 1Hz, and 3Hz). The load data was collected and verified for all tests to ensure loads were consistent across all tests.

**Table 3.** Average maximum power production as a function of torque and poling direction. All results in table are presented at the resistance of maximum power at 3Hz, 1.6MΩ. * represents a significant difference from RT-CLACS ($p<.05$).

| MMCLACS Group | Average Maximum Power 2N-m, 3Hz (μW) | Average Maximum Power 4N-m, 3Hz (μW) | Average Maximum Power 8N-m, 3Hz (μW) |
|---|---|---|---|
| R-CLACS | 0.063±0.039 | 0.26±0.14 | 1.14±0.55* |
| T-CLACS | 0.068±0.026 | 0.29±0.11 | 1.35±0.54* |
| RT-CLACS | 0.019±0.020 | 0.089±0.082 | 0.36±0.29 |

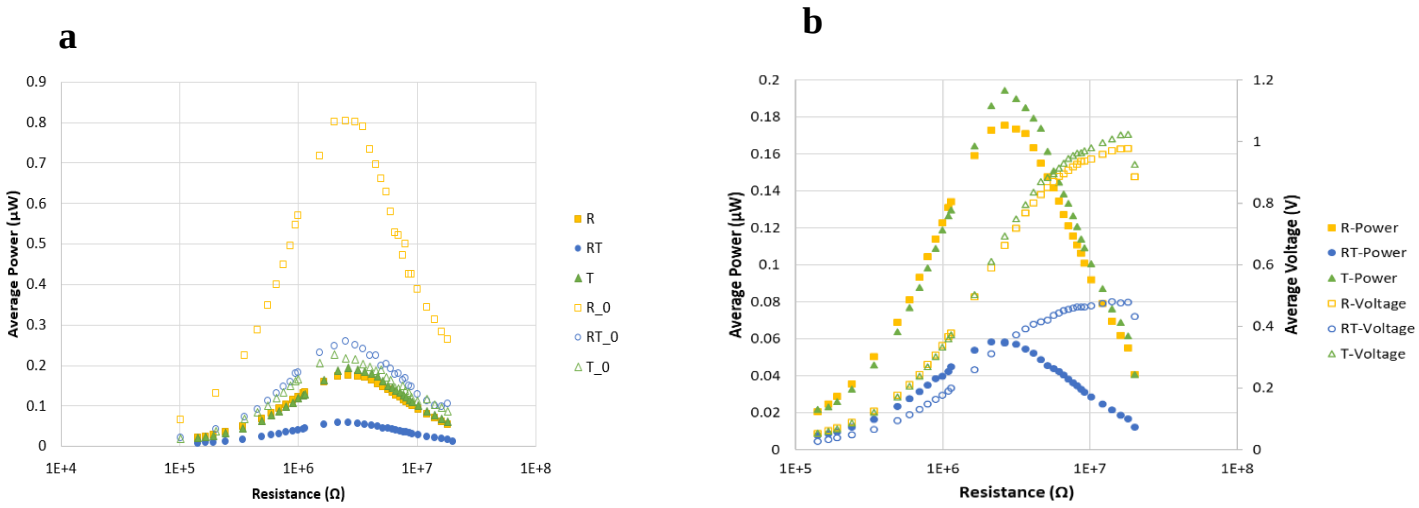


**Figure 37.** Average power and voltage generation from torsion. Average voltage output for each MMCLACS group as a function of resistance applied. Note the resistance is plotted on a log scale for clarity. All representative data presented at 4N-m, 2Hz loading condition. **a.** Each MMCLACS group and the cofired stack analogs (R_0, RT_0, T_0). **b.** Average power and voltage for each MMCLACS group. The voltage presented is the VRMS equivalent calculated from the average amplitude of the AC voltage collected at each resistance.

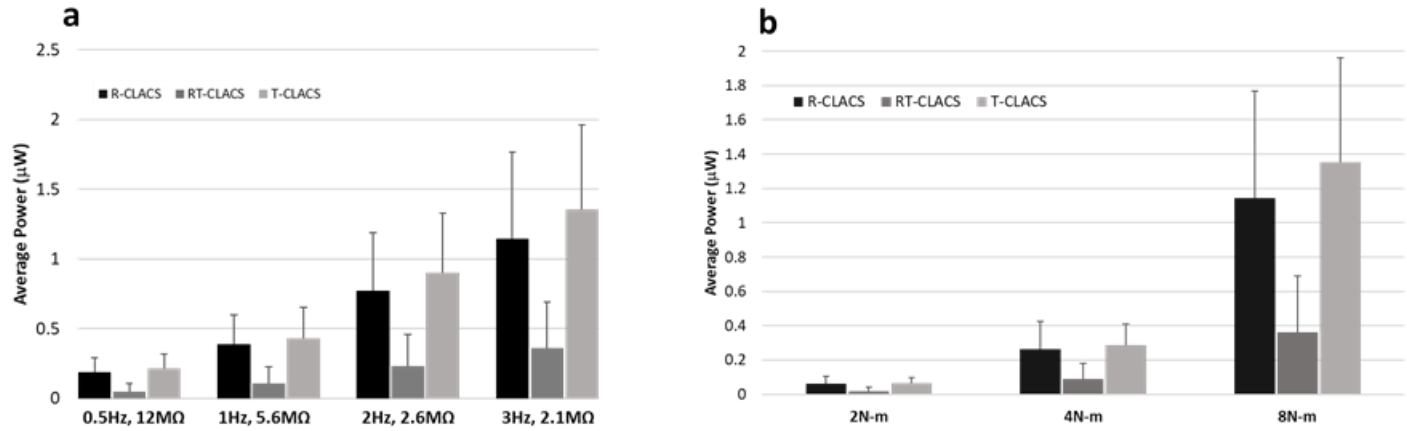


**Figure 38.** Average power as a function of poling direction. Error bars represent one standard deviation. **a.** Average power presented at 8N-m and the resistance of maximum power for each frequency. **b.** Power presented at 3Hz and 2.1MΩ.

Single Disc Analysis

To verify the intriguing results including the radial poled discs, a single disc analysis was performed. To remove the effects of the epoxy in the composite stacks tested, PZT discs were tested without encapsulation or compliant layers. Power output of a single radial poled disc was compared to that of a thickness poled disc under low compressive dynamic loads. Custom cylindrical fixtures were manufactured from aluminum (see Figure 39) and insulated from the platens. Screws were secured into the fixtures to collect the generated voltage across a resistance sweep. The fixtures were sanded with ultra-fine grit sandpaper to ensure a smooth and consistent loading surface on the individual discs. The individual discs were then placed on the bottom fixture with a small amount of a conductive lubricant (one part of a conductive epoxy) between the bottom electrode of the disc and the bottom fixture to ensure a slip surface. The same lubricant was used between the top fixture and the top electrode.

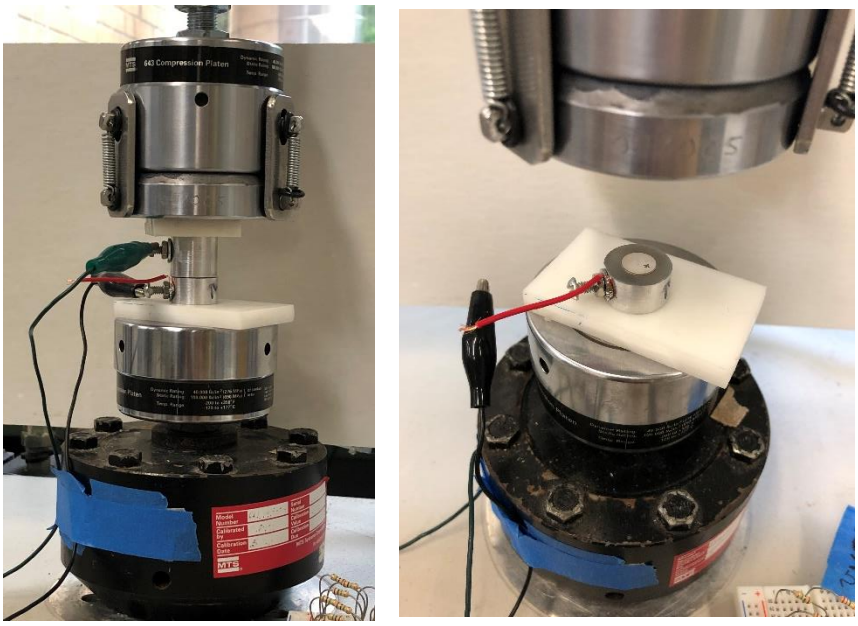


**Figure 39**. Single disc test set up.

The capacitance of each disc was measured prior to testing to ensure capacitance was not a contributing factor of power output differences. The capacitance of the radially-poled disc was 5.3nF and capacitance of the through-thickness poled discs was 5.4nF. A compressive preload of 100N was applied, followed by a cyclic 50N amplitude load at 1Hz, 2Hz and 3Hz. Voltage across a resistance sweep of 2MΩ-42MΩ was measured and power was calculated as done in the previous experiments (Figure 40).

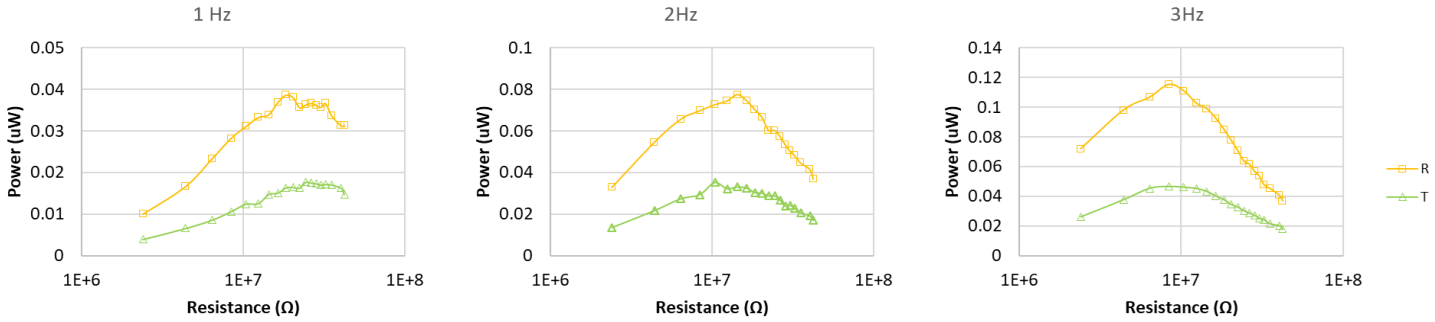


**Figure 40.** Power as a function of resistance for a radially poled disc (R) and a through-thickness poled disc (T). All plots presented at 50N amplitude load.

The radial poled disc (R) produced about double the power of the through-thickness disc (T) at each frequency. The maximum power was produced around the same resistances, inferring that the poling direction does not influence the source impedance of the disc. These results echo the differences found in the MMCLACS under compression. R-CLACS produced significantly more than the T-CLACS, and the power density of the R0 (stacks of R discs without a compliant layer) was higher than that of the T0 stacks.

To compare to the results found with the RT-CLACS, single discs were assembled and tested as explained above, without the influence of the epoxy encapsulation or compliant layers. The same aluminum fixtures were used in this test as above. To ensure a parallel electrical connection the same conductive lubricant was used between a thin piece of copper foil and the top electrode and bottom electrode of the bottom and top discs, respectively (Figure 41). The

lubricant was applied between each electrode and the copper foil to ensure an electrical connection. As with the above testing, capacitances were matched as closely as possible, given limited available discs. The R-R configuration consisted of two radially poled discs (disc 1 = 5.3nF, disc 2 = 5.3nF). The T-T configuration consisted of two through-thickness poled discs (disc 1 = 5.4nF, disc 2 = 5.5nF). The R-T configuration consisted of a radially poled disc on the bottom (disc 1 = 5.1nF) and a through-thickness poled disc on the top (disc 2 = 5.0nF).

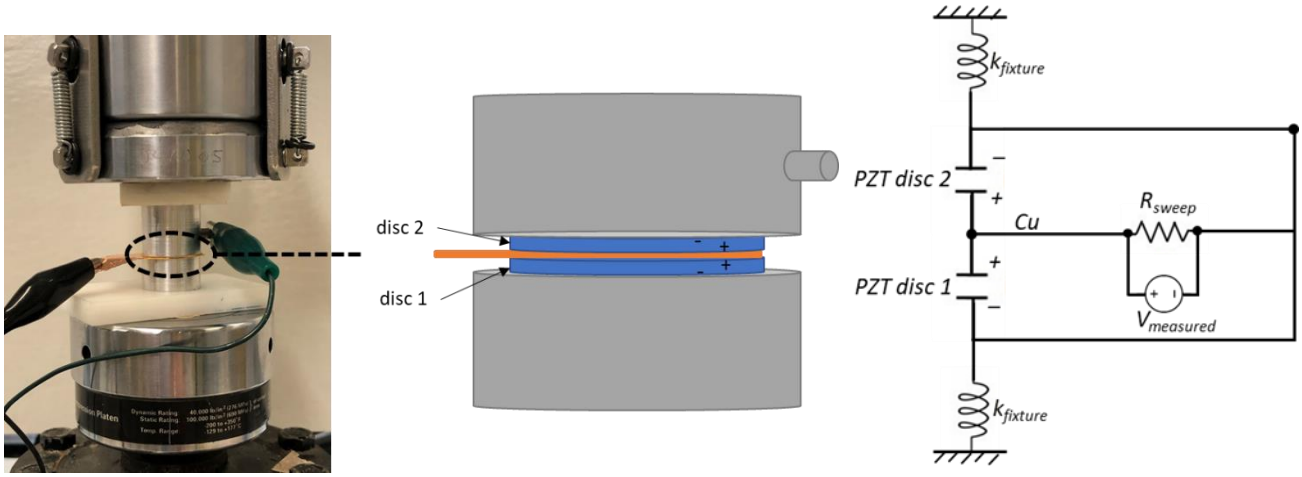


**Figure 41**. Two disc configuration test set up and circuit diagram.

Figure 42 presents the power generated from each configuration compared to the single R and T disc results. The RT configuration produced substantially more power than the RR and TT configurations, approximately double at all frequencies. This increase is slightly more than that found in the MMCLACS but was expected due to the findings of the RT-CLACS producing more power that both the R-CLACS and T-CLACS. The RR and TT configurations produced similar power across all three frequencies tested. These results don't exactly mirror the MMCLACS results where the R-CLACS produced significantly more power than the T-CLACS, demonstrating the increase in power due to the compliant layer expansion, especially in the R-CLACS. As expected, at maximum power the configurations with two discs connected

electrically in parallel produced more power at lower resistances (i.e. RR>R and TT>T). However, at higher resistances (>10MΩ) closer to the resistance of maximum power of the single discs, there was less of a difference, demonstrating the effect of source impedance and applied resistance.

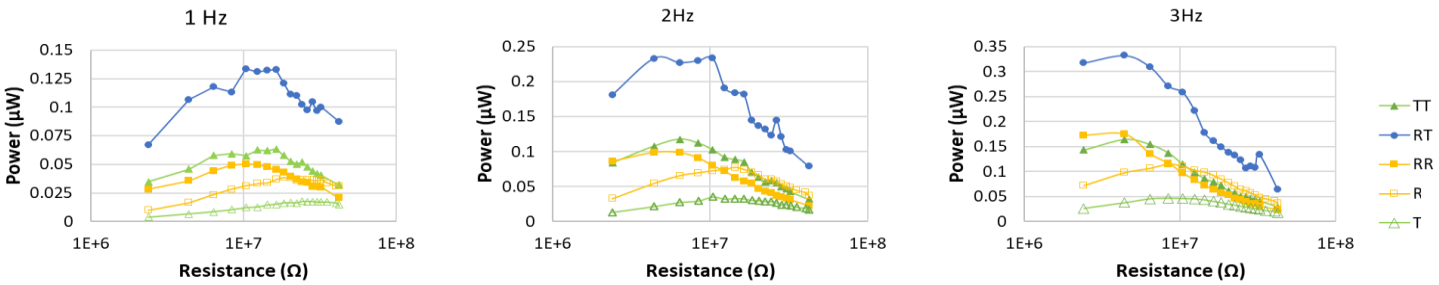


**Figure 42**. Power as a function of resistance for a radially poled disc (R) and a through-thickness poled disc (T) compared to the RR, TT and RT two disc configurations. All plots presented at 50N amplitude load.

This analysis should be expanded to test more discs in this manner. Piezoelectric discs tested in this fashion are sensitive to load surfaces, temperature and humidity changes, thus a full analysis would require a much larger sample size. However, the main goal of this analysis was to verify that a radially poled disc produced more power than a through-thickness poled disc. Given similar capacitances and the same loading conditions, the goal was to isolate the effect of the poling direction without influence of the CLACS structure, encapsulation, composite load transfer, or manufacturing changes. The results are consistent with the findings in the MMCLACS study, suggesting that under pure compression a radially poled disc produces more power at low frequencies, and an RT configuration produces more power than an RR or TT configuration.

To elucidate the exact mechanism and material piezoelectric properties contributing to these effects, a full finite element analysis should be completed. It is important to note that these relationships were all measured at frequencies well below the resonance frequency of this

material. Thus the assumptions that these relationships would hold true at higher frequencies should also be validated. It is likely that the increase in power when a radially poled disc and a through thickness poled disc are connected in parallel is a combination between mechanical stiffness and expansion interactions, as well as an electrical interaction and sharing of charge between the two discs. This phenomenon should be the focus of future work.

The use of radially poled discs is quite uncommon in industry. Most often rings, tubes, or hollow cylinders poled in the radial direction are used in actuator designs to create radial expansion or lateral deflection of the tip with clever electrode designs. Poling a ring or cylinder in the radial direction is a straightforward process, in which the electrodes are applied circumferentially on the outside and inside of the structure. This same electrode configuration is used to apply the electric field in order to displace the material in the desired fashion.

However, the process to pole a disc in the radial direction requires a more complex approach. Although not revealed by the manufacturer of the discs used in this study, it is assumed that the poling process occurred with a large bulk piece of material with external electrodes. After poling, another manufacturing process created the discs (i.e. wafering or punching) and an additional step was required to apply the top and bottom electrodes to each disc. These electrodes collect the charge generated under dynamic loads and are what were used to connect the discs electrically in parallel in the MMCLACS structure. Because of the complexity, a radial poled disc is inherently more expensive to manufacture and produce reliably. It is notable that an RT configuration is not possible in typical manufacturing methods of cofired generators or actuators and could be useful in the field to increase power generation at low frequencies. However, the cost of radially poling bulk material should be weighed with the increase in efficiency.

**Chapter 6: Design considerations for piezoelectrically powered electrical stimulation: the balance between power generation and fatigue resistance**

Manuscript prepared for submission to Journal of Mechanical Behavior of Biomedical Materials.

Planned submission February 2020

E.D. Krech[1,2], L.J. LaPierre[2], XXX[3], E.A. Friis[1,2,4]

[1]University of Kansas, Bioengineering Graduate Program, Lawrence, KS, USA;

[2]Evoke Medical, LLC, Lawrence, KS, USA;

[3]QorTek, Williamsport, PA, USA;

[4]University of Kansas, Department of Mechanical Engineering, Lawrence, KS, USA

**Corresponding Author:**

Elizabeth A. Friis
Professor, Mechanical Engineering
University of Kansas
1530 W. 15th St., 3138 Learned Hall
Lawrence, KS 66045
lfriis@ku.edu
785-550-3725
785-864-5254 (fax)

Declarations of interest: none

Abstract

Time and quality of bone healing from orthopedic surgeries, especially lumbar spinal fusion procedures, is problematic for many patient populations. To address this issue, clinicians often use electrical stimulation to improve surgery success rates and decrease healing time in patients suffering from incomplete healing, pseudarthrosis, or nonunion. Current invasive electrical stimulation devices require an implantable battery and a second surgery for removal. Piezoelectric composites within an interbody implant have generated sufficient power under physiologic loads to deliver pulsed electrical stimulation without a battery and have demonstrated promising preclinical bone growth and fusion success. The objective of the current study was to assess the power generation and fatigue resistance of three commercially manufactured piezocomposite configurations in a modified implant design to demonstrate efficacy as a tough biomaterial within osteogenic implants. The three configurations were electromechanically assessed under physiological lumbar loading conditions, and all configurations produced sufficient power to promote bone healing. Additionally, electrical and mechanical fatigue performance was assessed under high load, low cycle conditions. All configurations demonstrated runout with no gross mechanical failure and two configurations demonstrated electrical fatigue resistance. Future piezoelectric implant design decisions should be based on power generation needs to stimulate bone growth, as mechanical fatigue efficacy was proven for all piezocomposite configurations tested.

**Keywords**: electrical stimulation, piezoelectric composites, fatigue resistance, power generation, implant design

Introduction

Complete bone healing from a variety of orthopedic procedures is very challenging for many populations (Fingar *et al.*, 2014). Lumbar spinal fusions have increased over 200% in the last decade, with almost half a million procedures performed in 2017 (Deyo, 2015). Despite the recent innovation in interbody implant technology, nonunion and pseudarthrosis rates are as high as 47% in lumbar spinal fusion procedures (Einhorn, 1995; Ekegren *et al.*, 2018; Gan and Glazer, 2006; Knox and Chapman, 1993; Tzioupis and Giannoudis, 2007). Because there is no expectation for nonunions to heal spontaneously, surgical or other intervention is necessary to stimulate the healing process (Bhandari *et al.*, 2012). Healing is especially challenging in difficult-to-fuse populations, particularly patients with diabetes and tobacco users, both of which are associated with higher rates of pseudarthrosis, failed fusions and increased time to healing (Berman *et al.*, 2017; Browne *et al.*, 2007; Chung *et al.*, 2012; Kwiatkowski *et al.*, 1996; Marin *et al.*, 2018; Vo *et al.*, n.d.). As the incidence of diabetes is expected to increase substantially in the next decade, as well as a continuing rise in the percentage of patients with comorbidities, a cost-effective, efficient solution is necessary to help bone healing for these patients (Martin *et al.*, 2007).

To supplement bone healing and improve fracture and surgical fusion success rates, several adjunct therapies are used in addition to the primary implants for stabilization. One of the most common therapies used in spinal fusion is electrical stimulation. Implantable stimulators providing constant direct current (DC) stimulation applied directly to the fusion site has shown great success in long bone fractures and spinal fusions (Paterson *et al.*, 1980; Saxena *et al.*, 2005; Tejano *et al.*, 1996). Improvements in fusion rates and decreased healing times were linked to the constant DC stimulation, but required additional surgery to remove the battery pack, increasing

risk of infection and secondary wound healing issues evident with difficult-to-fuse patients (Geerlings and Hoepelman, 1999).

Piezoelectric materials emit electric charge from cyclic mechanical loading and have been explored as an alternative to batteries to harvest ambient recurring motion (i.e. walking) and subsequently power auxiliary devices (Li *et al.*, 2014). Piezoelectric ceramics have been used successfully to generate power from walking loads, but the power levels are limited by inefficiencies (Feenstra *et al.*, 2008; Kymissis *et al.*, 1998). At low frequencies as seen in human motion, the mismatch in device resonance frequency and loading frequency worsens the limited charge density and strain amplitude of piezoceramic materials, making energy transduction less effective (Jaffe *et al.*, 1971). Cofired stacks of piezoelectric elements connected electrically in parallel and stacked mechanically in series significantly lowers source impedance; increasing efficiency at lower resistances (Platt *et al.*, 2005). However, these piezoceramic stacked generators are incredibly stiff, brittle and could not withstand repetitive multiaxial loads, inhibiting direct use as an implant material.

In order to toughen the piezoceramic and increase functionality at lower resistances, Goetzinger *et al.* developed multilayer piezoelectric composite spinal fusion interbody implants by encapsulating lead zirconate titanate (PZT) macro fibers in a medical grade epoxy (Goetzinger *et al.*, 2016). These interbodies were designed to transduce cyclic walking loads to DC electrical signals that would be delivered directly to the intervertebral disc space through an attached electrode. The preclinical efficacy of these implants was demonstrated in a pilot ovine study, in which the histology, CT scans, and biomechanical data showed evidence of enhanced fusion in the active piezocomposite implants, compared to the controls that did not fuse and developed soft tissue callus (Friis *et al.*, 2015). Despite promising results, the difficult and

unreliable fabrication process limited replication, scalability and implementation as a tough implant material.

The use of traditional cofired piezoelectric stacks would improve manufacturability, while lowering source impedance and producing more power at lower resistances (Platt *et al.*, 2005), thus overcoming obstacles in practical implementation of the piezoelectric component of the implant. Krech *et al.* recently studied the power generation capability of compliant layer adaptive composite stacks (CLACS), a PZT stack with interdigitated compliant layers (E. D. Krech *et al.*, 2018; Ember D. Krech *et al.*, 2018). The compliant layers increased power generated from physiologic walking loads by 50%, a significant increase in power output efficiency at low frequencies. Similarly, Cadel *et al.* found that stacked PZT discs (a cofired stack analog) and CLACS included within an interbody implant design produced sufficient power needed to stimulate bone growth (Cadel *et al.*, 2018). Even within the limited space of a transforaminal lumbar interbody fusion implant with a graft window, utilizing PZT discs addressed fabrication concerns with the macro fiber composite, while increasing power production efficiency. Static or dynamic mechanical integrity of the piezocomposite implant material has not yet been assessed. The inclusion of the compliant layer in CLACS may not be cost-effective if it does not improve the power production and fatigue life of the material.

The purpose of this study was to assess the power production capability and fatigue performance of three different piezocomposite generator designs. It was hypothesized that the use of CLACS would increase power production and fatigue resistance under loading conditions seen in spinal fusion implants. The overall goal was to understand the most appropriate PZT stack generator configuration in a modified implant design to produce sufficient power to supply electrical stimulation, while maintaining mechanical integrity under fatigue loading conditions.

Methods

*Specimen Fabrication*

The present study was devised to design, validate and elucidate the power generation capability and fatigue resistance of cofired PZT stacks and CLACS to test feasibility for their use in orthopedic implants. To mimic scalable manufacturing methods to be used in a final implant design, commercially designed and manufactured piezoelectric stack generators were fabricated, with and without CLACS technology. The three configurations, as seen in Fig. 43, represent the generic implant design utilized to effectively gauge failure of the interfaces between materials, primarily the polymer encapsulation and brittle ceramic PZT, and electrical connections. Other mechanical stress concentrations common in standard implants were intentionally eliminated, as to isolate the fatigue life comparison of the three PZT configurations.

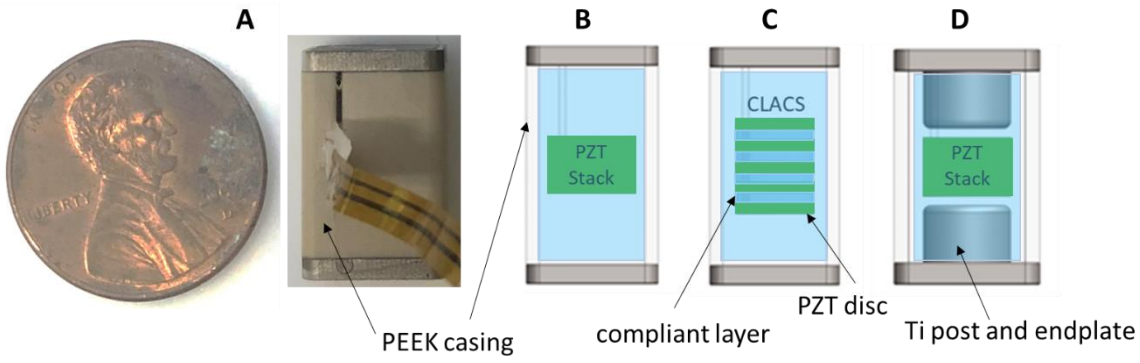


**Figure 43.** Three configurations assessed. A. The external PEEK casing was the same in all three configurations. B. Internal schematic of Configuration 1 (C1). B. Internal schematic of Configuration 2 (C2). Note the compliant layers in between each PZT disc and the epoxy encapsulation were the same material. C. Internal schematic of Configuration 3 (C3). Note that the endplates with the titanium post were encapsulated with the PEEK body and PZT stack. The epoxy encapsulation of each PZT stack is shown in blue.

All three configurations were manufactured and provided by QorTek and Evoke Medical. A worst case reasoning was utilized to design the configurations: mechanically the tallest height of an implant was used, and electrically the height and diameter of the PZT was limited to what would fit within the shortest implant height and footprint. The overall implant height (15mm)

and loaded footprint surface area (100mm$^2$) was constant across all configurations. Configuration 1 (C1) included a traditional cylindrical PZT cofired stack generator. Configuration 2 (C2) utilized the CLACS design from Krech *et al.*, utilizing PZT discs and interdigitated compliant layers. Configuration 3 (C3) included the same PZT stack as C1 with a titanium post at each end to enhance load transfer and subsequent power generation.

For C1 and C3, the cylindrical stack was a cofired 6mmØx3.2mm tall stack with 5 layers connected electrically in parallel and sintered together (Fig. 43B). The PZT was poled through-thickness post sintering. For C2 (Fig. 43C), CLACS were created with five 0.8mm thick PZT discs, interdigitated with cured EPO-TEK 301 (Epoxy Technology, Billerica, MA) compliant layers of the same thickness of the individual discs. The PZT discs were electroded, poled through-thickness, and subsequently connected electrically in parallel using conductive epoxy. For C3, the cylindrical stack with a titanium post, the same stack as C1 (6x3.2mm) was used but was encapsulated with a 6mmØ 4mm titanium post endplate (Fig. 1D). An error in the development of new manufacturing methods for these PZT configurations led to slight differences in PZT volume across the configurations. PZT properties were measured pre and post encapsulation to ensure correct electrical connection and material integrity following the potting process.

The overall goal of this study was to mechanically and electrically assess the performance of commercially produced CLACS (C2) as compared to a cofired piezoelectric generator (C1). The third configuration with the titanium post (C3) was an alternate way to enhance power from the stack by directing the load to the piezo stack. The balance between power production amplification and adequate resistance to fatigue failure was critical to understand across the three configurations, thus guiding configuration design decisions.

To capture the desired failure at material interfaces, the three configurations were designed to minimize geometric stress concentrations (insertion attachments) that would influence fatigue failure. The PEEK casings were 13mm tall, with a 10x10mm cross section. There was an 8mmØ through hole to house the PZT stacks. All PZT stacks were potted in the PEEK outer casing with EPO-TEK 301, a medical grade epoxy (Fig. 43). All stacks had a 1mm radial epoxy encapsulation and were centered within the height of the PEEK body, with epoxy filling in the remainder of the volume. Additionally, C1 and C2 had 1mm aluminum end plates adhered to the PEEK with EPO-TEK 301. For C3, the 1mm titanium endplates had a 4mm post extrusion, as seen in Fig 43D and were encapsulated with the PZT and PEEK bodies. Titanium was used in C3 to mimic final implant design and elucidate the effect of stiffness of the post to direct load to the PZT stack. This modified implant assembly represents materials and interface stress concentrations that will be present in final implant designs. All test specimen were x-rayed prior to testing to ensure no visible air bubbles in epoxy or other discontinuities existed in the encapsulation.

*Electromechanical Testing*

Using an MTS MiniBionix 858 test frame (MTS, Eden Prairie, MN), power production under physiologic compressive loads was compared. A 2.5kN load cell and self-aligning platen was used to ensure pure compressive loads were applied (Fig. 44). Physiologic stress experienced by lumbar spinal fusion implants was normalized to the surface area of the configurations. An 800N compressive preload was applied to ensure specimen were always in compression. Cyclic loads at three amplitudes (67N, 335N and 670N) were applied at three frequencies (1Hz, 2Hz and 5Hz). These loads and frequencies represent conservative estimates

for stresses experienced by orthopedic implants during walking and other typical human motion (Arshad *et al.*, 2017; Cromwell *et al.*, 1989).

For each load and frequency, voltage output of the piezo stack was measured across a shunting resistance sweep ranging from 23kΩ-800MΩ. Resistance range was chosen to characterize the behavior of each configuration at lower circuit resistances and capture the voltage output at the resonance resistance (matched impedance) for each PZT stack configuration and frequency. Voltage output was measured for 15 cycles at each load, frequency and resistance to ensure steady-state behavior. The average amplitude of the middle 5 cycles was used for the remaining analysis, and converted to RMS, $V_{RMS} = V_{amp}/\sqrt{2}$ to predict the expected DC output. Power was calculated for each load, frequency and resistance, $P = V_{RMS}^2/R$. Maximum power as a function of configuration was compared using a one-way ANOVA, with a Tukey-Kramer post-hoc analysis to assess differences between groups ($\alpha = .05$). This initial power production comparison was used to ensure that each PZT configuration produced sufficient power within the given designs.

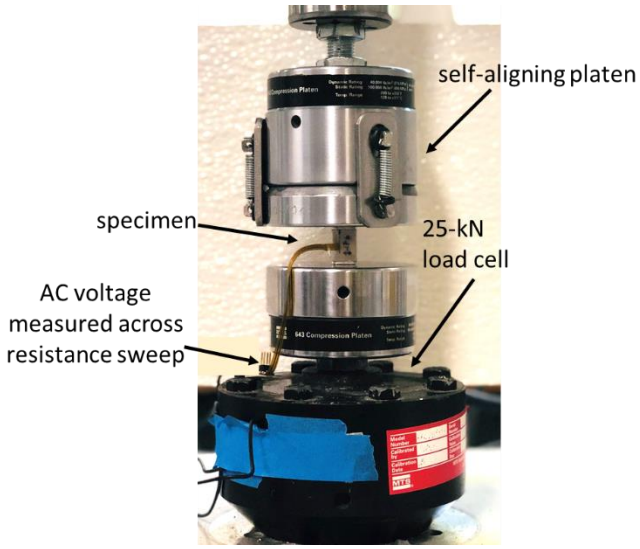


**Figure 44.** Electromechanical and fatigue test setup.

*Fatigue Testing*

Utilizing a modified ASTM F2077 testing protocol, the mechanical and electrical fatigue performance of each configuration was evaluated. Fatigue of orthopedic implants, specifically spinal fusion interbody implants, is typically tested to five million cycles at loads between 30-50% of the ultimate strength (ASTM, n.d.). At 5Hz, five million cycles would take over eleven days. Therefore, to make the study length tractable, a low cycle, high load fatigue test was conducted. Based on estimates of fatigue performance and average footprint (surface area) of similar lumbar implant designs, a failure load at 50,000 cycles was estimated to be approximately 6,000N (Peck *et al.*, 2018). This scaled load aims to accurately match predicted physiological stress levels in the final implant design. A ratio of maximum stress to minimum stress of 10 was used, as is consistent with compression fatigue testing of PEEK and PEEK composites (Jen and Lee, 1998; Lee *et al.*, 2012; Rae *et al.*, 2007). The loading frequency was 5Hz and tests were run in load control to match ASTM F2077. In summary, specimens were subjected to a 600 to 6,000N cyclic compressive load at 5Hz for 100,000 cycles, or until failure. The MTS MiniBionix with a self-aligning platen setup was used to avoid unwanted bending of the sample due to coaxial forces (Fig. 44).

Mechanical fatigue behavior of each configuration type was compared. Specimen were run until gross mechanical failure occurred (i.e. visible exterior crack formation/propagation) or runout with no mechanical issues after 100,000 cycles was achieved. A displacement limit was set in the loading program to stop cyclic loading if the specimen deformed beyond the failure values (> 10% of elastic deformation). Displacement was recorded for 15 cycles after every decade from 10 to $10^5$ cycles. Average peak-to-peak displacement was calculated for each data set to track mechanical degradation. It was expected that there would be high variability in the

behavior and failure in fatigue of the specimen, so if an average difference between configurations was not perceived, a pass or fail analysis was implemented. Mechanical fatigue resistance was considered successful if the number of cycles to failure was more than the cycles to failure of the existing implant data at a comparable stress ratio, as shown by the green check mark in Fig. 45. This analysis was created to understand material interface strength, predict mechanical fatigue resistance and inform future implant design decisions.

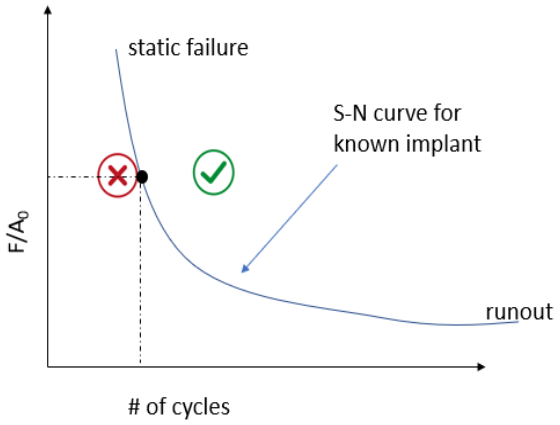


**Figure 45.** Representative S-N curve to demonstrate mechanical success criteria.

Electrical fatigue resistance of each configuration was also assessed. Capacitance values pre and post testing were recorded for each specimen to assess electrical fatigue performance of the PZT stack. Raw voltage was measured across a 10MΩ resistance for 15 cycles after every decade from 10 to $10^5$ cycles. The resistive load was chosen to match the resistance of the anticipated circuit in the final implant design. Voltage measurements were used to compare trends of electrical performance deterioration across the three configurations. Average peak-to-peak voltage was calculated for each data set. Electrical fatigue resistance was considered successful if the peak-to-peak voltage at 100,000 cycles was at least 50V, the minimum voltage required to pass through a rectifying circuit.

## Results

### *Power Generation*

Under physiological loads, the power generation of each configuration was measured to predict the performance of each PZT stack type in a final implant configuration. Table 4 summarizes the maximum power generation of each configuration as a function of the different load amplitudes and frequencies tested. As expected, based on accepted piezoelectric power generation as a function of applied resistance load, the power increased as the applied resistance load increased until the applied resistance load matched the impedance of the specimen, demonstrating maximum power production. At maximum power (670N, 5Hz) C2 produced significantly more power than C1 and C3, respectively ($p < .01$). The one-way ANOVA revealed no significant differences in C1 power generation in comparison with C3 power generation, although the trend was a 40% increase due to the titanium post in C3 ($p = .1$). Not accounting for variation in the PZT volume or $d_{33}$, the inclusion of CLACS in the PZT stack design in C2 increased power output 3.6-fold as compared to the cofired stack in C1. Similarly, C2 produced 2.5 times more power than C3. With the same PZT stack design and volume, there was a 1.4-fold increase in power due to the titanium post in C3 compared to C1.

As expected, all configurations followed expected trends in PZT power generation: a linear increase as frequency and load increase. The resistance of maximum power was consistent at each frequency for C1 and C3: 6-7MΩ at 5Hz, 20MΩ at 2Hz, and 32-34MΩ at 1Hz. The resistance of maximum power for C2 was slightly higher for 5Hz (9MΩ) and 1Hz (50MΩ). At a conservative estimate for a walking stress, (335N, 2Hz) all configurations produced satisfactory power at a reasonable resistance for circuit design (20MΩ): C1 produced 35μW, C2 produced 131μW, and C3 produced 52μW.

**Table 4.** Average maximum power generated ± one standard deviation. * represents significant difference from C2 ($p<.05$).

| Specimen Type | Measured $d_{33}$ (pC/N) | Max Power (μW) 670N/5Hz | Resistance of Max Power at 5Hz (MΩ) | 670N/2Hz Max Power (μW) | 335N/2Hz Max Power (μW) | 67N/2Hz Max Power (μW) | Resistance of Max Power at 2Hz (MΩ) | 670N/1Hz Max Power (μW) | 335N/1Hz Max Power (μW) | 67N/1Hz Max Power (μW) | Resistance of Max Power at 1Hz (MΩ) |
|---|---|---|---|---|---|---|---|---|---|---|---|
| C1 (n=9) | 1689 ± 390 | 363 ± 108* | 7 | 152 ± 42 | 35 ± 11 | 1.3 ± 0.57 | 20 | 76 ± 23 | 18 ± 6 | 0.71 ± 0.35 | 34 |
| C2 (n=5) | 1521 ± 608 | 1190 ± 395 | 9 | 560 ± 223 | 131 ± 58 | 3.8 ± 2.6 | 20 | 280 ± 101 | 66 ± 29 | 2.3 ± 1.6 | 50 |
| C3 (n=7) | 1808 ± 397 | 511 ± 155* | 6 | 216 ± 70 | 52 ± 20 | 2.1 ± 1.5 | 20 | 110 ± 40 | 26 ± 11 | 1.2 ± 1.0 | 32 |

Because volume was not constant across all configurations, power generation was normalized by the total volume of PZT in each configuration to compare power density as a more accurate figure of merit. The average power densities at 670N, 5Hz and the power densities at a walking load of 335N, 2Hz are shown in Fig. 46. Following the same trends as the overall power output, C2 had the largest power density, followed by C3 and C1, respectively. At lower resistances (< 2MΩ), C2 and C3 had similar power densities, but as resistance increased toward resonance, the average C2 power density increased considerably. The maximum power density was achieved at slightly higher resistances for C2, similar to power generation. At resistance of maximum power for each frequency, C2 increased power density compared to C1 and C3 by 3-fold and 2-fold, respectively. The C3 average power density was 1.4-fold higher than the C1 power density at all frequencies. These trends were consistent for all loads and frequencies tested. Although this measure does not account for the variation in the PZT $d_{33}$, it is a good indication of the expected power production for each configuration.

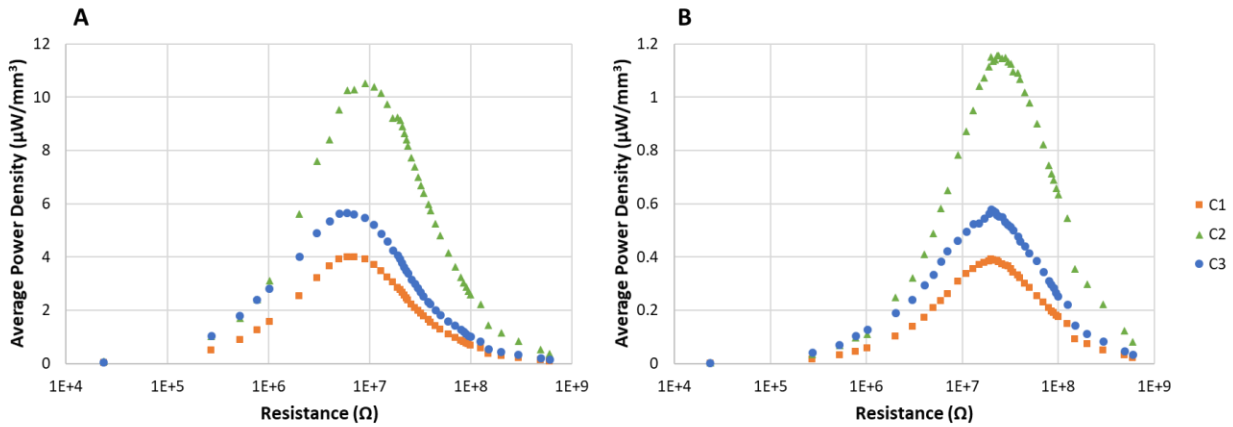


**Figure 46.** Average power density as a function of configuration type and applied resistance load. A. 670N and 5Hz. B. 335N and 2Hz.

To account for the variation in the PZT manufacturing changes across configuration type, power generation was normalized by the measured piezoelectric charge constant, $d_{33}$. The constant $d_{33}$ is a measure of the voltage generated per unit of dynamic force applied, and thus is used to predict expected charge generation for a given PZT material and/or configuration. The generated electrical charge per unit of input mechanical energy is directly proportional to the square of $d_{33}$, so the data presented is normalized by that factor. Fig. 47 presents representative data for individual specimen from each configuration grouped by similar $d_{33}$ values at 335N, 2Hz. Fig. 47A compares normalized power for specimen with a $d_{33}$ in the upper range; C1-26, C2-1, and C3-3 had measured values of 2425, 2143, and 2536 pC/N respectively. Fig. 47B compares normalized power for specimen with an average $d_{33}$; C1-17a, C2-4, and C3-18 had measured values of 2040, 1920, and 1871 pC/N respectively. Fig. 47C compares normalized power for specimen with a $d_{33}$ in the lower range; C1-5, C2-7, and C3-1 had measured values of 2040, 1920, and 1871 pC/N respectively.

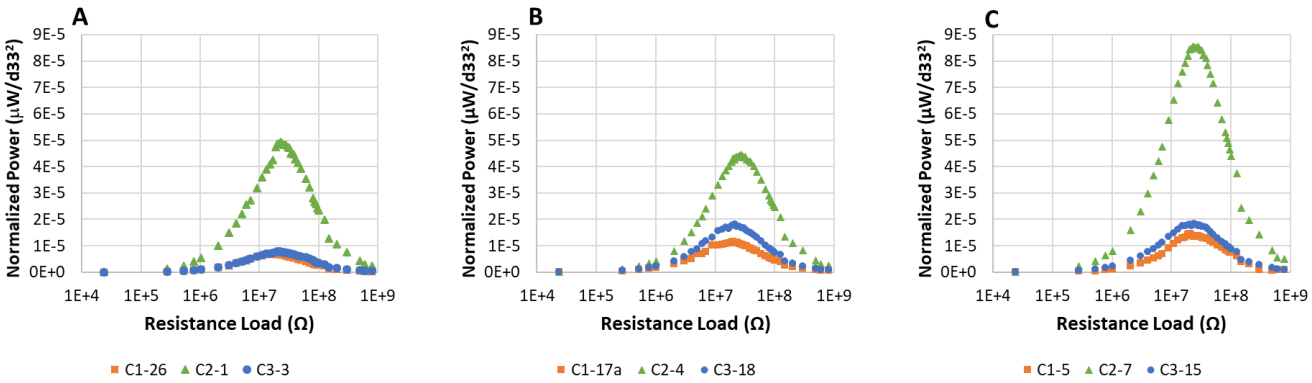


**Figure 47.** Normalized power as a function of configuration type and applied resistance load. Note these are representative data for specimen grouped with similar measured $d_{33}$ values. A. High $d_{33}$ group. B. Average $d_{33}$ group. C. Low $d_{33}$ group.

Following the same trends as power density, C2 had the highest normalized power. However, at both the high and low end of the measured $d_{33}$ values, the difference between the C3 and C1 groups decreased. As evidenced by the variation of normalized power within configurations, especially within C2, the power produced is greatly influenced by the $d_{33}$ of the PZT stack. Normalization by $d_{33}$ emphasizes the mechanical effect of CLACS in the C2 structure, as the normalized power presented is a function of the permittivity of the PZT material and the elastic compliance. When making further design decisions, this variation should be considered, measured and controlled.

*Fatigue*

The peak-to-peak displacement as a function of number of cycles is plotted for each specimen in Fig. 48. All specimen tested ran out to 100,000 cycles, without reaching the displacement failure limit. The gross mechanical behavior was a pass for all specimen in all configurations. There were no visible cracks in the PEEK body and/or the endplates. Although the displacement did not reach the failure limits, the peak-to-peak displacements can be used to predict likelihood of future failure. For a stable mechanical composite structure, the peak-to-peak displacement should slightly decrease after the initial steady-state is reached. In an unstable

structure the trend would be opposite, with an increase predicting future crack formation and potential failure.

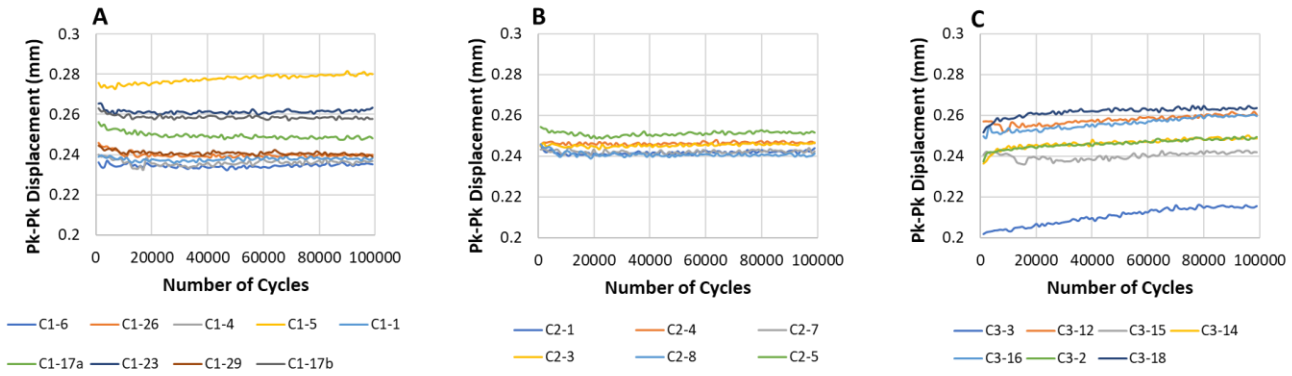


**Figure 48.** Peak-to-peak displacement as a function of number of cycles. A. Peak-to-peak displacement for all specimen in the C1 group. B. Peak-to-peak displacement for all specimen in the C2 group. C. Peak-to-peak displacement for all specimen in the C3 group.

There was a mixed response in the C1 group, demonstrated by the widespread data (Fig. 48A). However, on average C1 peak-to-peak displacement decreased by 1% throughout the test. In a few specimen (e.g. C1-5), a slight increase could be an indication of ensuing mechanical failure. None of the C2 specimen had an increase and remained stable after the initial settling period (Fig. 48B). On average, the peak-to-peak displacement decreased a minimal amount, 0.5% in the C2 group. Conversely, all C3 specimen demonstrated an increasing peak-to-peak displacement, indicative of impending failure. The average increase was 4% from the starting value (Fig. 48C).

The electrical fatigue performance of all specimens was measured in comparison to a threshold peak-to-peak voltage of 50V, which is required to pass through a post-processing circuit. Capacitance of each specimen was measured before and after the test as a more specific measure of PZT mechanical failure and/or depolarization of the material. For all configurations,

the voltage and capacitance dropped as the number of cycles increased. Table 5 shows the relationship between capacitance and final peak-to-peak voltage output. For C1, the average decrease in capacitance and peak-to-peak voltage was approximately 30%. For C2, the measured capacitance dropped 73%, while the peak-to-peak voltage only decreased 50%. For C3, five of the specimens electrically passed (exceeded the failure criteria) and the capacitance and voltage decreased by 46% and 25%, respectively. However, there was catastrophic failure in two of the C3 specimen, with a sudden drop in voltage output below the threshold before 20,000 cycles, and thus the averages presented in Table 5 represent the specimens that passed. For all specimens, the voltage dropped most significantly between 1,000 and 30,000 cycles but then stayed fairly constant for the remainder of the test. This phenomenon was consistent for all three configurations.

**Table 5.** Electrical fatigue performance of each configuration. Note that two C3 specimen did not pass electrically, thus are not included in these average values.

| Specimen Type | Cs Pre Test (nF) | Cs Post Test (nF) | Percent Decrease (%) | Pk-Pk Voltage at 1k Cycles (V) | Pk-Pk Voltage at 100k Cycles (V) | Percent Decrease (%) |
|---|---|---|---|---|---|---|
| C1 (n=9) | 2.4 ± 0.3 | 1.7± 0.2 | 31 | 287 ± 48 | 194 ± 48 | 32 |
| C2 (n=5) | 1.7 ± 0.5 | 0.46 ± 0.3 | 73 | 344 ± 137 | 172 ± 70 | 50 |
| C3 (n=5)* | 2.3 ± 0.2 | 1.3 ± 0.2 | 46 | 227 ± 74 | 170 ± 67 | 25 |

Discussion

This study was designed to compare three potential scalable PZT configurations for use within a spinal fusion interbody implant to power bone healing DC electrical stimulation delivery without the use of a battery. The PZT stacks within the implant will generate power under cyclic loads transmitted to the implant through loads similar to walking and other human motion, allowing bone healing DC stimulation to be applied directly to the fusion site. The objective was to correlate power production with fatigue resistance of the three PZT

configurations to inform future design decisions. The use of CLACS to increase power generation has previously been verified, however comparison to commercially produced cofired stacks has not been presented (Cadel *et al.*, 2019, 2018; E. D. Krech *et al.*, 2018; Ember D. Krech *et al.*, 2018).

CLACS, as implemented in C2, significantly increased power production by over 60% as compared to a traditional cofired stack (C1), even when accounting for variation in volume and $d_{33}$. Electrically, this technique utilizes principles of piezoelectric stacked generators to lower source impedance, while also increasing lateral strain on the piezoelectric elements due to compliant layer expansion, increasing power output (Ember D. Krech *et al.*, 2018). Mechanically, the toughened piezocomposite will more closely match the compliance of bone to prevent stress shielding and resist brittle fatigue failure of the implant, indicated by the stable displacement in the fatigue study. The power amplification of this material will allow small stacks to be included within existing orthopedic implant shapes, while still generating enough power to provide electric stimulation to the gap healing site. This will not change surgical techniques or require development of new instrumentation, increasing likelihood of clinician adoption.

Although C2 did produce the most power, there was more variation within the group, especially the $d_{33}$ values, as compared to both C1 and C3. It is important to note the CLACS were fabricated with crude manufacturing techniques to validate early stage product concepts. However, this could be indicative of future reliability and scalability concerns and should be balanced with the increased power production. Although the mechanical fatigue performance of C2 was superior, the electrical fatigue resulted in the highest drop in both capacitance and peak-to-peak voltage. Although no specimen had catastrophic electrical failure, and produced more

voltage than the threshold, the drop in capacitance was expected. The CLACS structure enhances the mechanical loading on discs, which may instigate de-poling of the PZT over time.

As expected, there was also an increase in power generation due to the titanium post in C3. Because the modulus of elasticity of PEEK is 3% that of the titanium, the load directed to the stack from the titanium post is expected to be about 12x the load carried by the PEEK/epoxy encapsulation. The increase in power generation as compared to C1 followed this reasoning. However, mechanical and electrical fatigue performance was affected by the additional stress concentration at the material interface and modulus mismatch, demonstrated in the decreased mechanical and electrical properties due to fatigue of the C3 group.

To better understand the internal failure modes, a specimen from each group was soaked in acetone to remove the epoxy/PEEK encapsulation (Fig. 49). Fig. 49A shows a brittle fatigue crack propagation through the cofired stack in a C1 specimen. As anticipated, in the C2 specimen the compliant layer between the PZT discs interrupted the crack propagation through the discs, as seen in Fig. 49B. Although not for the same purpose, scientists found that in electrical fatigue testing, the adhesive interlayer within a stack decreased stress crack formation and propagation, mirroring these results (van den Ende *et al.*, 2009). Although C3 maintained adequate gross macroscopic fatigue performance of the implant assembly, the PZT stack was significantly damaged with multiple cracks and degradation. The titanium post configuration would not be suitable for use under repetitive high loads because of the stress concentration overlap, resulting in severe mechanical failure of the stack (Fig. 49C).

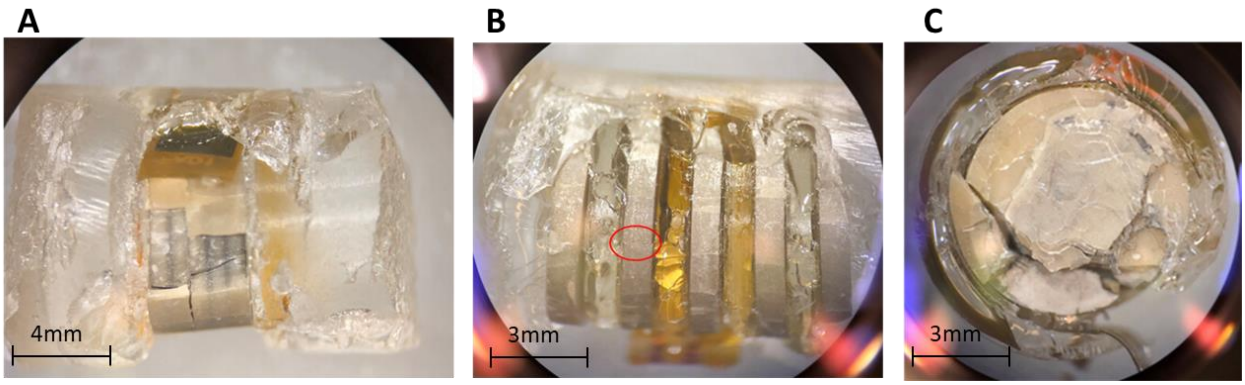


**Figure 49.** Internal views of PZT configurations after 100,000 cycles. A. Crack propagation through a C1 stack, side view. B. Crack in one PZT disc show in a C2 CLACS stack, side view. C. Gross mechanical failure of C3 stack, top view.

In traditional composites fatigue testing, the low cycle fatigue limit is considered a reliability estimate for safety, insurance risks and life cycle estimates (Harik and Bogetti, 2003). The stress-life (S-N) approach for fatigue analysis is used primarily for materials screening and is useful for initial process of materials selection of implant materials subjected to high cyclic loading conditions, as seen in all orthopedic implants (Teoh, 2000). Fatigue behavior of piezoelectric stacks has also been analyzed using this approach (Platt *et al.*, 2005). For these reasons, the S-N approach was used to assess the fatigue resistance of the three configurations of implant designs. The results of this study illustrate the mechanisms of premature failure within the different stack types and a clear necessity to consider both electrical and mechanical resistance to fatigue, to prevent brittle failure of the piezoelectric stacks. It will also be critical to ensure a complete encapsulation of the PZT ceramic to prevent crack propagation through the external implant design.

All three PZT configurations produced sufficient power (>30µW) under simulated walking loads to supply bone healing DC power through a rectifying circuit. Although different manufacturing processes, power densities in this study compare to similar studies assessing power generation of PZT stacks in spinal fusion implants (Cadel *et al.*, 2018). In order to deliver

appropriate DC current density levels through an attached electrode, a rectifying and conditioning circuit will be necessary to convert the AC voltage produced by the PZT in response to cyclic loads to a DC negative signal. The circuit design and subsequent resistance will be an important consideration when designing the most efficient PZT generator with a matched impedance. As the number of layers in a cofired PZT stack and CLACS increases, the resistance at which maximum power occurs decreases (Cadel *et al.*, 2018; Platt *et al.*, 2005). Thus, circuit design should also influence the selection of the most effective PZT configuration in final implant design.

The use of a piezocomposite within an implant provides an integrative approach to stimulate bone healing. Piezoelectric materials only produce power under cyclic loading, and that rectified power would stimulate an additional bone healing response. However, if the implant is not cyclically loaded or the stack can no longer produce sufficient power, the implant will still function as a standard interbody implant, providing stabilization at the fusion site. As proven here in C1 and C2 electrical fatigue performance, power is expected even after years of cyclic loading of the implant. However, because the electrical stimulation would be an addition to the mechanical stabilization provided by the implant, the mechanical behavior of the material is more critical as it could affect adverse patient outcomes. All three configurations studied in this work exceeded expected mechanical performance. These results validate the use of piezocomposites as load bearing power generators within implants.

Fatigue of PEEK biomaterials has primarily been approached in the context of specific implant designs (Kurtz and Devine, 2007), and the goal of this study was to give rationale for final implant design by elucidating early failure mechanisms of the proposed design configurations. The loads used in this study were considerably high loads for this test and were

only used to assess the gross failure of the three configuration designs. The most common failure in spinal fusion interbody implants occurs at the insertion mechanism (Peck *et al.*, 2018). This study purposely removed mechanical stress concentrations (i.e. insertion points) to best understand the failure modes related to the material interfaces. However, future studies should account for both material interfaces and mechanical stress concentrations. Repeat testing of the final implant design and PZT configuration at reasonable loads and longer cycles will need to be completed to characterize mechanical and electrical fatigue of final implant designs.

## Conclusions

A piezoelectrically powered implant as proposed here would eliminate the need for a battery pack, decreasing potential for infection, substantially decreasing cost for patients, hospitals and insurance companies, and eliminating the need for a second surgery. Higher risk of infection, secondary wound healing issues and repetitive intervention decrease value of current internal electrical stimulation devices. Although current methods of providing DC stimulation have shown clinical efficacy, the drawbacks of current clinical devices have resulted in limited though they have potential success for helping patients heal. This study compared the power production and fatigue resistance of three PZT configurations in a modified implant design. All configurations produced enough power to supply bone healing DC stimulation under walking loads and mechanically passed in fatigue. Thus, fatigue is not the limiting factor in PZT configuration design. Future PZT generator design decisions can be based on power requirements and DC output acceptance criteria, although as demonstrated, microscopic failure could be an issue to consider. Because of their adaptability, PZT stacks able to withstand physiological loads and electrically adjusted to enhance effectiveness at low frequencies would

allow successful incorporation into orthopedic implants to provide internal DC stimulation at the healing site without a battery pack and could address a large clinical need.

Acknowledgements

This work was supported by an NIH STTR Phase II grant (R44AR070088). The authors would also like to thank the Madison and Lila Self Graduate Fellowship for generous funding of graduate research at The University of Kansas.

References

Arshad, R., Angelini, L., Zander, T., Di Puccio, F., El-Rich, M., Schmidt, H., 2017. Spinal loads and trunk muscles forces during level walking – A combined in vivo and in silico study on six subjects. Journal of Biomechanics. https://doi.org/10.1016/j.jbiomech.2017.08.020

ASTM F2077-18, Test Methods for Intervertebral Body Fusion Devices, ASTM International, West Conshohocken, PA, 2018, www.astm.org

Berman, D., Oren, J.H., Bendo, J., Spivak, J., 2017. The Effect of Smoking on Spinal Fusion. Int J Spine Surg 11. https://doi.org/10.14444/4029

Bhandari, M., Fong, K., Sprague, S., Williams, D., Petrisor, B., 2012. Variability in the definition and perceived causes of delayed unions and nonunions: a cross-sectional, multinational survey of orthopaedic surgeons. J Bone Joint Surg Am 94, e1091-1096. https://doi.org/10.2106/JBJS.K.01344

Browne, J.A., Cook, C., Pietrobon, R., Bethel, M.A., Richardson, W.J., 2007. Diabetes and Early Postoperative Outcomes Following Lumbar Fusion. Spine 32, 2214. https://doi.org/10.1097/BRS.0b013e31814b1bc0

Cadel, E.S., Frazer, L.L., Krech, E.D., Fischer, K.J., Friis, E.A., 2019. Analysis of how compliant layers and encapsulation affect power generated from piezoelectric stacked composites for bone healing medical devices. J Biomed Mater Res A 107, 2610–2618. https://doi.org/10.1002/jbm.a.36767

Cadel, E.S., Krech, E.D., Arnold, P.M., Friis, E.A., 2018. Stacked PZT Discs Generate Necessary Power for Bone Healing through Electrical Stimulation in a Composite Spinal Fusion Implant. Bioengineering 5, 90. https://doi.org/10.3390/bioengineering5040090

Chung, H.Y., Machado, P., van der Heijde, D., D'Agostino, M.-A., Dougados, M., 2012. Smokers in early axial spondyloarthritis have earlier disease onset, more disease activity, inflammation and damage, and poorer function and health-related quality of life: results from the DESIR cohort. Ann. Rheum. Dis. 71, 809–816. https://doi.org/10.1136/annrheumdis-2011-200180

Cromwell, R., Schultz, A.B., Beck, R., Warwick, D., 1989. Loads on the lumbar trunk during level walking. J. Orthop. Res. 7, 371–377. https://doi.org/10.1002/jor.1100070309

Deyo, R.A., 2015. Fusion surgery for lumbar degenerative disc disease: still more questions than answers. The Spine Journal 15, 272–274. https://doi.org/10.1016/j.spinee.2014.11.004

Einhorn, T.A., 1995. Enhancement of fracture-healing. Journal of Bone 77, 940–956.

Ekegren, C.L., Edwards, E.R., de Steiger, R., Gabbe, B.J., 2018. Incidence, Costs and Predictors of Non-Union, Delayed Union and Mal-Union Following Long Bone Fracture. Int J Environ Res Public Health 15. https://doi.org/10.3390/ijerph15122845

Feenstra, J., Granstrom, J., Sodano, H., 2008. Energy harvesting through a backpack employing a mechanically amplified piezoelectric stack. Mechanical Systems and Signal Processing 22, 721–734. https://doi.org/10.1016/j.ymssp.2007.09.015

Fingar, K. (Truven H.A., Stocs, C. (AHRQ), Weiss, A. (Truven H.A., Steiner, C. (AHRQ), 2014. Most Frequent Operation Room Procedures Performed in U.S. Hospitals, 2003-2012 (HCUP Statistical Brief #186). Agency for Helathcare Research and Quality, Rockville, MD.

Friis, E., Galvis, S., Arnold, P., 2015. DC Stimulation for Spinal Fusion with a Piezoelectric Composite Material Interbody Implant: An Ovine Pilot Study.

Gan, J.C., Glazer, P.A., 2006. Electrical stimulation therapies for spinal fusions: current concepts. Eur Spine J 15, 1301–1311. https://doi.org/10.1007/s00586-006-0087-y

Geerlings, S.E., Hoepelman, A.I., 1999. Immune dysfunction in patients with diabetes mellitus (DM). FEMS Immunol. Med. Microbiol. 26, 259–265. https://doi.org/10.1111/j.1574-695X.1999.tb01397.x

Goetzinger, N.C., Tobaben, E.J., Domann, J.P., Arnold, P.M., Friis, E.A., 2016. Composite piezoelectric spinal fusion implant: Effects of stacked generators. J. Biomed. Mater. Res. 104, 158–164. https://doi.org/10.1002/jbm.b.33365

Harik, V.M., Bogetti, T.A., 2003. Low Cycle Fatigue of Composite Laminates: A Damage-mode-sensitive Model. Journal of Composite Materials 37, 597–610. https://doi.org/10.1177/002199803029731

Jaffe, B., Cook jr., W.R., Jaffe, H., 1971. CHAPTER 12 - APPLICATIONS OF PIEZOELECTRIC CERAMICS, in: Piezoelectric Ceramics. Academic Press, pp. 271–280. https://doi.org/10.1016/B978-0-12-379550-2.50016-8

Jen, M.-H.R., Lee, C.-H., 1998. Strength and life in thermoplastic composite laminates under static and fatigue loads. Part I: Experimental. International Journal of Fatigue 20, 605–615. https://doi.org/10.1016/S0142-1123(98)00029-2

Knox, B., Chapman, T., 1993. Anterior Lumbar Interbody Fusion for Discogram Concordant Pain. Journal of Spinal Disorders 6, 242–244.

Krech, Ember D., Barrett, R.M., Cadel, E.S., Friis, E.A., 2018. Power Generation Amplification and Stack Toughening via Compliant Layer Interdigitation V002T07A010. https://doi.org/10.1115/SMASIS2018-8043

Krech, E. D., Cadel, E.S., Barrett, R.M., Friis, E.A., 2018. Effect of compliant layers within piezoelectric composites on power generation providing electrical stimulation in low frequency applications. Journal of the Mechanical Behavior of Biomedical Materials 88, 340–345. https://doi.org/10.1016/j.jmbbm.2018.08.027

Kurtz, S.M., Devine, J.N., 2007. PEEK Biomaterials in Trauma, Orthopedic, and Spinal Implants. Biomaterials 28, 4845–4869. https://doi.org/10.1016/j.biomaterials.2007.07.013

Kwiatkowski, T.C., Hanley, E.N., Ramp, W.K., 1996. Cigarette smoking and its orthopedic consequences. Am J. Orthop. 25, 590–597.

Kymissis, J., Kendall, C., Paradiso, J., Gershenfeld, N., 1998. Parasitic power harvesting in shoes, in: Digest of Papers. Second International Symposium on Wearable Computers (Cat. No.98EX215). Presented at the Digest of Papers. Second International Symposium on Wearable Computers (Cat. No.98EX215), pp. 132–139. https://doi.org/10.1109/ISWC.1998.729539

Lee, W.-T., Koak, J.-Y., Lim, Y.-J., Kim, S.-K., Kwon, H.-B., Kim, M.-J., 2012. Stress shielding and fatigue limits of poly-ether-ether-ketone dental implants. J. Biomed. Mater. Res. Part B Appl. Biomater. 100, 1044–1052. https://doi.org/10.1002/jbm.b.32669

Li, H., Tian, C., Deng, Z.D., 2014. Energy harvesting from low frequency applications using piezoelectric materials. Applied Physics Reviews 1, 041301. https://doi.org/10.1063/1.4900845

Marin, C., Luyten, F.P., Van der Schueren, B., Kerckhofs, G., Vandamme, K., 2018. The Impact of Type 2 Diabetes on Bone Fracture Healing. Front Endocrinol (Lausanne) 9, 6. https://doi.org/10.3389/fendo.2018.00006

Martin, B.I., Mirza, S.K., Comstock, B.A., Gray, D.T., Kreuter, W., Deyo, R.A., 2007. Are Lumbar Spine Reoperation Rates Falling With Greater Use of Fusion Surgery and New Surgical Technology? Spine 32, 2119–2126. https://doi.org/10.1097/BRS.0b013e318145a56a

Paterson, D.C., Lewis, G.N., Cass, C.A., 1980. Treatment of delayed union and nonunion with an implanted direct current stimulator. Clin. Orthop. Relat. Res. 117–128.
Peck, J.H., Kavlock, K.D., Showalter, B.L., Ferrell, B.M., Peck, D.G., Dmitriev, A.E., 2018. Mechanical performance of lumbar intervertebral body fusion devices: An analysis of data submitted to the Food and Drug Administration. Journal of Biomechanics 78, 87–93. https://doi.org/10.1016/j.jbiomech.2018.07.022
Platt, S.R., Farritor, S., Haider, H., 2005. On low-frequency electric power generation with PZT ceramics. IEEE/ASME Transactions on Mechatronics 10, 240–252. https://doi.org/10.1109/TMECH.2005.844704
Rae, P.J., Brown, E.N., Orler, E.B., 2007. The mechanical properties of poly(ether-ether-ketone) (PEEK) with emphasis on the large compressive strain response. Polymer 48, 598–615. https://doi.org/10.1016/j.polymer.2006.11.032
Saxena, A., DiDomenico, L.A., Widtfeldt, A., Adams, T., Kim, W., 2005. Implantable Electrical Bone Stimulation for Arthrodeses of the Foot and Ankle in High-Risk Patients: A Multicenter Study. The Journal of Foot and Ankle Surgery 44, 450–454. https://doi.org/10.1053/j.jfas.2005.07.018
Tejano, N.A., Puno, R., Ignacio, J.M., 1996. The use of implantable direct current stimulation in multilevel spinal fusion without instrumentation. A prospective clinical and radiographic evaluation with long-term follow-up. Spine 21, 1904–1908.
Teoh, S.H., 2000. Fatigue of biomaterials: a review. International Journal of Fatigue 22, 825–837. https://doi.org/10.1016/S0142-1123(00)00052-9
Tzioupis, C., Giannoudis, P.V., 2007. Prevalence of long-bone non-unions. Injury 38 Suppl 2, S3-9.
van den Ende, D.A., Bos, B., Groen, W.A., Dortmans, L.M.J.G., 2009. Lifetime of piezoceramic multilayer actuators: Interplay of material properties and actuator design. J Electroceram 22, 163–170. https://doi.org/10.1007/s10832-007-9411-0
Vo, N., Wang, D., Sowa, G., Witt, W., Ngo, K., Coelho, P., Bedison, R., Byer, B., Studer, R., Lee, J., Di, Y.P., Kang, J., n.d. Differential effects of nicotine and tobacco smoke condensate on human annulus fibrosus cell metabolism. Journal of Orthopaedic Research 29, 1585–1591. https://doi.org/10.1002/jor.21417

## Chapter 7: Conclusions and Future Work

### Major Findings and Conclusions

The motivation of this research was to further develop a practical solution to address the costly and rising incidence of failed fusion and nonunions resulting from orthopedic procedures and delayed or incomplete bone healing. Developed from an understanding of electrical potentials regulating healthy bone growth and regeneration, electrical stimulation devices were designed to stimulate the bone healing process. Although methods of providing direct current (DC) stimulation have shown clinical efficacy, the drawbacks of present devices have limited use and potential success in helping patients heal. A piezoelectrically powered implant as proposed here would eliminate the need for a battery pack, decreasing potential for infection, substantially decreasing cost for patients, hospitals and insurance companies, and eliminating the need for a second surgery. Building on the preclinical success of a stacked piezocomposite spinal fusion implant, compliant layer adaptive composite stacks (CLACS), and later mixed-mode CLACS (MMCLACS) were designed to address the scalability issues of piezoelectric fiber composites, while providing a more efficient power generation biomaterial that could resist fatigue and be adapted to incorporate within standard orthopedic implants.

#### *CLACS*

Chapters 3 and 4 present an assessment of CLACS as a load-bearing piezocomposite biomaterial that combines the benefits of stacked piezoelectric elements with composite materials research to improve mechanical properties and increase power generation at physiologic loads and frequencies. The addition of the compliant layer interdigitated between PZT discs within a stack increased power generation, and as the thickness of that layer increased power also increased. The experimental and theoretical analysis of CLACS illustrate the unique structure and mechanics of the novel approach to increase power generation at low frequencies.

Electrically, this technique utilizes principles of piezoelectric stacked generators to lower source impedance, while also increasing lateral strain on the piezoelectric elements due to compliant layer expansion, increasing power output. Mechanically, the toughened piezocomposite will more closely match the compliance of bone to prevent stress shielding and resist brittle fatigue failure of the implant. The significant power amplification of CLACS will allow small stacks to be included within existing orthopedic implant shapes, while still generating enough power to provide electric stimulation to the gap healing site. This will not change surgical techniques or require development of new instrumentation, increasing likelihood of clinician adoption.

*MMCLACS*

In Chapter 5 MMCLACS were proposed and initially investigated. Utilizing the understanding of the CLACS structure, the effect of poling direction on power generation was investigated under multiaxial loads. The unique layup of CLACS allows individual elements with varying poling directions to be connected electrically in parallel, creating a novel power generation structure. The functional performance of MMCLACS was validated, showing the impact of poling direction on power generation. Under compressive loads, a mixed stack of alternating radially poled and through-thickness poled discs increased power generation as compared to a CLACS stack consisting of all through-thickness poled or radially poled discs. Torsional loads produced limited power, but design would need to be optimized for use in most applications.

MMCLACS produce more power than traditional CLACS under compressive loads. This additional increase in power could aid in the design of implants in which higher power densities are needed due to larger electrode surface areas or lower load amplitudes or frequencies. Because

minimal power was produced in torsion, implants should be designed to apply purely dynamic compressive loads on the piezocomposite insert of the implant in order to generate sufficient power for electrical stimulation. Additionally, an MMCLACS structure may produce more power under alternate mechanical loading conditions, like ultrasound. Many patients are non-weight bearing following orthopedic procedures, and ultrasound could be used during this time to produce power from the implant and start the healing process. The increase in efficiency seen in MMCLACS and the ability to tailor poling direction could be optimized to generate usable power from ultrasound loading and walking loads.

*Fatigue*

Chapter 6 compared the power production and fatigue resistance of three PZT configurations in a modified implant design. All configurations produced enough power to supply bone healing DC stimulation under simulated walking loads and mechanically passed the fatigue test. Thus, fatigue is not the limiting factor in PZT configuration design. Future PZT generator design decisions can be based on power requirements and DC output acceptance criteria, although as demonstrated, microscopic failure could be an issue to consider. Commercially fabricated CLACS significantly increased power generation, as is consistent with previous findings. Additionally, CLACS showed promising fatigue resistance properties, although manufacturing methods should be improved and standardized to decrease variability. Because of their adaptability, PZT stacks able to withstand physiological loads and electrically adjusted to enhance effectiveness at low frequencies would allow successful incorporation into orthopedic implants to provide internal DC stimulation at the healing site without a battery pack and could address a large clinical need.

*Energy Harvesting Potential*

Both CLACS and MMCLACS were originally designed for use in implants as a lower impedance piezoelectric material and structural load bearing element in mechanical design. However, as demonstrated in this work, they also exhibit an originally unexpected and significant increase in power generation compared to traditional cofired stacks without compliant layers. For a given volume of PZT, CLACS produced over 60% more power than industry standard cofired stacks, and MMCLACS produced and additional 20% more than CLACS. This level of power generation enhancement is not common in the field, especially at such low frequencies so far below resonance. Other methods for increasing power generation at low frequencies, primarily benders, are limited in their efficiency and design restrictions inhibit incorporation into structural design.

The higher power densities generated from CLACS and MMCLACS suggest that wide and varied use of this technology could greatly increase efficiency of energy harvesting from human motion, roadways, wearables, wind energy, etc. The ability to overcome efficiency losses due to frequency mismatches provides a promising route for further exploration and a practical material for energy harvesting implementation utilizing existing devices and technology. The CLACS and MMCLACS innovations presented in this work provide a novel solution for more effective energy harvesting and power generation and open up design and translation opportunities.

## Future Work

*CLACS Modeling and Optimization*

This work presents the initial design and experimental characterization of the CLACS and MMCLACS technology. Although initially investigated, the mechanisms underlying the

additional charge generation due to the compliant layer expansion and mixed poling directions are not fully understood. As such, a comprehensive finite element model (FEM) should be created, including both a mechanical strain analysis and a piezoelectric property analysis. Further work characterizing and defining relationships of PZT disc/compliant layer aspect ratio and stiffness could generate an ideal composition for desired applications. It is likely that a specific compliant layer material and thickness would optimize power generation of CLACS and MMCLACS and should be further explored.

The amplification factor presented in Chapter 4 illustrates the relationship of the piezoelectric properties and the stiffness ratio between the compliant layer the PZT on power generation. These ratios could be optimized to balance both mechanical strength of the overall structure and power generation efficiency. Because the addition of the compliant layer increases strain generation in the piezoelectric material, there could be a risk of de-poling the PZT under high loads or frequencies. Consequently, the relationship between the stiffness of the two materials should be investigated in depth, concluding what the optimal range is to most effectively increase power generation without de-poling the piezoelectric material. Similarly, the aspect ratio of the PZT elements likely influences the power amplification and could also be optimized utilizing an FEM approach.

The PZT elements studied in this work spanned both hard and soft PZT materials and two poling directions, demonstrating the versatility of CLACS power amplification across PZT types and poling directions. However, the analysis was only completed at low frequencies. Future experimental work should investigate the relationship between frequency and the compliant layer thickness and material properties. The data suggests that there may be a frequency below resonance that the effect of the compliant layer becomes negligible. PZT discs were utilized in

this study, but other forms of PZT elements, like rings, should be investigated. The mechanical deformation of such structures differs from discs, and could change the effect of CLACS, though it is expected that there would be a similar power generation amplification due to the increased strain.

Although this work was focused on initial characterization, further work should explore ability of MMCLACS to produce power from cyclic tensile loads, something that is not possible for traditional piezoceramic energy harvesting devices. The MMCLACS configurations presented in this work are conceptual constructions that are not yet optimized to achieve maximum overall combined power generation from addition of compliant layers and mixed poling directions. This work presents one possible configuration of alternating poling directions, but several other approaches can be imagined, capitalizing on disc position within the stack and incorporating overall device structure into design decisions. An elaborate finite element analysis of both conventional CLACS and MMCLACS is of great interest, is under way, and left for further investigation.

*Implant Design*

The primary focus of this dissertation that led to the invention of CLACS was to develop a scalable, efficient biomaterial that could be included in multiple implants as a piezoelectric generator. As such, the efficiency of power generation is a critical design constraint because volume of piezoelectric material is limited by certain implant shapes and sizes. The power generation must be balanced by the fatigue resistance of the material required of a robust biomaterial. It was proven that CLACS and MMCLACS can be utilized as a mechanism to increase power generation capability of the material for inclusion into multiple implant types. However, the standard industry manufacturing practices of PZT stacks would need to be adjusted

to reliably fabricate CLACS. Early commercial manufacturing techniques were developed and validated in Chapter 6, but further refinement of those processes would be required for large scale manufacturing of this material, and should be investigated. Quality control systems would be critical for adoption as a trusted biomaterial for use in implants.

Fatigue resistance of CLACS was proven at high loads and predicted promising runout potential. A future study should assess the fatigue resistance of the final implant design under more reasonable loads for the full five million cycles according to ASTM standards. In addition, a full mechanical property analysis should be completed for incorporation within other orthopedic implants, especially bending and impact testing. If impact resistance of CLACS is an issue, coefficient of thermal expansion pre-compression techniques could be explored as a way to incorporate power amplification and impact resistance. Moving forward with implant design, the full battery of ASTM and ISO biocompatibility tests should be completed on the piezocomposites incorporated into each implant design.

The next step in implant design is to fully integrate the piezocomposite generator and accompanying circuit into existing implant designs. Once that development process is complete, preclinical studies should be completed and compared to the initial pilot study results to verify the changes in the piezocomposite and circuit design match the promising bone growth results. In addition, the final implant designs will need to be developed in tandem with regulatory considerations so FDA clearance and reimbursement strategies are aligned with the product development cycle. The results presented in this dissertation provide promising feasibility results for piezocomposites, specifically CLACS to be used as a power generation material within implants to stimulate bone growth and improve patient outcomes, though the further development of this platform technology could lead the charge in energy harvesting.

# Appendices

## Appendix A: CLACS Fabrication Protocols

### Disc Electrical Connection Protocol

*Always wear gloves and work on a clean surface. Avoid touching the discs with your fingers as much as possible. Be VERY careful not to scratch the fired-on silver electrode off the surfaces of the discs.

1. Test the poling direction of each disc
    a. Using a voltmeter, turn it to DC voltage.
    b. Place a piece of aluminum sheet metal on a flat surface.
    c. Place a PZT disc on the sheet. Be sure the bottom electrode of the disc is touching the metal sheet. The sheet is now electrically connected to the bottom electrode.
    d. ***GENTLY*** touch one of the leads to the top of the disc and the other on the metal sheet.
    e. Lean over, and exhale with a quick puff of air over the disc.
    f. Read the voltage on the voltmeter. If the positive lead from the voltmeter is touching the top of the disc AND the voltage is positive, as seen in the figure below, mark the top of the disc. This is the positive side. Conversely, if the positive (black) lead is touching the top of the disc, and the voltage is negative, you will mark the bottom side of the disc.
    g. Repeat this for each disc.

    NOTE: some of the discs will have a red dot on them from the manufacturer. These often bleed through to adjacent discs in the package, so do NOT assume that the sides with the red dot are all positive.

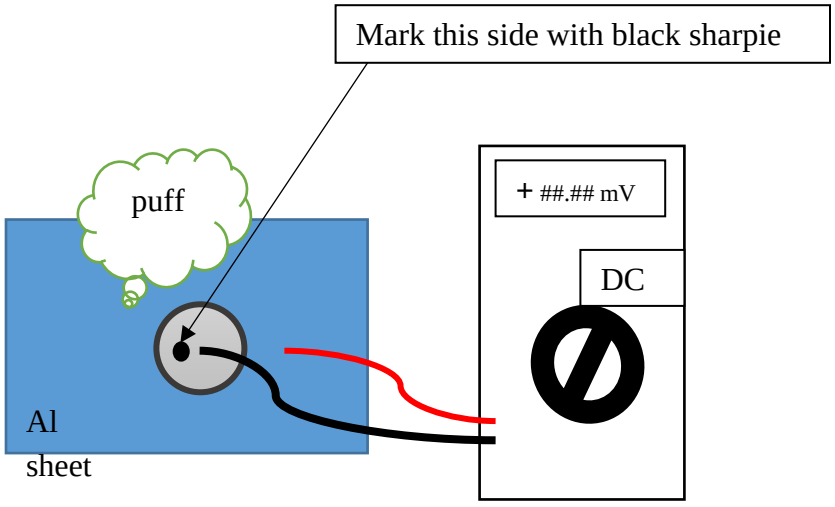


2. Using the thick copper foil, cut two strips for each specimen. They should be about 6-8 inches long and 1/16 in thick. Clean with rubbing alcohol
    a. Make sure your strips are no crinkled and are straight!

3. Place a 3inch piece of red silicone, shiny side up on a long piece of delrin. Tape it down on the edges. Place a 1/2inch circle silicone stencil on top of the other piece of silicone. Clean both with rubbing alcohol.
4. Place one of the copper strips between the two pieces of silicone in the top third of the circle. You should be able to see a tiny bit of each circle on top of the strip. Tape the ends of the strip down. See the figure below.

   NOTE: it is much easier to cut the copper strips after encapsulation, so making them a little longer than you think is never a bad idea.

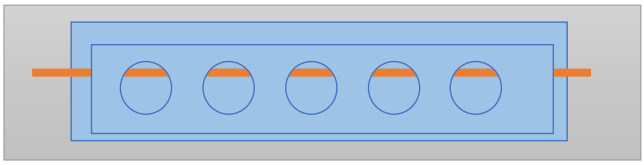

5. If there is not a batch of conductive epoxy made, make a batch. If there is one in the freezer, be sure to pull it out and let it thaw for about 10 minutes.
6. Spread a generous amount of conductive epoxy on the copper strip in each circle cut out.
   a. It is VERY important that you do not get any conductive epoxy on the inside edges of the silicone. Wipe it off immediately with a q-tip if you do.
   b. You want enough epoxy so that the discs are successfully adhered to the copper strip, but not too much so that it smears around the edge and connects the top and bottom electrodes. Ask if you are not sure!

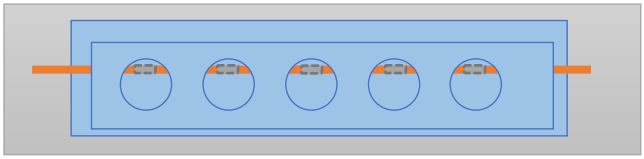

7. Carefully place the discs inside the holes. Be sure that all the positive marked sides are facing up.
   a. It is CRITICAL that you electrically connect all the positive sides and all the negative sides separately. Don't forget to test the poling direction as described above, mark the positive side, and place each disc with the positive side up!
   b. The holes in the silicone are significantly larger than the discs. It is easiest to align each disc so that it is touching the top of the hole. This ensures your connected discs will be straight and in a line.
   c. Try to align all the black dots toward the bottom. See figure below. You should try to cover the dots with the epoxy so they do not smear off during encapsulation.

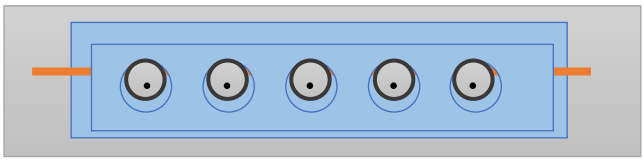

8. Take the second copper strip and align it on the bottom third of the discs – covering the black dots. Be sure that the copper strips will not touch when you fold the specimen.
   a. It is easier to tape one side and then fold it out of the way. Make sure you mark where you need to smear the conductive epoxy.

9. Use tweezers to lightly press the discs down and spread conductive epoxy on the bottom of the circle to connect tops of the discs and the second copper strip.
    a. Be gentle! Don't scratch the electrode off with your tweezers.
    b. Be careful not to let the epoxy smear down around the edges.

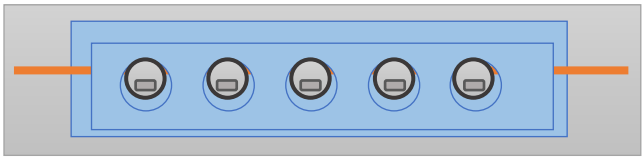

10. Carefully align the copper strip with the conductive epoxy and press down so that is sticks to each slice.
    a. The slices are thinner than the silicone. It is SUPER important that you leave some slack on the copper strip, so that it can deform and adhere to the discs.
        i. DO NOT PULL THE STRIP TAUGHT!

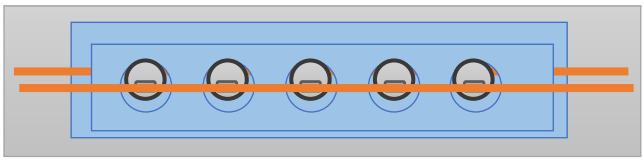

11. Cover each disc with a silicone circle, shiny side down toward the disc.
    a. Press the circle firmly into the hole in the silicone to be sure that the conductive epoxy, copper strips and discs all adhere together.

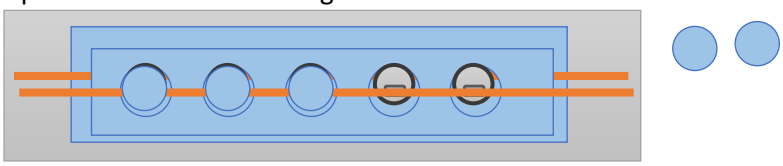

12. Place a weight (a long piece of steel or other metal by the oven) on top of the assembly.
    a. Be sure the weight is covering each of the discs. Add extra weight if you think there is a chance the discs and copper may not adhere.

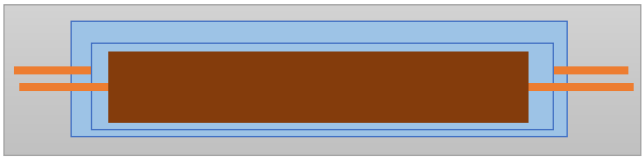

13. Cure in the oven at 100°C for 2 hours.
    a. If you need a shorter cure time, refer to the EpoTek spec sheet. 120°C for 30 minutes usually works as well.
14. Pull it out of the oven, and let it cool.
15. Carefully remove the silicone stencil from the connected discs. There is a slit through the middle of each one. Separate the sides and pull out from in between the copper strips.
    a. Be very careful not to pull up on the copper strips when taking off the molds and the tape.
16. Test the connected discs electrically to make sure everything is connected properly.

a. Test that the positive and negative electrodes are not connected. When the leads from the voltmeter are touching each one, the resistance should read overload. See figure below.

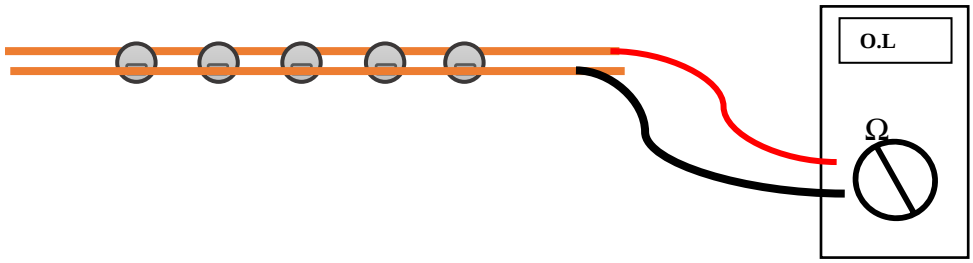


b. Check that each electrode is successfully connected to each disc. When one lead is touching the copper strip and the other lead is touching a disc, the resistance should be very low. See figure below.
c. Check both sides and each disc.

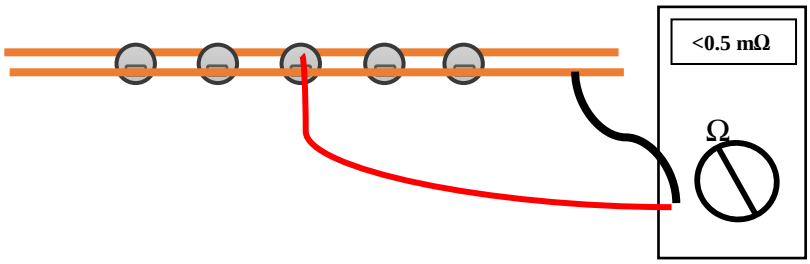

**Disc Stacking Protocol**

*Always wear gloves and work on a clean surface. Avoid touching the discs with your fingers as much as possible. Be VERY careful not to scratch the fired-on silver electrode off the surfaces of the discs.

1. Double check that all the electrical connections are sound, that each copper strip is securely adhered to each disc, and that the positive and negative electrodes are not touching.
    a. See Disc Electrical Connection Protocol for testing method.
2. Make a batch of neat epoxy. The lease amount possible (5g).
    a. You will need to mix this epoxy, and let it sit for at least 2 hours to get goopy. If you need epoxy for something else, make some and just let a little set out for the 2 hours.
    b. Once it gets goopy enough, you have about 30 minutes until it is too sticky to work with. Be sure you have everything ready to go so that you can finish accordingly.
3. Fold the discs, accordion style.
    a. With a spatula, press down lightly, just to the right of disc 1.
        i. You want to place the spatula carefully so that when you fold, the copper creases directly in the middle of the space between discs 1 and 2. The outer edge should be in the middle of the space between the two discs.
    b. Pick up the strips to the right of disc 5 and fold over, from right to left, so that the top of disc 1 is touching the top of disc 2.
        i. ALIGN THE DISCS AS BEST AS POSSIBLE!
    c. Continue this process, as shown below, each time placing the spatula just to the right/left of the disc you are folding on top of, see placement below.

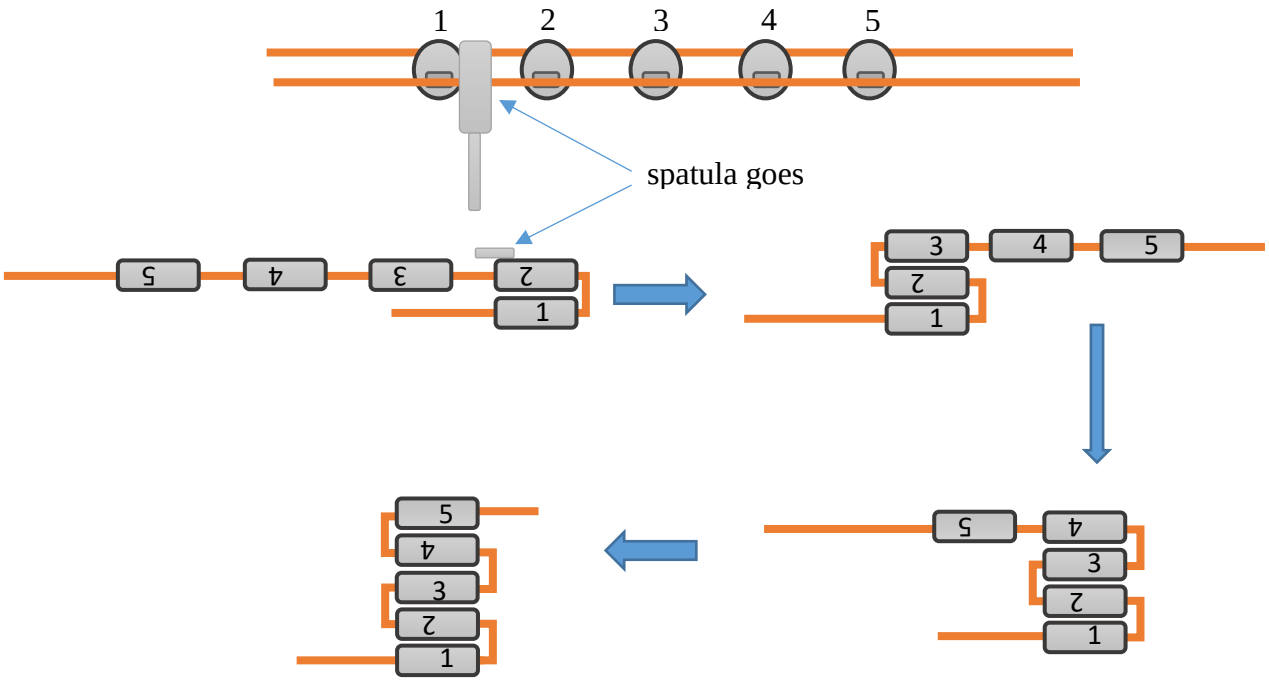


4. Crease each of the copper folds with tweezers so that the stack stays together.
5. Cut the extra electrode (inside) off the top of disc 1 and the bottom of disc 5.

a. They need to be removed for proper encapsulation, and to ensure that the two electrodes do not touch and short the specimen.
b. You are leaving the copper strip that is on the outside of the stack. Use scissors to cut, as close to the edge of the disc as possible, the copper strip that is on the inside of each slice. See figure below.
    i. Make sure that the cut edges that curl up a bit, do not bend up and touch the opposite electrode.

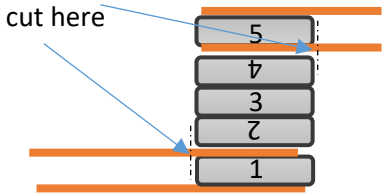


6. Using the goopy epoxy (2 hours post mixing), you are going to adhere the stack together. If you are NOT adding cured epoxy slices in between the discs, follow the next step. IF you ARE separating the discs with cured epoxy slices, skip to step 9.
7. Using a spatula, spread a VERY thin layer of the goopy epoxy in between each disc.
    a. You want just enough to adhere the discs together. Do NOT put a glob of epoxy on the discs.
    b. The epoxy should be viscous enough that it stays just in between the discs and does not flow over the edges.

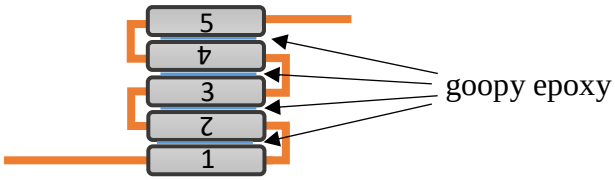


8. Once the epoxy is in between each disc, carefully align the discs. Place the stack on a piece of red silicone. Place a large red silicone circle on the top of a stack, and then place a few nuts on top to ensure all the discs will be adhered together. Leave to cure for ~5-6 hours.
    a. The shiny side of the silicone circles will stick to the nut. This will be easier to balance on top. If you need to put some stabilizing blocks on the sides of the stack to make sure that it stays straight, please do.
    b. There may be some uneven gaps between the discs due to globs of conductive epoxy. Just make sure there is enough epoxy that the discs will adhere as one unit.

*THE STACK NEEDS TO BE STRAIGHT AND ALIGNED!

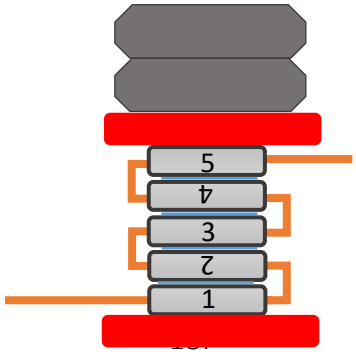

9. If you are placing cured epoxy slices between each disc, make sure you have recorded the thickness of each slice and calculated an average and standard deviation.
    a. Spread a VERY thin layer of goopy epoxy in between each disc (top and bottom of adjacent discs).
    b. Slide the cured epoxy slice in between the discs.
        i. Don't worry too much about alignment at this point. The slice will move around. You will align at the end.
    c. Continue to spread epoxy and slide in the slices in between each disc.
    d. After the last slice is placed between disc 4 and 5, align the edges of the epoxy slices. The piezo discs should be centered on the square epoxy slices, and all the epoxy slices should be aligned.
        i. It is easiest to align them with your fingers, and then use tweezers and squeeze lightly on either side, to ensure they are perfectly aligned.
        NOTE: it is CRITICAL that the epoxy slices are *almost perfectly aligned for encapsulation. If they are crooked, the specimen will not fit in the encapsulation jig.
10. Place the stack on a piece of red silicone. Place a large red silicone circle on the top of a stack, and then place a few nuts on top to ensure all the discs will be adhered together. Leave to cure for ~5-6 hours.
    a. The shiny side of the silicone circles will stick to the nut. This will be easier to balance on top. If you need to put some stabilizing blocks on the sides of the stack to make sure that it stays straight, please do.

*THE STACK NEEDS TO BE STRAIGHT AND ALIGNED!

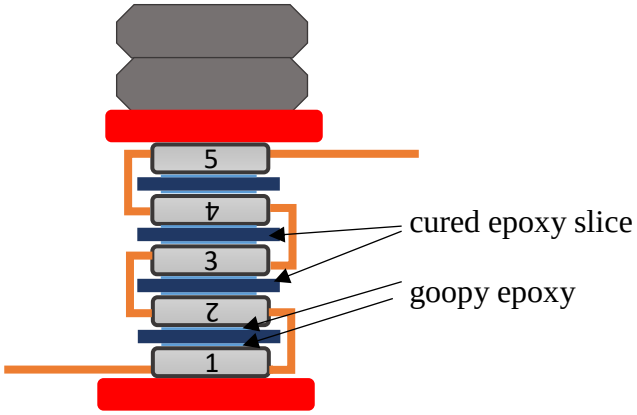


11. After ~6 hours, carefully remove the nuts and silicone. Check to make sure that the stack is still electrically connected properly.

**Disc Specimen Encapsulation Protocol**

*Always wear gloves and work on a clean surface. Avoid touching the discs with your fingers as much as possible. Be VERY careful not to scratch the fired-on silver electrode off the surfaces of the discs.

1. Clean each of the dragon skin molds with rubbing alcohol. Use a Qtip to get the inside and the top surface of the mold.
2. Make a batch of matrix epoxy.
    a. Be sure to mix properly.
3. Check each of the stacks to ensure they are connected properly electrically and mechanically adhered together.
4. Fold the longest copper strip back over itself, so that both strips are coming out of the same side of the stack.
    a. Fold the strip over itself with tweezers and crease the fold.

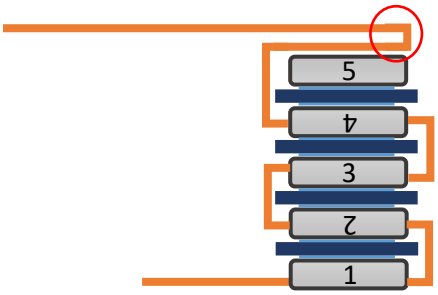


5. Using tweezers, carefully fold each of the copper folds on the sides of the stack so that they are touching the epoxy slices.
    a. Be sure that when you fold, you do not touch the top or bottom of any of the piezo discs. This will cause a short. Test electrically with voltmeter.

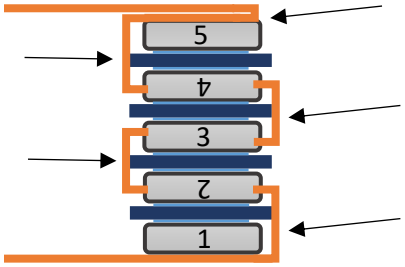


6. Using a syringe or a pipette, fill the dragon skin mold about 2/3 of the way with epoxy.
7. Place the stack into the mold, with the copper strips up.
    a. Be sure to push the stack all the way to the bottom. The epoxy slices are the same size as the cut out in the mold, so it should fit snugly.
    b. Try to make sure there is an equal amount of epoxy on the top and bottom of the stack.
    c. Make sure the discs are parallel with the top and bottom of the mold.
        i. The angle of the discs has a big effect on power output.

*MAKE SURE THE DISCS ARE PARALLEL WITH THE TOP AND BOTTOM OF THE MOLD!!!!

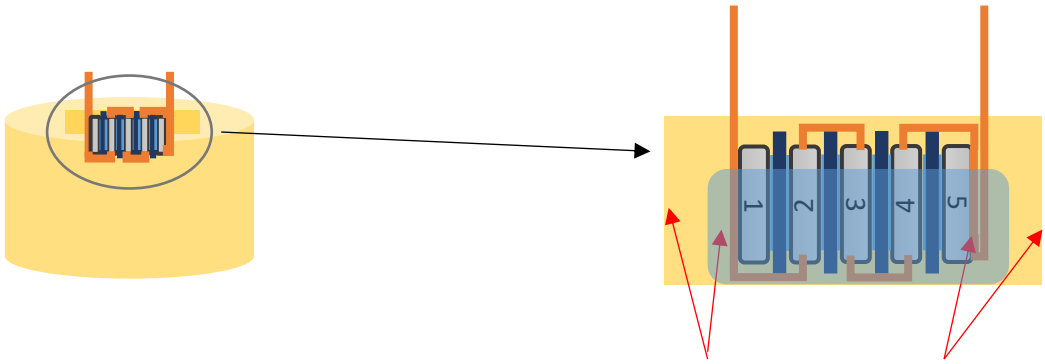


8. Using the syringe or pipette, add more epoxy until all the copper folds, epoxy slices and discs are covered.
    a. The epoxy may bubble up on the top a bit, that is okay.
    b. The epoxy may also spread around the opening, that is also okay. You can dremel off the edges to make sure the top and bottom are flat after curing.

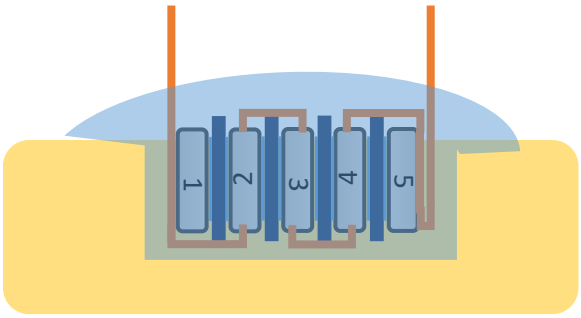


9. Using a T-pin or tweezers, try to pop all the air bubble that you can see in the epoxy.
    a. They often move towards the interface between the copper strips and the epoxy. Either pop them, or push them out to the edges.
10. Let cure for 24 hours at room temperature.
11. Place the molds in the oven at RT, turn on the oven to 65°C, and post cure for 2 hours.
12. Take the specimen out of the mold.
    a. Be sure to keep track of which specimen was cured in which mold.
13. You will most likely need to dremel off the edges of the epoxy that ran over so that all the faces are flat.
    a. *Carefully* use the dremel to sand off the edges.

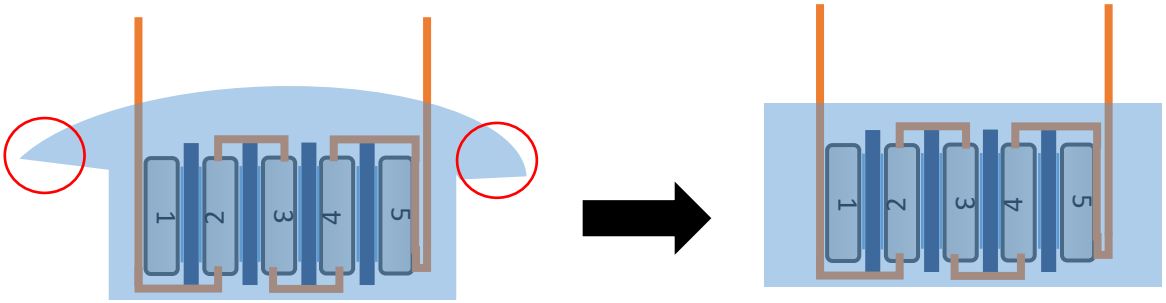

**Disc Electromechanical Testing Protocol**

*This test uses the MTS uniaxial machine. If you are not familiar with the function of the machine, please ask for help and make sure you know how to operate the machine and run the MPT software.

1. Turn on the MTS and start the Station Manager program. Run the Function Generator for about 30 minutes to allow the machine to warm up.
    a. Be sure that you follow the proper protocol and turn on the water to cool the machine. There is a checklist by the MTS computer – follow it!
    b. The machine should be warm to the touch. I usually touch the middle of the cross head.
2. Stop the Function Generator and open the MPT – Ember Piezo Testing file.
3. Open the Meters and Scope. This allows you to see the readings while you get everything set up and while you are testing.
4. Click the New Specimen button and type in the file name that you want the data to be saved under.
    a. The naming convention should be the following: 2017_05_03_TS45
        i. Where TS45 is the sample being tested
5. Unlock the cross head and move it down so that the top platen is about 3 inches above the bottom cross head. Lock down the nuts.
    a. BE SURE YOU LOCK THE CROSS HEAD IN PLACE!
        i. During testing you do not want the actuator fully extended. Adjust the height of the cross head accordingly.
6. Place a small piece of fine grit sand paper in the center of the bottom platen. Center the specimen on the sand paper. Place another small piece of sand paper, grit side down to the top of the specimen. See figure below.
    a. This ensures the specimen does not slip on the platens. Make sure the grit side of the pieces of sandpaper are on the specimen, NOT on the platens.

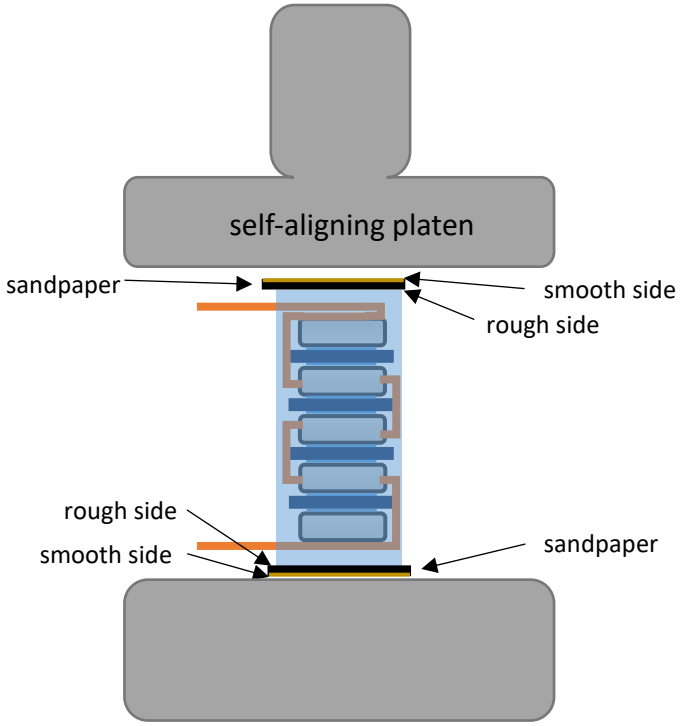

7. Using the Remote Station Control, slowly move the top platen down until it is about 2mm above the top of the specimen.
8. Zero the force and displacement using the Auto Offset button on the RSC.
9. Slowly move the top platen down and apply ~10-20N preload on the specimen.
    a. DO NOT MOVE QUICKLY! The force can jump up quickly once the platen is touching the top of the specimen.
    b. If the top platen looks very crooked, take the specimen out and sand down the uneven side. It is SUPER important that the specimen is flat, so that the loading across the top and bottom surfaces is equal.
10. Connect the positive and negative leads to the two copper strips on the specimen.
    a. Make sure the copper strips are NOT touching the metal platens. Also check to make sure the alligator clips are not touching.
        i. It is very helpful to tape the alligator clips to the side of the load cell so that they are not pulling on the copper strips. See figure below.
11. Clip the two green leads (the positive lead from the MTS and the other side of the green clip from the specimen) together. The figure below shows the set up for the beginning of the test.
    a. These will be the clips you clip to the resistors, but the first resistance in the sweep is zero.
    b. Make sure the metal clips are not touching the MTS. Put a piece of Teflon under them, if necessary.

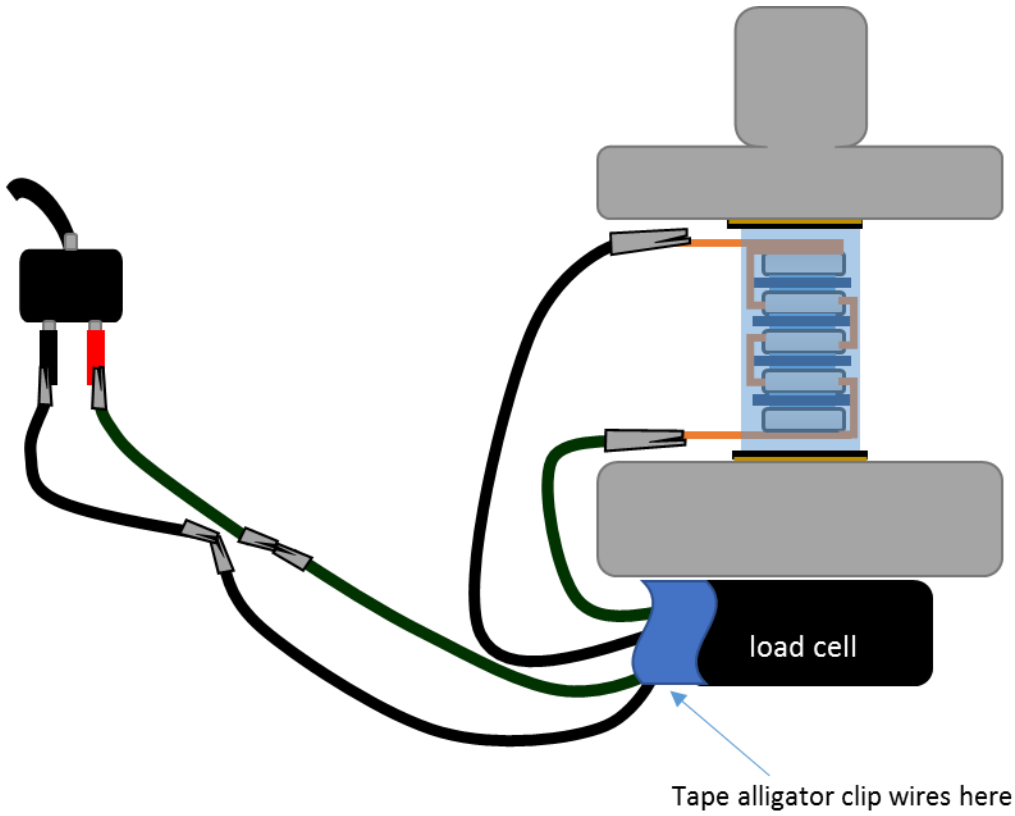

12. Double check that everything is connected properly, the cross head is locked, etc. Start the MPT program.
    a. During the preload, carefully watch the specimen, with hand over the Emergency Stop button. Sometimes, if the specimen is not loaded properly, or something else goes wrong in the manufacturing, it will break and will usually break during the initial preload.
    b. Listen carefully and watch the specimen. If you hear any cracking or see something that doesn't look right, STOP the test. Pressing the Emergency Stop button should stop the test, and it will pause at the current load.
        i. Once stopped, make sure you unlock, and enable the RSC. Use the dial to slowly unload the specimen and remove it.
13. Record the max peak voltage on the voltage sheet in the specimen book.
14. When prompted to continue to RL2, unclip the two green alligator clips (positive lead from MTS) and clip one on each side of the resistance on the RC-box. See figure below.

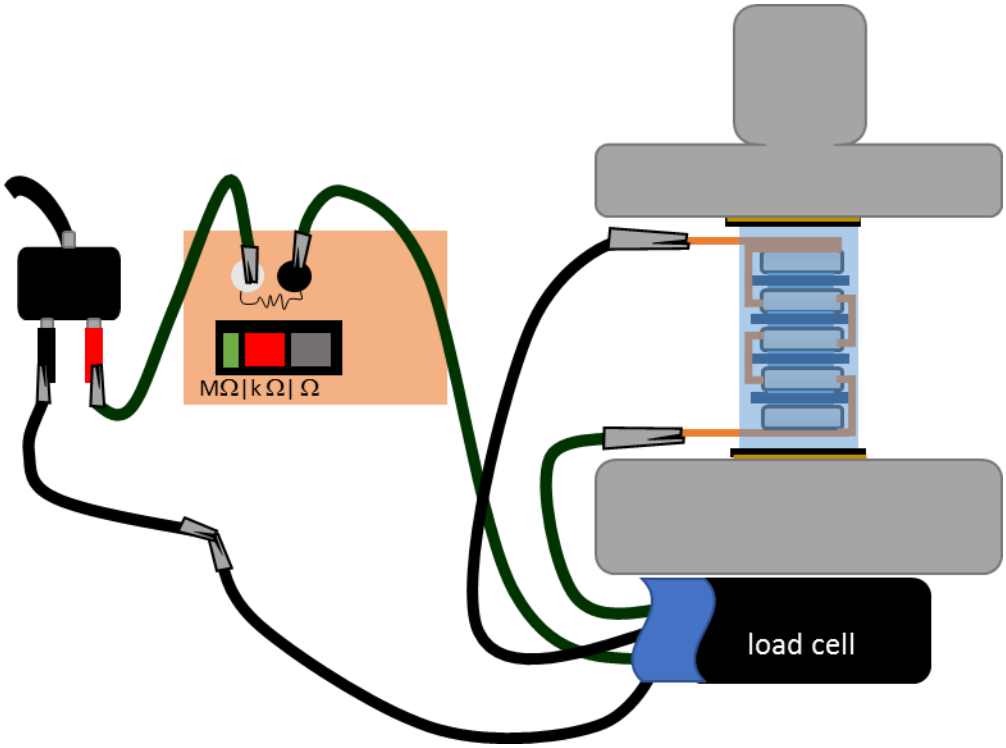


15. Follow the Resistance Sweep.
    a. When you need to switch from the RC-box to the breadboards, follow the instructions on the resistance sweep page. There are pictures of each breadboard that explicitly show which resistors you need to connect to.
    b. The MPT program is written for a sweep with 38 resistances. There are only 37 on the protocol. Just run the last one twice.
        i. This also gives you a buffer. If you mess up one, be sure to mark it down, and just fix it on the next one. Be sure to account for your error in your data analysis.

16. At the end of the test, after the last resistance load finishes, the top cross head will return to the zero position. Unclip the alligator clips from the specimen, and put it back in its home.
17. Unlock the cross head and move it back up.
    a. It is SUPER important to move it back up high enough so that when the actuator arm is fully extended, the platens do not touch.
18. Turn off the hydraulics, and close the Station Manager program. Do NOT save the station parameters.
19. Turn off the HPU. It is easiest to turn it to low, and then either press the E stop, or turn the switch to off.
20. Turn off the water.
21. Open the Shortcut to Specimens on the desktop, find the specimen folder and copy to a USB for data analysis. Log off the computer.

Appendix B: Resistance Sweeps

Resistance sweep used for Chapter 3 and Chapter 4 studies.

**MTS Resistance Sweep Version 2**

| Resistance Load | Resistance | Board | Resistors |
|---|---|---|---|
| RL 1 | 0 MΩ | N/A | |
| RL 2 | 0.015 MΩ | 0 | RC-box* |
| RL 3 | 0.03 MΩ | 0 | RC-box |
| RL 4 | 0.04 MΩ | 0 | RC-box |
| RL 5 | 0.045 MΩ | 0 | RC-box |
| RL 6 | 0.06 MΩ | 0 | RC-box |
| RL 7 | 0.075 MΩ | 0 | RC-box |
| RL 8 | 0.1 MΩ | 0 | RC-box |
| RL 9 | 0.25 MΩ | 0 | RC-box |
| RL 10 | 0.5 MΩ | 0 | RC-box |
| RL 11 | 1 MΩ | 0 | RC-box |
| RL 12 | 1.5 MΩ | 0 | RC-box |
| RL 13 | 2 MΩ | 0 | RC-box |
| RL 14 | 2.5 MΩ | 0 | RC-box |
| RL 15 | 3 MΩ | 0 | RC-box |
| RL 16 | 3.5 MΩ | 0 | RC-box |
| RL 17 | 4 MΩ | 0 | RC-box |
| RL 18 | 5 MΩ | 0 | RC-box |
| RL 19 | 6 MΩ | 0 | RC-box |
| RL 20 | 7 MΩ | 0 | RC-box |
| RL 21 | 8 MΩ | 0 | RC-box |
| RL 22 | 8.5 MΩ | 0 | RC-box |
| RL 23 | 9 MΩ | 0 | RC-box |
| RL 24 | 9.5 MΩ | 0 | RC-box |
| RL 25 | 10.14 MΩ | 1 | 9 |
| RL 26 | 12.299 MΩ | 1 | 9+1-2** |
| RL 27 | 16.357 MΩ | 1 | 9+1-6 |
| RL 28 | 18.5 MΩ | 1 | 9+1-8 |
| RL 29 | 29.45 MΩ | 1 | 9-10 |
| RL 30 | 39.49 MΩ | 1 | 9-11 |
| RL 31 | 63.4 MΩ | 2 | A-14*** |
| RL 32 | 125 MΩ | 2 | A-18 |
| RL 33 | 219.8 MΩ | 2 | A-23 |
| RL 34 | 396.1 MΩ | 2 | A-28 |
| RL 35 | 715 MΩ | 2 | A-31 |
| RL 36 | 1.25 GΩ | 3 | B-C (35-38)**** |
| RL 37 | 5 GΩ | 3 | B-C |

*clip the negative lead from the MTS to the black connector (resistance) on the "RC-box" and clip the negative lead from the insert to the white connector (resistance) on

**1-3 means resistors 1 through 3 in series. The negative lead from the MTS should be clipped to one side of the first resistor, and

***The negative lead from the MTS should be clipped to A, and the negative lead from the implant to the front of the corresponding resistor.

****clip negative lead from the MTS to C and negative lead from the implant to D on resistor 38. Resistors 34-38 should be connected in *parallel*. Pull out corresponding resistor.

Resistance Sweep used for Chapter 5 study.

| MTS Resistance Sweep Version 2 | | | |
|---|---|---|---|
| Resistance Load | Resistance | Board | Resistors |
| RL 1 | 0 MΩ | N/A | |
| RL 2 | 0.025 MΩ | 0 | RC-box* |
| RL 3 | 0.05 MΩ | 0 | RC-box |
| RL 4 | 0.1 MΩ | 0 | RC-box |
| RL 5 | 0.2 MΩ | 0 | RC-box |
| RL 6 | 0.35 MΩ | 0 | RC-box |
| RL 7 | 0.45 MΩ | 0 | RC-box |
| RL 8 | 0.55 MΩ | 0 | RC-box |
| RL 9 | 0.65 MΩ | 0 | RC-box |
| RL 10 | 0.75 MΩ | 0 | RC-box |
| RL 11 | 0.85 MΩ | 0 | RC-box |
| RL 12 | 0.95 MΩ | 0 | RC-box |
| RL 13 | 1 MΩ | 0 | RC-box |
| RL 14 | 1.5 MΩ | 0 | RC-box |
| RL 15 | 2 MΩ | 0 | RC-box |
| RL 16 | 2.5 MΩ | 0 | RC-box |
| RL 17 | 3 MΩ | 0 | RC-box |
| RL 18 | 3.5 MΩ | 0 | RC-box |
| RL 19 | 4 MΩ | 0 | RC-box |
| RL 20 | 4.5 MΩ | 0 | RC-box |
| RL 21 | 5 MΩ | 0 | RC-box |
| RL 22 | 5.5 MΩ | 0 | RC-box |
| RL 23 | 6 MΩ | 0 | RC-box |
| RL 24 | 6.5 MΩ | 0 | RC-box |
| RL 25 | 7 MΩ | 0 | RC-box |
| RL 26 | 7.5 MΩ | 0 | RC-box |
| RL 27 | 8 MΩ | 0 | RC-box |
| RL 28 | 8.5 MΩ | 0 | RC-box |
| RL 29 | 9 MΩ | 0 | RC-box |
| RL 30 | 9.5 MΩ | 0 | RC-box |
| RL 31 | 10 MΩ | 1 | GR RC-box** |
| RL 32 | 12 MΩ | 2 | Both RC's*** |
| RL 33 | 14 MΩ | 2 | Both RC's |
| RL 34 | 16 MΩ | 2 | Both RC's |
| RL 35 | 18 MΩ | 2 | Both RC's |
| RL 36 | 20 MΩ | 2 | Both RC's |

Resistance Sweep used for Chapter 6 study.

| MTS Resistance Sweep Aim 3 AC Power Sweep | | |
|---|---|---|
| Resistance Load | Resistance | Resistors |
| RL 1 | 0 MΩ | N/A |
| RL 2 | 0.25 MΩ | IET RC* |
| RL 3 | 0.5 MΩ | IET RC |
| RL 4 | 0.75 MΩ | IET RC |
| RL 5 | 1 MΩ | IET RC |
| RL 6 | 2 MΩ | IET RC |
| RL 7 | 3 MΩ | IET RC |
| RL 8 | 4 MΩ | IET RC |
| RL 9 | 5 MΩ | IET RC |
| RL 10 | 6 MΩ | IET RC |
| RL 11 | 7 MΩ | IET RC |
| RL 12 | 9 MΩ | IET RC |
| RL 13 | 11 MΩ | PB10M** + IET 1M |
| RL 14 | 13 MΩ | PB10M + IET 3M |
| RL 15 | 15 MΩ | PB10M + IET 5M |
| RL 16 | 17 MΩ | PB10M + IET 7M |
| RL 17 | 19 MΩ | PB10M + IET 9M |
| RL 18 | 20 MΩ | A-12*** + IET 5M |
| RL 19 | 21 MΩ | A-12 + IET 6M |
| RL 20 | 22 MΩ | A-12 + IET 7M |
| RL 21 | 23 MΩ | A-12 + IET 8M |
| RL 22 | 24 MΩ | A-12 + IET 9M |
| RL 23 | 26 MΩ | A-12 + PB 10M + IET 1M |
| RL 24 | 28 MΩ | A-12 + PB 10M + IET 3M |
| RL 25 | 30 MΩ | A-12 + PB 10M + IET 5M |
| RL 26 | 32 MΩ | A-12 + PB 10M + IET 7M |
| RL 27 | 34 MΩ | A-12 + PB 10M + IET 9M |
| RL 28 | 38 MΩ | A-13 |
| RL 29 | 40 MΩ | A-13 + IET 2M |
| RL 30 | 45 MΩ | A-13 + IET 7M |
| RL 31 | 50 MΩ | A-13 + PB 10M + IET 2M |
| RL 32 | 60 MΩ | A-14 + IET 7M |
| RL 33 | 70 MΩ | A-14 + PB10+ IET 7M |
| RL 34 | 80 MΩ | A-15 + IET 7M |
| RL 35 | 85 MΩ | A-15 + PB10 + IET2M |
| RL 36 | 90 MΩ | A-15 + PB10 + IET 7M |
| RL 37 | 95 MΩ | A-16 |
| RL 38 | 100 MΩ | A-16 + IET 5M |
| RL 39 | 125 MΩ | A-17 + IET 7M |
| RL 40 | 150 MΩ | A-18.5 + IET 5M |
| RL 41 | 200 MΩ | A-22 + IET 5M |
| RL 42 | 296 MΩ | A-27 + PB10M + IET 9.5M |
| RL 43 | 493 MΩ | A-29 + PB10M + IET 9M |
| RL 44 | 602 MΩ | A-31 |
| RL 45 | 803 MΩ | A-33 |

*clip the negative lead from the MTS to the black connector (resistance) on the "RC-box" and clip the negative lead from the insert to the white connector (resistance) on the tan IET RC-box.
Flip red/green dials to control Mohm reistances.

**The blue PB RC box should be connected in series with tan RC-box and all switches open for 1M-4M (far left column).

***The negative lead from the MTS should be clipped to A, and the negative lead from the implant to the front of the corresponding resistor.

Appendix C: Code

*Power: Compression*

MATLAB code written to analyze voltage data and calculate power output of piezo composites during compression testing. This code was modified for each study, but the basics were the same for each.

```
%Data Analysis for Testing Piezoelectric Composites
%Originally written by John Doman in 2013
%Updated by Ember Krech in JUNE 2019


%*****AIM 3 AC Power******
%Clear data
clear
close all
clc

%***Be sure to change specimen_name and file_location and Rmts if necessary



%% Input Parameters

%**This should be updated if you add resistors when voltage signal saturates

Rmts = 2E6; %ohms %fixed MTS electrical resistance
Rmts = 23.65e3; %ohms %there is one resistor (1 kohm) in parallel with the
2E6 resistance

%MAKE SURE TO DOUBLE CHECK THE RESISTANCE SWEEP VALUES!


numCatch = 0;
%% Load Desired Data
count = 1;
specimen_name = ['C2-2_full']; %desired filename for the excel file with
analyzed data
file_location = ['F:\AC Power\2019_06_13_C2-2_ACpower\']; %raw MTS data file
location
output_file = ['Data ' specimen_name];


%This is the complete resistance sweep (37 resistances from .025Mohm to
20Mohm) - modify line 35 as necessary
Resistance_Sweep = [0 .25e6 0.5e6 0.75e6 1e6 2e6 3e6 4e6 5e6 6e6 7e6 9e6 11e6
13e6 15e6 17e6 19e6 20e6 21e6 22e6 23e6 24e6 26e6 28e6 30e6 32e6 34e6 38e6
40e6 45e6 50e6 60e6 70e6 80e6 85e6 90e6 95e6 100e6 125e6 150e6 200e6 296e6
493e6 602e6 803e6];
%Resistance_Sweep = [0 0 1e6 2e6 3e6 4e6 5e6 7e6 9e6 11e6 13e6 17e6 20e6 26e6
30e6 34e6 40e6 45e6 50e6 60e6 70e6 80e6 90e6 100e6 125e6 150e6 200e6 296e6
493e6 802e6 820e6 1066e6 1e9 2e9 3e9 4e9 5e9];
load = [1 2 3];%number of loads used (100N, 500N, 1000N)
```

```
frequency = [1 2 3 5]; %number of frequencies used for each loading cycle
(1Hz, 2Hz, 3Hz, 5Hz)


freqCount = 0;
for iFreq = 1:length(frequency)

    freqCount = freqCount +1;

    for iLoad = 1:length(load)

        for iResistor = 1:length(Resistance_Sweep)

%             iFreq = 1;   %You can change these to look at specific data
%             iLoad = 1;
%             iResistor = 18;

            name=[file_location 'specimen_xx_x_g33_PE_02_load_'
num2str(load(iLoad),'%.1d') '_' num2str(frequency(iFreq),'%.2d') 'Hz_Rl_'
num2str(iResistor,'%.2d.dat')];
            Reference_column(iLoad,iFreq,iResistor) =
{['specimen_xx_x_g33_PE_02_load_' num2str(iLoad,'%.1d') '_'
num2str(iFreq,'%.2d') 'Hz_Rl_' num2str(iResistor,'%.2d')]};

            dat = dlmread(name,'\t',5,0); %read in MTS data files

            Rvar = Resistance_Sweep(iResistor);


            %Store the data values into individual variables
            time = dat(:,1);
            axial_count = dat(:,2);
            axial_count = axial_count - min(axial_count) +1;
            x = -dat(:,3)*10^-3;    %m
            force = -dat(:,4);      %N
            voltage = dat(:,5);    %Volt

            %Plot raw voltage data
%             figure()
%             plot(voltage)
%             figure()
%             plot(force)

            %% Filter the data to eliminate excess noise

            %Calculate the sample frequency
            deltaT = diff(time);
            DeltaT = mean(deltaT);
            fs = 1 / DeltaT;

            %initial variables to use a low pass butterworth filter
            %fc = 8; %Hz - cuttoff frequency
            fc=12;
%
%             if iFreq == 1
%                 fc = 4;       %Hz - cuttoff frequency
%             elseif iFreq == 2
```

```
%                 fc = 6;
%               elseif iFreq == 3
%                 fc = 8;
%               else
%                 fc = 10;
%               end
%
              %filter the data to eliminate the excess noise. filter all data
so
              %that they are subject to the same phase delay
                  [b,a] = butter(5,2*fc/fs);
                  x  = filtfilt(b,a,x);
                  F = filtfilt(b,a,force);
                  Vmts = filtfilt (b,a,voltage);

                  %Plot filtered voltage data
%
%                   figure()
%                   subplot(2,1,1), plot(voltage)
%                   subplot(2,1,2), plot(Vmts)
%                   figure()
%                   subplot(2,1,1), plot(force)
%                   subplot(2,1,2), plot(F)
%
              %Eliminate the initial and final portions of the data
              %The MTS collects 15 cycles of each force, at each frequency,
              %we only want to analyze the middle section (steady-state)

              time = time(axial_count > 5 & axial_count < 27);
              x = x(axial_count > 5 & axial_count < 27);
              F = F(axial_count > 5 & axial_count < 27);
              Vmts = Vmts(axial_count > 5 & axial_count < 27);
              axial_count = axial_count(axial_count > 5 & axial_count < 27);

%               figure()
%               plot(Vmts)

              %% Segment the data into 5 loading and unloading cycles
              %This can be used to calcualte specimen stiffness, and d33/g33
              %loading cycles
              cycle1 = [10:2:18];

              time = time(axial_count >= min(cycle1) & axial_count <=
max(cycle1));
              x = x(axial_count >= min(cycle1) & axial_count <= max(cycle1));
              F = F(axial_count >= min(cycle1) & axial_count <= max(cycle1));
              Vmts = Vmts(axial_count >= min(cycle1) & axial_count <=
max(cycle1));
              axial_count = axial_count(axial_count >= min(cycle1) &
axial_count <= max(cycle1));

              timeL=time(find(ismember(axial_count,cycle1)));
              xL=x(find(ismember(axial_count,cycle1)));
              FL=F(find(ismember(axial_count,cycle1)));
              VL=Vmts(find(ismember(axial_count,cycle1)));

              timeU=time(find(ismember(axial_count,cycle1+1)));
```

```
            xU=x(find(ismember(axial_count,cycle1+1)));
            FU=F(find(ismember(axial_count,cycle1+1)));
            VU=Vmts(find(ismember(axial_count,cycle1+1)));

%                   figure()
%                   plot(timeL, VL,'.')
%                   hold on
%                   plot(timeU, VU,'.r')
%                   plot(time, Vmts,'g-')
%                   figure()
%                   plot(timeL, FL,'.')
%                   hold on
%                   plot(timeU, FU,'.r')
%                   plot(time, Vmts,'g-')


            %% Analyze Data

            %Now we have 5 middle cycles of filtered and phase corrected data
for
            %each variable. This test was run in g33 setup, with a variable
            %load resistance. The output voltage and power for each each
            %resistance can now be analyzed


                        Vmts = Vmts*(1/sqrt(2)); %convert to RMS voltage
                        Vout = Vmts.*(1+Rvar/Rmts);     %scale voltage by the
applied resistance to find voltage produced by the implant
                        Vamp = (max(Vout) - (min(Vout)))/2;     %calculate
voltage amplitude peak-to-peak
                        P = Vout.^2./(Rvar+Rmts);
%instantaneous power
                        Pavg = trapz(time,P) * 1/(max(time) - min(time));
%average power for all 5 cycles
                        Pmax = Vamp.^2./(Rvar+Rmts);             %peak power
per cycle
                        Pmaxu = Pmax*(10^6);
%

%
            %% Store data to output
            output(count,:) = {load(iLoad), [max(F)-min(F)],
frequency(iFreq),...
                Rvar+Rmts, Vamp, Pavg, Pmax, Pmaxu};

            count = count + 1;

          clear Vmts Vmts_shifted Rvar Vamp Pavg Pmax Vout Pmaxu
        end

    end

end


%% Output to an excel sheet for later analysis
output_header = {'Load' 'F-Range (N)' 'Frequency (Hz)' 'Resistance (ohm)' ...
```

```
    'Voltage (V)' 'Pavg (W)' 'Pmax (W)' 'Pmax (uW)'};

output = [output_header; output];

    xlswrite([output_file '.xlsx'], output_header,1, 'A1')
    xlswrite([output_file '.xlsx'],
output(2:length(Resistance_Sweep)+1,:),'Sheet1','A2')

for ii = 2:12
    xlswrite([output_file '.xlsx'], output_header,ii, 'A1')
    xlswrite([output_file '.xlsx'], output((ii-
1)*length(Resistance_Sweep)+2:length(Resistance_Sweep)*ii+1,:),ii,'A2')
end


xlswrite([output_file '.xlsx'],output,13,'A1')

disp('Done')
```

*Power: Torsion*

MATLAB code written to analyze voltage data and calculate power output of piezo composites during torsion testing from Chapter 5. Power was calculated using the same method as compression, but several changes were made to account for changes due to loading in torsion.

```
%Data Analysis for Testing Piezoelectric Composites
%Originally written by John Doman in 2013
%Updated by Ember Krech in September 2018

%*****AIM 2 TORSION TESTING ON BIAXIAL MACHINE******
%Clear data
clear
 close all
clc

%***Be sure to change specimen_name and file_location and Rmts if necessary
%***FOR MIXED SPECIMEN

%% Input Parameters

%**This should be updated if you add resistors when voltage signal saturates

% Rmts = 2E6; %ohms %fixed MTS electrical resistance
Rmts = 141.3e3;
%Rmts = 1.487e3; %ohms %there is one resistor (1 kohm) in parallel with the
2E6 resistance

%MAKE SURE TO DOUBLE CHECK THE RESISTANCE SWEEP VALUES!

numCatch = 0;
%% Load Desired Data
count = 1;
specimen_name = ['R4_torsion_corrected2']; %desired filename for the excel
file with analyzed data
```

```
file_location = ['I:\mts data\2018_09_28_R4torsion\']; %raw MTS data file
location
output_file = ['Data ' specimen_name];

%This is the complete resistance sweep (37 resistances from .025Mohm to
20Mohm) - modify line 35 as necessary
Resistance_Sweep = [0 0.025e6  0.05e6 0.1e6 0.2e6 0.35e6 0.45e6 0.55e6 0.65e6
0.75e6 0.85e6 0.95e6 1e6 1.5e6 2e6 2.5e6 3e6 3.5e6 4e6 4.5e6 5e6 5.5e6 6e6
6.5e6 7e6 7.5e6 8e6 8.5e6 9e6 10e6 12e6 14e6 16e6 18e6 20e6];
% Resistance_Sweep = [0 0.025e6 0.1e6 0.3e6 0.8e6 1e6 3e6 6e6 9e6 15e6];
% Resistance_Sweep = [0 3e6 8e6 20e6];
load = [1 2 3];%number of loads used (100N, 500N, 1000N)
frequency = [1 2 3 4]; %number of frequencies used for each loading cycle
(1Hz, 2Hz, 3Hz, 5Hz)

freqCount = 0;
for iFreq = 1:length(frequency)

    freqCount = freqCount +1;

    for iLoad = 1:length(load)

        for iResistor = 1:length(Resistance_Sweep)

            iLoad = 3;
            iFreq = 1;
            iResistor = 24;

            name=[file_location 'specimen_MMtorsion_load_'
num2str(load(iLoad),'%.1d') '_' num2str(frequency(iFreq),'%.2d') 'Hz_Rl_'
num2str(iResistor,'%.2d.dat')];
            Reference_column(iLoad,iFreq,iResistor) = {['specimenXX_load_'
num2str(iLoad,'%.1d') '_' num2str(iFreq,'%.2d') 'Hz_Rl_'
num2str(iResistor,'%.2d')]};

            dat = dlmread(name,'\t',5,0); %read in MTS data files

            Rvar = Resistance_Sweep(iResistor);

            %Store the data values into individual variables
            time = dat(:,1);
            axial_count = dat(:,2);
            axial_count = axial_count - min(axial_count) +1;
            x = -dat(:,3)*10^-3;   %m
            F = -dat(:,4);     %N
            voltage = dat(:,5); %Volt
            angle = dat(:,6); %deg
            T = dat(:,7)*10^-3; %N-m
            torsional_count = dat(:,8);
            torsional_count = torsional_count - min(torsional_count) +1;


            %Plot raw voltage data
%             figure()
%             plot(voltage)
%
            %% Filter the data to eliminate excess noise
```

```
            %Calculate the sample frequency
            deltaT = diff(time);
            DeltaT = mean(deltaT);
            fs = 1 / DeltaT;

            %initial variables to use a low pass butterworth filter
            fc = 8;

%             if iFreq == 4
%                 fc = 2;       %Hz - cuttoff frequency
%             elseif iFreq == 3
%                 fc = 5;
%             elseif iFreq == 2
%                 fc = 3;
%             else
%                 fc = 2;
%             end

            %filter the data to eliminate the excess noise. filter all data
so
            %that they are subject to the same phase delay
                [b,a] = butter(5,2*fc/fs);
                x  = filtfilt(b,a,x);
                F = filtfilt(b,a,F);
                Vmts = filtfilt(b,a,voltage);
                angle = filtfilt(b,a,angle);
                T = filtfilt(b,a,T);

%                 Plot filtered voltage data
                figure()
                plot(Vmts)
                figure()
                subplot(2,1,1), plot(voltage)
                subplot(2,1,2), plot(Vmts)

            %Eliminate the initial and final portions of the data
            %The MTS collects 15 cycles of each force, at each frequency,
            %we only want to analyze the middle section (steady-state)

            time = time(torsional_count > 5 & torsional_count < 27);
            x = x(torsional_count > 5 & torsional_count < 27);
            F = F(torsional_count > 5 & torsional_count < 27);
            Vmts = Vmts(torsional_count > 5 & torsional_count < 27);
            angle = angle(torsional_count > 5 & torsional_count < 27);
            T = T(torsional_count > 5 & torsional_count < 27);
            torsional_count = torsional_count(torsional_count > 5 &
torsional_count < 27);

%             figure()
%             plot(Vmts)
%             subplot(4,1,3), plot(Vmts)

            %% Segment the data into 5 loading and unloading cycles
            %This can be used to calcualte specimen stiffness, and d33/g33
            %loading cycles
            cycle1 = [5:2:15];
```

```
            time = time(torsional_count >= min(cycle1) & torsional_count <=
max(cycle1));
            x = x(torsional_count >= min(cycle1) & torsional_count <=
max(cycle1));
            F = F(torsional_count >= min(cycle1) & torsional_count <=
max(cycle1));
            Vmts = Vmts(torsional_count >= min(cycle1) & torsional_count <=
max(cycle1));
            torsional_count = torsional_count(torsional_count >= min(cycle1)
& torsional_count <= max(cycle1));
%
            %subplot(4,1,4), plot(Vmts)
            timeL=time(find(ismember(torsional_count,cycle1)));
            xL=x(find(ismember(torsional_count,cycle1)));
            FL=F(find(ismember(torsional_count,cycle1)));
            VL=Vmts(find(ismember(torsional_count,cycle1)));
            TL=T(find(ismember(torsional_count,cycle1)));

            timeU=time(find(ismember(torsional_count,cycle1+1)));
            xU=x(find(ismember(torsional_count,cycle1+1)));
            FU=F(find(ismember(torsional_count,cycle1+1)));
            VU=Vmts(find(ismember(torsional_count,cycle1+1)));
            TU=T(find(ismember(torsional_count,cycle1+1)));

                    figure()
                    plot(timeL, VL,'.')
                    hold on
                    plot(timeU, VU,'.r')
                    plot(time, Vmts,'g-')


            %% Analyze Data

            %Now we have 5 middle cycles of filtered and phase corrected data
for
            %each variable. This test was run in g33 setup, with a variable
            %load resistance. The output voltage and power for each each
            %resistance can now be analyzed


                        Vmts = Vmts*(1/sqrt(2)); %convert to RMS voltage
                        Vout = Vmts.*(1+Rvar/Rmts);     %scale voltage by the
applied resistance to find voltage produced by the implant
                        Vamp = (max(Vout) - (min(Vout)))/2;     %calculate
voltage amplitude peak-to-peak
                        P = Vout.^2./(Rvar+Rmts);
%instantaneous power
                        Pavg = trapz(time,P) * 1/(max(time) - min(time));
%average power for all 5 cycles
                        Pmax = Vamp.^2./(Rvar+Rmts);             %peak power
per cycle
%             figure()
%           plot(Vout);
%
            %% Store data to output
```

```
            output(count,:) = {load(iLoad), [max(T)-min(T)],
frequency(iFreq),...
                Rvar+Rmts, Vamp, Pavg, Pmax};

            count = count + 1;

           clear Vmts voltage Rvar Vamp Pavg Pmax Vout
        end

    end

end


%% Output to an excel sheet for later analysis
output_header = {'Load' 'T-Range (N-m)' 'Frequency (Hz)' 'Resistance (ohm)'
...
    'Voltage (V)' 'Pavg (W)' 'Pmax (W)'};

output = [output_header; output];

    xlswrite([output_file '.xlsx'], output_header,1, 'A1')
    xlswrite([output_file '.xlsx'],
output(2:length(Resistance_Sweep)+1,:),'Sheet1','A2')

for ii = 2:12
    xlswrite([output_file '.xlsx'], output_header,ii, 'A1')
    xlswrite([output_file '.xlsx'], output((ii-
1)*length(Resistance_Sweep)+2:length(Resistance_Sweep)*ii+1,:),ii,'A2')
end

    xlswrite([output_file '.xlsx'],output,13,'A1')
disp('Done')
```

### *Fatigue*

```
clc
clear all
close all

file_location = ['\\Client\F$\Fatigue\C3\C3-12\2019_10_03_C3-12_fatigue\'];
output_file1 = ['C3_12fatigue'];
name=[file_location '10kdata.dat'];
dat = dlmread(name,'\t',5,0);

Rmts = 23e3;
Rsweep = 10e6;

disp = dat(:,3);
volt = dat(:,5);
volt = (volt*(Rmts+Rsweep))/Rmts;
axialcount = dat(:,2);
axial_count = axialcount - min(axialcount);

c = ischange(axial_count,'MaxNumChanges',99);
```

```
x = find(c);
count(:,1) = axialcount(1:x(1)-1);
count(:,2) = axialcount(x(1):x(2)-1);
count(:,3) = axialcount(x(2):x(3)-1);
count(:,4) = axialcount(x(3):x(4)-1);
count(:,5) = axialcount(x(4):x(5)-1);
count(:,6) = axialcount(x(5):x(6)-1);
count(:,7) = axialcount(x(6):x(7)-1);
count(:,8) = axialcount(x(7):x(8)-1);
count(:,9) = axialcount(x(8):x(9)-1);
count(:,10) = axialcount(x(9):x(10)-1);
count(:,11) = axialcount(x(10):x(11)-2);
count(:,12) = axialcount(x(11):x(12)-1);
count(:,13) = axialcount(x(12):x(13)-1);
count(:,14) = axialcount(x(13):x(14)-2);
count(:,15) = axialcount(x(14):x(15)-1);
count(:,16) = axialcount(x(15):x(16)-1);
count(:,17) = axialcount(x(16):x(17)-2);
count(:,18) = axialcount(x(17):x(18)-1);
count(:,19) = axialcount(x(18):x(19)-1);
count(:,20) = axialcount(x(19):x(20)-1);
count(:,21) = axialcount(x(20):x(21)-1);
count(:,22) = axialcount(x(21):x(22)-1);
count(:,23) = axialcount(x(22):x(23)-1);
count(:,24) = axialcount(x(23):x(24)-1);
count(:,25) = axialcount(x(24):x(25)-1);
count(:,26) = axialcount(x(25):x(26)-1);
count(:,27) = axialcount(x(26):x(27)-1);
count(:,28) = axialcount(x(27):x(28)-2);
count(:,29) = axialcount(x(28):x(29)-1);
count(:,30) = axialcount(x(29):x(30)-1);
count(:,31) = axialcount(x(30):x(31)-2);
count(:,32) = axialcount(x(31):x(32)-1);
count(:,33) = axialcount(x(32):x(33)-1);
count(:,34) = axialcount(x(33):x(34)-1);
count(:,35) = axialcount(x(34):x(35)-1);
count(:,36) = axialcount(x(35):x(36)-1);
count(:,37) = axialcount(x(36):x(37)-1);
count(:,38) = axialcount(x(37):x(38)-1);
count(:,39) = axialcount(x(38):x(39)-1);
count(:,40) = axialcount(x(39):x(40)-1);
count(:,41) = axialcount(x(40):x(41)-1);
count(:,42) = axialcount(x(41):x(42)-2);
count(:,43) = axialcount(x(42):x(43)-1);
count(:,44) = axialcount(x(43):x(44)-1);
count(:,45) = axialcount(x(44):x(45)-2);
count(:,46) = axialcount(x(45):x(46)-1);
count(:,47) = axialcount(x(46):x(47)-1);
count(:,48) = axialcount(x(47):x(48)-2);
count(:,49) = axialcount(x(48):x(49)-1);
count(:,50) = axialcount(x(49):x(50)-1);
count(:,51) = axialcount(x(50):x(51)-1);
count(:,52) = axialcount(x(51):x(52)-1);
count(:,53) = axialcount(x(52):x(53)-1);
count(:,54) = axialcount(x(53):x(54)-1);
count(:,55) = axialcount(x(54):x(55)-1);
count(:,56) = axialcount(x(55):x(56)-1);
```

```
count(:,57) = axialcount(x(56):x(57)-1);
count(:,58) = axialcount(x(57):x(58)-1);
count(:,59) = axialcount(x(58):x(59)-2);
count(:,60) = axialcount(x(59):x(60)-1);
count(:,61) = axialcount(x(60):x(61)-1);
count(:,62) = axialcount(x(61):x(62)-2);
count(:,63) = axialcount(x(62):x(63)-1);
count(:,64) = axialcount(x(63):x(64)-1);
count(:,65) = axialcount(x(64):x(65)-1);
count(:,66) = axialcount(x(65):x(66)-1);
count(:,67) = axialcount(x(66):x(67)-1);
count(:,68) = axialcount(x(67):x(68)-1);
count(:,69) = axialcount(x(68):x(69)-1);
count(:,70) = axialcount(x(69):x(70)-1);
count(:,71) = axialcount(x(70):x(71)-1);
count(:,72) = axialcount(x(71):x(72)-1);
count(:,73) = axialcount(x(72):x(73)-2);
count(:,74) = axialcount(x(73):x(74)-1);
count(:,75) = axialcount(x(74):x(75)-1);
count(:,76) = axialcount(x(75):x(76)-2);
count(:,77) = axialcount(x(76):x(77)-1);
count(:,78) = axialcount(x(77):x(78)-1);
count(:,79) = axialcount(x(78):x(79)-2);
count(:,80) = axialcount(x(79):x(80)-1);
count(:,81) = axialcount(x(80):x(81)-1);
count(:,82) = axialcount(x(81):x(82)-1);
count(:,83) = axialcount(x(82):x(83)-1);
count(:,84) = axialcount(x(83):x(84)-1);
count(:,85) = axialcount(x(84):x(85)-1);
count(:,86) = axialcount(x(85):x(86)-1);
count(:,87) = axialcount(x(86):x(87)-1);
count(:,88) = axialcount(x(87):x(88)-1);
count(:,89) = axialcount(x(88):x(89)-1);
count(:,90) = axialcount(x(89):x(90)-2);
count(:,91) = axialcount(x(90):x(91)-1);
count(:,92) = axialcount(x(91):x(92)-1);
count(:,93) = axialcount(x(92):x(93)-2);
count(:,94) = axialcount(x(93):x(94)-1);
count(:,95) = axialcount(x(94):x(95)-1);
count(:,96) = axialcount(x(95):x(96)-1);
count(:,97) = axialcount(x(96):x(97)-1);
count(:,98) = axialcount(x(97):x(98)-1);
count(:,99) = axialcount(x(98):x(99)-1);

%%new section
voltageout(:,1) = volt(1:x(1)-1);
voltageout(:,2) = volt(x(1):x(2)-1);
voltageout(:,3) = volt(x(2):x(3)-1);
voltageout(:,4) = volt(x(3):x(4)-1);
voltageout(:,5) = volt(x(4):x(5)-1);
voltageout(:,6) = volt(x(5):x(6)-1);
voltageout(:,7) = volt(x(6):x(7)-1);
voltageout(:,8) = volt(x(7):x(8)-1);
voltageout(:,9) = volt(x(8):x(9)-1);
voltageout(:,10) = volt(x(9):x(10)-1);
voltageout(:,11) = volt(x(10):x(11)-2);
voltageout(:,12) = volt(x(11):x(12)-1);
```

```
voltageout(:,13) = volt(x(12):x(13)-1);
voltageout(:,14) = volt(x(13):x(14)-2);
voltageout(:,15) = volt(x(14):x(15)-1);
voltageout(:,16) = volt(x(15):x(16)-1);
voltageout(:,17) = volt(x(16):x(17)-2);
voltageout(:,18) = volt(x(17):x(18)-1);
voltageout(:,19) = volt(x(18):x(19)-1);
voltageout(:,20) = volt(x(19):x(20)-1);
voltageout(:,21) = volt(x(20):x(21)-1);
voltageout(:,22) = volt(x(21):x(22)-1);
voltageout(:,23) = volt(x(22):x(23)-1);
voltageout(:,24) = volt(x(23):x(24)-1);
voltageout(:,25) = volt(x(24):x(25)-1);
voltageout(:,26) = volt(x(25):x(26)-1);
voltageout(:,27) = volt(x(26):x(27)-1);
voltageout(:,28) = volt(x(27):x(28)-2);
voltageout(:,29) = volt(x(28):x(29)-1);
voltageout(:,30) = volt(x(29):x(30)-1);
voltageout(:,31) = volt(x(30):x(31)-2);
voltageout(:,32) = volt(x(31):x(32)-1);
voltageout(:,33) = volt(x(32):x(33)-1);
voltageout(:,34) = volt(x(33):x(34)-1);
voltageout(:,35) = volt(x(34):x(35)-1);
voltageout(:,36) = volt(x(35):x(36)-1);
voltageout(:,37) = volt(x(36):x(37)-1);
voltageout(:,38) = volt(x(37):x(38)-1);
voltageout(:,39) = volt(x(38):x(39)-1);
voltageout(:,40) = volt(x(39):x(40)-1);
voltageout(:,41) = volt(x(40):x(41)-1);
voltageout(:,42) = volt(x(41):x(42)-2);
voltageout(:,43) = volt(x(42):x(43)-1);
voltageout(:,44) = volt(x(43):x(44)-1);
voltageout(:,45) = volt(x(44):x(45)-2);
voltageout(:,46) = volt(x(45):x(46)-1);
voltageout(:,47) = volt(x(46):x(47)-1);
voltageout(:,48) = volt(x(47):x(48)-2);
voltageout(:,49) = volt(x(48):x(49)-1);
voltageout(:,50) = volt(x(49):x(50)-1);
voltageout(:,51) = volt(x(50):x(51)-1);
voltageout(:,52) = volt(x(51):x(52)-1);
voltageout(:,53) = volt(x(52):x(53)-1);
voltageout(:,54) = volt(x(53):x(54)-1);
voltageout(:,55) = volt(x(54):x(55)-1);
voltageout(:,56) = volt(x(55):x(56)-1);
voltageout(:,57) = volt(x(56):x(57)-1);
voltageout(:,58) = volt(x(57):x(58)-1);
voltageout(:,59) = volt(x(58):x(59)-2);
voltageout(:,60) = volt(x(59):x(60)-1);
voltageout(:,61) = volt(x(60):x(61)-1);
voltageout(:,62) = volt(x(61):x(62)-2);
voltageout(:,63) = volt(x(62):x(63)-1);
voltageout(:,64) = volt(x(63):x(64)-1);
voltageout(:,65) = volt(x(64):x(65)-1);
voltageout(:,66) = volt(x(65):x(66)-1);
voltageout(:,67) = volt(x(66):x(67)-1);
voltageout(:,68) = volt(x(67):x(68)-1);
voltageout(:,69) = volt(x(68):x(69)-1);
```

```
voltageout(:,70) = volt(x(69):x(70)-1);
voltageout(:,71) = volt(x(70):x(71)-1);
voltageout(:,72) = volt(x(71):x(72)-1);
voltageout(:,73) = volt(x(72):x(73)-2);
voltageout(:,74) = volt(x(73):x(74)-1);
voltageout(:,75) = volt(x(74):x(75)-1);
voltageout(:,76) = volt(x(75):x(76)-2);
voltageout(:,77) = volt(x(76):x(77)-1);
voltageout(:,78) = volt(x(77):x(78)-1);
voltageout(:,79) = volt(x(78):x(79)-2);
voltageout(:,80) = volt(x(79):x(80)-1);
voltageout(:,81) = volt(x(80):x(81)-1);
voltageout(:,82) = volt(x(81):x(82)-1);
voltageout(:,83) = volt(x(82):x(83)-1);
voltageout(:,84) = volt(x(83):x(84)-1);
voltageout(:,85) = volt(x(84):x(85)-1);
voltageout(:,86) = volt(x(85):x(86)-1);
voltageout(:,87) = volt(x(86):x(87)-1);
voltageout(:,88) = volt(x(87):x(88)-1);
voltageout(:,89) = volt(x(88):x(89)-1);
voltageout(:,90) = volt(x(89):x(90)-2);
voltageout(:,91) = volt(x(90):x(91)-1);
voltageout(:,92) = volt(x(91):x(92)-1);
voltageout(:,93) = volt(x(92):x(93)-2);
voltageout(:,94) = volt(x(93):x(94)-1);
voltageout(:,95) = volt(x(94):x(95)-1);
voltageout(:,96) = volt(x(95):x(96)-1);
voltageout(:,97) = volt(x(96):x(97)-1);
voltageout(:,98) = volt(x(97):x(98)-1);
voltageout(:,99) = volt(x(98):x(99)-1);


dispout(:,1) = disp(1:x(1)-1);
dispout(:,2) = disp(x(1):x(2)-1);
dispout(:,3) = disp(x(2):x(3)-1);
dispout(:,4) = disp(x(3):x(4)-1);
dispout(:,5) = disp(x(4):x(5)-1);
dispout(:,6) = disp(x(5):x(6)-1);
dispout(:,7) = disp(x(6):x(7)-1);
dispout(:,8) = disp(x(7):x(8)-1);
dispout(:,9) = disp(x(8):x(9)-1);
dispout(:,10) = disp(x(9):x(10)-1);
dispout(:,11) = disp(x(10):x(11)-2);
dispout(:,12) = disp(x(11):x(12)-1);
dispout(:,13) = disp(x(12):x(13)-1);
dispout(:,14) = disp(x(13):x(14)-2);
dispout(:,15) = disp(x(14):x(15)-1);
dispout(:,16) = disp(x(15):x(16)-1);
dispout(:,17) = disp(x(16):x(17)-2);
dispout(:,18) = disp(x(17):x(18)-1);
dispout(:,19) = disp(x(18):x(19)-1);
dispout(:,20) = disp(x(19):x(20)-1);
dispout(:,21) = disp(x(20):x(21)-1);
dispout(:,22) = disp(x(21):x(22)-1);
dispout(:,23) = disp(x(22):x(23)-1);
dispout(:,24) = disp(x(23):x(24)-1);
dispout(:,25) = disp(x(24):x(25)-1);
```

```
dispout(:,26) = disp(x(25):x(26)-1);
dispout(:,27) = disp(x(26):x(27)-1);
dispout(:,28) = disp(x(27):x(28)-2);
dispout(:,29) = disp(x(28):x(29)-1);
dispout(:,30) = disp(x(29):x(30)-1);
dispout(:,31) = disp(x(30):x(31)-2);
dispout(:,32) = disp(x(31):x(32)-1);
dispout(:,33) = disp(x(32):x(33)-1);
dispout(:,34) = disp(x(33):x(34)-1);
dispout(:,35) = disp(x(34):x(35)-1);
dispout(:,36) = disp(x(35):x(36)-1);
dispout(:,37) = disp(x(36):x(37)-1);
dispout(:,38) = disp(x(37):x(38)-1);
dispout(:,39) = disp(x(38):x(39)-1);
dispout(:,40) = disp(x(39):x(40)-1);
dispout(:,41) = disp(x(40):x(41)-1);
dispout(:,42) = disp(x(41):x(42)-2);
dispout(:,43) = disp(x(42):x(43)-1);
dispout(:,44) = disp(x(43):x(44)-1);
dispout(:,45) = disp(x(44):x(45)-2);
dispout(:,46) = disp(x(45):x(46)-1);
dispout(:,47) = disp(x(46):x(47)-1);
dispout(:,48) = disp(x(47):x(48)-2);
dispout(:,49) = disp(x(48):x(49)-1);
dispout(:,50) = disp(x(49):x(50)-1);
dispout(:,51) = disp(x(50):x(51)-1);
dispout(:,52) = disp(x(51):x(52)-1);
dispout(:,53) = disp(x(52):x(53)-1);
dispout(:,54) = disp(x(53):x(54)-1);
dispout(:,55) = disp(x(54):x(55)-1);
dispout(:,56) = disp(x(55):x(56)-1);
dispout(:,57) = disp(x(56):x(57)-1);
dispout(:,58) = disp(x(57):x(58)-1);
dispout(:,59) = disp(x(58):x(59)-2);
dispout(:,60) = disp(x(59):x(60)-1);
dispout(:,61) = disp(x(60):x(61)-1);
dispout(:,62) = disp(x(61):x(62)-2);
dispout(:,63) = disp(x(62):x(63)-1);
dispout(:,64) = disp(x(63):x(64)-1);
dispout(:,65) = disp(x(64):x(65)-1);
dispout(:,66) = disp(x(65):x(66)-1);
dispout(:,67) = disp(x(66):x(67)-1);
dispout(:,68) = disp(x(67):x(68)-1);
dispout(:,69) = disp(x(68):x(69)-1);
dispout(:,70) = disp(x(69):x(70)-1);
dispout(:,71) = disp(x(70):x(71)-1);
dispout(:,72) = disp(x(71):x(72)-1);
dispout(:,73) = disp(x(72):x(73)-2);
dispout(:,74) = disp(x(73):x(74)-1);
dispout(:,75) = disp(x(74):x(75)-1);
dispout(:,76) = disp(x(75):x(76)-2);
dispout(:,77) = disp(x(76):x(77)-1);
dispout(:,78) = disp(x(77):x(78)-1);
dispout(:,79) = disp(x(78):x(79)-2);
dispout(:,80) = disp(x(79):x(80)-1);
dispout(:,81) = disp(x(80):x(81)-1);
dispout(:,82) = disp(x(81):x(82)-1);
```

```
dispout(:,83) = disp(x(82):x(83)-1);
dispout(:,84) = disp(x(83):x(84)-1);
dispout(:,85) = disp(x(84):x(85)-1);
dispout(:,86) = disp(x(85):x(86)-1);
dispout(:,87) = disp(x(86):x(87)-1);
dispout(:,88) = disp(x(87):x(88)-1);
dispout(:,89) = disp(x(88):x(89)-1);
dispout(:,90) = disp(x(89):x(90)-2);
dispout(:,91) = disp(x(90):x(91)-1);
dispout(:,92) = disp(x(91):x(92)-1);
dispout(:,93) = disp(x(92):x(93)-2);
dispout(:,94) = disp(x(93):x(94)-1);
dispout(:,95) = disp(x(94):x(95)-1);
dispout(:,96) = disp(x(95):x(96)-1);
dispout(:,97) = disp(x(96):x(97)-1);
dispout(:,98) = disp(x(97):x(98)-1);
dispout(:,99) = disp(x(98):x(99)-1);



output_header = {'1k' '2k' '3k' '4k' '5k' '6k' '7k' '8k' '9k' '10k'...
    '11k' '12k' '13k' '14k' '15k' '16k' '17k' '18k' '19k' '20k'...
    '21k' '22k' '23k' '24k' '25k' '26k' '27k' '28k' '29k' '30k'...
    '31k' '32k' '33k' '34k' '35k' '36k' '37k' '38k' '39k' '40k'...
    '41k' '42k' '43k' '44k' '45k' '46k' '47k' '48k' '49k' '50k'...
    '51k' '52k' '53k' '54k' '55k' '56k' '57k' '58k' '59k' '60k'...
    '61k' '62k' '63k' '64k' '65k' '66k' '67k' '68k' '69k' '70k'...
    '71k' '72k' '73k' '74k' '75k' '76k' '77k' '78k' '79k' '80k'...
    '81k' '82k' '83k' '84k' '85k' '86k' '87k' '88k' '89k' '90k'...
    '91k' '92k' '93k' '94k' '95k' '96k' '97k' '98k' '99k' '100k'};
xlswrite([output_file1 '.xlsx'], output_header, 1, 'A1')
xlswrite([output_file1 '.xlsx'],  voltageout, 1, 'A2')
xlswrite([output_file1 '.xlsx'], output_header, 2, 'A1')
xlswrite([output_file1 '.xlsx'], dispout, 2, 'A2')

disp ('DONE!')
```